Statistical Study of the Global Constraints Governing Magnetic Reconnection at the Earth's Magnetopause

Bayane Michotte de Welle

université
PARIS-SACLAY

Statistical Study of the Global Constraints Governing Magnetic Reconnection at the Earth's Magnetopause

Étude statistique des contraintes globales gouvernant la reconnexion magnétique à la magnétopause terrestre

Thèse de doctorat de l'Université Paris-Saclay

École doctorale n° 127 Astronomie et Astrophysique d'Ile de France
Spécialité de doctorat: Astronomie et astrophysique
Graduate School : Physique
Référent: : Faculté des Sciences d'Orsay

Thèse préparée au **Laboratoire de Physique des Plasmas** (Université Paris-Saclay, CNRS, École polytechnique), sous la direction de **Roch SMETS**, Maitre de conférence, et la co-direction de **Nicolas AUNAI**, Chargé de recherche.

Thèse soutenue à Palaiseau, le 22 Mars 2024, par

Bayane Michotte de Welle

Composition du jury:

Membres du jury avec voix délibérative

Frédéric Baudin Astronome, Université Paris-Saclay	Président
Alexis Rouillard Chargé de recherche - HDR, Institut de recherche en astrophysique et planétologie	Rapporteur et examinateur
Benjamin Grison Chargé de recherche - HDR, Institute of Atmospheric Physics, Prague	Rapporteur et examinateur
Aurélie Marchaudon Directrice de recherche, Institut de recherche en astrophysique et planétologie	Examinatrice
Michael Hesse Directeur de recherche, NASA	Examinateur

Thèse de doctorat

NNT: 2024UPASP019

When one sun sinks below the horizon, a thousand suns take its place.

Old Sanskrit verse

Titre: Étude statistique des contraintes globales gouvernant la reconnexion magnétique à la magnétopause terrestre

Mots clés: Reconnexion Magnétique, Magnetopause, Magnétogaine, Magnetosphere

Résumé: La reconnexion magnétique est le mécanisme principal à l'œuvre dans le couplage entre la magnétosphère terrestre et le vent solaire magnétisé. L'efficacité du processus dépend grandement d'où il se déroule sur la magnétopause. La localisation de la ligne X en fonction des propriétés du milieu interplanétaire reste, à ce jour, l'une des questions clés de la physique magnétosphérique en raison de son caractère multi-échelles. L'une des principale difficulté tient dans notre quasi complète méconnaissance de l'environnement plasma et magnétique à grande échelle sur la magnétopause, et comment celles-ci évoluent avec les conditions interplanétaires. Ces propriétés sont aujourd'hui accessibles uniquement au travers de modèles, analytiques ou numériques. Cette thèse apporte de nouvelles contraintes observationnelle au problème de la localisation de la reconnexion en proposant la reconstruction et l'analyse des variations spatiales et grande échelle des variations spatiales du plasma et champ magnétique dans la magnétogaine et sur la magnétopause Un nouvelle méthode est développée afin de collecter et traiter deux décennies de données in-situ des missions Cluster, Double Star, THEMIS et MMS. Nous proposons en premier lieu de reconstruire la structure globale et 3D du champ magnétique drapé dans la magnétogaine, démontrant que l'hypothèse d'un drapé magnétostatique sans courant ne correspond pas aux observations pour environ 30% des orientations du champ interplanétaire. Nous examinons ensuite la variation, dans la magnétogaine, de l'amplitude du champ magnétique et de la densité du plasma, ainsi que leur dépendance en l'orientation du champ interplanétaire, en soulignant leur couplage non linéaire avec la reconnexion à la magnétopause. Enfin, la reconstruction des variations spatiales, sur la magnétopause, du cisaillement magnétique, de la densité de courant et du taux de reconnexion, en fonction de l'orientation du champ interplanétaire et du dipôle terrestre, nous a permis de mieux comprendre les rôles respectifs des contraintes globales et locales dans la localisation possible de la X-line.

Title: Statistical Study of the Global Constraints Governing Magnetic Reconnection at the Earth's Magnetopause.

Keywords: Magnetic reconnection, Magnetopause, Magnetosheath, Magnetosphere

Abstract: Magnetic reconnection is the primary mechanism through which the Earth's magnetosphere couples to the surrounding magnetized solar wind. The efficiency of this coupling largely depends on where the reconnection occurs on the magnetopause. Determining the location of so-called reconnection X-lines, as a function of the upstream interplanetary conditions, remains a long-standing challenge in magnetospheric physics due to its multiscale character. Progress is hampered by the fact that the plasma and field properties that constrain where reconnection can develop on the magnetopause are themselves poorly understood, and so far only accessed through global magnetohydrodynamics simulations. This thesis brings new observational constraints to this problem through the reconstruction of 3D global spatial variations of the plasma and magnetic field on the dayside magnetosheath and magnetopause. A new methodology was developed to collect and process two decades of in-situ measurements from the Cluster, Double Star, THEMIS, and MMS missions. We first reconstructed the global 3D magnetic draping of the interplanetary magnetic field (IMF) in the magnetosheath, whose structure is demonstrated to be controlled by the plasma flow in this region in a way that invalidates widely used vacuum magnetostatic draping assumptions in about 30% of the IMF orientations. We then examine the variation of magnetic field amplitude and plasma density in the magnetosheath and their dependence on the IMF orientation, and highlight their nonlinear coupling with magnetopause reconnection. Finally reconstructions of the spatial distributions magnetic shear, current density and reconnection rate on the dayside magnetopause,for different dipole tilts and IMF orientations, allowed us to better understand the interplay between local and global constraints on the location of reconnection X-lines.

Présentation de la thèse

La magnétosphère terrestre est une région confinée du milieu interplanétaire par une fine couche de courant appelée la magnétopause. Ce confinement à grande échelle peut cependant être brisé par un processus de plasma appelé reconnexion magnétique. En permettant la connexion des lignes du champ magnétique interplanétaire à celles de la magnétosphère, la reconnexion permet l'entrée de masse, d'impulsion et d'énergie dans la magnétosphère.

Au-delà de l'intérêt fondamental qui sous-tend l'étude de ce processus universel, dont les applications vont de la physique solaire aux systèmes astrophysiques exotiques lointains tels que les magnétosphères d'étoiles à neutrons, comprendre les conditions dans lesquelles la reconnexion opère à la magnétopause est d'une importance capitale pour notre capacité à prédire quantitativement l'état global de l'environnement plasma terrestre. Ainsi, la compréhension de la reconnexion magnétique à la magnétopause terrestre peut également être vue comme une étape nécessaire des applications dites de météorologie spatiale.

Cette thèse s'est concentrée sur le problème de la localisation de la reconnexion à la surface de la magnétopause. Il s'agit d'une question d'une importance capitale, car la réponse déterminera l'efficacité du couplage de la magnétosphère à au milieu interplanétaire. Cette question peut sembler relativement simple aux premiers abords reste en fait un défi majeur de la physique magnétosphérique en raison du caractère multi-échelle de la reconnexion magnétique. Nous cherchons à localiser une ligne d'une épaisseur de l'ordre de 10 km sur la surface de la magnétopause terrestre qui s'étend sur environ 100 milliards de kilomètres carrés. Pour compliquer un peu les choses, la magnétopause est constamment en mouvement, oscillant à des vitesses allant jusqu'à 100 kilomètres par seconde. De plus, les grandeurs physiques importantes dans la reconnexion magnétique tel que le champ magnétique sont très variables. En effet, les propriétés du champ magnétique interplanétaire et du vent solaire en amont de la magnetopause varie de manière significative sur des échelles allant de quelques minutes à quelques dizaines de minutes.

Les scientifiques étudient généralement la reconnexion magnétique en utilisant des mesures de satellites in situ. Cela présente un défi en soi, car les données se présentent sous forme de séries temporelles où les variations spatiales et temporelles sont mélangées, et où le caractère local des mesures entrave la compréhension de l'aspect global du système. En conséquence, notre compréhension des aspects globaux de ce problème provient principalement de la modélisation numérique et manque cruellement de contraintes observationnelles.

Ce travail de thèse vise à apporter des contraintes observationnelles à notre compréhension des aspects globaux de la reconnexion magnétique sur le côté jour de la magnétopause. L'idée fondatrice qui motive ce travail est qu'après des décennies de mesures effectuées par de multiples missions spatiales en orbite autour de la Terre, nous disposons désormais d'un volume important de données. Utilisées conjointement, cette masse de données peut apporter des informations précieuses. Ce manuscrit expose nos conclusions au travers des 5 chapitres résumés ci-dessous.

Chapitre 1 : La reconnexion magnétique à la magnétopause terrestre

Nous commencerons par un rapide survol historique, retraçant l'évolution et la convergence de la compréhension des relations Soleil-Terre par la communauté scientifique. Cette rétrospective permettra d'établir les concepts clés essentiels à la compréhension du contenu de cette thèse, telle que l'introduction du vent solaire et du champ magnétique interplanétaire, mais également la façon dont leur interaction avec la magnétosphère structure l'environnement plasma proche de la Terre : l'arc de choc, la magnétogaine et la magnétopause. Ensuite, nous présenterons les concepts sous-jacents au processus de reconnexion magnétique, en détaillant son effet sur la topologie du champ magnétique, et en définissant la notion de ligne X – le long de laquelle la reconnexion se produit – qui est centrale à cette thèse. L'accent sera ensuite mis sur le contexte spécifique de la reconnexion magnétique au sein de la magnétosphère. Nous explorerons le rôle de la reconnexion magnétique dans ce système et passerons brièvement en revue les signatures observationnelles associées à ce phénomène. Après cette introduction, nous nous pencherons sur le problème de

la localisation des lignes X à la magnétopause et procéderons à une revue de la littérature. Cette section présentera les différents modèles et idées proposés au cours du temps, en discutant leurs hypothèses et méthodologies sous-jacentes, ainsi que leurs degrés de cohérence entre eux.

Chapitre 2 : Méthodologie globale

Le défi central de ces travaux de thèse consiste à utiliser des données in situ pour reconstruire une perspective globale tridimensionnelle du côté jour de la magnétopause terrestre. Cet objectif a nécessité un traitement relativement important des données et de développer des méthodologies innovantes, souvent basées sur l'apprentissage automatique. Ce deuxième chapitre détaille la méthodologie commune à toutes les études réalisées dans le cadre de cette thèse.

Chapitre 3 : Drapé du champ magnétique dans la magnétogaine

L'un des paramètres les plus importants dans la reconnexion magnétique est le cisaillement du champ magnétique de part et d'autre de la magnétopause. Alors que la géométrie du champ est plutôt bien comprise du côté magnétosphérique, son orientation est moins bien connue du côté de la magnétogaine. À grande échelle, le champ magnétique interplanétaire ne peut pas pénétrer la magnétosphère, il se drape donc autour de la magnétopause. La manière dont ce drapé se produit, en fonction de l'orientation du champ magnétique interplanétaire, détermine le cisaillement du champ magnétique à la magnétopause, et représente donc la première contrainte sur la reconnexion à l'échelle globale de la magnétopause. Malgré des décennies d'études, notre compréhension de la manière dont le champ magnétique se drape autour de la magnétopause reste incomplète en raison du caractère local des données des satellites. Le chapitre 3 détaillera comment nous avons reconstruit la structure 3D globale du drapé du champ magnétique et identifiés trois régimes principaux. Parmi ceux-ci un en particulier, représentant environ 30% de toutes les conditions du champ magnétique interplanétaire, remet en question la façon habituelle dont les lignes de reconnexion magnétique sont modélisées sur la magnétopause. Les résultats de cette étude ont été publiés dans la revue à comité de lecture Journal of Geophysical Research Space Physics en 2022.

Chapitre 4 : Empilement magnétique et déplétion du plasma dans la magnétogaine

L'orientation du champ magnétique n'est pas le seul élément important contraignant la reconnexion magnétique. La vitesse d'évolution du processus, appelée taux de reconnexion, dépend également de manière critique du saut d'amplitude du champ magnétique et de la densité de plasma de part et d'autre la couche de courant. Au contact de la magnétosphère, le vent solaire est fortement ralenti. Le champ magnétique et plasma s'empilent sur la magnétopause, avant d'être en partie transmis par reconnexion à travers la magnétopause et, pour la majorité, déviés dans les flancs de la magnétogaine. Le chapitre 4 vise à appliquer la même méthodologie que le chapitre 3, mais cette fois-ci pour reconstruire la distribution spatiale de l'amplitude du champ magnétique et de la densité de plasma à travers la magnétogaine, et en particulier à proximité de la magnétopause. Ce chapitre révèle comment l'accumulation de flux magnétique dépend de l'orientation du champ magnétique interplanétaire. Les résultats révèlent également clairement l'existence d'une couche déplétion du plasma et sa relation causale avec l'empilement magnétique. Enfin, le chapitre examine les asymétries se développant entre les côtés quasi-perpendiculaires et quasi-parallèles de la magnétogaine, mettant notamment en avant les raisons pour lesquelles le rôle critique de l'orientation du champ magnétique interplanétaire a échappé travaux antérieurs. Les travaux détaillés dans ce chapitre sont, au moment de la rédaction de ce manuscrit, majoritairement abouti et feront l'objet d'un article qui sera soumis pour publication dans les prochains mois.

Chapitre 5 : Contraintes globales sur la reconnexion magnétique à la magnétopause

Les chapitres 3 et 4 nous ont permis d'acquérir une bien meilleure compréhension de l'aspect global de la magnétogaine diurne. En utilisant des techniques similaires de collecte de données dans la magnétosphère, le chapitre 5 sera alors en mesure de reconstruire les distributions spatiales de quantités clés pour la reconnection magnétique. Plus précisément, les travaux de ce chapitre porteront tout d'abord sur la construction à la magnétopause de cartes de l'angle de cisaillement magnétique, de la densité de courant et de l'estimation du taux de reconnexion, en fonction de l'orientation du champ magnétique interplanétaire et de l'angle d'inclinaison du dipôle. Ces travaux montrent que, bien qu'elles soient évidemment corrélées entre elles, les distributions spatiales des quantités susmentionnées ne sont pas structurées de la même manière. Par conséquent, les lignes X modélisées à partir des distributions de ces quantités peuvent présenter des différences significatives que ce chapitre explique et discute. Les résultats obtenus dans ce chapitre ont été soumis pour publication dans le Journal of Geophysical Research Space Physics et sont actuellement en cours d'évaluation.

Remerciements

Rêver un impossible rêve
Porter le chagrin des départs

La quête - Jacques Brel

Alors que cette importante journée de ma vie se clôt, je ressens énormément de gratitude d'avoir été entourée de personnes si importantes pour moi.

D'abord, mon directeur de thèse, Nicolas, qui a toujours été là pour me guider et me faire éviter les écueils qui guettent les jeunes, et des fois les moins jeunes, doctorants. Maintenant je pars voguer vers d'autres horizons et j'espère que je saurai me montrer à la hauteur de tes enseignements. Ton soutien a été inestimable, je t'en serai toujours reconnaissante. Aux futurs doctorants qui auront la chance de travailler sous sa direction : ne vous laissez pas tromper par son humour irrévérencieux et l'air un peu bourru qu'il s'amuse parfois à prendre. Je vous assure, vous ne pourriez pas trouver de meilleur directeur de thèse.

À Alexis, qui, car il est parfois réticent à accepter les remerciements, lira sûrement ces mots en haussant les épaules et affirmant qu'il ne faisait que son travail : je te suis très reconnaissante pour m'avoir apporté ton aide depuis mes débuts au laboratoire. Merci également pour toutes ces conversations stimulantes.

Je tiens également à dire un grand merci à Roch qui a accepté d'être mon directeur officiel de thèse. Merci à Gérard pour son humour pince-sans-rire, et surtout pour le sérieux avec lequel il a répondu aux questions que j'ai pu poser lors de mes passages souvent impromptus dans son bureau. Merci également à Benoit Lavraud et Vincent Génot qui à distance ont suivi l'évolution de mes travaux et m'ont prodigué de précieux conseils. J'ai une pensée particulière pour Gautier, qui m'a précédé en thèse, ainsi qu'à Ambre, qui prend maintenant la relève. J'ai particulièrement aimé travailler avec vous et j'espère que le futur nous réserve de nombreuses collaborations.

Un grand merci à l'équipe des plasmas spatiaux – et à Etienne, qui en était le responsable pendant la majeure partie de ma thèse – pour avoir financé ma participation à de nombreuses conférences.

Je tiens particulièrement à exprimer ma gratitude à Marilyne pour sa constante bienveillance et son soutien. Un grand merci également à Cherifa et au reste de l'équipe administrative pour leur aide.

Je souhaite remercier de manière générale toutes les personnes du laboratoire (Nadjirou, Pierre, Olivier, Fouad, Malik, Lina, Bruno, Saé, etc.) qui font du LPP un lieu si accueillant. Grâce à vous, le laboratoire est devenu comme une seconde maison pour moi, parfois de manière un peu trop littérale !

Anna et Tarek (mon partenaire de crime), vous rencontrer a été une des plus grande joie de ma thèse. Je sais que votre soutien a eu un impact majeur sur ma capacité à franchir les différentes épreuves du doctorat, qui, soyons honnêtes, n'est pas toujours facile. Je tiens également à saluer tous les autres doctorants, et maintenant amis, que j'ai pu rencontrer ces dernières années : Giulio, Paco, Pauline, Benoît, Renaud, Davide, Vincent, Xue, et bien d'autres.

Finalement, je tiens également à remercier chaleureusement Alexis Rouillard et Benjamin Grison pour avoir accepté le rôle de rapporteurs pour ma thèse, ainsi qu'Aurélie Marchaudon, Michael Hesse et Frédéric Baudin pour avoir accepté de faire partie du jury de thèse.

Je tiens à exprimer ma plus profonde gratitude à ma famille : à mon père, qui m'a insufflé très jeune la soif d'apprendre, et à ma mère, qui a toujours cru en moi. Un merci tout spécial à mes deux frères, Yacin et Madyan, qui sont mes piliers. Je ne serais pas là où je suis aujourd'hui sans vous, et je souhaite que, quoi que l'avenir me réserve, je puisse continuer à vous rendre fiers de moi. Je remercie également mes deux belles-sœurs pour leur soutien et leurs précieux conseils.

À Saha et Jeanna, on ne peut pas rêvé meilleures amies, je vous remercie pour votre soutien constant et de faire partie de ma vie. Jordi, bien que nous ne parvenions à nous voir pas plus de deux fois par an, ces deux jours sont extrêmement importants pour moi. Lucas, merci d'avoir écouté mes plaintes et mes espoirs concernant mes travaux pour lorsque qu'on rentrait du labo. Ton soutien à été très important à pour moi. À Clementine, merci pour ta présence et ton humour mon amie. À Marion, parce qu'on en a fait du chemin depuis la L2. Je tiens à faire une mention spéciale à Saha et Clémentine, car peu de gens ont la chance d'avoir des amies qui traversent le globe pour assister à une soutenance de thèse. Je tiens également à saluer et a remercier tout mes amis: Bachra, Anaé, Julie, Albertine, Yehudi, Rémi, Sarah, etc.

À tous ceux que j'ai déjà nommés, ainsi qu'à ceux que je n'ai pas mentionnés mais qui se reconnaîtront : merci encore.

Contents

Thesis Overview

The Earth's magnetosphere is the region confined from the interplanetary medium by a thin current layer called the *magnetopause*. This large scale confinement can, however, be broken by a plasma process called *magnetic reconnection*. By enabling the connection of Interplanetary Magnetic Field (IMF) lines to those of the magnetosphere, reconnection allows the loading of mass, momentum and energy within the magnetosphere.

Besides the fundamental interest underlying the study of such a universal process whose applications range from solar physics to remote exotic astrophysical systems such as neutron star magnetospheres, understanding the conditions under which reconnection operates at the magnetopause is of critical importance regarding our ability to quantitatively predict the overall state of the Earth's plasma environment. Understanding reconnection of magnetic fields at the Earth's magnetopause can also thus be seen as a necessary milestone upstream of so-called *space weather* applications.

This thesis has been focused on the specific but important problem of understanding where reconnection occurs on the magnetopause surface. A question that is of critical importance since the answer will determine how efficiently the magnetosphere couples to its environment. This question, which may seem relatively simple, is still challenging us today, owing to its multi-scale character and could be seen as the space equivalent of finding the needle in the haystack. We are here looking for localizing a line whose thickness is of the order of 10km, on a surface, the Earth's magnetopause, that is immense, as it spans over approximately 100 billion square kilometers. To complicate things a bit, our haystack, the magnetopause, is always moving back and forth and oscillates, at speeds up to 100 kilometers per second. Additionally, the boundary itself is highly dynamical, with the orientation of the IMF and the properties of the upstream solar wind varying significantly within minutes to tens of minutes.

Scientists typically tackle this challenge using in-situ spacecraft measurements, another challenge in itself since data takes the form of time series where spatial and temporal variations are mixed, and where the local character of the measurements hampers the understanding of the global aspect of the system. Consequently, our understanding about these global aspects of the problem mainly emanate from numerical modeling and critically lack observational constraints.

This thesis aims at bringing new constraints, from a purely observational standpoint, to our understanding of the global aspects of magnetic reconnection on the dayside magnetopause. The founding idea motivating this work is that, after decades of measurements throughout multiple missions orbiting the Earth in various orbital and solar wind conditions, we now have accumulated a substantial volume of data. Used together, this massive amount of data may bring invaluable insights. This manuscript tries to relate our findings through 5 chapters that the following sections now summarize.

Chapter 1: Magnetic Reconnection at the Earth's Magnetopause

The first chapter of this thesis lays the foundational concepts necessary for understanding the work presented herein. We begin with a swift historical overview, tracing how the scientific community's understanding of Sun-Earth relations has evolved and converged to its current state. This retrospective will establish key concepts essential to our study, such as introducing what the solar wind and the IMF are and their properties, and above all how their interaction with the magnetosphere structures the near Earth plasma environment: the bow shock, magnetosheath, and magnetopause. Then, we will introduce the concepts underlying the process of magnetic reconnection, detailing its effect on the magnetic field topology and defining the notion of X-line - along which reconnection occurs - that is central to this thesis. The focus will then shift to the specific context of magnetic reconnection within the magnetosphere. We will explore the role of magnetic

reconnection in this system and briefly review the observational signatures associated with this phenomenon. Following this introduction we will delve into the X-line location problem and conduct a literature review. This section will present various models and ideas proposed along time, discussing their underlying assumptions and methodologies, as well as to what extent they are consistent with one another.

Chapter 2: Global Methodology

The important challenge of this thesis consists in using in-situ data to reconstruct a global three-dimensional perspective of the Earth's dayside magnetosphere. This objective has necessitated a fair amount of data processing and innovative methodologies, often based on machine learning, that are common to all studies made in this thesis, that will be presented - in extensive detail - throughout the second chapter.

Chapter 3: Magnetic Draping in the Magnetosheath

Chapter 3 will constitute the first scientific work of this thesis. The most important property of reconnecting systems stands in the localized shear of the magnetic field orientation. The magnetopause itself, is the boundary where the magnetic field is sheared between the IMF and the magnetospheric field. While the geometry of the field is rather well understood on the magnetospheric side of the boundary, its orientation is less well known on the magnetosheath side. The IMF, on large scale, cannot penetrate the magnetosphere, therefore drapes around the magnetopause. The detailed way this draping occurs, as a function of how the IMF is orientated, critically determines how the magnetic field is sheared at the magnetopause, and therefore represents an important, if not the first, global scale constraint on reconnection occurring there. Despite decades of studies, our understanding of this global scale properties has remained rather coarse and fragmented owing to the local character of spacecraft data. Chapter 3 will detail how we have reconstructed the 3D global structure of the draping and identified three main regimes of draping patterns, among which, one in particular, representing about 30% of all IMF conditions, challenges the usual way magnetic reconnection lines are modeled on the magnetopause. Results of this study have been published in the peer-reviewed Journal of Geophysical Research Space Physics in 2022.

Chapter 4: Magnetic Pileup and Plasma depletion Layer in the Magnetosheath

The orientation of the magnetic field is not the only important aspect constraining magnetic reconnection. The speed at which the process evolves, the so-called *reconnection rate*, also critically depends on the jump in the magnetic field amplitude and plasma density across the current layer. As it impacts the magnetosphere, the solar wind slows down and piles-up onto the obstacle along with the magnetic flux, before being partly transmitted through reconnection across the magnetopause and, for the most part, deflected around the system. The pileup of plasma density and magnetic flux, in the magnetosheath, is, like for the draping pattern, not well understood nor constrained from a global and observational perspective. The goal of Chapter 4 is to apply the same methodology as Chapter 3, but this time to reconstruct the spatial distribution of the magnetic field amplitude and plasma density throughout the magnetosheath, and in particular adjacent to the magnetopause. This chapter reveals how the magnetic flux pileup depends on the IMF orientation. Results also clearly reveal the existence of the so-called Plasma Depletion Layer and its causal relationship with the magnetic pileup, for different IMF orientations. Finally, the chapter examines the effects underlying the spatial asymmetries developing between the quasi-perpendicular and quasi-parallel sides of the magnetosheath, in particular putting forwards the reasons why previous works have missed the critical role of the IMF orientation. The work detailed in this chapter has, at the moment this manuscript is written, mostly converged and will be formally written in an article submitted for publication in the forthcoming months.

Chapter 5: Global Constraints on Magnetic Reconnection at the Magnetopause

Chapters 3 and 4 have allowed us to gain a much better understanding of the global aspect of the dayside magnetosheath. Using similar techniques for gathering data in the magnetosphere, chapter 5 will then be in a position to reconstruct detailed maps of key quantities on the magnetopause itself. More specifically, the work in this chapter will first of all focus on building magnetopause maps of the magnetic shear angle, current density, and reconnection rate estimate, as a function of the IMF orientation and dipole tilt angle. This work then shows that, while they are obviously correlated with one another, the spatial distribution of the aforementioned quantities, are not structured the same way. As a result, candidate X-lines whose location are obtained from these distributions can show significant differences which this chapter explains and discuss. Results obtained in this chapter have been submitted for publication in Journal of Geophysical Research Space Physics, and are currently in review.

Chapter 1

Magnetic Reconnection at the Earth's Magnetopause

Contents

1.1 Sun-Earth relations

This section aims to introduce the plasma environment at Earth based on discoveries made by the scientific community. It should be noted that this is not an exhaustive historical account and does not delve into scientific controversies; rather, it focuses on advancements that have led to our current understanding of this plasma environment. A more detailed and comprehensive overview can be found in the following reviews, which were the primary sources of information for this section [Akasofu, 2015; Cowley, 2016; Kane, 2005; Lakhina and Tsurutani, 2016; Owens and Forsyth, 2013; Parker, 2001; Song and Russell, 1997; Stern, 1989].

1.1.1 Early observations of Sun-Earth interactions

Research on the interaction between the Sun and the Earth really began in the 19th century. In 1808, von Humboldt measured significant magnetic disturbances in the Earth's magnetic field and concomitantly observed the presence of aurorae borealis [von Humboldt, 1808]. These observations led him to suggest a connection between the two phenomena and to coin the term *magnetic storm*. Schwabe [1843] identified the solar cycle with a period of approximately 10 years through a study of the evolution of sunspots on the Sun's surface. Few years later, Lamont [1851] observed disturbances in the daily magnetic declination variations that lasted for approximately 10 years. However, at that time, Lamont did not make any connection with the solar cycle. Only a year later, Sabine [1852] made the connection and demonstrated the relationship between sunspot maxima and minima and the observed magnetic disturbances, making him the first to successfully correlate the occurrence of magnetic storm with the solar activity. In 1859, Carrington made the first well-documented observation of a solar flare [Carrington, 1859]. He observed a short-lived, intensely bright, and white light on the surface of the Sun. A day later, following this observation, the Earth experienced the largest geomagnetic storm ever reported in modern history. However, Carrington hesitated to definitively establish a causal link between the two events, suggesting it might be coincidental. Fast forward to the early 20th century, Maunder [1905] observed a recurring 27-day period in geomagnetic disturbances and linked it to solar activity. Maunder proposed that this phenomenon originated from restricted magnetic active areas on the Sun, which rotated with the solar surface. Bartels [1932] investigated this recurring 27-day period in geomagnetic disturbances. He noted that this period did not correspond to any visible features on the Sun, speculating that it might arise from regions that were not observable through direct astrophysical methods. These regions were later identified as uni-polar magnetic regions (i.e. coronal holes) [Ness and Wilcox, 1965]. Finally, it took the scientific community more than a century from its early observations to definitely establish the relationship between geomagnetic activities and the solar activity (e.g. Hale [1931]; Newton [1943]; Snyder et al. [1963]).

1.1.2 Solar wind and interplanetary magnetic field: interaction vectors

It was towards the end of the 19th century that the idea of the interplanetary medium potentially containing charged particles first emerged. Goldstein [1881] hypothesized, while studying electric discharge in dilute gases, that the sun emits charged particles into space which could be the source of electric and magnetic phenomena at Earth. Birkeland [1901] conducted a study known as the *Terrella* experiment, whereby a small spherical electromagnet was exposed to a current of cathodic rays (i.e. electron flux), resulting in findings exhibiting similarities in form and nature to the aurora phenomenon. Initially assuming that the source of the electron flux could come from the upper atmosphere of the Earth, he later suggested that aurora was a direct result of electron beam produced by the Sun. Stormer [1918] supported this hypothesis by computing particle trajectories between the Sun and the Earth, revealing that charged particles are confined to the polar regions of the Earth. However, Lindemann [1919] disputed this theory, stating that the electrostatic repulsion between the electrons would disperse the beam before it could reach the Earth. He proposed instead that it should be a neutral ionised stream of particles. Upon observing the

comets' tail consistently pointing away from the sun, Biermann [1951] proposed that the sun emits a continual flow of particles with a velocity of 500 to 1500 km.s^{-1} and a ion density of 500 cm^{-3}. Parker [1958] demonstrated that the Sun's atmosphere, given the gravitational force and the pressure gradient, is not in hydrostatic equilibrium but instead continuously expels a plasma stream. He further established that the characteristic of Biermann [1951]'s outflow would be consistent with the observed temperature of the solar corona. He named this plasma flow from the Sun the *solar wind*. However, his theory faced significant opposition until the first in-situ measurements definitively confirmed its validity. Lunik 2, launched in 1959, measured a continuous stream of high-speed ions, but did not provide velocity measurements [Gringauz et al., 1960]. Later, Explorer 10 measured ion velocities between 120 and 660 km.s^{-1} generally away from the Sun and ion densities between 6 and 20 cm^{-3} [Bridge et al., 1962]. It is, however, now believed that the spacecraft never reached the undisturbed interplanetary medium. Therefore, the Mariner 2 probe made the first plasma measurements of the pristine solar wind, measuring ion velocities between 400 and 700 km.s^{-1} always away from the Sun [Neugebauer and Snyder, 1962].

The discovery of the IMF was even more elusive than that of the solar wind. It was not until 1949 that the presence of a large-scale magnetic field, causing the polarization of starlight due to its effect on non-spherical dust, in the interstellar medium was discovered [Hall, 1949; Hiltner, 1949], and it was thought to extend into the interplanetary medium. However, this hypothesis was challenged by Davis [1955]), who, using the Biermann [1951] solar wind characteristic, estimated that the interstellar magnetic field could not reach a distance smaller than several hundred Astronomical Unit (AU) from the Sun. The following year, Morrison [1956] theorized that a magnetic field tangled in a plasma cloud be emitted by the Sun, whose magnetic field had been discovered a few decades earlier by observing Zeeman effects in sunspots [Hale, 1908]. In his 1958 article, Parker proposed that the expansion of the solar corona would cause the Sun's magnetic field to extend into the interplanetary medium [Parker, 1958]. Furthermore, he proposed that the Sun's rotation would structure the magnetic field lines into a spiral, as shown in Figure 1.1, now known as the *Parker spiral*. The Mariner 2 spacecraft was not magnetically clean due to the presence of active current loops and magnetic structural material. As a result, it was only able to provide measurements of the fluctuations of the magnetic field [Davis, 1965]. The Interplanetary Monitoring Platform 1 (IMP1) probe provided the first in-situ measurements of the IMF with an average magnetic field amplitude of approximately 6 nT [Ness and Wilcox, 1964]. It was then discovered that during the 27-day rotation period of the Sun, the IMF would point toward or away from the Sun in successive periods of about one week corresponding to approximately four *sectors* co-rotating with the Sun [Ness and Wilcox, 1964; Wilcox and Ness, 1965]. Schulz [1973] interpreted these away and toward sectors as related to the presence of a Heliospheric Current Sheet (HCS) produced by the dominant dipole and weaker higher-order components of the Sun magnetic field. If the measurement is taken on the positive (resp. negative) polarity side of the HCS, the IMF is more likely to point away (resp. toward) from the Sun.

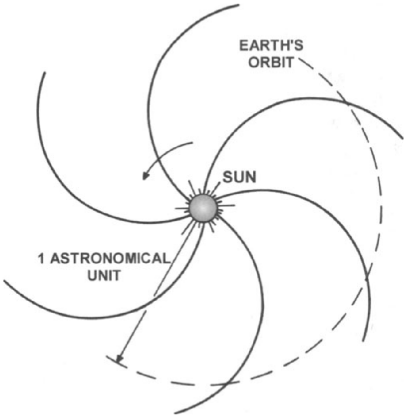

Figure 1.1: Projection onto the solar ecliptic plane of the magnetic field lines of the Parker spiral. Figure from Bittencourt [2004]

Figure 1.2 displays the distributions of various physical properties of the solar wind and IMF over more than 25 years of the OMNI data (see Section 2.3.5). At approximately 1 AU, the average velocity and ion density of the solar wind are about 400 km.s^{-1} and 5 cm^{-3}, respectively, resulting in an average dynamical pressure of 2 nPa. An important characteristic of the solar wind is that it propagates at supersonic speed in the interplanetary medium. The average amplitude of the IMF is about 5 nT. The distribution of the B_x component has two maxima, which are related to the aforementioned away (i.e. negative values of B_x) and toward (i.e. positive values of B_x) sectors

of the IMF. The IMF B_y component measurements are split into two distributions depending on whether their associated B_x component is negative or positive. Positive B_y values are primarily associated with negative B_x values and vice versa due to the orientation of the magnetic field lines in the Parker spiral (see Figure 1.1). The distribution of B_z by the IMF corresponds to a Gaussian centered on zero, indicating that the magnetic field in the ecliptic plane is predominantly eastward or westward.

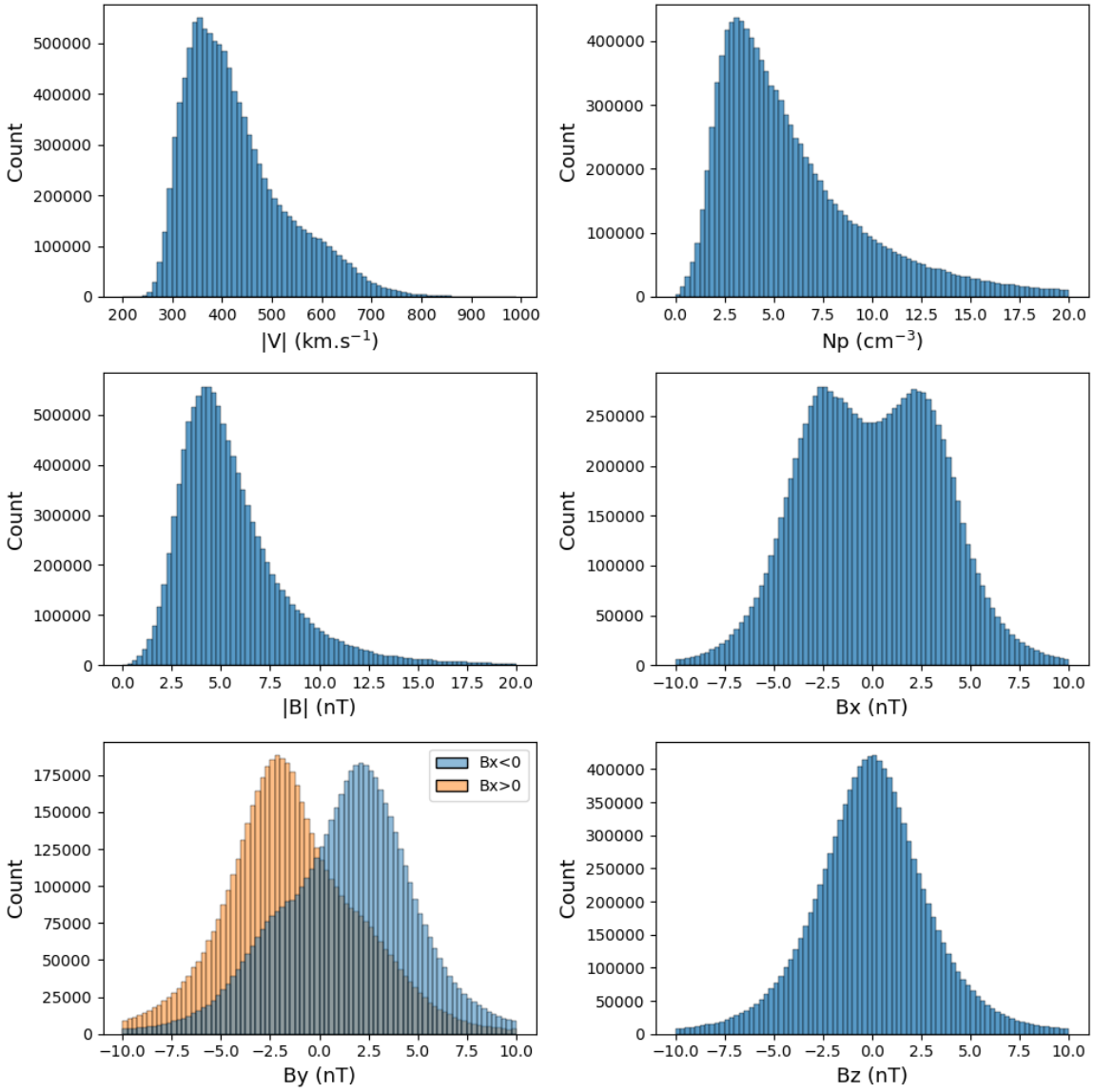

Figure 1.2: Distribution of the solar wind and IMF parameters of the OMNI database between 1995 and 2021: the velocity |V| (top left), the proton density Np (top right), the amplitude of the IMF |B| (middle left), the IMF B_x component (middle right), the IMF B_y component (bottom left), and the IMF B_z component (bottom right). The measurements of the By component are separated into two distributions based on whether their associated B_x component is negative or positive.

1.1.3 The plasma environment of the Earth: close to open magnetosphere

It was discovered in the late 16th and early 17th centuries that the Earth possesses a magnetic field [Gilbert, 1600]. Based on Lindemann [1919]'s suggestion, that the Sun emits neutral beams of ionized particles, Chapman and Ferraro [1930, 1931a,b] hypothesized that it would compress the Earth's magnetic field to form a comet-shaped cavity. At the time, this magnetic cavity —called

the *magnetosphere* only about 30 years later [Gold, 1959]— was considered transient as the particle streams were believed to occur only sporadically. The suggestion by Parker [1958] that the Sun continuously emits a plasma stream rectified this assumption. However, at that time, it was believed that the magnetosphere was closed to the solar wind, except in the magnetospheric cusp, which would be deflected by the Earth's magnetic field, as shown in Figure 1.3.

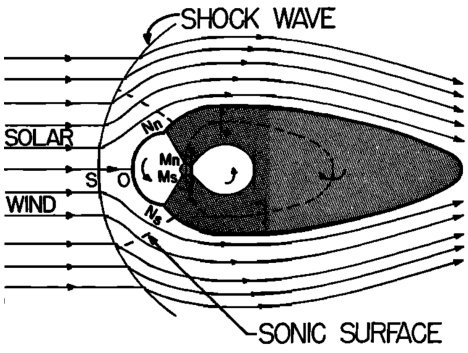

Figure 1.3: Schematic of the closed magnetosphere in the noon meridional plane. Figure from Kellogg [1962].

The presence of the *bow shock* upstream of the magnetosphere was independently described by Axford [1962]; Gold [1962]; and Kellogg [1962] (Figure 1.3). However, Zhigulev [1959] seems to have been the first to intuit the existence of this standing shock wave but this information remained to be verified as the article is no longer online. The bow shock forms because the magnetosphere impedes the supersonic propagation of the solar wind, which decelerates abruptly, leading to the formation of the collisionless shock wave. Downstream of the bow shock, which constitutes the boundary delimiting the near-Earth plasma environment, the subsonic solar wind is deflected and flows around the magnetosphere. Although the presence of the bow shock indicates the existence of a region between the pristine interplanetary medium and the magnetosphere, this region was only referred to as the *magnetosheath* in Dessler and Fejer [1963]. The average subsolar distance of the bow shock is about 13 Re (i.e. Earth radius = 6371 km) upstream of the Earth [Formisano, 1979; Jelínek et al., 2012; Jeřáb et al., 2005].

The term *magnetopause* was first introduced by Sonett and Abrams [1963] to describe the "magnetospheric-interplanetary transition region" (i.e. the magnetosheath). However, the term was quickly adapted to describe the outer boundary of the magnetosphere [Dessler and Fejer, 1963]. This boundary forms due to the inability of two highly conductive plasma with distinct magnetic fields, such as the shocked solar wind and the magnetosphere, to intermix as demonstrated by Alfvén [1942] in his frozen-in theorem. Consequently, after being modified while crossing the bow shock [Mihalov et al., 1969], the IMF propagates through the magnetosheath and drapes around the magnetosphere [Behannon and Fairfield, 1969; Fairfield, 1967]. The difference in magnitude and orientation between the magnetic fields of these two regions forms the current layer known as the magnetopause. The location of the magnetopause arises from the pressure equilibrium between the shocked solar wind and the magnetosphere. The highly dynamic nature of the upstream solar wind parameters leads to substantial variability in the boundary's position. The average subsolar distance (i.e. along the Sun-Earth axis) of the magnetopause is typically located approximately 10 Re upstream of Earth [Jelínek et al., 2012; Lin et al., 2010; Shue et al., 1998].

In the late 1940s, Giovanelli [1947, 1948] postulated that solar flares could result from the presence of magnetic neutral points, which would allow electron acceleration in the presence of large-scale electric fields. This theory led Hoyle [1949] to suggest that the magnetic field carried by ionized beams emitted from the Sun could create neutral points upon interacting with Earth's magnetic dipole. He further proposed that particles accelerated at these neutral points could be responsible for the aurora phenomena. Dungey [1961], Hoyle's PhD student, building upon his previous studies of this acceleration mechanism [Dungey, 1953, 1958], proposed what is now known as the *Dungey cycle* which will be explain in more detailed in Section 1.2.2. Figure 1.4 depicts

Dungey's theory, suggesting that an *"interplanetary field pointing roughly southward"* would lead to the formation of neutral points on both the dayside and nightside of the magnetosphere and that the magnetic field lines would *"have both, one, or no feet on the ground, the other ends going to infinity"*. This theory introduces a change in the connectivity and topology of magnetic field lines in a process that would later be termed *magnetic reconnection*. A significant outcome of this phenomena is the opening of the magnetopause, which permits matter, momentum, and energy from the interplanetary medium to enter into the magnetosphere. Consequently, this led to a shift in our understanding from a closed magnetosphere to an open magnetosphere paradigm.

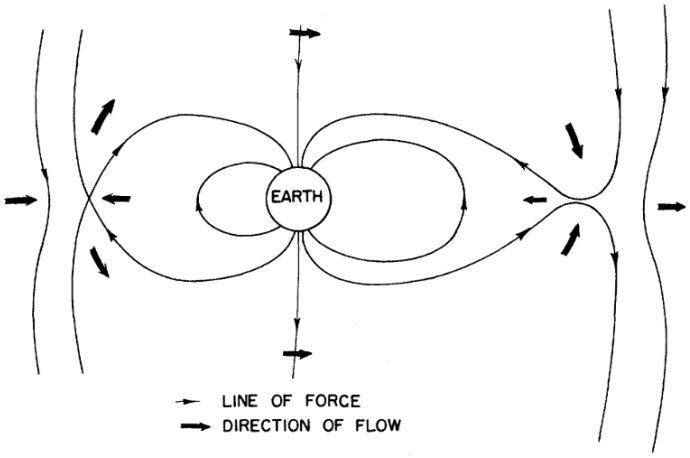

Figure 1.4: Schematic of the open magnetosphere in a plane containing neutral points. Figure from Dungey [1961].

As the number of spacecraft has grown and the quality of their measurements improved, our understanding of the various regions of the magnetosphere has correspondingly expanded. As shown in Figure 1.5, the magnetosphere is constituted by:

- The *polar cusps* are regions where Earth's dipolar magnetic field fans out from the magnetic poles of the Earth.
- The *lobes* are regions characterized by open magnetic field lines -lines that penetrate the Earth's surface on one end while extending into interplanetary space on the other- predominantly extending in tail of the magnetosphere (i.e. the *magnetotail*).
- The *plasma sheet* is a current sheet produced by the orientation, Earthward in the northern hemisphere and anti-Earthward in the southern hemisphere, of the magnetic fields in the magnetotail.
- The *plasmasphere* is a dense and cold plasma of the magnetosphere, is situated just outside the ionosphere.
- The *Van Allen radiation belts* correspond to regions where energetic particles trapped on closed magnetic field lines.

Figure 1.6 gives an example of in-situ spacecraft data measured in the near-Earth environment. The data show the signatures typically seen in an outbound trajectory from the magnetosphere to the solar wind, going through the magnetosheath region. The magnetosphere is characterized by the strongest magnetic field amplitude, lowest density, and most stagnant plasma of all three regions. The solar wind is easily recognized as a comparatively dense plasma flowing at supersonic speed during the last part of the time interval. The magnetosheath is the region in between these two, downstream of the bow shock where the plasma is heated, compressed and flows around the obstacle after having been decelerated to a subsonic speed. In that region, the magnetic field

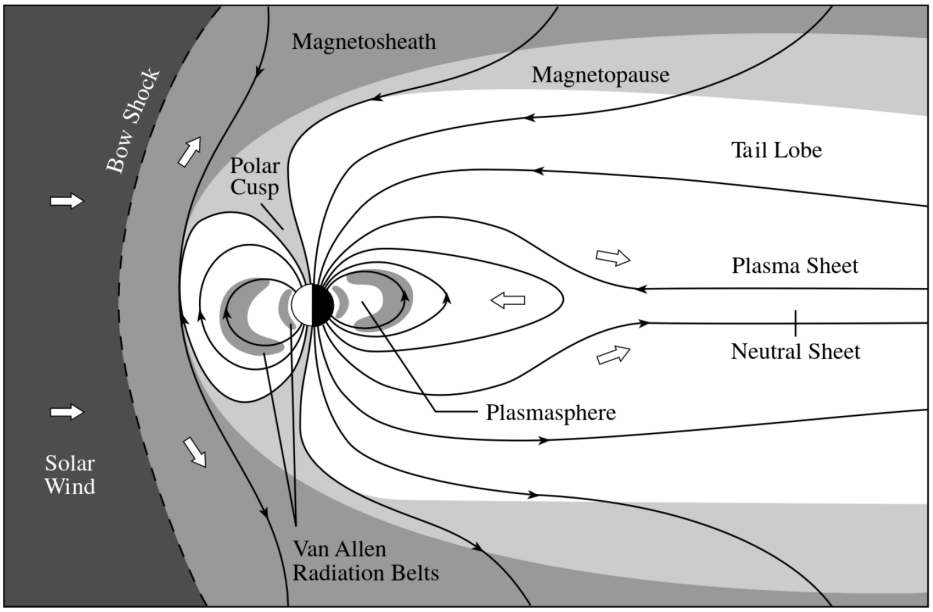

Figure 1.5: Schematic of near-Earth plasma environment in the meridional plane. Figure from Lang [2011].

increases in amplitude and drapes around the magnetopause. Tables 1.1 and 1.2 present the typical values of the physical parameters in the subsolar magnetosphere and magnetosheath, respectively.

Magnetospheric parameter	Typical value
n_{msp} (cm^{-3})	0.1
B_{msp} (nT)	56
$T_{i,msp}$ ($\times 10^5$ K)	2.4×10^3
$C_{A,msp}$ (km/s)	3.9×10^3
β_{msp}	0.27

Table 1.1: Typical values of magnetospheric parameters at Earth's subsolar magnetopause [Cassak and Fuselier, 2016]. n , B, T_i, C_A, and β correspond to the density, magnetic field amplitude, ion temperature, Alfven velocity, and plasma beta, respectively.

Magnetosheath parameter	Mean	Median
n_{msh} (cm^{-3})	34.8	27.6
B_{msh} (nT)	24.8	22.4
$T_{i,msh}$ ($\times 10^5$ K)	12	9.5
$C_{A,msh}$ (km/s)	92	93
β_{msh}	2.4	1.8

Table 1.2: Typical values of magnetosheath parameters at Earth's subsolar magnetopause derived from average properties of the solar wind [Cassak and Fuselier, 2016]. n , B, T_i, C_A, and β correspond to the density, magnetic field amplitude, ion temperature, Alfven velocity, and plasma beta, respectively.

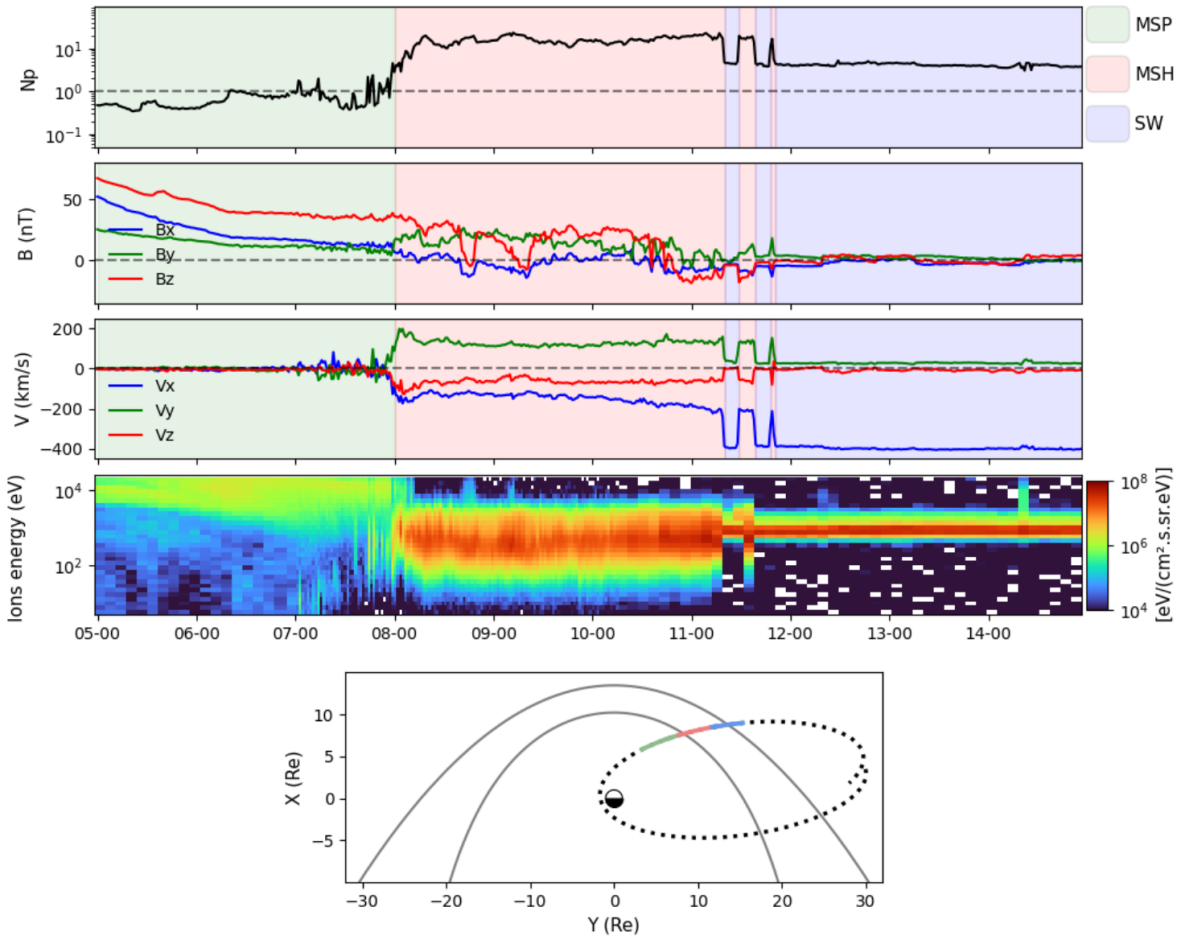

Figure 1.6: In-situ data and orbit from THEMIS B probe on 16 May 2008. From top to bottom are represented: the ion density, the magnetic field components, the velocity components, the omnidirectional energy fluxes of ions and the orbit of the probe on a 5-day period with the dotted line. The green, red, and blue color filling and line colors correspond to measurement in the magnetosphere, magnetosheath and solar wind respectively. In the last panel, the bow shock [Jelínek et al., 2012] and magnetopause [Shue et al., 1998] are represented as solid gray lines.

1.2 Magnetic reconnection

Magnetic reconnection is a ubiquitous process across various astrophysical magnetic environments, including the solar corona [Klimchuk, 2006; Leake et al., 2020; Priest, 1997, 1998; Yokoyama and Shibata, 1996], planetary magnetospheres [Eastwood et al., 2008; Fuselier and Lewis, 2011; Grodent et al., 2004; Louarn et al., 2015; Slavin et al., 2009], the heliopause [Cairns and Fuselier, 2018; Lavraud et al., 2023; Macek, 1989; Nickeler and Fahr, 2005], accretion disks [Kadowaki et al., 2018; Ripperda et al., 2020; Santos-Lima et al., 2012], and compact object magnetospheres [Bransgrove et al., 2021; Carrasco et al., 2021; Komissarov, 2006; Most and Philippov, 2023]. This process has two crucial aspects: firstly, it enables the transfer of matter, momentum, and energy between different plasma environments. Secondly, it converts magnetic energy into thermal and bulk kinetic energy.

1.2.1 Concept of magnetic reconnection

The concept of magnetic reconnection was first introduced by Dungey [1953] as a mechanism for particle acceleration. Figure 1.7 shows a standard picture of this process in the reconnection plane in 2D. Reconnection involves two plasmas with magnetic fields, $\mathbf{B}_1$ and $\mathbf{B}_2$, sheared over a short distance, resulting in the existence of a so-called current sheet in the (XZ) plane. The presence of anti-parallel components in these magnetic fields enables the field lines to "break" and "recon-

nect" with one another. Such interaction results in an abrupt change connectivity of the magnetic field lines, leading to the formation of new significantly curved reconnected field lines. The magnetic tension caused by this curvature accelerates the plasma, generating *outflows* on both sides of the reconnection region. The depletion of plasma in the outflow area facilitates a sustained *inflow*, which transports additional magnetic fields into the reconnection zone, perpetuating further merging. This mechanism is behind the tearing instability [Furth et al., 1963] allowing magnetic reconnection to persist autonomously, without external forcing.

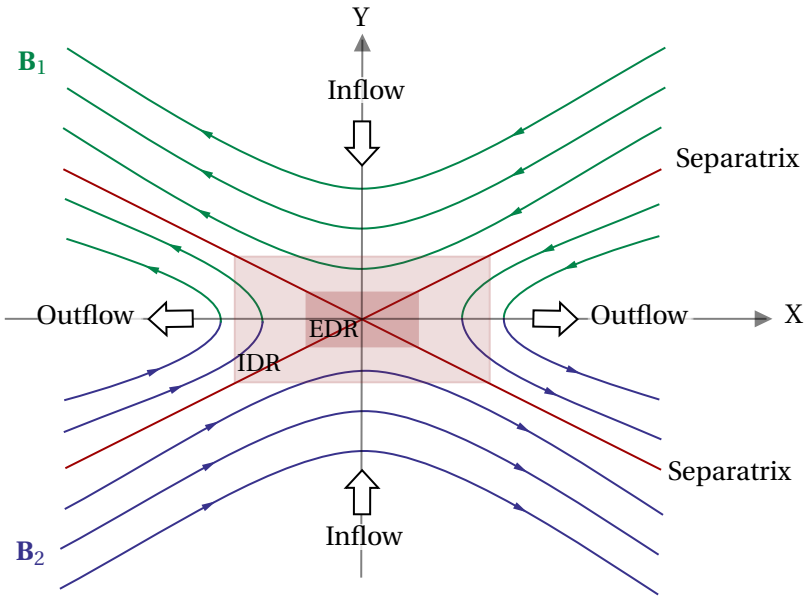

Figure 1.7: Schematic illustration of magnetic reconnection in the reconnecting plane (XY). The green ($\mathbf{B}_1$) and blue ($\mathbf{B}_2$) lines represent the upstream magnetic field lines that will undergo reconnection, while the green-blue bicolor lines correspond to the magnetotic lines that have already reconnected. The red lines are the separatrices. The arrows indicate the plasma inflow and outflow. The lighter and darker red rectangles represent the IDR and EDR.

The magnetic field topology defines two separatrices that separate four distinct regions of magnetic connectivity. The point of intersection of these separatrices is identified as the *X-point*, the location where magnetic reconnection occurs. In a three-dimensional context, there is not just one X-point, but rather a line, called *X-line*, as shown in Figure 1.8. The reconnecting component of the magnetic fields, B_{x_1} and B_{x_2}, are the components locally perpendicular to the X-line, while the components locally parallel to the X-line, B_{z_1} and B_{z_2}, form the *guide field*.

According to the principle of magnetic flux conservation in collisionless plasmas [Alfvén, 1942], magnetic field lines in environments such as the near-Earth space do not "break". Yet, the concept of magnetic reconnection relies on the ability to change the connectivity of magnetic field lines. To reconcile this, physical processes that are typically neglected in ideal Magnetohydrodynamics (MHD) need to be reintroduced. These processes help release the constraints imposed by the frozen-in condition, allowing the merging to occur. Initially, it was hypothesized that an electrical resistivity, caused by collisions between electrons and ions in the reconnection area (known as the *diffusion region*), would enable the diffusion of the magnetic field and permit reconnection [Parker, 1957; Sweet, 1958]. However, this dissipation mechanism was deemed too slow to account for the time scale of explosive release of energy observed in phenomena like solar flares [Biskamp, 1996; Hesse and Cassak, 2020]. Subsequent findings revealed that fast reconnection is facilitated by the Hall electric field produced by the difference of size between the Ion Diffusion Region (IDR) and the Electron Diffusion Region (EDR), where the ion and electron decouple from the magnetic field, respectively [Cassak and Fuselier, 2016; Mandt et al., 1994].

The *reconnection rate* is defined as the quantity of magnetic flux reconnected per time unit, quantifying the speed of this process. This rate corresponds locally to the electric field component

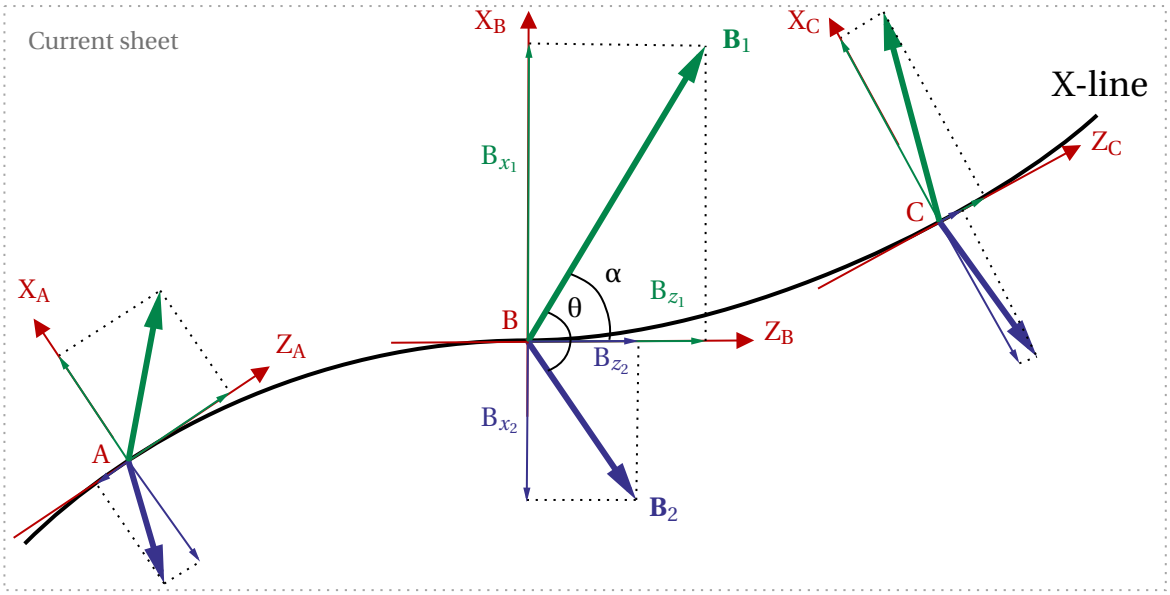

Figure 1.8: Schematic illustration of magnetic reconnection in the current sheet plane. The X-line is represented as the thick solid black line. The green ($\mathbf{B}_1$) and blue ($\mathbf{B}_2$) vectors represent the upstream magnetic fields that undergo reconnection. B_{x_1} and B_{x_2} correspond to the reconnecting components at each of the locations A, B and C. B_{z_1} and B_{z_2} are the components that form the guide field asymptotically. θ corresponds to the magnetic shear angle. α is the angle between $\mathbf{B}_1$ and the X-line.

parallel to the X-line. Cassak and Shay [2007] proposed a MHD scaling law for the reconnection rate in the case of asymmetric (i.e. with arbitrary magnetic fields $\mathbf{B}_1$ and $\mathbf{B}_2$ and mass densities ρ_1 and ρ_2) anti-parallel (i.e. $\theta = 180°$) reconnection. This scaling law is expressed in Equation 1.1, where v_{out} represents the outflow speed. This outflow speed corresponds to the asymmetric Alfven speed ($C_{A,asym}$) detailed in Equation 1.2. Additionally, δ/Δ represent the aspect ratio of the reconnection region is approximately equal to 0.1 [Liu et al., 2017]. These two equations indicates that the reconnection rate depends on the amplitude of the magnetic field, as well as on the mass densities on both sides of the current layer.

$$R \sim \frac{B_1 B_2}{B_1 + B_2} \frac{2\delta}{\Delta} v_{out} \tag{1.1}$$

$$v_{out}^2 \approx C_{A,asym}^2 = \frac{B_1 B_2}{\mu_0} \frac{B_1 + B_2}{\rho_1 B_2 + \rho_2 B_1} \tag{1.2}$$

1.2.2 Magnetic reconnection in the magnetosphere

Figure 1.9 illustrates the distinct phases of the Dungey cycle of magnetic reconnection in the magnetosphere for a due southward IMF [Dungey, 1961]. The description starts, in panel A, by highlighting in blue and red, IMF and magnetospheric field lines. These lines will reconnect at low latitude on the dayside magnetopause, as visible on panel B. That newly opened magnetospheric line, showed in purple, will then be convected tailward and become part of the lobes, in panel C. Eventually, these lobes field lines can reconnect together in the plasma sheet, represented in panel D. The newly closed red field line will then be convected Earthward and eventually brought back to the dayside where the cycle can start again.

Figure 1.10 illustrates a geomagnetic scenario with a due northward IMF orientation. Under such conditions, observational signatures indicate magnetic reconnection occurs at high latitudes polewards of the cusps. Here the draped IMF lines are almost parallel to the closed magnetospheric field lines across the majority of the dayside and it is unclear whether very low shear reconnection occurs there. In contrast, the high-latitude open magnetic field lines within the lobes exhibit an anti-parallel alignment relative to the IMF, easily leading to accelerated particles when

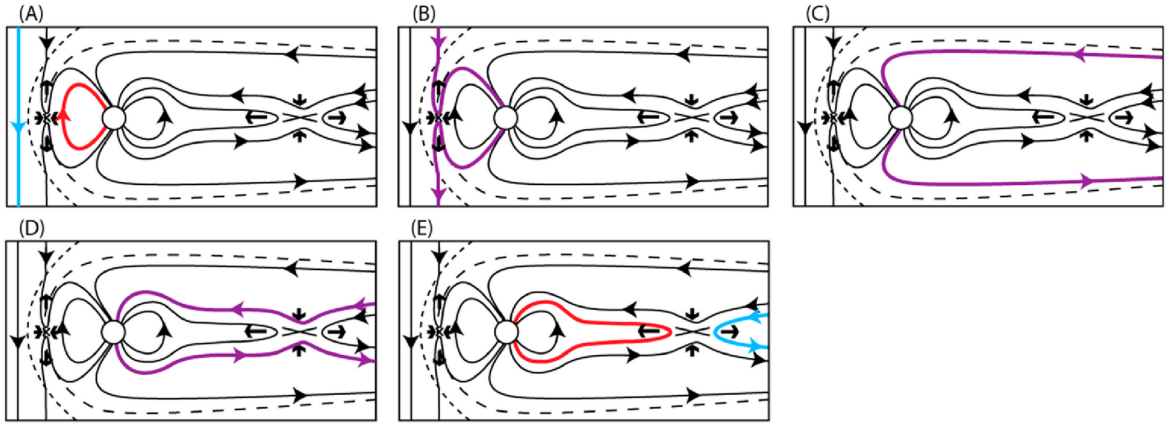

Figure 1.9: Schematic illustration of the Dungey cycle. The blue, red, and purple lines correspond to magnetic field lines with none, two, and one foot anchored to the Earth's dipole, respectively. Figure from Eastwood et al. [2015].

reconnection occurs there. Such high latitude reconnection sites lead to the formation of new closed geomagnetic field lines on the dayside. Concurrently, two magnetic field lines, each possibly having both ends extending into the interplanetary medium, travel anti-sunward along the solar wind. Conversely, the newly formed closed field line experiences a sunward convection, effectively opposing the solar wind flow. Northward IMF reconnection tends to deplete the magnetic flux in the magnetotail.

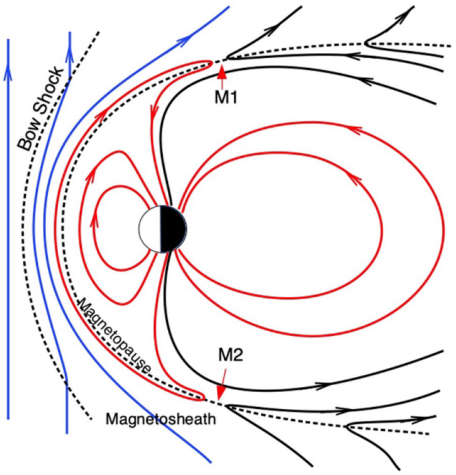

Figure 1.10: Magnetic reconnection in the magnetosphere for due northward IMF. The blue and red lines represent IMF and closed field lines, respectively. M1 or M2 indicates a magnetic reconnection site. Figure from Li et al. [2021].

In 1979, Paschmann et al. [1979] reported the first strong in-situ evidence of magnetic reconnection at the magnetopause, using the International Sun-Earth Explorer (ISEE) spacecraft, observing plasma acceleration characteristics of the reconnection outflow. Shortly thereafter, Sonnerup et al. [1981] observed a non-zero normal component to the magnetopause of the magnetic field, accompanied by accelerated plasma flow, strongly indicating the presence of magnetic reconnection. Twenty years later, Phan et al. [2000] observed for the first time bi-directional jets -also known as *reversal jets*- with the Equator-S and Geotail spacecraft, consistent with the probes crossing an X-line. In 2016, Burch et al. [2016] reported the first observation of the EDR made with the MMS mission. The identification of an EDR is the closest observation one can make from an X-line and offers crucial insight into the mechanisms enabling reconnection.

Figure 1.11 presents in-situ evidence of magnetic reconnection measured by the MMS-3 spacecraft. It shows several southward-oriented plasma jets at the start of the observed time inter-

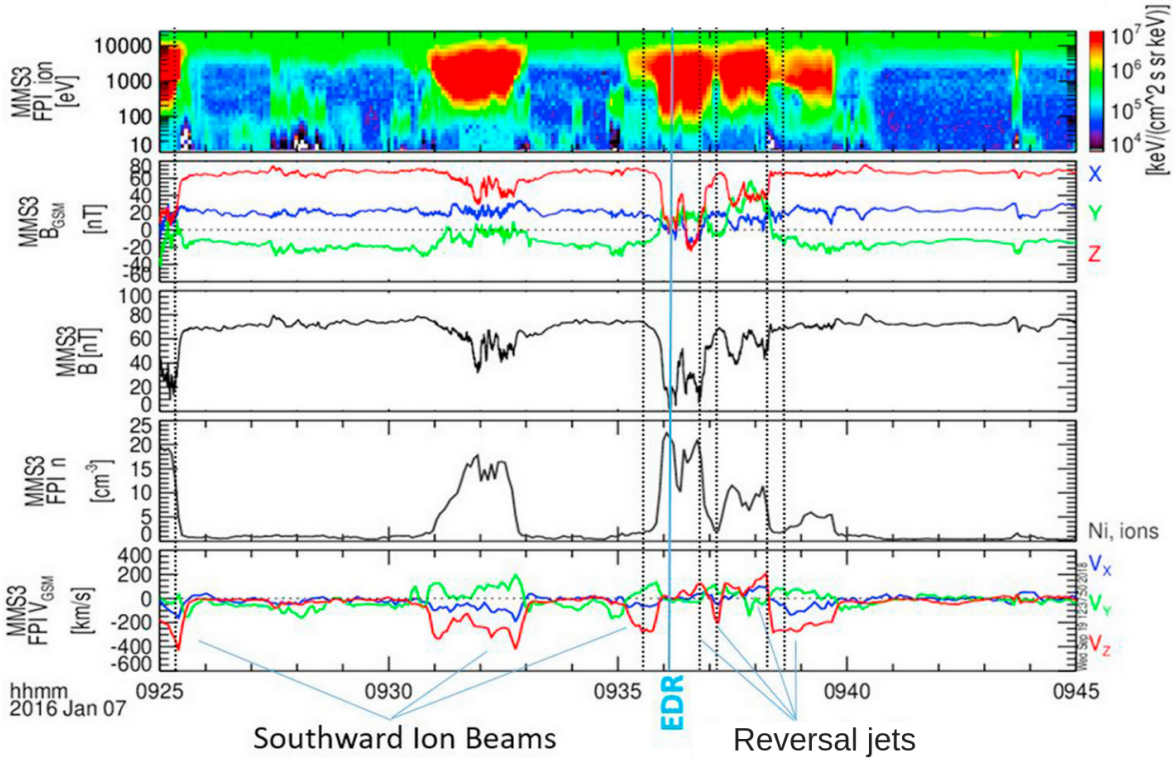

Figure 1.11: Magnetopause crossings on January 7 2016 by the MMS-3 spacecraft. From top to bottom are represented: the energy flux spectrogram, the magnetic field, ion density, and ion bulk velocity. Figure adapted from Trattner et al. [2021a].

val. This orientation indicates that the spacecraft is positioned south of the reconnection site. Notably, given the proximity of the probe to the subsolar point, the ambient plasma flow in the pristine magnetosheath is very low. Therefore, the significant velocity observed is predominantly attributed to plasma acceleration occurring during the reconnection process. Furthermore, the observed increase of the ion density, a characteristic of the magnetosheath, coupled with the presence of high-energy particles in the energy flux spectrogram, typical of the magnetospheric plasma, indicates that the spacecraft is situated within the *boundary layer*. This region is characterized by the intermixing of plasma from the magnetosheath and magnetosphere during the reconnection process. In the latter portion of the observed time interval, reversal jets were detected, characterized by alternating southward and northward flows, or vice versa. This pattern indicates that the spacecraft transitioned from one side of the outflow region to the other, thereby suggesting it crossed the X-line. Prior to this observation of reversal jets, an EDR was identified, marked by a distinctive crescent-shaped electron velocity distribution [Hesse et al., 2014] not shown in the figure.

1.3 The X-line location problem: a literature review

Observations reveal signatures of magnetic reconnection occuring polewards (resp. equatorwards) of the cusps for northward (resp. southward) IMF orientations. For symmetry reasons, in the absence of a dipole tilt, it is expected that the reconnection regions in due southward conditions extend along a line collocated with the equator. For any other IMF orientation or dipole tilt angle, which, incidentally encompass the vast majority of the upstream conditions, the location where reconnection occurs is largely unknown.

Reconnection theory [Cassak and Fuselier, 2016; Hesse and Cassak, 2020; Hesse et al., 2005] does a priori not impose reconnection to occur at the magnetopause along one or multiple X-lines, nor it imposes their length. Observations tend to be consistent with the existence of a single X-line

with a global size extent [Dunlop et al., 2011; Phan et al., 2000, 2001, 2006; Walsh et al., 2017; Zhou et al., 2017]. It is, of course, challenging to ascertain with certainty whether spacecraft observe a X-line due to the inherent local nature of in-situ measurements. Global resistive MHD simulations also reveal the existence of a system wide single X-line [Eggington et al., 2020; Glocer et al., 2016; Komar et al., 2015; Souza et al., 2017]. However, models with the lowest resistivities also show fragmented, short, numerous X-lines [Burkholder et al., 2023; Glocer et al., 2016]. It is not clear whether these plasmoid dominated weakly resistive reconnection regimes are relevant to the case of the collisionless magnetopause system, although plasmoids, often called rather Flux Transfer Event (FTE) in observational studies, are often seen at the magnetopause. In this manuscript, we are going to put our studies in the paradigm where there is a single long X-line, mostly for simplicity reasons.

Answering the question of where that single X-line could locate is critical regarding the subsequent state of the magnetosphere. Knowing where the X-line is, globally on the magnetopause, determines what the local values of upstream parameters controling reconnection (jump of the magnetic amplitude and direction, of the density, etc.) are, and also which magnetic component will merge by imposing the local orientation of the X-line relative to the sheared magnetic field, thus the local reconnection rate. Overall, the location of the X-line therefore determines the global reconnection rate at the magnetopause and thus how much mass, momentum, energy and magnetic flux can penetrate within the magnetosphere.

The problem of locating the X-line is a multiscale challenge. It is not clear, whether the global state of the magnetopause in terms of the large scale variations of the magnetic field and other quantities, will drive where the X-line is; if the X-line is the global result of a series of local alignments with orientations imposed by the local magnetic shear and other upstream properties, or even is a combination of global and local scale constraints.

Historically, two opposing scenarios have been proposed for predicting the location of the X-line: the anti-parallel reconnection scenario, according to which reconnection can only occur in locations where the magnetic fields are anti-parallel; and a scenario where reconnection of only components of the magnetic field is also possible, implying that reconnection could occur over a much wider range of conditions and locations. However, this disagreement has become outdated as numerous observations of component reconnection (e.g. Daly et al. [1984]; Pu et al. [2005]; Scurry et al. [1994]) have invalidated anti-parallel reconnection as the sole scenario.

The problem is nowadays tackled following two main approaches. On the one hand, some studies focus on the sub-problem consisting in determining the orientation an X-line would follow, given the local upstream conditions. This so-called *local approach* to the localization problem emphasizes the importance of local constraints in governing the orientation of the X-line, from which a global X-line can eventually be constructed. On the other hand, some other studies consider a global X-line can be determined by some global scale constraints existing on the magnetopause, resulting from the interaction of the magnetosphere and the solar wind and IMF. In this scenario that we shall call the *global approach* to the localization problem, the local orientation of the X-line is merely a consequence of these large scale constraints and local physical effects play virtually no role. In the following, we will review the various ideas and results driven by these two approaches.

1.3.1 The local approach: the orientation of the X-line

The first study addressing the problem of the X-line location from a local perspective was proposed by Sonnerup [1974] who suggested that the orientation is such that the component of the magnetic field parallel to the X-line ($B_{\parallel}$, the so-called guide field) is constant across the current sheet, as shown in panel a of Figure 1.12. According to Ampere's law, a non-uniform $B_{\parallel}$ would result in a current perpendicular to the X-line ($J_{\perp}$), i.e. in the reconnection plane. This would produce an asymmetry in the $J_{\perp} \times B_n$ force on each side of the X-line owing to the reversal of B_n. Sonnerup argued that, while this asymmetry in the reconnection outflows can not be excluded entirely, it was "unlikely". Thus, if the current in the reconnection plane should vanish, Equation 1.3 can be

used to determine the X-line orientation α, based on the outside (B_o) and inside (B_i) magnetic fields. θ and α correspond to the magnetic shear angle and the angle between B_o and the X-line, respectively. This idea has later been used to model global X-lines on the magnetopause [Gonzalez and Mozer, 1974; Hill, 1975].

$$\tan\alpha = \frac{B_o/B_i - \cos\theta}{\sin\theta} \tag{1.3}$$

An important implication is that configurations where $\cos\theta > B_o/B_i$ would yield a negative value for α, as depicted in panel b of Figure 1.12. This implies that the magnetic fields' perpendicular components to the X-line are parallel rather than antiparallel which geometrically precludes reconnection from occurring.

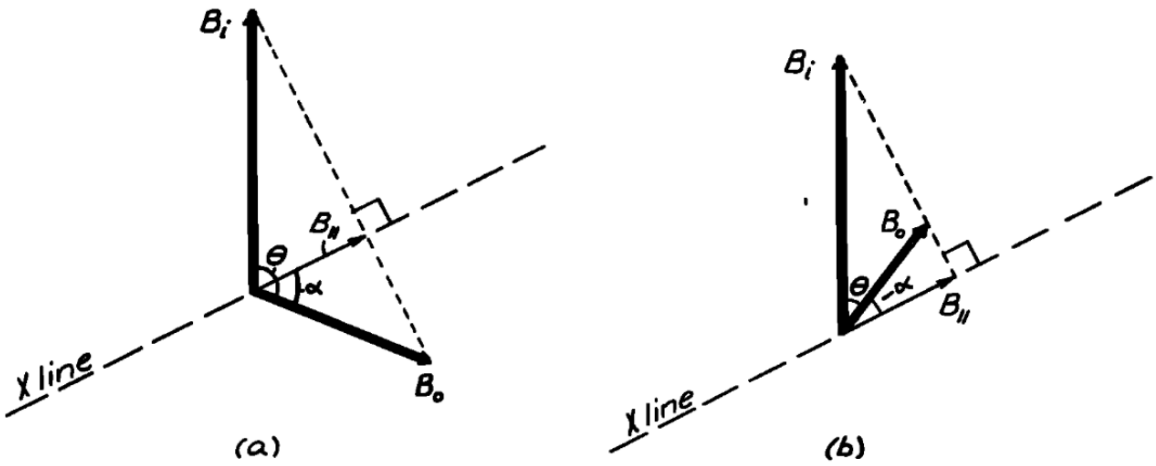

Figure 1.12: Orientation of the X-line for $\cos\theta < B_o/B_i$ and $\cos\theta > B_o/B_i$ in panel a and b, respectively. Figure from Sonnerup [1974]. The configuration of panel b precludes reconnection from happening.

$$\theta_{crit} = \cos^{-1}(B_o/B_i) \tag{1.4}$$

The restriction imposed by this model on reconnection, prohibiting it from occurring below a critical magnetic shear angle θ_{crit} (Equation 1.4), seems overly restrictive given that it is only based on the assumption that it is "unlikely" for the reconnection outflow to be asymmetric. For typical magnetic field amplitudes referenced in Tables 1.1 and 1.2, this model yields a θ_{crit} of approximately 65° at the subsolar magnetopause, below which reconnection would be theoretically forbidden.

Swisdak and Drake [2007] furthermore argued that maintaining pressure equilibrium under the condition of a constant guide field would require the thermal pressure gradient at the X-line to vanish, thereby adding another rather restrictive constraint for reconnection to occur at the magnetopause.

This assumption of a constant guide field has later been challenged by the study of Cowley [1976] where the author inferred constraints on magnetic reconnection from the MHD equations. First, the reconnecting component and the inflow perpendicular to the X-line must reverse across the current layer, but they can have different amplitudes on either side. Then, the magnitude of the magnetic field parallel to the X-line may be arbitrary, and vary across the current, so that the current density in the diffusion region may not be parallel to the X-line. These constraints allow the X-line to have any orientation between the two upstream magnetic field vectors as shown in Figure 1.13.

Moore et al. [2002] was the first study to use the local approach to build a global X-line. In his model, the X-line is integrated by following the orientation given by the bisection of the magnetic field on each sides of the magnetopause. The reason for choosing the bisection orientation here is justified by the wish to have anti-symmetric reconnecting components - a premise wrongly

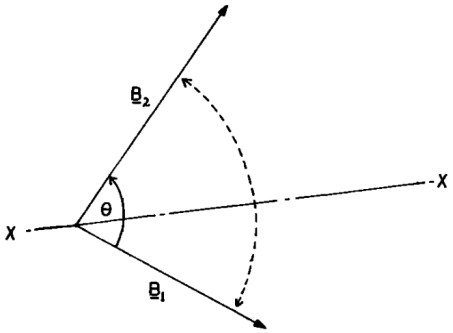

Figure 1.13: The schematic shows the range of X-line orientations allowed (dashed arrow) for the given magnetic fields (B_1 and B_2). θ correspond to the magnetic shear angle. Figure from Cowley [1976].

attributed to Cowley [1976] - in a context where the authors imposed equal asymptotic magnetic field amplitudes. Incidentally, in such a symmetric magnetopause model, the bisection also equals to the perpendicular bisector proposed by Sonnerup [1974], as seen on Figure 1.14. Reconstructing a global X-line from this requires deciding a point from which the integration should start. Moore et al. [2002] suggested somewhat arbitrarily that the X-line passes where the reconnecting components are the largest.

In this model, the magnetic field within the magnetosphere is obtained using Tsyganenko and Stern [1996]'s model. The orientation of the magnetic field in the magnetosheath is determined by considering only the B_y and B_z components of the IMF (i.e., components perpendicular to the Earth-Sun axis), with the B_x component arising from the curvature of the magnetopause so that the magnetic field is tangential to its surface. It was also assumed that the amplitudes of the magnetosheath and magnetospheric magnetic fields are equal.

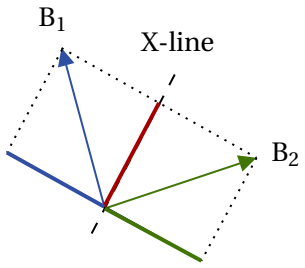

Figure 1.14: The bisection of the magnetic shear angle between two magnetic field vectors of same amplitude, B_1 and B_2, results in the formation of equal anti-parallel (illustrated by the blue and green lines) and parallel (indicated by the red line) components relative to the X-line.

Figure 1.15 shows the predictions made by Moore et al. (2002) for various orientations of the IMF. The findings indicate that for most IMF orientations, except for a strictly northward direction, the predicted X-lines intersect at, or in close proximity to, the subsolar point. Additionally, certain orientations, particularly northward ones, may lead to the model forecasting two X-lines due to the existence of two symmetrically positioned start points in both magnetospheric lobes.

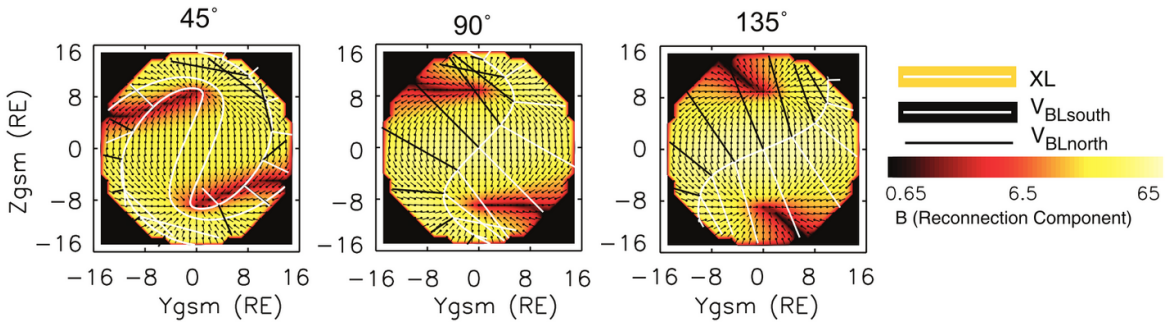

Figure 1.15: The color coded map represents reconnecting component magnitude on the dayside magnetopause, as view from the sun, for IMF clock angle of 45°, 90°, and 130°. The curved white lines that correspond to the X-lines predicted by Moore et al. [2002]'s model. The straight black and white lines represent the boundary layer flow rooted in the northern and southern hemispheres, respectively. Figure adapted from Moore et al. [2002].

Swisdak et al. [2003] proposed a mechanism possibly adding an additional constraint regarding the orientation of the X-line. Whenever a gradient of the thermal pressure exists in a current sheet separating non-coplanar magnetic field orientations, a diamagnetic current must exist. For thin electron scale current sheets, the electron diamagnetic drift associated with this current will dominate that of the ions. Swisdak et al. suggests that, in certain conditions, this drift may be faster than the typical reconnection outflow speed, thereby essentially forbidding reconnection to happen with an X-line perpendicular to that plane. Weirdly, this idea has, to our knowledge, never been used to constrain the orientation of the X-line, as originally intended, but rather used to determined whether reconnection would occur or not [Maheshwari et al., 2022; Phan et al., 2013] at a specific location assuming, somewhat paradoxically, that the X-line would locally align with the M direction provided by an Minimum Variance Analysis (MVA) or along the bisection of the upstream magnetic fields.

Only few years later, Swisdak and Drake [2007] proposed an alternative idea according to which the X-line is oriented along the direction that maximizes the estimated outflow velocity v_0 (Equation 1.5) derived from the MHD equations. They consider a system of arbitrary densities (ρ_1 and ρ_2) and magnetic fields (B_1 and B_2), oriented such that the X-line is along the Z-axis and the reconnection plane corresponds to the (XY) plane such as shown in Figure 1.16.

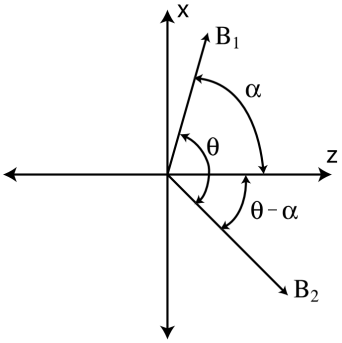

Figure 1.16: Coordinate system with the X-line oriented along the Z-axis, while the reconnecting component of the magnetic fields is along the X-axis. θ is the magnetic shear angle and α is an unknown angle giving the orientation of the X-line in respect to the B_1 magnetic field. Figure from Swisdak and Drake [2007].

$$v_0^2 = \frac{B_1 \sin\alpha + B_2 \sin(\theta - \alpha)}{\mu_0} \left(\frac{\rho_1}{B_1 \sin\alpha} + \frac{\rho_2}{B_2 \sin(\theta - \alpha)} \right)^{-1} \tag{1.5}$$

In Equation 1.5, θ corresponds to the magnetic shear angle and α is the unknown angle between the B_1 and the X-line (Figure 1.16). Therefore, given the magnetic fields and densities values, the orientation of the X-line can be determined such as $\partial v_0^2 / \partial \alpha = 0$.

The X-line is found to bisect the upstream magnetic fields (i.e. $\alpha = \theta/2$) in several cases, such as:

- for anti-parallel magnetic fields (i.e. $\theta = \pi$)
- for equal densities on both sides of the current layer (i.e. $\rho_1 = \rho_2$)
- if $B_2/B1 >> |1 - \rho_1/\rho_2|$ or $B_2/B1 << |1 - \rho_1/\rho_2|$.

Finally, the authors note that if the density ratio is not significantly different from 1, $\alpha = \theta/2$ gives a good approximation of the orientation of the X-line. However, it is worth noting that, given the typical parameters in the magnetosphere (Table 1.1) and magnetosheath (Table 1.2), the density ratio is approximately of $\rho_1/\rho_2 \approx 10^{-2}$. This raises questions about the potential impact of this density disparity on the orientation of the X-line.

The underlying idea of the Swisdak and Drake [2007] is that the orientation of the X-line maximizing the reconnection outflow would be also the one maximizing the reconnection rate. This is

also the scenario proposed by [Borovsky, 2013] who suggested that a X-line oriented to maximize the local reconnection rate would enable the maximum reduction of the system's energy.

Borovsky generalized the MHD scaling law for asymmetric reconnection rate formulated by Cassak and Shay [2007] for non-antiparallel reconnection with Equation 1.6. As shown Figure 1.17, θ represents the IMF clock angle (see Section 2.7.5), which serves as a proxy for the magnetic shear angle at the magnetopause, B_m and B_s denote the magnetic field in the magnetosphere and in the magnetosheath, respectively. ρ_m and ρ_s correspond to the ion mass densities in the magnetosphere and in the magnetosheath.

$$R_{CS} = \frac{2\delta}{\Delta} \frac{(B_m \sin(\alpha) + B_s \sin(\theta - \alpha))^{3/2}}{\sqrt{\mu_0 \left(\rho_s B_m \sin(\alpha) + \rho_m B_s \sin(\theta - \alpha)\right)}} \tag{1.6}$$

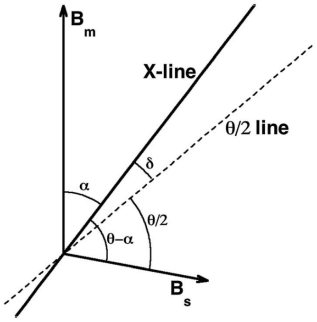

Figure 1.17: The angles associated with the orientation of the reconnection X-line. B_m and B_s correspond to the magnetic field in the magnetosphere and in the magnetosheath, respectively. Figure from Borovsky [2013].

Equation 1.7, which is derived to maximize the reconnection rate of Equation 1.6, estimates the angle α_{CS} of the X-line in respect to the magnetospheric field. Additionally, Equation 1.8 provides the angle α_{CSB} of the X-line relative to the magnetospheric field, derived from the maximization of the Cassak-Shay-Birn reconnection rate formula for non-antiparallel reconnection. This formula is based on the Cassak-Shay equation with accounting for the compressibility of the plasma flow near the reconnection site [Birn et al., 2010]. It should be noted that these two equations are obtained assuming a density ratio of $\rho_m/\rho_s = 1/6$. However, they exhibit relative insensitivity to variations in the density ratio provided that $\rho_m/\rho_s << 1$. Additionally, the applicability of these relations is constrained to cases where the magnetic field strength ratio satisfies $B_m/B_s \geq 1$.

$$\alpha_{CS} \approx \theta/2 - 15^\circ \left(1 - \sqrt{1 + \frac{B_m}{B_s}}\right) \sin(\theta) \tag{1.7}$$

$$\alpha_{CSB} \approx \theta/2 - 15^\circ \left(1 - 1.38 \left(\frac{B_m}{B_s}\right)^{-0.9} + 0.619 \left(\frac{B_m}{B_s}\right)^{-2}\right) \sin(\theta) \tag{1.8}$$

Figure 1.18 presents the orientation of the X-line, with α_{CS} in the upper panel and α_{CSB} in the bottom panel, for different magnetic field strength ratio B_m/B_s. It reveals that both Equation 1.7 and Equation 1.8 predict an X-line orientation that is closer to the magnetospheric magnetic field orientation than the bisection of the upstream magnetic fields θ/2. Specifically, for a magnetic field strength ratio of $B_m/B_s = 2$ — which approximately corresponds to the typical magnetic field amplitudes in the magnetosphere and magnetosheath as listed in Tables 1.1 and 1.2, respectively — the angular deviation from θ/2 is between 5° and 10° for the average orientation of the IMF (i.e. θ=90°). While this difference in the predicted orientations may seem way too small to be accessible to in-situ observations, it is worth noting that from a global perspective, it could results in vastly different X-lines depending the distribution of plasma and field on the magnetopause.

Hesse et al. [2013] used Particle-in-cell (PIC) simulations to investigate the impact of X-line orientation on reconnection rate. For the same initial setup, a series of 2.5D simulations (imposing

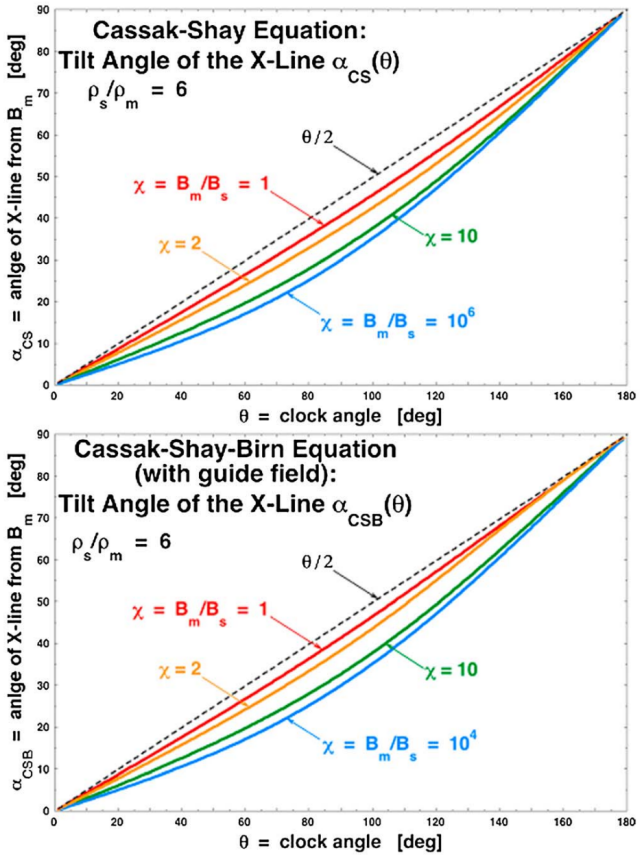

Figure 1.18: Angle α of the reconnection X-line in respect to the direction of the magnetospheric magnetic field is plotted as a function of the IMF clock angle θ taken as proxy of the magnetic shear angle. The colors are for various values of the ratio of the magnetospheric to magnetosheath magnetic field strengths $\chi = B_m/B_s$. Figure from Borovsky [2013].

the X-line to be out of the simulated plane) are performed, each rotated around the normal to the current sheet from the Sonnerup [1974]'s plane where the guide field is constant.

Figure 1.19 shows a schematic of the initial simulation setup and methodology. The y-axis represents the orientation of the X-line, which produces the reconnecting components of the magnetic field, B_u and B_d. Then the simulation plane is rotated by an angle α, which results in a new X-line orientation along the y'-axis, leading to different reconnecting components B'_u and B'_d. Nine simulations were conducted for various α angles.

The reconnection rate was measured for each simulation and its maximum value is represented by the blue points in Figure 1.20. Knowing the X-line orientation thereby reconnecting components, the authors calculated the reconnection rate predicted by the Cassak and Shay [2007] MHD scaling law. They also proposed that, for a given orientation of the upstream magnetic fields, the reconnection rate should be directly proportional to the "magnetic energy density"[1] available to reconnection, as expressed in Equation 1.9. The results presented in Figure 1.20 show the reconnection rate, as a function of the orientation of the X-line, aligns very well with the scaling of the available magnetic energy.

$$R \propto B'^2_u B'^2_d = (B_u \cos\alpha + B_d \sin\alpha)^2 (B_u \sin\alpha + B_d \cos\alpha)^2 \tag{1.9}$$

An important, and not anticipated consequence of this result is that the solution to $\partial R/\partial\alpha = 0$ incidentally corresponds to the bisection of the upstream magnetic fields. In a similar study using hybrid PIC simulations and different initial setups, Aunai et al. [2016] also found that the bisection

[1] Normally, the magnetic energy is defined with all components of the vector. However, only merging components drive the reconnection process, hence the ad hoc definition of "available magnetic energgy" based on the merging components only.

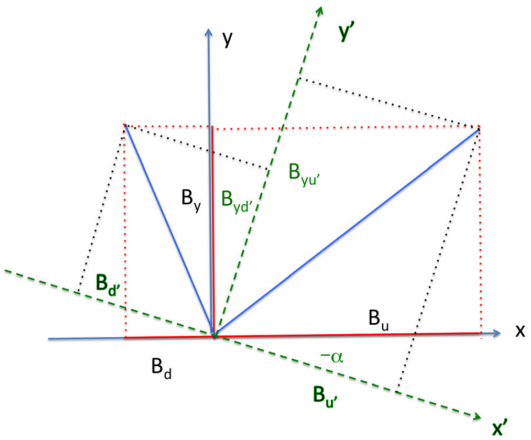

Figure 1.19: Magnetic configurations of the simulations. The y-axis represents the orientation of the X-line, which produces the reconnecting components of the magnetic field, B_u and B_d. α correspond to the rotation of the simulation plane which results in a new X-line orientation along the y'-axis, leading to different reconnecting components B'_u and B'_d. Figure from Hesse et al. [2013].

of the upstream magnetic field maximizes the locally reconnection rate. In a study employing both 3D and companion 2.5D PIC simulations, Liu et al. [2018] showed that the X-line is oriented along the direction that maximizes the reconnection rate, aligning with the theoretically predicted bisection orientation.

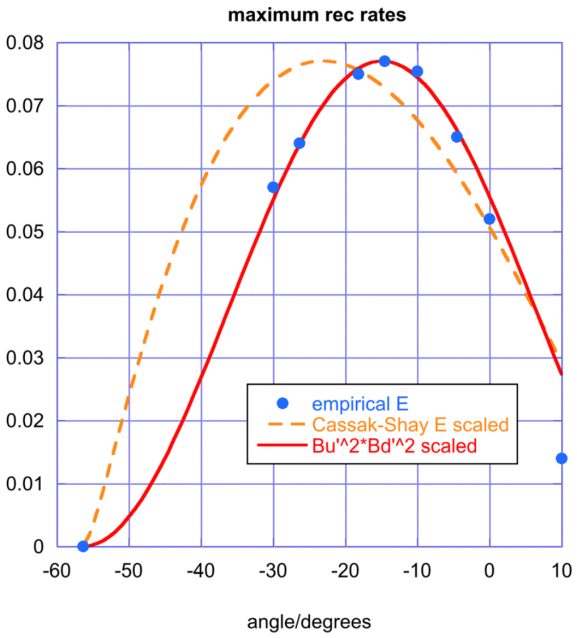

Figure 1.20: The blue points represent the maximum reconnection rate measured in the different simulations. The dashed orange and solid red lines correspond to the estimate of the reconnection obtained with Cassak and Shay [2007] and Hesse et al. [2013] scaling laws, respectively. Figure from Hesse et al. [2013].

1.3.2 Global approach: the position of the X-line

The first model proposing a X-line based on the global approach on the magnetopause, to our knowledge, was proposed by Crooker et al. [1979]. From the argument that the "growth times [of the tearing instability] are the shortest for anti-parallel fields", reconnection should preferentially occur at the magnetopause in regions exhibiting such a configuration. The positions of the recon-

nection lines were qualitatively identified by considering the orientation of the IMF perpendicular to the Earth-Sun axis and sketching (i.e. the author did not use an analytical model) the magnetospheric magnetic field lines, such as shown in Figure 1.21.

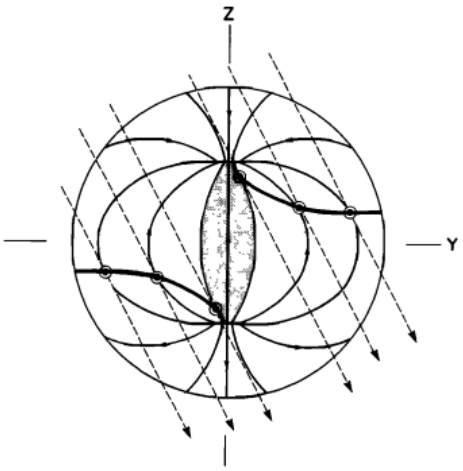

Figure 1.21: Schematic of the dayside magnetopause as viewed from the sun. The solid lines represent the magnetic field lines of the magnetosphere, while the dashed lines represent the magnetic field lines of the magnetosheath. The reconnection lines are represented by the bold solid lines The shaded area near the noon axis does not contain anti-parallel magnetic fields. Figure from Crooker et al. [1979].

Luhmann et al. [1984] expanded on the Crooker et al. [1979] qualitative model, this time using analytical models for both the magnetosphere and the magnetosheath magnetic fields to determine these regions. Here, the empirical model proposed by Hedgecock et al. [1979] was used to compute the magnetic field in the magnetosphere. On the magnetosheath side, the magnetic field orientation was determined by propagating the IMF using a gasdynamic model [Spreiter and Stahara, 1980]. This approach enabled a more realistic representation of the IMF by accounting for the magnetic draping.

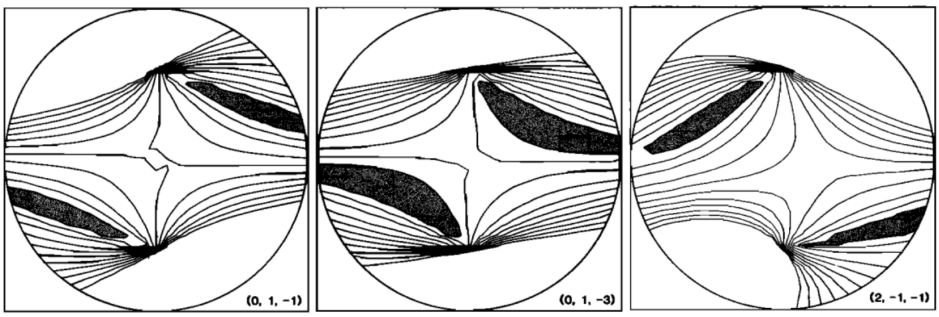

Figure 1.22: Contours on the dayside magnetopause as viewed from the sun of the cosine of the magnetic shear angle using models of magnetic fields for both the magnetosphere and the magnetosheath. The shaded areas correspond to the anti-parallel regions (values equal or inferior to -0.98). The components of the IMF are specified at the bottom right of each panel. Figure adapted from Luhmann et al. [1984].

Figure 1.22 illustrates the predictions of Luhmann et al. [1984]'s model for different IMF orientations. The localization of the anti-parallel regions are found in relative good agreement with the qualitative prediction of Crooker et al. [1979]. For most IMF orientations, the model predicts the formation of two X-lines that converge towards the polar cusps. The radial component of the IMF disrupts the rotational symmetry around the Earth-Sun line between the two anti-parallel regions, as seen in the last panel of Figure 1.22. More importantly, these models [Crooker et al., 1979; Luhmann et al., 1984] predict that magnetic merging would occur in the subsolar region only for due southward IMF. However, not only have numerous observations of component reconnection been made, but they have often been located in or near the subsolar region (e.g. Petrinec et al. [2022]).

Subsequent models have thus focused on proposing X-line locations that could explore regions of component reconnection. Using a idea similar to that of Crooker et al. [1979], Alexeev et al. [1998] proposed that magnetic merging occurs in response to a current-driven instability. Therefore, they suggested that magnetic reconnection would take place in regions on the magnetopause where the current exceeds a critical threshold value.

This study uses the Kobel and Fluckiger [1994] and Alexeev and Bobrovnikov [1996] models of the magnetic field for the magnetosheath and magnetosphere, respectively, and assumes that the current density constant across the magnetopause. The critical current is determined as the one on the contour delimiting the area, on the magnetopause, enclosing the magnetic flux that is estimated to be reconnected for a given IMF condition, based in Newell et al. [1989]'s observational constraints.

Figure 1.23 shows the predictions of Alexeev et al. [1998]'s model for different IMF orientations. For most IMF orientations, the regions where the current exceeds the threshold value are centered around a tilted subsolar reconnection line spanning the dayside magnetopause. The model predicts that for northward IMF, such as in the left panel of Figure 1.23, reconnection should occur polewards of the cusps, but it does not cease entirely on the dayside magnetopause unless the IMF points due north.

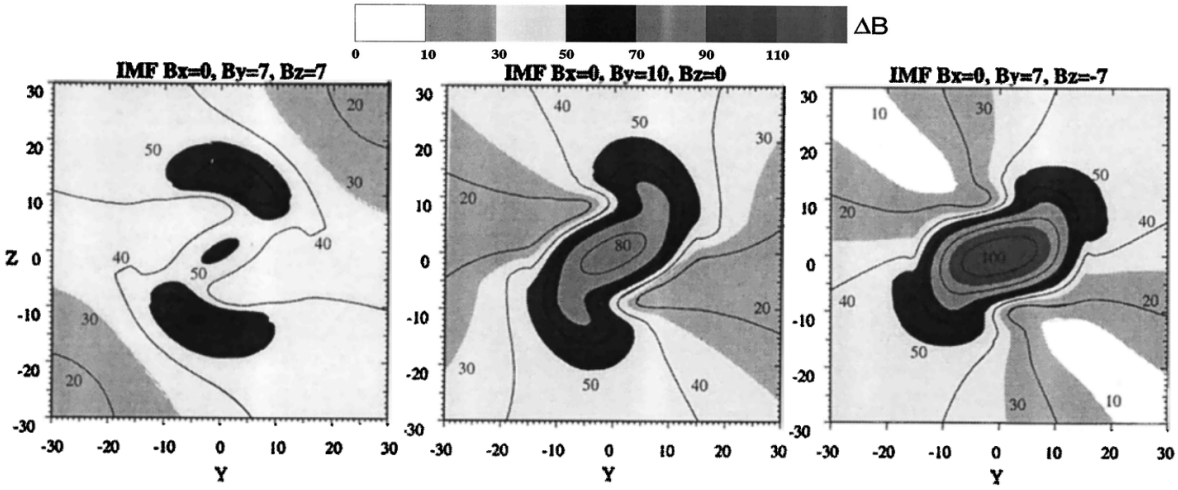

Figure 1.23: Contour of the constant jump in magnetic fields on the magnetopause as viewed from the Sun. ΔB= 50 nT (black shaded regions) is considered the minimum threshold at which magnetic reconnection could occur. Figure adapted from Alexeev et al. [1998].

This model estimates a relatively large region within which magnetic reconnection could occur, as opposed to predicting a specific X-line. Recent studies Komar et al. [2015] and Souza et al. [2017], inspired from these results, but focusing on determining X-lines, rather define it as the line that maximizes the distribution of the current density on the magnetopause. We will see, in Chapter 5, that this thesis also follows this idea, but this time using purely observations to reconstruct the current density maps.

Trattner et al. [2007] proposed an X-line model that combines anti-parallel and component reconnection, known as the *Maximum Magnetic Shear*. The model was developed using the low-velocity cutoff method [Onsager et al., 1991], which analyzes the velocity distributions of ions accelerated by the reconnection process and subsequently precipitating into the polar cusps. The left panel of Figure 1.24 shows an example of these distributions measured by the POLAR spacecraft in the northern cusp. The right panel shows three peaks in the 1D velocity distribution along the magnetic field direction, with:

- $V_{\parallel}$ ≈0 km.s^{-1} corresponding to the ion of the magnetosphere.
- $V_{\parallel}$ ≈400 km.s^{-1}, noted V_e, corresponding to incident ions propagating towards the polar cusp.

- $V_{\parallel} \approx$-750 km.s^{-1}, noted V_m, corresponding to the fastest ions that had time to precipitate in the polar cusp before being mirrored at low latitude.

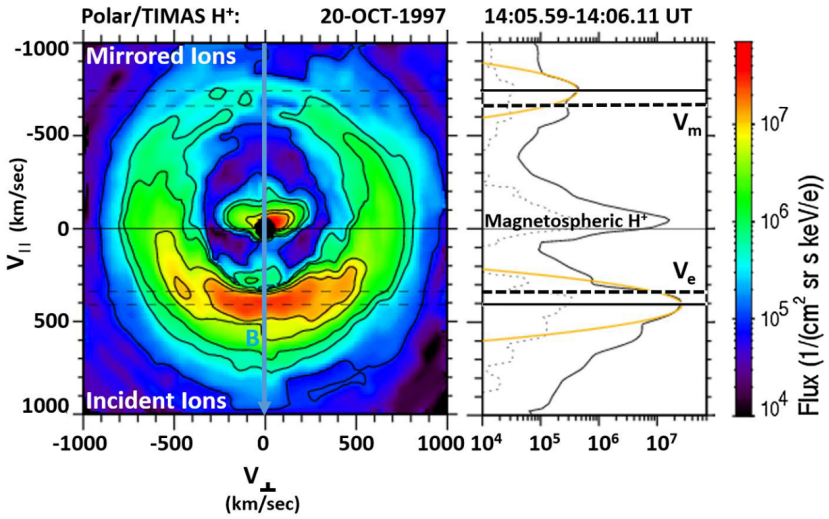

Figure 1.24: 2D cut of the 3D ion velocity distribution measured by the Polar spacecraft in the left panel. $V_{\parallel}$ and $V_{\perp}$ correspond to the velocity parallel and perpendicular to the magnetic field, respectively. The right panel shows the 1D cut along the direction of the magnetic field. V_e and V_m correspond to the incident and mirrored velocity, respectively. Figure from Trattner et al. [2021b].

Utilizing the identified cutoff velocities, V_e and V_m, the X-line's position can be estimated. The assumption, as illustrated in Figure 1.25, is that at the time of the measurement, ions injected from the reconnection site would have traversed a distance X_r along the magnetic field line to the spacecraft's location at velocity V_e. Meanwhile, mirrored ions would have covered a distance of $X_r + 2X_m$, where X_m corresponds to the span from the spacecraft to the mirror point, traveling at velocity V_m. Therefore, the position of the X-line is inferred using Equation 1.10 once the mirror point's location and the trajectory of the magnetic field line have been determined with the magnetospheric magnetic field model proposed by Tsyganenko and Stern [1996].

$$\frac{X_r}{X_m} = \frac{2V_e}{V_m - V_e} \tag{1.10}$$

The black squares in the three panels of Figure 1.26 indicate the estimated location of the reconnection site, using the low-velocity cutoff method, for different IMF and dipole tilt orientations. These observations were correlated with the spatial distribution of the magnetic shear angle at the magnetopause obtained with the models of magnetic field of Kobel and Fluckiger [1994] and Tsyganenko and Stern [1996] for the magnetosheath and the magnetosphere, respectively. It was determined that the X-line is localized only in the anti-parallel regions for strongly southward IMF ($155° < \theta_{cl} = \tan^{-1}(B_y/B_z) < 205°$ with $\theta_{cl} \in [0, 2\pi]$) or for dominant B_x component ($B_x/\|\mathbf{B}\| > 0.7$). For other conditions such as dominant B_y components, as in Figure 1.26, reconnection may occur at anti-parallel location on the flanks but most of the X-line extends in the component reconnection region by maximizing the magnetic shear angle Trattner et al. [2016, 2021b].

1.3.3 Evaluation of the different models

Komar et al. [2015] compared the predictions of various X-line models to the magnetic separator of global resistive MHD simulations made for different IMF clock (30°, 60°, 90°, 120°, 150°, 165°) and dipole tilt (0, 15°) angles. The evaluated models include: the maximum magnetic shear model [Trattner et al., 2007], maximization of the asymmetric reconnection outflow speed [Swisdak and Drake, 2007], maximization of the asymmetric reconnection rate [Borovsky, 2013], maximization

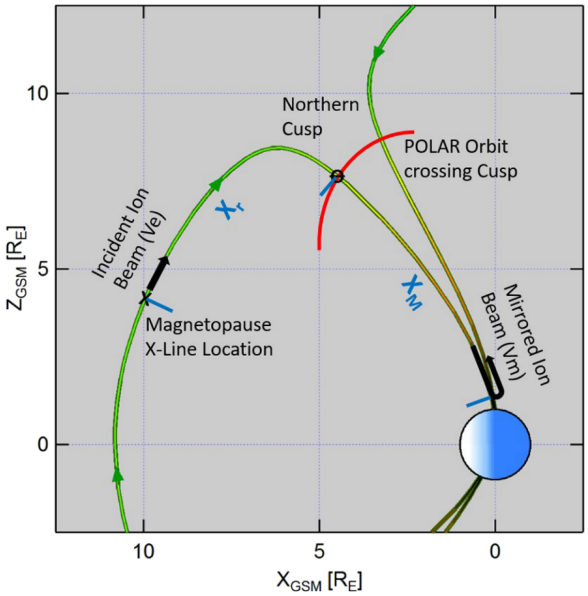

Figure 1.25: Schematic diagram of ion injection into the northern cusp from newly reconnected field lines and those reflected at low altitude. V_e and V_m correspond to the incident and mirrored velocity, respectively. X_r (resp. X_m) corresponds to the distance between the Polar spacecraft and the X-line location (resp. the ionospheric mirror point). Figure from Trattner et al. [2021b].

of the reconnection energy [Hesse et al., 2013], the maximization of the current density magnitude [Alexeev et al., 1998], and constant guide field [Sonnerup, 1974].

The study revealed that for southward IMF conditions with no dipole tilt, the predictions of different X-line models deviated from the magnetic separators by a few Earth radii. Among the tested models, the asymmetric outflow speed and asymmetric reconnection rate models exhibited slightly better results. In contrast, when the IMF was northward with no dipole tilt, none of the models accurately replicated the entire magnetic separator. However, the maximum magnetic shear model demonstrated some success in reproducing the portion of the separator located in the region of anti-parallel magnetic fields at high latitude. With a positive dipole tilt angle of 15°, all models performed relatively well for the southward IMF condition, but showed the greatest discrepancy with the magnetic separator of all the tested conditions for the northward IMF. It can be concluded that this study did not find evidence of the predominance of one model over the other.

It is important to note that in this study, the models categorized under the *local approach* in section 1.3.1 —such as the reconnection outflow speed [Swisdak and Drake, 2007], maximization of the asymmetric reconnection rate [Borovsky, 2013], and maximization of the reconnection energy [Hesse et al., 2013]— were not employed to determine the local orientation of the X-line as originally intended by the models. Instead, these models were adapted to maximize globally a considered quantity, diverging from their initially defined local applications. Therefore, local orientations of the X-lines obtained from this maximization procedure may differ from those predicted by the original model. We shall revisite this discrepancy between local and global approaches in Chapter 5.

Souza et al. [2017] used 75 single reconnection jets observations made with the THEMIS mission to evaluate predictions of three models: the maximum magnetic shear model [Trattner et al., 2007], maximization of the asymmetric reconnection outflow speed [Swisdak and Drake, 2007], and the maximization of the current density magnitude [Alexeev et al., 1998]. The 75 reconnection jets were matched to a global MHD simulation with parameters closest to the actual conditions observed in the solar wind. The simulation was run for different IMF clock (120°, 150°, and 180°) and dipole tilt (0°, 10°, 20°, or 30°) angles. Subsequently, the orientation of the jets was compared to the predicted outflow orientation among the various tested X-line models, obtained using the

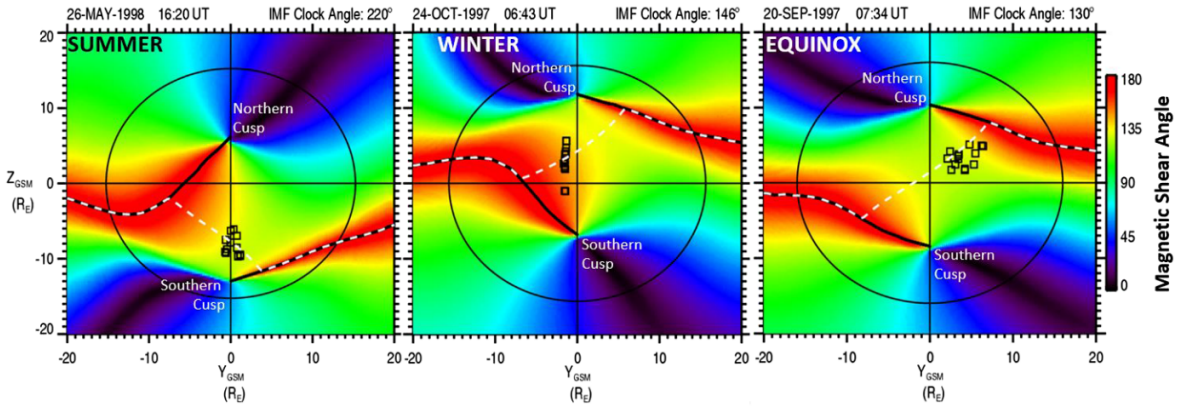

Figure 1.26: Spatial distribution of the magnetic shear angle across the dayside magnetopause, as seen from the Sun, for different IMF and dipole tilt orientations. Black squares represent the locations of the X-line at the magnetopause, determined by the low-velocity cutoff method. The black solid lines correspond to the region of anti-parallel magnetic field. The white dashed lines correspond to the X-lines predicted bu the Maximum magnetic Shear angle model. Figure from Trattner et al. [2021b].

physical parameters on the magnetopause of the simulation. Again, no X-line model was found to statistically outperform the others. Similarly to Komar et al. [2015], this study does not use local models as they were originally envisioned.

Trattner et al. [2017] identified 302 reversal jets with the MMS mission. The observed locations of these jets were compared with the predictions of the Maximum Magnetic Shear model [Trattner et al., 2007]. The comparison revealed that 249 of the 302 reversal jets observations were located within a 2 Re proximity to the X-line predicted by the Maximum Magnetic Shear model. However, this study did not assess or compare the performance of other models to that of the maximum magnetic shear model. In a previous study, Trattner et al. [2012] observed a notable discrepancy between the predictions of the maximum magnetic shear model and in-situ observations of magnetic reconnection for an IMF with a predominant B_x component. The authors suggested that the Kobel and Fluckiger [1994] model may not properly model the magnetic field of the magnetosheath under these conditions.

Recently, Qudsi et al. [2023] compared the position of 274 reversal jets to location of the X-line predicted by different models [Hesse et al., 2013; Moore et al., 2002; Swisdak and Drake, 2007; Trattner et al., 2007]. The global distributions of the magnetic fields were obtained with the Tsyganenko and Stern [1996] and Kobel and Fluckiger [1994] models. Additionally, a constant particle density of 0.1 cm^{-3} was used for the magnetosphere, and the density measured by the Magnetospheric Multiscale (MMS) spacecraft was used for the magnetosheath due to the lack of an analytical model for plasma density in these regions. However, similar to the studies mentioned above, this research did not find clear evidence of the superiority of one model over the other. In this study, the local orientation models [Hesse et al., 2013; Swisdak and Drake, 2007] were again not used as they were initially defined.

1.4 What is needed to go forwards?

Since magnetic reconnection theory was first proposed, numerous X-line models have been developed. Models that aim to predict the orientation of magnetic reconnection often rely on assumptions about the immediate conditions at the reconnection sites. Thus, predicting a global X-line using either local or global approach models requires a comprehensive understanding and modeling of the global distribution of certain quantities, such as magnetic field and plasma density, on both sides of the magnetopause. These conditions, so far the magnetic field, are usually obtained from modeling. However, there has been no spatial comparison between existing models, such as

those for the magnetic field, and in-situ data. Thus, it is of prior importance to acquire the spatial distribution of the crucial quantity involved in the reconnection process at the magnetopause.

Although there are a limited number of studies assessing the different X-line models, available evidence does not support the predominance of any single model over others. None of the models tested so far perfectly match the measured X-line position for all tested IMF orientations in studies using global simulation. It should also be noted that the location of reconnection is impacted by IMF and solar wind conditions, which constitute a vast parameter space that is currently inaccessible to parametric studies using high-resolution simulations. Additionally, the accuracy of this approach depends on the realism of the physical formalism used, often resistive MHD, which remains unclear.

Similarly, the studies using signatures of reconnection obtained from in-situ spacecraft measurements did not reveal the prevalence of any model. This is because this methodology involves a significant level of uncertainty due to the high level of fluctuations in plasma and field measurements, the difficulty of determining the causal upstream conditions of the observed events, and the local nature of in-situ measurements. Drawing relevant conclusions about the relative performance of different models in predicting the global location of the X-line would necessitate a substantial increase in the availability of magnetopause reconnection signatures to effectively mitigate the noise inherent to such studies.

In light of the challenges associated with evaluating the validity of existing models for magnetic reconnection, this thesis adopts a different approach. Rather than attempting to study models with in-situ observations of magnetic reconnection and/or numerical or analytical modeling, we have chosen to take to take a step back and solve a problem that should be the first to address: being able to actually look at the system under study, at the relevant scale, and from observations. Our aim is, instead, to understand how the spatial distributions of quantities important in magnetic reconnection constrain this process at the magnetopause. However, this approach is contingent on the ability to accurately obtain such constraints globally at the magnetopause.

Decades of data from multiple missions that have explored the system along various orbital and upstream conditions are now available. This presents a unique opportunity to finally obtain the spatial distribution of quantities important in the reconnection process from a observational standpoint. This thesis aims to fulfill this objective. However, achieving this goal presents significant challenges, most of which involve developing a new methodology to gather and process a comprehensive dataset of in-situ measurements under a wide array of upstream conditions. This will heavily rely on the usage of machine learning algorithms. Chapter 2 details on the different step of this methodology. Given the critical role of magnetic field orientation in the reconnection process, our initial focus, in Chapter 3, is on reconstructing the draping of the magnetic field in the magnetosheath corresponding to side of the magnetopause where the field is the most variable. Chapter 4 then shifts attention to variations in magnetic field amplitude and plasma density within the magnetosheath, which are also key factors constraining the boundary condition for magnetopause reconnection. Building on the insights gained from these studies, which demonstrate our capability for global reconstruction of these quantities' distributions, Chapter 5 presents a study mapping the magnetic shear angle, current density, and reconnection rate on the magnetopause, and discusses how they constrain magnetic reconnection therein.

1.5 Bibliography

Akasofu, S. I.: Paradigm transitions in solar-terrestrial physics from 1900: my personal view, History of Geo- and Space Sciences, 6, 23–43, https://doi.org/10.5194/hgss-6-23-2015, 2015. 6

Alexeev, I. I. and Bobrovnikov, S. Y.: Tail current sheet dynamics during substorm, in: International Conference on Substorms, edited by Rolfe, E. J. and Kaldeich, B., vol. 389 of *ESA Special Publication*, p. 417, 1996. 25

Alexeev, I. I., Sibeck, D. G., and Bobrovnikov, S. Y.: Concerning the location of magnetopause merging as a function of the magnetopause current strength, , 103, 6675–6684, https://doi.org/10.1029/97JA02863, 1998. 25, 27

Alfvén, H.: Existence of electromagnetic-hydrodynamic waves, Nature, 150, 405–406, 1942. 9, 13

Aunai, N., Hesse, M., Lavraud, B., Dargent, J., and Smets, R.: Orientation of the X-line in asymmetric magnetic reconnection, Journal of Plasma Physics, 82, 535820401, https://doi.org/10.1017/S0022377816000647, 2016. 22

Axford, W. I.: The Interaction between the Solar Wind and the Earth's Magnetosphere, , 67, 3791–3796, https://doi.org/10.1029/JZ067i010p03791, 1962. 9

Bartels, J.: Terrestrial-magnetic activity and its relations to solar phenomena, Terrestrial Magnetism and Atmospheric Electricity, 37, 1, https://doi.org/10.1029/TE037i001p00001, 1932. 6

Behannon, K. W. and Fairfield, D. H.: Spatial variations of the magnetosheath magnetic field, Planetary and Space Science, 17, 1803–1816, https://doi.org/10.1016/0032-0633(69)90056-7, 1969. 9

Biermann, L.: Kometenschweife und solare Korpuskularstrahlung, , 29, 274, 1951. 7

Birkeland, K.: Résultats des rescherches magnéthiques faites par l'expédition Norvégienne de 1899–1900, Archives des Sciences Physiques et Naturelles, pp. 565–586, 1901. 6

Birn, J., Borovsky, J. E., Hesse, M., and Schindler, K.: Scaling of asymmetric reconnection in compressible plasmas, Physics of Plasmas, 17, 052108, https://doi.org/10.1063/1.3429676, 2010. 21

Biskamp, D.: Magnetic reconnection in plasmas, Astrophysics and Space Science, 242, 165–207, 1996. 13

Bittencourt, J. A.: Fundamentals of plasma physics, Springer Science & Business Media, 2004. 7

Borovsky, J. E.: Physical improvements to the solar wind reconnection control function for the Earth's magnetosphere, Journal of Geophysical Research (Space Physics), 118, 2113–2121, https://doi.org/10.1002/jgra.50110, 2013. 21, 22, 26, 27

Bransgrove, A., Ripperda, B., and Philippov, A.: Magnetic hair and reconnection in black hole magnetospheres, Physical Review Letters, 127, 055 101, 2021. 12

Bridge, H. S., Dilworth, C., Lazarus, A. J., Lyon, E. F., Rossi, B., and Scherb, F.: Direct Observations of the Interplanetary Plasma, Journal of the Physical Society of Japan Supplement, 17, 553, 1962. 7

Burch, J. L., Torbert, R. B., Phan, T. D., Chen, L. J., Moore, T. E., Ergun, R. E., Eastwood, J. P., Gershman, D. J., Cassak, P. A., Argall, M. R., Wang, S., Hesse, M., Pollock, C. J., Giles, B. L., Nakamura, R., Mauk, B. H., Fuselier, S. A., Russell, C. T., Strangeway, R. J., Drake, J. F., Shay, M. A., Khotyaintsev, Y. V., Lindqvist, P. A., Marklund, G., Wilder, F. D., Young, D. T., Torkar, K., Goldstein, J., Dorelli, J. C., Avanov, L. A., Oka, M., Baker, D. N., Jaynes, A. N., Goodrich, K. A., Cohen, I. J., Turner, D. L., Fennell, J. F., Blake, J. B., Clemmons, J., Goldman, M., Newman, D., Petrinec, S. M., Trattner, K. J.,

Lavraud, B., Reiff, P. H., Baumjohann, W., Magnes, W., Steller, M., Lewis, W., Saito, Y., Coffey, V., and Chandler, M.: Electron-scale measurements of magnetic reconnection in space, Science, 352, aaf2939, https://doi.org/10.1126/science.aaf2939, 2016. 15

Burkholder, B. L., Chen, L.-J., Sorathia, K., Sciola, A., Merkin, S., Trattner, K. J., Gershman, D., Ma, X., and Connor, H.: The complexity of the day-side X-line during southward interplanetary magnetic field, Frontiers in Astronomy and Space Sciences, 10, 1175697, https://doi.org/10.3389/fspas.2023.1175697, 2023. 17

Cairns, I. H. and Fuselier, S.: Electron and ion heating due to magnetic reconnection at the heliopause, in: Journal of Physics: Conference Series, vol. 1100, p. 012004, IOP Publishing, 2018. 12

Carrasco, F., Shibata, M., and Reula, O.: Magnetospheres of black hole-neutron star binaries, Physical Review D, 104, 063 004, 2021. 12

Carrington, R. C.: Description of a Singular Appearance seen in the Sun on September 1, 1859, , 20, 13–15, https://doi.org/10.1093/mnras/20.1.13, 1859. 6

Cassak, P. A. and Fuselier, S. A.: Reconnection at Earth's Dayside Magnetopause, in: Magnetic Reconnection: Concepts and Applications, edited by Gonzalez, W. and Parker, E., vol. 427 of *Astrophysics and Space Science Library*, p. 213, https://doi.org/10.1007/978-3-319-26432-5_6, 2016. 11, 13, 16

Cassak, P. A. and Shay, M. A.: Scaling of asymmetric magnetic reconnection: General theory and collisional simulations, Physics of Plasmas, 14, 102114, https://doi.org/10.1063/1.2795630, 2007. 14, 21, 22, 23

Chapman, S. and Ferraro, V. C. A.: A New Theory of Magnetic Storms., , 126, 129–130, https://doi.org/10.1038/126129a0, 1930. 8

Chapman, S. and Ferraro, V. C. A.: A new theory of magnetic storms, Terrestrial Magnetism and Atmospheric Electricity, 36, 77, https://doi.org/10.1029/TE036i002p00077, 1931a. 8

Chapman, S. and Ferraro, V. C. A.: A new theory of magnetic storms, Terrestrial Magnetism and Atmospheric Electricity, 36, 171, https://doi.org/10.1029/TE036i003p00171, 1931b. 8

Cowley, S. W.: Hoyle and the magnetosphere, Astronomy & Geophysics, 57, 1–12, 2016. 6

Cowley, S. W. H.: Comments on the merging of nonantiparallel magnetic fields, , 81, 3455, https://doi.org/10.1029/JA081i019p03455, 1976. 18, 19

Crooker, N. U., Eastman, T. E., and Stiles, G. S.: Observations of plasma depletion in the magnetosheath at the dayside magnetopause, , 84, 869–874, https://doi.org/10.1029/JA084iA03p00869, 1979. 23, 24, 25

Daly, P. W., Saunders, M. A., Rijnbeek, R. P., Sckopke, N., and Russell, C. T.: The distribution of reconnection geometry in flux transfer events using energetic ion, plasma and magnetic data, , 89, 3843–3854, https://doi.org/10.1029/JA089iA06p03843, 1984. 17

Davis, L.: Interplanetary Magnetic Fields and Cosmic Rays, Physical Review, 100, 1440–1444, https://doi.org/10.1103/PhysRev.100.1440, 1955. 7

Davis, L.: Mariner II observations relevant to solar fields, in: Stellar and Solar Magnetic Fields, vol. 22, p. 202, 1965. 7

Dessler, A. J. and Fejer, J. A.: Interpretation of K_p index and M-region geomagnetic storms, , 11, 505–511, https://doi.org/10.1016/0032-0633(63)90074-6, 1963. 9

Dungey, J. W.: Origin of Cosmic Rays, Physical Review, 91, 766–766, https://doi.org/10.1103/PhysRev.91.766, 1953. 9, 12

Dungey, J. W.: Cosmic electrodynamics, Cambridge University Press, 1958. 9

Dungey, J. W.: Interplanetary Magnetic Field and the Auroral Zones, , 6, 47–48, https://doi.org/10.1103/PhysRevLett.6.47, 1961. 9, 10, 14

Dunlop, M. W., Zhang, Q. H., Bogdanova, Y. V., Lockwood, M., Pu, Z., Hasegawa, H., Wang, J., Taylor, M. G. G. T., Berchem, J., Lavraud, B., Eastwood, J., Volwerk, M., Shen, C., Shi, J. K., Constantinescu, D., Frey, H., Fazakerley, A. N., Sibeck, D., Escoubet, P., Wild, J. A., and Liu, Z. X.: Extended Magnetic Reconnection across the Dayside Magnetopause, , 107, 025004, https://doi.org/10.1103/PhysRevLett.107.025004, 2011. 17

Eastwood, J., Brain, D., Halekas, J., Drake, J., Phan, T., Øieroset, M., Mitchell, D., Lin, R., and Acuña, M.: Evidence for collisionless magnetic reconnection at Mars, Geophysical Research Letters, 35, 2008. 12

Eastwood, J. P., Hietala, H., Toth, G., Phan, T. D., and Fujimoto, M.: What Controls the Structure and Dynamics of Earth's Magnetosphere?, , 188, 251–286, https://doi.org/10.1007/s11214-014-0050-x, 2015. 15

Eggington, J. W. B., Eastwood, J. P., Mejnertsen, L., Desai, R. T., and Chittenden, J. P.: Dipole Tilt Effect on Magnetopause Reconnection and the Steady-State Magnetosphere-Ionosphere System: Global MHD Simulations, Journal of Geophysical Research (Space Physics), 125, e27510, https://doi.org/10.1029/2019JA027510, 2020. 17

Fairfield, D. H.: The ordered magnetic field of the magnetosheath, vol. 72 of *Journal of Geophysical Research*, https://doi.org/10.1029/jz072i023p05865, 1967. 9

Formisano, V.: The three-dimensional shape of the bow shock., Nuovo Cimento C Geophysics Space Physics C, 2C, 681–692, https://doi.org/10.1007/BF02558125, 1979. 9

Furth, H. P., Killeen, J., and Rosenbluth, M. N.: Finite-Resistivity Instabilities of a Sheet Pinch, Physics of Fluids, 6, 459–484, https://doi.org/10.1063/1.1706761, 1963. 13

Fuselier, S. and Lewis, W.: Properties of near-Earth magnetic reconnection from in-situ observations, Space Science Reviews, 160, 95–121, 2011. 12

Gilbert, G.: De magnete, magneticisque corporibus, et de magno magnete tellure; Physiologia nova, plurimis & argumentis, & experimentis demonstrata, Petrus Short, 1600. 8

Giovanelli, R. G.: Magnetic and Electric Phenomena in the Sun's Atmosphere associated with Sunspots, , 107, 338, https://doi.org/10.1093/mnras/107.4.338, 1947. 9

Giovanelli, R. G.: Chromospheric Flares, , 108, 163, https://doi.org/10.1093/mnras/108.2.163, 1948. 9

Glocer, A., Dorelli, J., Toth, G., Komar, C. M., and Cassak, P. A.: Separator reconnection at the magnetopause for predominantly northward and southward IMF: Techniques and results, Journal of Geophysical Research (Space Physics), 121, 140–156, https://doi.org/10.1002/2015JA021417, 2016. 17

Gold, T.: Motions in the Magnetosphere of the Earth, , 64, 1219–1224, https://doi.org/10.1029/JZ064i009p01219, 1959. 9

Gold, T.: Magnetic Storms, , 1, 100–114, https://doi.org/10.1007/BF00174637, 1962. 9

Goldstein, E.: Ueber die Entladung der Electricität in verdünnten Gasen, Annalen der Physik, 248, 249–279, https://doi.org/10.1002/andp.18812480205, 1881. 6

Gonzalez, W. D. and Mozer, F. S.: A quantitative model for the potential resulting from reconnection with an arbitrary interplanetary magnetic field, , 79, 4186, https://doi.org/10.1029/JA079i028p04186, 1974. 18

Gringauz, K. I., Bezrokikh, V. V., Ozerov, V. D., and Rybchinskii, R. E.: A Study of the Interplanetary Ionized Gas, High-Energy Electrons and Corpuscular Radiation from the Sun by Means of the Three-Electrode Trap for Charged Particles on the Second Soviet Cosmic Rocket, Soviet Physics Doklady, 5, 361, 1960. 7

Grodent, D., Gérard, J.-C., Clarke, J., Gladstone, G., and Waite Jr, J.: A possible auroral signature of a magnetotail reconnection process on Jupiter, Journal of Geophysical Research: Space Physics, 109, 2004. 12

Hale, G. E.: On the Probable Existence of a Magnetic Field in Sun-Spots, , 28, 315, https://doi.org/10.1086/141602, 1908. 7

Hale, G. E.: The Spectrohelioscope and its Work. Part III. Solar Eruptions and Their Apparent Terrestrial Effects, , 73, 379, https://doi.org/10.1086/143316, 1931. 6

Hall, J. S.: Observations of the Polarized Light from Stars, Science, 109, 166–167, https://doi.org/10.1126/science.109.2825.166, 1949. 7

Hedgecock, P., Thomas, B., Cornwall, A., and Davis, C.: A dipole-tilt dependent model of the Earths magnetosphere, Imperial College preprint, 1979. 24

Hesse, M. and Cassak, P. A.: Magnetic Reconnection in the Space Sciences: Past, Present, and Future, Journal of Geophysical Research (Space Physics), 125, e25935, https://doi.org/10.1029/2018JA025935, 2020. 13, 16

Hesse, M., Forbes, T. G., and Birn, J.: On the Relation between Reconnected Magnetic Flux and Parallel Electric Fields in the Solar Corona, , 631, 1227–1238, https://doi.org/10.1086/432677, 2005. 16

Hesse, M., Aunai, N., Zenitani, S., Kuznetsova, M., and Birn, J.: Aspects of collisionless magnetic reconnection in asymmetric systems, Physics of Plasmas, 20, 061210, https://doi.org/10.1063/1.4811467, 2013. 21, 23, 27, 28

Hesse, M., Aunai, N., Sibeck, D., and Birn, J.: On the electron diffusion region in planar, asymmetric, systems, , 41, 8673–8680, https://doi.org/10.1002/2014GL061586, 2014. 16

Hill, T. W.: Magnetic merging in a collisionless plasma, , 80, 4689, https://doi.org/10.1029/JA080i034p04689, 1975. 18

Hiltner, W. A.: On the Presence of Polarization in the Continuous Radiation of Stars. II., , 109, 471, https://doi.org/10.1086/145151, 1949. 7

Hoyle, F.: Some recent researches in solar physics, Cambridge University Press, 1949. 9

Jelínek, K., Němeček, Z., and Šafránková, J.: A new approach to magnetopause and bow shock modeling based on automated region identification, Journal of Geophysical Research (Space Physics), 117, A05208, https://doi.org/10.1029/2011JA017252, 2012. 9, 12

Jeřáb, M., Němeček, Z., Šafránková, J., Jelínek, K., and Měrka, J.: Improved bow shock model with dependence on the IMF strength, Planetary and Space Science, 53, 85–93, https://doi.org/10.1016/j.pss.2004.09.032, 2005. 9

Kadowaki, L. H., Dal Pino, E. M. D. G., and Stone, J. M.: MHD instabilities in accretion disks and their implications in driving fast magnetic reconnection, The Astrophysical Journal, 864, 52, 2018. 12

Kane, R. P.: Sun Earth relation: Historical development and present status A brief review, Advances in Space Research, 35, 866–881, https://doi.org/10.1016/j.asr.2005.03.142, 2005. 6

Kellogg, P. J.: Flow of Plasma around the Earth, , 67, 3805–3811, https://doi.org/10.1029/JZ067i010p03805, 1962. 9

Klimchuk, J. A.: On solving the coronal heating problem, Solar Physics, 234, 41–77, 2006. 12

Kobel, E. and Fluckiger, E. O.: A model of the steady state magnetic field in the magnetosheath, , 99, 23 617–23 622, https://doi.org/10.1029/94JA01778, 1994. 25, 26, 28

Komar, C. M., Fermo, R. L., and Cassak, P. A.: Comparative analysis of dayside magnetic reconnection models in global magnetosphere simulations, Journal of Geophysical Research (Space Physics), 120, 276–294, https://doi.org/10.1002/2014JA020587, 2015. 17, 25, 26, 28

Komissarov, S.: Simulations of the axisymmetric magnetospheres of neutron stars, Monthly Notices of the Royal Astronomical Society, 367, 19–31, 2006. 12

Lakhina, G. S. and Tsurutani, B. T.: Geomagnetic storms: historical perspective to modern view, Geoscience Letters, 3, 5, https://doi.org/10.1186/s40562-016-0037-4, 2016. 6

Lamont: Ueber die zehnjährige Periode, welche sich in der Grösse der täglichen Bewegung der Magnetnadel darstellt, Annalen der Physik, 160, 572–582, https://doi.org/10.1002/andp.18511601206, 1851. 6

Lang, K. R.: The Cambridge guide to the solar system, Cambridge University Press, 2011. 11

Lavraud, B., Opher, M., Dialynas, K., Turner, D., Eriksson, S., Provornikova, E., Kornbleuth, M., Mostafavi, P., Fedorov, A., Richardson, J., et al.: What is the heliopause? Importance of magnetic reconnection and measurement requirements, Frontiers in Astronomy and Space Sciences, 10, 1060 618, 2023. 12

Leake, J. E., Daldorff, L. K., and Klimchuk, J. A.: The onset of 3D magnetic reconnection and heating in the solar corona, The Astrophysical Journal, 891, 62, 2020. 12

Li, W., Wu, L., Ge, Y., and Lü, L.-Z.: Magnetotail Configuration Under Northward IMF Conditions, Journal of Geophysical Research (Space Physics), 126, e28634, https://doi.org/10.1029/2020JA028634, 2021. 15

Lin, R. L., Zhang, X. X., Liu, S. Q., Wang, Y. L., and Gong, J. C.: A three-dimensional asymmetric magnetopause model, Journal of Geophysical Research (Space Physics), 115, A04207, https://doi.org/10.1029/2009JA014235, 2010. 9

Lindemann, F. A.: LXX. Note on the theory of magnetic storms, The London, Edinburgh, and Dublin Philosophical Magazine and Journal of Science, 38, 669–684, 1919. 6, 8

Liu, Y.-H., Hesse, M., Guo, F., Daughton, W., Li, H., Cassak, P. A., and Shay, M. A.: Why does Steady-State Magnetic Reconnection have a Maximum Local Rate of Order 0.1?, , 118, 085101, https://doi.org/10.1103/PhysRevLett.118.085101, 2017. 14

Liu, Y.-H., Hesse, M., Li, T. C., Kuznetsova, M., and Le, A.: Orientation and Stability of Asymmetric Magnetic Reconnection X Line, Journal of Geophysical Research (Space Physics), 123, 4908–4920, https://doi.org/10.1029/2018JA025410, 2018. 23

Louarn, P., Andre, N., Jackman, C. M., Kasahara, S., Kronberg, E. A., and Vogt, M. F.: Magnetic reconnection and associated transient phenomena within the magnetospheres of Jupiter and Saturn, Space Science Reviews, 187, 181–227, 2015. 12

Luhmann, J. G., Walker, R. J., Russell, C. T., Crooker, N. U., Spreiter, J. R., and Stahara, S. S.: Patterns of Potential Magnetic Field Merging Sites on the Dayside Magnetopause, , 89, 1739–1742, https://doi.org/10.1029/JA089iA03p01739, 1984. 24

Macek, W.: Reconnection at the Heliopause, Advances in Space Research, 9, 257–261, 1989. 12

Maheshwari, K., Phan, T. D., Øieroset, M., Fargette, N., Lavraud, B., Burch, J. L., Strangeway, R. J., Gershman, D. J., and Giles, B. L.: Investigation of the Diamagnetic Drift Condition for the Suppression of Magnetic Reconnection in 3D Interlinked Reconnection Events with Magnetic Flux Pileup, , 940, 177, https://doi.org/10.3847/1538-4357/ac9405, 2022. 20

Mandt, M. E., Denton, R. E., and Drake, J. F.: Transition to whistler mediated magnetic reconnection, , 21, 73–76, https://doi.org/10.1029/93GL03382, 1994. 13

Maunder, E. W.: Magnetic disturbances and associated sun-spots, , 65, 666, https://doi.org/10.1093/mnras/65.7.666, 1905. 6

Mihalov, J., Sonett, C., and Wolfe, J.: MHD Rankine—Hugoniot equations applied to earth's bow shock, Journal of Plasma Physics, 3, 449–463, 1969. 9

Moore, T. E., Fok, M. C., and Chandler, M. O.: The dayside reconnection X line, Journal of Geophysical Research (Space Physics), 107, 1332, https://doi.org/10.1029/2002JA009381, 2002. 18, 19, 28

Morrison, P.: Solar origin of cosmic-ray time variations, Physical Review, 101, 1397, 1956. 7

Most, E. R. and Philippov, A. A.: Reconnection-powered fast radio transients from coalescing neutron star binaries, Physical Review Letters, 130, 245 201, 2023. 12

Ness, N. F. and Wilcox, J. M.: Solar Origin of the Interplanetary Magnetic Field, , 13, 461–464, https://doi.org/10.1103/PhysRevLett.13.461, 1964. 7

Ness, N. F. and Wilcox, J. M.: Sector Structure of the Quiet Interplanetary Magnetic Field, Science, 148, 1592–1594, https://doi.org/10.1126/science.148.3677.1592, 1965. 6

Neugebauer, M. and Snyder, C. W.: Solar Plasma Experiment, Science, 138, 1095–1097, https://doi.org/10.1126/science.138.3545.1095.a, 1962. 7

Newell, P. T., Meng, C.-I., Sibeck, D. G., and Lepping, R.: Some low-altitude cusp dependencies on the interplanetary magnetic field, , 94, 8921–8927, https://doi.org/10.1029/JA094iA07p08921, 1989. 25

Newton, H. W.: Solar flares and magnetic storms, , 103, 244, https://doi.org/10.1093/mnras/103.5.244, 1943. 6

Nickeler, D. H. and Fahr, H.-J.: Reconnection at the heliopause, Advances in Space Research, 35, 2067–2072, 2005. 12

Onsager, T. G., Thomsen, M. F., Elphic, R. C., and Gosling, J. T.: Model of electron and ion distributions in the plasma sheet boundary layer, , 96, 20 999–21 011, https://doi.org/10.1029/91JA01983, 1991. 25

Owens, M. J. and Forsyth, R. J.: The heliospheric magnetic field, Living Reviews in Solar Physics, 10, 1–52, 2013. 6

Parker, E. N.: Sweet's Mechanism for Merging Magnetic Fields in Conducting Fluids, , 62, 509–520, https://doi.org/10.1029/JZ062i004p00509, 1957. 13

Parker, E. N.: Dynamics of the Interplanetary Gas and Magnetic Fields., The Astrophysical Journal, 128, 664, https://doi.org/10.1086/146579, 1958. 7, 9

Parker, E. N.: A history of early work on the heliospheric magnetic field, , 106, 15 797–15 802, https://doi.org/10.1029/2000JA000100, 2001. 6

Paschmann, G., Sonnerup, B. Ö., Papamastorakis, I., Sckopke, N., Haerendel, G., Bame, S., Asbridge, J., Gosling, J., Russell, C., and Elphic, R.: Plasma acceleration at the Earth's magnetopause: Evidence for reconnection, Nature, 282, 243–246, 1979. 15

Petrinec, S. M., Burch, J. L., Fuselier, S. A., Trattner, K. J., Giles, B. L., and Strangeway, R. J.: On the Occurrence of Magnetic Reconnection Along the Terrestrial Magnetopause, Using Magnetospheric Multiscale (MMS) Observations in Proximity to the Reconnection Site, Journal of Geophysical Research (Space Physics), 127, e29669, https://doi.org/10.1029/2021JA029669, 2022. 24

Phan, T. D., Kistler, L. M., Klecker, B., Haerendel, G., Paschmann, G., Sonnerup, B. U. Ö., Baumjohann, W., Bavassano-Cattaneo, M. B., Carlson, C. W., DiLellis, A. M., Fornacon, K. H., Frank, L. A., Fujimoto, M., Georgescu, E., Kokubun, S., Moebius, E., Mukai, T., Øieroset, M., Paterson, W. R., and Reme, H.: Extended magnetic reconnection at the Earth's magnetopause from detection of bi-directional jets, , 404, 848–850, https://doi.org/10.1038/35009050, 2000. 15, 17

Phan, T. D., Freeman, M. P., Kistler, L. M., Klecker, B., Haerendel, G., Paschmann, G., Sonnerup, B. U. Ö., Baumjohann, W., Bavassano-Cattaneo, M. B., Carlson, C. W., DiLellis, A. M., Fornacon, K. H., Frank, L. A., Fujimoto, M., Georgescu, E., Kokubun, S., Moebius, E., Mukai, T., Paterson, W. R., and Reme, H.: Evidence for an extended reconnection line at the dayside magnetopause, Earth, Planets and Space, 53, 619–625, https://doi.org/10.1186/BF03353281, 2001. 17

Phan, T. D., Hasegawa, H., Fujimoto, M., Oieroset, M., Mukai, T., Lin, R. P., and Paterson, W.: Simultaneous Geotail and Wind observations of reconnection at the subsolar and tail flank magnetopause, , 33, L09104, https://doi.org/10.1029/2006GL025756, 2006. 17

Phan, T. D., Paschmann, G., Gosling, J. T., Oieroset, M., Fujimoto, M., Drake, J. F., and Angelopoulos, V.: The dependence of magnetic reconnection on plasma β and magnetic shear: Evidence from magnetopause observations, , 40, 11–16, https://doi.org/10.1029/2012GL054528, 2013. 20

Priest, E.: Three-dimensional magnetic reconnection in the solar corona, Physics of plasmas, 4, 1945–1952, 1997. 12

Priest, E.: Heating the solar corona by magnetic reconnection, Astrophysics and Space science, 264, 77–100, 1998. 12

Pu, Z. Y., Xiao, C. J., Zhang, X. G., Huang, Z. Y., Fu, S. Y., Liu, Z. X., Dunlop, M. W., Zong, Q. G., Carr, C. M., Réme, H., Dandouras, I., Fazakerley, A., Phan, T., Zhang, T. L., Zhang, H., and Wang, X. G.: Double Star TC-1 observations of component reconnection at the dayside magnetopause: a preliminary study, Annales Geophysicae, 23, 2889–2895, https://doi.org/10.5194/angeo-23-2889-2005, 2005. 17

Qudsi, R. A., Walsh, B. M., Broll, J., Atz, E., and Haaland, S.: Statistical Comparison of Various Dayside Magnetopause Reconnection X-Line Prediction Models, Journal of Geophysical Research (Space Physics), 128, e2023JA031644, https://doi.org/10.1029/2023JA031644, 2023. 28

Ripperda, B., Bacchini, F., and Philippov, A. A.: Magnetic reconnection and hot spot formation in black hole accretion disks, The Astrophysical Journal, 900, 100, 2020. 12

Sabine, E.: On Periodical Laws Discoverable in the Mean Effects of the Larger Magnetic Disturbances. No. II, Philosophical Transactions of the Royal Society of London Series I, 142, 103–124, 1852. 6

Santos-Lima, R., Dal Pino, E. d. G., and Lazarian, A.: The role of turbulent magnetic reconnection in the formation of rotationally supported protostellar disks, The Astrophysical Journal, 747, 21, 2012. 12

Schulz, M.: Interplanetary sector structure and the helliomagnetic equator, , 24, 371–383, https://doi.org/10.1007/BF02637162, 1973. 7

Schwabe, M.: Die Sonne. Von Herrn Hofrath Schwabe, Astronomische Nachrichten, 20, 283, https://doi.org/10.1002/asna.18430201706, 1843. 6

Scurry, L., Russell, C. T., and Gosling, J. T.: A statistical study of accelerated flow events at the dayside magnetopause, , 99, 14,815–14,829, https://doi.org/10.1029/94JA00793, 1994. 17

Shue, J. H., Song, P., Russell, C. T., Steinberg, J. T., Chao, J. K., Zastenker, G., Vaisberg, O. L., Kokubun, S., Singer, H. J., Detman, T. R., and Kawano, H.: Magnetopause location under extreme solar wind conditions, JGR, 103, 17 691–17 700, https://doi.org/10.1029/98JA01103, 1998. 9, 12

Slavin, J. A., Acuña, M. H., Anderson, B. J., Baker, D. N., Benna, M., Boardsen, S. A., Gloeckler, G., Gold, R. E., Ho, G. C., Korth, H., et al.: MESSENGER observations of magnetic reconnection in Mercury's magnetosphere, science, 324, 606–610, 2009. 12

Snyder, C. W., Neugebauer, M., and Rao, U. R.: The Solar Wind Velocity and Its Correlation with Cosmic-Ray Variations and with Solar and Geomagnetic Activity, , 68, 6361, https://doi.org/10.1029/JZ068i024p06361, 1963. 6

Sonett, C. P. and Abrams, I. J.: The Distant Geomagnetic Field, 3, Disorder and Shocks in the Magnetopause, , 68, 1233–1263, https://doi.org/10.1029/JZ068i005p01233, 1963. 9

Song, P. and Russell, C. T.: What do we really know about the magnetosheath?, Advances in Space Research, 20, 747–765, https://doi.org/10.1016/S0273-1177(97)00466-3, 1997. 6

Sonnerup, B. U. Ö.: Magnetopause reconnection rate, , 79, 1546–1549, https://doi.org/10.1029/JA079i010p01546, 1974. 17, 18, 19, 22, 27

Sonnerup, B. U. O., Paschmann, G., Papamastorakis, I., Sckopke, N., Haerendel, G., Bame, S. J., Asbridge, J. R., Gosling, J. T., and Russell, C. T.: Evidence for magnetic field reconnection at the earth's magnetopause, , 86, 10 049–10 067, https://doi.org/10.1029/JA086iA12p10049, 1981. 15

Souza, V. M., Gonzalez, W. D., Sibeck, D. G., Koga, D., Walsh, B. M., and Mendes, O.: Comparative study of three reconnection X line models at the Earth's dayside magnetopause using in situ observations, Journal of Geophysical Research (Space Physics), 122, 4228–4250, https://doi.org/10.1002/2016JA023790, 2017. 17, 25, 27

Spreiter, J. R. and Stahara, S. S.: A new predictive model for determining solar wind-terrestrial planet interactions, , 85, 6769–6777, https://doi.org/10.1029/JA085iA12p06769, 1980. 24

Stern, D. P.: A brief history of magnetospheric physics before the spaceflight era, Reviews of Geophysics, 27, 103–114, 1989. 6

Stormer, C.: La Theorie Corpusculaire des Aurores Boreales., L'Astronomie, 32, 153–159, 1918. 6

Sweet, P.: 14. The neutral point theory of solar flares, in: Symposium-International Astronomical Union, vol. 6, pp. 123–134, Cambridge University Press, 1958. 13

Swisdak, M. and Drake, J. F.: Orientation of the reconnection X-line, , 34, L11106, https://doi.org/10.1029/2007GL029815, 2007. 18, 20, 26, 27, 28

Swisdak, M., Rogers, B. N., Drake, J. F., and Shay, M. A.: Diamagnetic suppression of component magnetic reconnection at the magnetopause, Journal of Geophysical Research (Space Physics), 108, 1218, https://doi.org/10.1029/2002JA009726, 2003. 20

Trattner, K. J., Mulcock, J. S., Petrinec, S. M., and Fuselier, S. A.: Location of the reconnection line at the magnetopause during southward IMF conditions, , 34, L03108, https://doi.org/10.1029/2006GL028397, 2007. 25, 26, 27, 28

Trattner, K. J., Petrinec, S. M., Fuselier, S. A., Omidi, N., and Sibeck, D. G.: Evidence of multiple reconnection lines at the magnetopause from cusp observations, Journal of Geophysical Research (Space Physics), 117, A01213, https://doi.org/10.1029/2011JA017080, 2012. 28

Trattner, K. J., Burch, J. L., Ergun, R., Fuselier, S. A., Gomez, R. G., Grimes, E. W., Lewis, W. S., Mauk, B., Petrinec, S. M., Pollock, C. J., Phan, T. D., Vines, S. K., Wilder, F. D., and Young, D. T.: The response time of the magnetopause reconnection location to changes in the solar wind: MMS case study, , 43, 4673–4682, https://doi.org/10.1002/2016GL068554, 2016. 26

Trattner, K. J., Burch, J. L., Ergun, R., Eriksson, S., Fuselier, S. A., Giles, B. L., Gomez, R. G., Grimes, E. W., Lewis, W. S., Mauk, B., Petrinec, S. M., Russell, C. T., Strangeway, R. J., Trenchi, L., and Wilder, F. D.: The MMS Dayside Magnetic Reconnection Locations During Phase 1 and Their Relation to the Predictions of the Maximum Magnetic Shear Model, Journal of Geophysical Research (Space Physics), 122, 11,991–12,005, https://doi.org/10.1002/2017JA024488, 2017. 28

Trattner, K. J., Fuselier, S. A., Petrinec, S. M., Burch, J. L., Ergun, R., and Grimes, E. W.: Long and Active Magnetopause Reconnection X Lines During Changing IMF Conditions, Journal of Geophysical Research (Space Physics), 126, e28926, https://doi.org/10.1029/2020JA028926, 2021a. 16

Trattner, K. J., Petrinec, S. M., and Fuselier, S. A.: The Location of Magnetic Reconnection at Earth's Magnetopause, , 217, 41, https://doi.org/10.1007/s11214-021-00817-8, 2021b. 26, 27, 28

Tsyganenko, N. A. and Stern, D. P.: Modeling the global magnetic field of the large-scale Birkeland current systems, , 101, 27 187–27 198, https://doi.org/10.1029/96JA02735, 1996. 19, 26, 28

von Humboldt, A.: Die vollständigste aller bisherigen Beobachtungen über den Einfluss des Nordlichts auf die Magnetnadel angestellt, Annalen der Physik, 29, 425–429, https://doi.org/10.1002/andp.18080290806, 1808. 6

Walsh, B. M., Komar, C. M., and Pfau-Kempf, Y.: Spacecraft measurements constraining the spatial extent of a magnetopause reconnection X line, , 44, 3038–3046, https://doi.org/10.1002/2017GL073379, 2017. 17

Wilcox, J. M. and Ness, N. F.: Quasi-Stationary Corotating Structure in the Interplanetary Medium, , 70, 5793–5805, https://doi.org/10.1029/JZ070i023p05793, 1965. 7

Yokoyama, T. and Shibata, K.: Numerical simulation of solar coronal X-ray jets based on the magnetic reconnection model, Publications of the Astronomical Society of Japan, 48, 353–376, 1996. 12

Zhigulev, V.: Concerning the interaction of currents flowing in a conducting medium with the earth's magnetic field, in: Doklady Akad. Nauk SSSR„ vol. 127, pp. 1001–1004, 1959. 9

Zhou, M., Ashour-Abdalla, M., Deng, X., Pang, Y., Fu, H., Walker, R., Lapenta, G., Huang, S., Xu, X., and Tang, R.: Observation of Three-Dimensional Magnetic Reconnection in the Terrestrial Magnetotail, Journal of Geophysical Research (Space Physics), 122, 9513–9520, https://doi.org/10.1002/2017JA024597, 2017. 17

Chapter 2

Global Methodology

Contents

2.1 Introduction

This work aims to investigate magnetic reconnection at the Earth's magnetopause, with a focus on improving our understanding of how the location of the X-line is constrained by the properties of the magnetopause from a global scale perspective. On one hand, in-situ observations of magnetic reconnection (e.g. Dunlop et al. [2011]; Phan et al. [2003]; Retinò et al. [2005]) provide a limited local perspective that cannot, as is, lead to a global understanding of the location of the process. On the other hand, our current understanding of where the X-line is located globally, is based solely on numerical (e.g. Eggington et al. [2020]; Glocer et al. [2016]; Komar et al. [2015]) or analytical (e.g. Alexeev et al. [1998]; Moore et al. [2002]; Trattner et al. [2007]) models that make assumptions such as resistive dissipation or analytically modeled properties at the magnetopause. Therefore, an important step forward consists in obtaining and studying the physical constraints on magnetopause reconnection using only in-situ measurements.

Obtaining the global and three-dimensional plasma and magnetic properties in the magnetosheath and at the magnetopause as a function of the IMF orientation and solar wind conditions from only in-situ data is quite challenging. Indeed, in the immense and highly dynamical system that is the near-Earth plasma environment, in-situ measurements are intrinsically local in both space and time. Firstly, the data is heavily spatially biased by the satellite orbital planes. Reconstructing the spatial physical properties of the system from observations thus imperiously requires having multiple spacecraft on significantly different orbits. Secondly, understanding their dependence on the IMF orientation requires the constant monitoring of the upstream solar wind from yet another spacecraft. And even if such data was available, estimating the causal IMF orientation for each measurement may come with possibly substantial errors that call for large statistics for the results to be relevant. Then, in-situ data carries many small scale plasma and magnetic fluctuations from which the macro-scale properties can only stand out if using again a large number of uncorrelated measurements. Unfortunately, the complexity of the time series makes it difficult to automatize the identification of time intervals during which the spacecraft explores regions of interest. Data selection is often performed manually, hampering large statistics, consequently adding substantial uncertainties when drawing conclusions. Last but not least, is the fact that multivariate time series such as spacecraft measurements actually represent slices in an unsteady complex three-dimensional system in which the instantaneous position of the spacecraft relative to plasma structures (i.e. magnetopause and bow shock) is unknown. This space/time ambiguity substantially complicates the reconstruction of spatial variations, which requires the considered quantity, measured at a given time, to be positioned relative to the magnetopause and the bow shock boundaries.

This chapter details the different steps of the data processing pipeline designed to reconstruct and analyze the global physical properties in the magnetosheath and at the magnetopause using only in-situ measurements.

2.2 From Local Measurements to a Global Representation: Overview

This section provides an overview of the processing pipeline common to all the studies conducted throughout this PhD research. Detailed descriptions of each step of this pipeline can be found in the following sections of this chapter.

Data from four spacecraft missions outlined in Section 2.3, spanning from 2001 to 2021, were utilized for this research. In the first step of this pipeline, all available data points from the magnetosheath and magnetosphere were automatically selected using a machine learning algorithm, as explained in Section 2.4. The state of the near-Earth plasma environment is strongly correlated to the upstream IMF and solar wind conditions, both in terms of the measurements themselves and their spatial locations relative to the system boundaries. Therefore, an important step of this pipeline is to pair each measurement with the properties of its causal IMF and solar wind (see details in section 2.5). This pairing will enable the reconstruction of the spatial distribution of

quantities as a function of the upstream conditions. However, if used as is, the points would not give a fair representation of the spatial structure in the magnetosheath or near the magnetopause because two points spatially close may be at a different distance from the magnetopause and bow shock for their respective solar wind and IMF conditions. Therefore, it is necessary to reposition each data point relative to the same shock and magnetopause, parameterized with average solar wind and IMF conditions. Therefore, the pairing procedure will also prove to be useful for repositioning measurements relative to the system boundaries. Section 2.6 presents the machine learning methods used for this position normalization. Depending on the particular phenomena being studied or the specific region under investigation, such as the magnetosheath or magnetopause, the measurements are transformed into a particular coordinate system. Section 2.7 introduces the different coordinate systems used in this work. Finally, Section 2.8 provides insights into the method employed to obtain the 3D spatial distribution of the wanted quantities (e.g. magnetic field, ion density).

2.3 Missions, Instrumentation, and Measurements

In this section, we present the missions and measurements that are used in this Ph.D. work. We provide an overview of each mission's characteristics and objectives, followed by a description of its orbits and phases, and finally present the specific instruments and measurements used in the different studies of this manuscript. It should be noticed that the primary objective of this section is to gather, in the same place, information disseminated across various sources and websites that are important when working with in-situ measurements.

2.3.1 The Cluster mission

Mission overview

Cluster is a mission of the European Space Agency (ESA). This mission corresponds actually to Cluster II, because the initial Cluster I mission was destroyed during the 1996 Ariane 5 rocket explosion. It comprises four identical spacecraft arranged to fly in a tetrahedral formation. Two of the spacecraft were launched in July 2000, and the remaining two in August of that same year. The spacecraft were originally named Rumba, Salsa, Samba, and Tango, but are commonly referred to as Cluster 1 (C1), Cluster 2 (C2), Cluster 3 (C3), and Cluster 4 (C4) by the scientific community. The initial exploitation period was designated as 27 months, but it has been prolonged for over two decades and is presently anticipated to terminate in September 2024. However, the instruments that measured the composition and three-dimensional distribution of ions for Clusters 2 and 4 were non-functional from the outset or ceased operating for Cluster 3 in 2009. But this did not

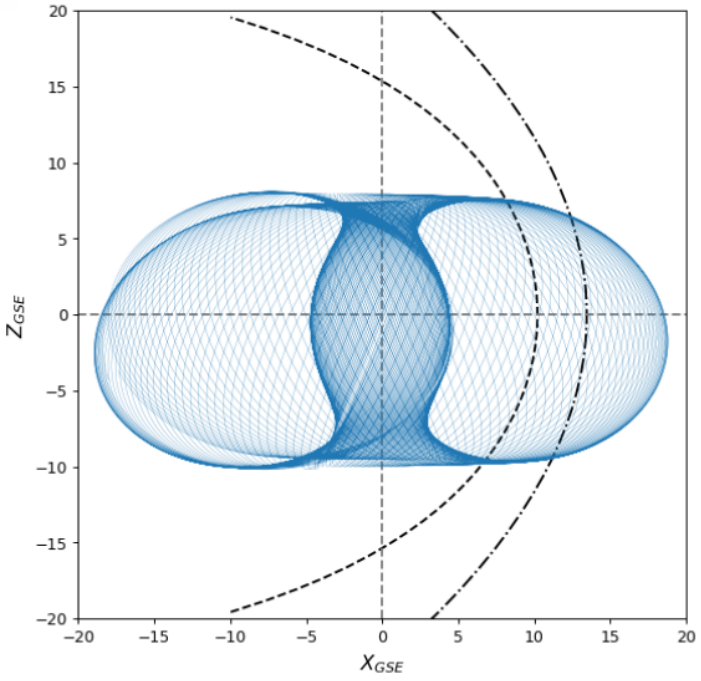

Figure 2.1: Orbit of the C1 probe in the (XZ) plane between September 19th, 2002 and September 18th, 2003. The dashed and dash-dotted black lines correspond to the magnetopause and bow shock, respectively.

hinder the main objective of the mission, which was to study the magnetic and electric fields in three dimensions for the first time. Specifically, the mission aimed to investigate the magnetic reconnection process at the ion scale.

Orbits

The Cluster mission has an elliptical polar orbit that ranges from 2,000 km to 130,000 km (i.e. approximately 20 RE), with an inclination between 64.8 and 90 degrees relative to the equatorial plane. During a 54-hour orbital period, the four spacecraft explore both cusp regions with a distance between them ranging from 10 to 10,000 km. The figure 2.1 shows the orbits of the Cluster 1 probe around Earth over a period of one year. Due to the large apogee, the satellites passe through different regions of the near-Earth plasma environment throughout the year, including the magnetotail, dayside and flank magnetosheath, and solar wind.

Instruments and measurements

The Fluxgate Magnetometer (FGM) [Balogh et al., 2001] provides measurements of the magnetic field. It has five sensitivity ranges ranging from ±256 nT to ±65,500 nT and offers four modes: the Normal Mode (C) operating at 22.4 Hz, Burst Mode (D) at 67.3 Hz, Extended Mode (E) at 0.25 Hz, and Housekeeping Mode (All) at 0.19 Hz. This work uses the magnetic field measurements in Geocentric Solar Magnetospheric (GSM) coordinates at spin resolution (i.e. approximately 4-second resolution).

The Cluster Ion Spectrometry-Hot Ion Analyser (CIS-HIA) instrument [Rème et al., 2001] provides measurements of plasma moments (ion density, temperature, and bulk velocity) with a 4-second resolution. The HIA instrument has several operating modes detailed in Figure 2.1. They can be categorize into two categories: The magnetospheric and magnetosheath modes (mode 6 and modes 8 to 14 modes) has particle distribution functions with 62 energy channels and 88 solid angle distributions, and the solar wind modes (modes 0 to 5) that offer a finer energy resolution but at the expense of reduced energy sweep range. The solar wind modes, optimized for typical energy ranges observed in the solar wind, do not perform well for the calculation of plasma moments in the magnetosphere and magnetosheath, where both low- and high-energy are present. For instance, Figure 2.2 shows a change of mode of the instrument in the magnetosheath region. When the HIA instrument transitions from magnetosheath/magnetotail mode number 12 to solar wind mode number 3, a significant reduction in ion density, velocity components, and ion temperature is observed. However, the FGM instrument did not detect any significant changes in the measured magnetic field. This indicates that the sudden decrease in HIA quantities is caused by the mode transition, as it coincides with the mode change temporally. Since this work focuses mainly on the physical properties of the magnetosheath and magnetosphere region, we retained only the HIA data from the magnetospheric and magnetosheath modes, excluding measurements from the solar wind modes even though they could have occurred in the magnetosheath.

Due to the unavailability of HIA measurements on Cluster 2, 4, and on Cluster 3 after 2009, we used data from Cluster 1 for the period between January 2001 and December 2019 and from Cluster 3 until November 2009. All measurements were resampled to a 5-second resolution to align with datasets from other missions. Finally, data points with missing plasma or field measurements are discarded.

Mode	Description
0	solar wind mode
1	solar wind/upstreaming ions mode
2	solar wind mode
3	solar wind/upstreaming ions mode
4	solar wind - data compression mode
5	solar wind/upstreaming ions - data compression mode
6	magnetosphere - mode 2
7	PROM operation
8	magnetosphere - mode 1
9	magnetosphere - mode 2
10	magnetosphere - mode 3
11	magnetosheath/magnetotail - mode 1
12	magnetosheath/magnetotail - mode 2
13	magnetosphere - data compression - mode 1
14	magnetosheath/magnetotail - data compression - mode 2
15	calibration/test mode

Table 2.1: HIA operational modes [Rème et al., 2005].

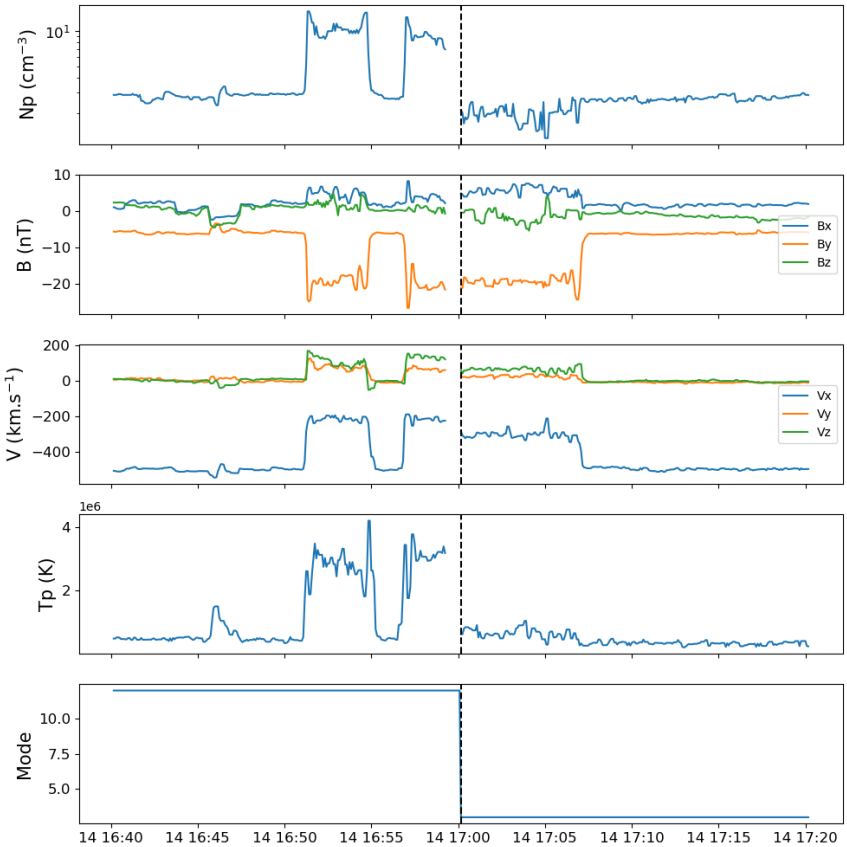

Figure 2.2: The data from the Cluster 1 spacecraft on February 14th, 2001 presented from the top to the bottom panel correspond to: ion density, magnetic field components, velocity components, ion temperature, and the operational mode. The vertical dashed line indicates the transition from operational mode 12 to 3.

2.3.2 The Double Star mission

Mission overview

Double Star is a joint mission between the China National Space Administration (CNSA) and the European Space Agency (ESA). The mission comprises two satellites, Tan Ce 1 (TC-1) in an equatorial orbit and Tan Ce 2 (TC-2) in a polar orbit. TC-1 and TC-2 were launched in December of 2003 and July of 2004, respectively. TC-1 ended in October of 2007. This mission was designed to complement the Cluster mission to provide an unprecedented coverage of near-Earth space. The Double Star spacecraft are equipped with eight European instruments, seven of which are identical to those of Cluster, and eight Chinese instruments for measuring magnetic fields, electric fields, waves, and particles. The main objectives of the mission are to study magnetic reconnection at the magnetopause and in the magnetotail, and to understand the mechanism behind magnetospheric storms and substorms. Only the TC-1 probe is used in this work. The TC-2 spacecraft, with an apogee of about 6 Re, is too distant from the magnetopause to be of interest in this study.

Orbits

The TC-1 spacecraft has an elliptical orbit with an apogee of approximately 12 Re, inclined at 28.5 degrees relative to the equator, and completes an orbital period every 27.4 hours. The Figure 2.3 shows the orbits of the spacecraft over 7 months. The spacecraft mainly explores the magnetosphere and magnetosheath, with its apogee slightly falling short of the average location of the bow shock's subsolar point (i.e. approximately 13 Re).

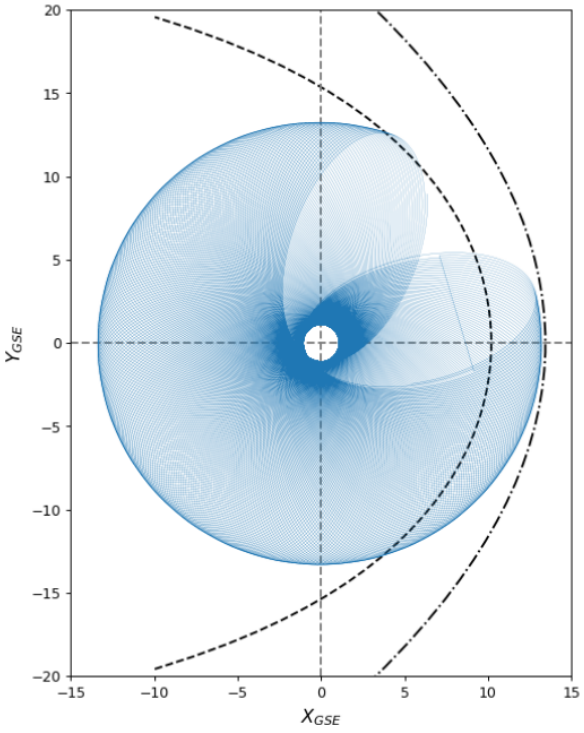

Figure 2.3: Orbit of the TC-1 probe in the equatorial plane between August 1st, 2004 and March 1st, 2005. The dashed and dash-dotted black lines correspond to the magnetopause and bow shock, respectively.

Instruments and measurements

The Fluxgate Magnetometer (FGM) [Carr et al., 2005] provides measurements of the magnetic field. It has five sensitivity ranges ranging from ±128 nT to ±32,764 nT and offers three modes: the Normal Mode (C) operating at 22.4 Hz, Gradiometer Mode (A) at 12.6 Hz, and Housekeeping Mode (All) at 0.19 Hz. This work uses the magnetic field measurements in GSM coordinates at spin resolution (i.e. approximately 4-second resolution).

The Hot Ion Analyser (HIA) [Rème et al., 2005] is spare a model of the Cluster mission and therefore its measurements should be processed in the same manner. It provides ion density, temperature, and bulk velocity measurements at a resolution of 4 seconds. Similarly to the Cluster mission, all measurements are resampled at a 5-second resolution and data points with missing plasma or field measurements are discarded.

2.3.3 The THEMIS mission

Mission overview

Time History of Events and Macroscale Interactions during Substorms (THEMIS) is a NASA mission launched in February 2007. The nominal period of the mission was initially two years but has since been extended, and it is currently in its 17th year of operation. It consists of five identical satellites named THEMIS A (THA) or Probe 5 (P5), THEMIS B (THB) or Probe 1 (P1), THEMIS C (THC) or Probe 2 (P2), THEMIS D (THD) or Probe 3 (P3), and THEMIS E (THE) or Probe 4 (P4). Each spacecraft has on board five instruments: flux-gate and search-coil magnetometers, an electric field instrument, an electrostatic analyzer, and a solid-state telescope. The THEMIS mission aims to study magnetic reconnection and the dynamics of mass and energy transfer in the near-Earth space environment.

Since 2010, THEMIS B and C have been sent to orbit the Moon and transitioned into the ARTEMIS (i.e. Acceleration, Reconnection, Turbulence, and Electrodynamics of the Moon's Interaction with the Sun) part of the THEMIS mission. The ARTEMIS mission aims to explore the lunar atmosphere, examine properties and phenomena in the far magnetotail and magnetosheath, and investigate turbulence in the different near-Earth regions.

Orbits and phases

The THEMIS mission spacecraft have equatorial orbits (inclination of about 16°) with the apogees during the initial phase of 10 Re, 30 Re, 20 Re, and 12 Re for the THA, THB, THC, and THD and E, respectively (Fig. 2.4). In August 2009, the orbits of the THB and THC spacecraft change dramatically as they sent into orbit around the Moon at a distance of about 60 Re from Earth, becoming the ARTEMIS phase of the mission (Fig. 2.5). From October 2008, the THA, THD, and THE probes have their apogee varying between 12 and 15 Re (Fig. 2.5). The different spacecraft of the THEMIS mission offer good coverage of the various regions of the magnetosphere (i.e., the dayside, the dawn and dusk sides of the magnetosphere, and the magnetotail) and in particular of the magnetopause due to the relatively short apogees of the THA, THD, and THE spacecraft. The ARTEMIS B and C probes investigate the near-lunar environment, solar wind, and the far night side of the magnetosheath and magnetotail.

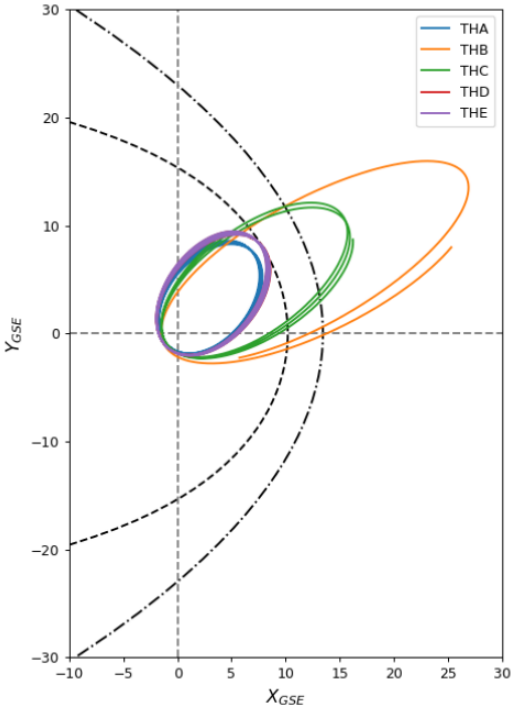

Figure 2.4: Orbits of the five THEMIS spacecraft in the equatorial plane between July 10th, 2008 and July 15th, 2008. The dashed and dash-dotted black lines correspond to the magnetopause and bow shock, respectively. The location of the THD probe is concealed below that of the THE spacecraft.

Instruments and measurements

The Fluxgate Magnetometer (FGM) [Auster et al., 2008] provided the magnetic field measurements in GSM coordinates. The instrument has three modes: high-resolution mode with a frequency of 128 Hz (*FGH*), low-resolution mode with a frequency of 4 Hz (*FGL*), and spin-resolution mode (*FGS*) with a resolution of 0.33 Hz which is approximately 3 seconds. In this work, we use the spin-resolution mode (*FGS*) in GSM coordinates.

The Electrostatic Analyzer (ESA) [McFadden et al., 2008] provided ground-processed ion energy fluxes and moments such as density, velocity, and temperature. This data is available in three

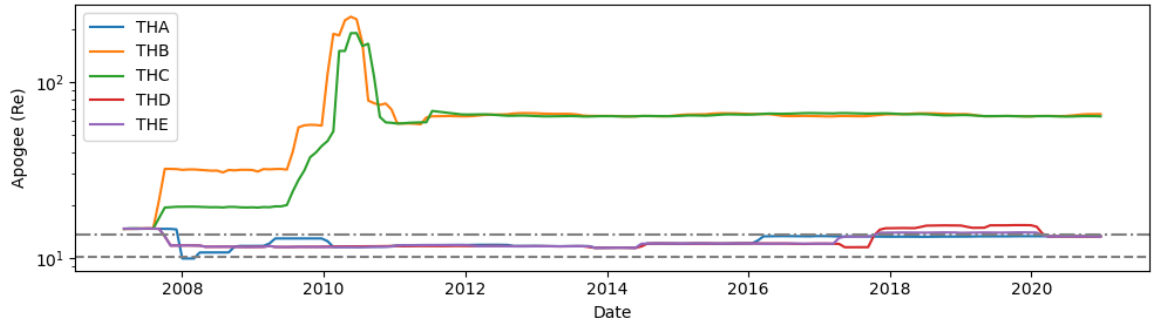

Figure 2.5: Radius of the apogees of the THEMIS spacecraft along the mission duration. The dotted gray and dash-dotted gray lines represent the average subsolar position of the magnetopause and bow shock, respectively.

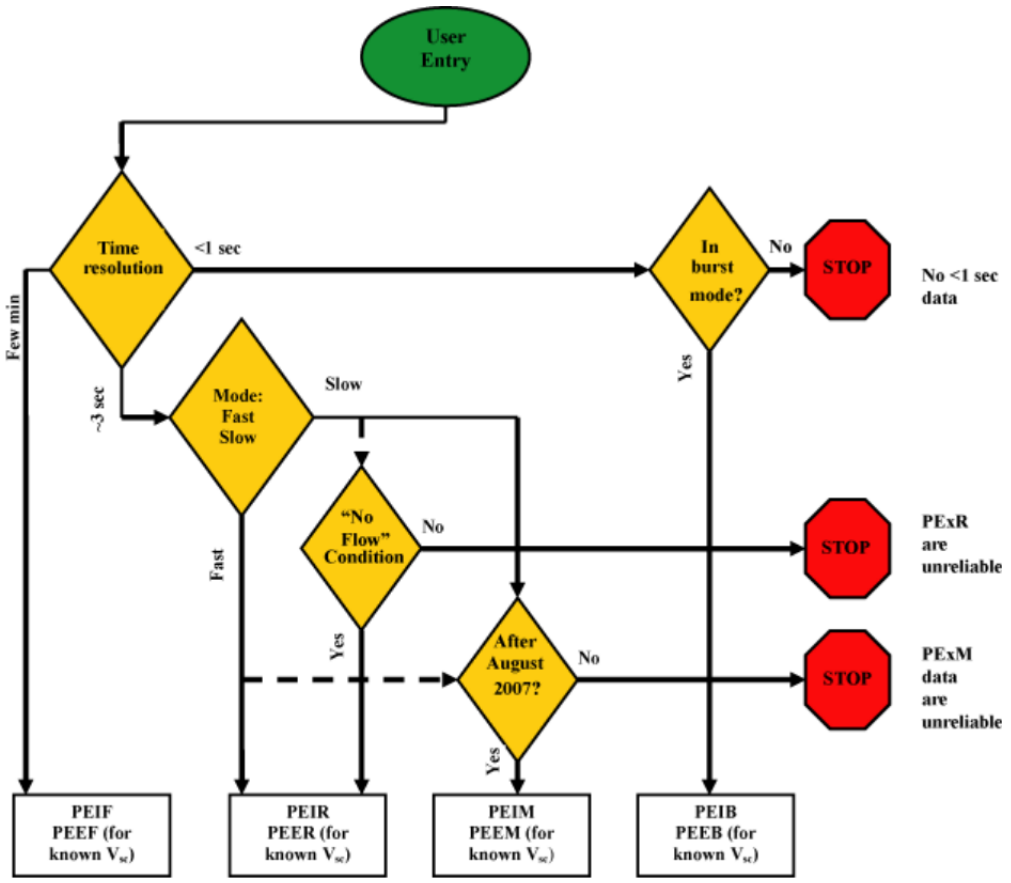

Figure 2.6: Data flow of the different mode of the ESA instrument. The acronym PEI and PEE stand for Particle ESA Ion and Electron, respectively. The letters F, R, M, and B at the end of this acronym stand for the full, reduced, onboard moment, and burst modes, respectively. Source: https://themis.igpp.ucla.edu/esa_flow_diagram.shtml

modes: The *Full* mode offers high angular resolution but has limited time resolution of roughly 2 minutes. The *Reduced* mode sacrifices some angular resolution for a high time resolution of approximately 3 seconds. This mode has two sub-modes, the *Fast-Survey* and *Slow-Survey* modes. The *Slow-Survey* mode provides particle distribution functions using 32 omni-directional (i.e. a singular solid-angle distribution) energy channels This mode cannot determine the ion bulk velocity. On the other hand, the *Fast-Survey* mode has distribution functions with 24 energy channels and 50 solid-angle distributions. Finally, the *Burst* mode delivers both high angular and time resolution but only on brief and sporadic time intervals of 5 minutes. This instrument also provides moments calculated on-board, however, these measurements are only valid after August

2007. Figure 2.6 presents the data flow for selecting the appropriate mode. For a time resolution of a few seconds and to obtain the ion bulk velocity measurements, we use the data provided by the *Reduced* mode (PEIR for Particle ESA Ion Reduced) in *Fast-Survey* mode. Then, to fill in missing data, the available onboard moments are used to complete the dataset.

For this work, the THA, THD, and THE measurements are taken from September 2007 to December 2020; and from September 2007 to August 2009 for the THB and THC data. All the measurements are resampled to a 5-second period.

2.3.4 The Magnetospheric MultiScale mission

Mission overview

MMS is a mission from NASA launched in March 2015 designed for a nominal period of two years but still in operation. The mission features four identical spacecraft, MMS 1 to MMS 4, flying in varying formations throughout its lifespan and maintaining inter-spacecraft distances ranging from 10 to 100 km. Each spacecraft is equipped with plasma particles instruments, energetic particle detectors, magnetometers, and instruments for measuring electric fields. The primary objective of the mission was to analyze magnetic reconnection at the electron scale, specifically the Electron Diffusion Region (EDR) that was not accessible until this mission. This was made possible through the small distances maintained between the spacecraft and the unprecedented data acquisition frequency of the onboard instruments (i.e. approximately 0.125 seconds, 30 milliseconds, and 8 milliseconds for the ions, electrons and magnetic field instruments, respectively).

Orbits and phases

The spacecraft of the MMS mission have equatorial orbits with an inclination in respect to the equator of 28°. The apogees of the spacecraft varying over time, going from 12 Re in the initial phase of the mission to 25 Re around Mars 2017 and 30 Re in January 2019. Before the orbit change in 2017 as shown in Figure 2.7, the probes mostly explore the dayside magnetopause and the magnetosphere.

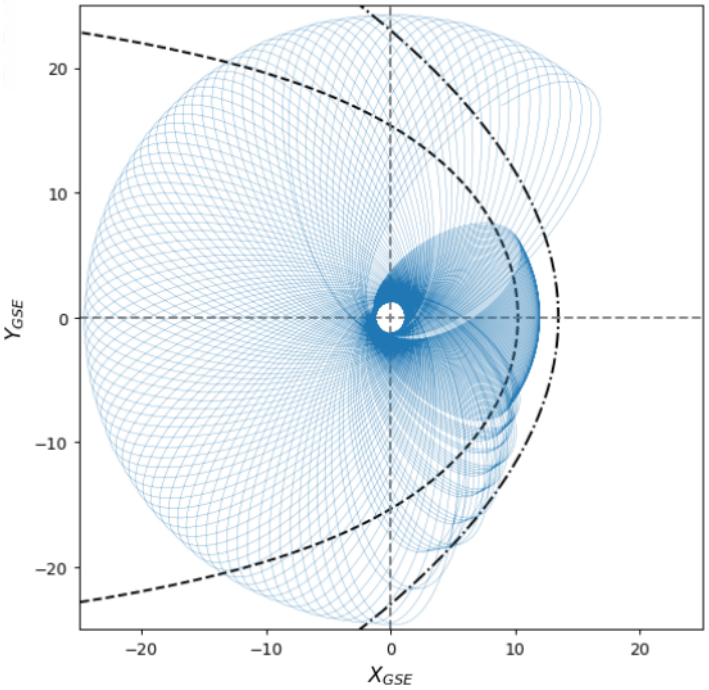

Figure 2.7: Orbit of the MMS1 spacecraft in the equatorial plane between November 26th, 2016 and November 25th, 2017. The dashed and dash-dotted black lines correspond to the magnetopause and bow shock, respectively.

Instruments and measurements

The plasma moments (ion density, ion temperature, ion bulk speed) are provided by the mode *Fast-Survey* of the Fast Plasma Investigation (FPI) instrument [Pollock et al., 2016] with a time resolution of 4.5 seconds. This instrument has also two other modes that was not used in this work, the *Slow-Survey* with a time resolution of 1 minute, and the *Burst* mode with a resolution of 0.125 seconds.

The magnetic field in GSM coordinates is provided by the *Survey* mode of the Fluxgate Magnetometer (FGM) [Russell et al., 2016] with a resolution of 0.125 seconds. While not used during this work, the FGM instrument has also *Burst* mode with a resolution 8 milliseconds.

Since the measurements from the 4 MMS spacecraft are extremely similar when resampled at 5 seconds temporal resolution due to the proximity of the probes, only the MMS 1 data are used from September 2015 to July 2019.

2.3.5 The OMNI database

Database overview

The OMNI dataset [King and Papitashvili, 2005] consists of multi-spacecraft measurements of the plasma and IMF properties in the solar wind with hourly to one-minute resolutions. The initial dataset measurements were provided by IMP-1 in 1963, and then by other probes (IMP-8, ISEE-3, Geotail) during their travels through the solar wind. Currently, measurements for the database are obtained by spacecraft specifically designed to monitor solar wind, namely Wind, ACE (Advanced Composition Explorer), and DSCOVR (Deep Space Climate Observatory). These spacecraft orbiting close to the L1 Lagrange point, located approximately 230 Earth radii upstream of Earth on the Earth-Sun axis. Their measurements are propagated to the position of the nose of the bow shock, estimated with the analytical model of Farris and Russell [1994].

Measurements

The OMNI database provides measurements of magnetic field, plasma velocity, ion density, ion temperature, dynamic pressure, plasma beta, Mach number, and the position of the bow shock subsolar point at 1 minute resolution from 2000 to 2021. In this work, the measurements are interpolated with a time resolution of 5 seconds to accommodate the resolution of the missions data used in this thesis.

2.4 Identification of the Near-Earth Environment

The near-Earth plasma environment (see Section 1.1.3) consists of different regions – such as the magnetospheric cusps, the magnetopause, the boundary layers, and the foreshock within the solar wind, among others – where various phenomena take place. Since this thesis concentrates on the global constraints (i.e., the distribution of the magnetic shear, current density, etc.) on magnetopause reconnection, it is sufficient to identify the following primary regions: the magnetosphere, magnetosheath, and solar wind. We will therefore now detail how.

2.4.1 Different selection methods used in the literature

A first method, frequently adopted in the literature (e.g. Kaymaz et al. [1992]; Petrinec [2013]; Phan and Paschmann [1995]), for identifying a particular region of the near-Earth plasma environment is to visually inspect the in-situ measurements. Although this method is expected to yield the best accuracy, it is fastidious and time-consuming, which tends to hinder large statistics.

Another approach, used in prior studies (e.g. Dimmock and Nykyri [2013]; Dimmock et al. [2014, 2016]; Verigin et al. [2006]; Zhang et al. [2019]), to identify the magnetosphere, magnetosheath, or solar wind region relies on discriminating data based on analytical models of the bow shock and magnetopause. This approach, summarized in Equation 2.1, uses the relative position radial of the spacecraft ($R_{S/C}$) in relation to those of the magnetopause (R_{mp}) and the bow shock (R_{bs}), predicted under upstream solar wind and IMF conditions. However, the average root-mean-square error (RMSE) of analytical models of the magnetopause is about 1.25 Re [Wang et al., 2013],

and is even greater for bow shock models [Merka et al., 2003]. Using such models is possible, but would result in the mixing of measurements from different regions near the boundaries, such as magnetosphere and magnetosheath data points close to the magnetopause or magnetosheath and solar wind data points near the bow shock. Another issue associated with using such models also possibly biases the selection of the measurements by the underlying assumptions of the models such as their dependency on the solar wind control parameters or the symmetry and shape of the boundaries.

$$\text{if} \quad \begin{cases} R_{S/C} \leq R_{mp} & \longrightarrow \quad \text{Magnetosphere} \\ R_{mp} \leq R_{S/C} \leq R_{bs} & \longrightarrow \quad \text{Magnetosheath} \\ R_{bs} \leq R_{S/C} & \longrightarrow \quad \text{Solar wind} \end{cases} \tag{2.1}$$

The regions can also be identified with the properties of the data therein using a combination of empirically fixed thresholds. For instance, Jelínek et al. [2012] developed a method using thresholds on the magnetic field strength (B) and the proton density (N_p) normalized by the IMF amplitude (B_{OMNI}) and proton density (N_{OMNI}), respectively, as shown in Figure 2.8. However, Nguyen et al. [2022] showed that the data from the different regions are not linearly separable, suggesting that this approach based on a threshold is not optimal. This lack of linearity can be primarily attributed to the magnetosheath as its state is strongly related to the conditions in the solar wind and is inherently inhomogeneous from equatorial to higher latitudinal regions and from the quasi-parallel side to quasi-perpendicular one [Dimmock et al., 2020]. Consequently, certain measurements taken within the magnetosheath, such as those in the flank or quasi-parallel side, may be erroneously categorized as solar wind data; or as magnetosphere for the subsolar region due to the presence of magnetic pileup and depletion layer. Likewise, the high proton density observed in the foreshock or magnetospheric cusp can lead to misclassification of solar wind or magnetosphere measurements as magnetosheath data.

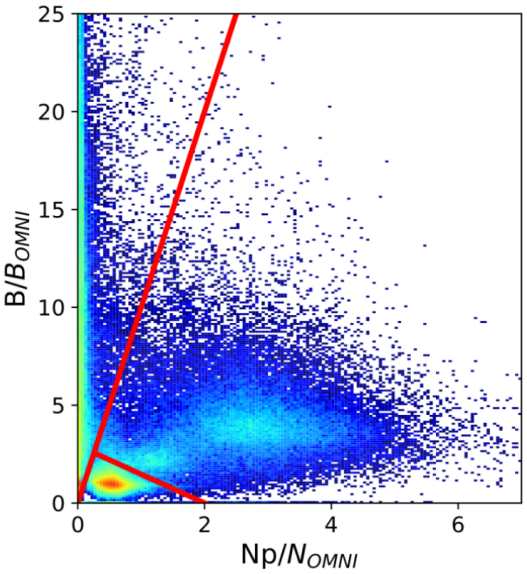

Figure 2.8: 2D histogram of magnetic field strength (B) and proton density (N_p) measurements of the THEMIS B probe normalized by the corresponding OMNI data. The solid red lines indicate a possible set of linear boundaries we could define to separate: the magnetosphere ($B/B_{OMNI} >> 1$ and $N_p/N_{OMNI} < 1$), the magnetosheath ($B/B_{OMNI} > 1$ and $N_p/N_{OMNI} > 1$), and the solar wind ($B/B_{OMNI} \approx 1$ and $N_p/N_{OMNI} \approx 1$). Figure adapted from Nguyen et al. [2022]

Recently, new classifying methods based on statistical learning have been developed. Deep learning classification using convolutional neural networks has reached excellent performances for isolating measurements made in the different regions of the near-Earth plasma environment [Breuillard et al., 2020; Olshevsky et al., 2021]. Similar precision was also obtained with a Gradient Boosting classifier (GBC) algorithm [Nguyen et al., 2022]. This last method offers the advantage of speed and simplicity compared to deep neural network architectures. Consequently, it has been chosen as the preferred method for the selection of measurements used in the different studies conducted in this PhD work and next section will detail this method a bit further.

2.4.2 Region identification with a Gradient Boosting Classifier algorithm

We will explain labeling and specificities in training on the time series. The initial step in using a supervised machine learning method (i.e. training a model on labeled data) involves creating a *training* and *test* datasets with the labeled measurements. The training dataset represents a

subset of the available labeled measurements that will be used to train the model. The testing dataset is a distinct subset of the data that the model has not encountered previously during the training phase. Its purpose is to evaluate the performance of the model and determine its ability to generalize to unseen data.

The datasets of the missions comprise eight input variables, which include the ion bulk velocity components (V_x, V_y, V_z), the magnetic field components (B_x, B_y, B_z), the ion density (N_p), and temperature (T_p). This research centers on the magnetosheath and the magnetopause. Consequently, data collected at Earthward distances exceeding 5 Re from the magnetopause, derived from the Shue et al. [1998] model and parameterized by upstream IMF and solar wind parameters, have been excluded. For labeling, training and evaluating the GBC model, the data are resampled at a 1-minute resolution.

The various stages of the identification method that utilize the GBC algorithm primarily rely on the approach outlined in Nguyen et al. [2022] on which I contributed to during my Master 2 internship, especially adapting it to the specific requirements of the ARTEMIS mission. While following the original approach, some modifications were made in this work.

Labeling of the data

We use a supervised learning method, which means that the measurements must be labeled by visual inspection to give the model a reference from which to learn and be evaluated. Each data point of the labeled datasets is associated with an integer index representing:

- *class 0:* Magnetosphere data points, characterized by high magnetic field and temperature, low ion bulk flow and density.
- *class 2:* Solar wind data points, characterized by intermediate density and magnetic field, rapid ion bulk flow, and lower temperature.
- *class 1:* Data points that do not fall into either the solar wind or magnetosphere categories are identified as magnetosheath points. These points correspond to denser regions with intermediate plasma velocity and magnetic field. Under this definition, any region downstream of the bow shock that is not part of the magnetosphere is considered part of the magnetosheath. This encompasses pristine magnetosheath points as well as regions composed of mixed plasmas, such as reconnection outflows and various magnetosphere and magnetosheath boundary layers.

The labels are assigned through a process of visual inspection, where specific time intervals are identified as belonging to one of the aforementioned classes. For example, in Figure 2.10, each of the data points within the time interval from 8:00 AM to 10:40 AM is classified as a magnetospheric point and assigned a label value of 0. Subsequently, data collected from 10:40 AM to 2:20 PM are designated as magnetosheath and labeled with a value of 1, and so forth.

The accuracy assessment of a machine learning algorithm holds validity solely when it is applied to previously unseen data that shares statistical similarities with the dataset utilized for training and evaluation. Therefore, it is essential to ensure that the labeled data encompasses the various types of measurements that the machine learning model will encounter when used on the massive unseen database. A particular aspect of the near-Earth plasma environment is its important inhomogeneity, ranging from the subsolar to the flank magnetosheath, from the lobes to the low-latitude magnetosphere, and from the pristine solar wind to the foreshock. Hence, it is imperative that the labeled dataset encompasses a good coverage, as shown in Figure 2.9 for the THEMIS mission, of the diverse orbits of the spacecraft to ensure the algorithm's applicability to unseen measurements (i.e. not in the labeled dataset). Therefore, labeled datasets have been created for each mission, with the total number of data points displayed in Table 2.2. In particular, the THEMIS labeled dataset primarily comprises measurements from the THB probe, which possesses the largest apogee, and THA/THE probes with the smallest apogee. This selection ensures

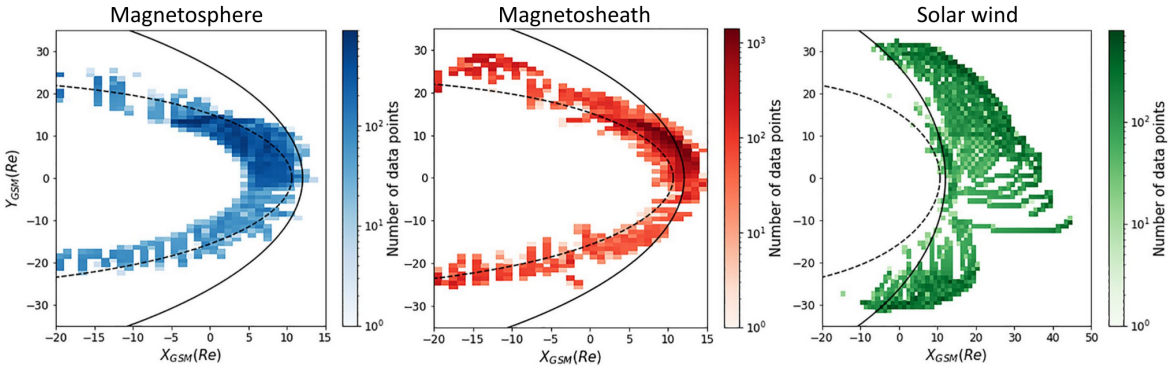

Figure 2.9: Spatial coverage of the labeled THEMIS dataset projected in the (XY) plane. From the left to the right panels is represented the bin count of the point labeled as : magnetosphere, magnetosheath, and solar wind. The solid and dotted black lines correspond to the modeled bow shock [Jeřáb et al., 2005] and magnetopause [Lin et al., 2010], respectively. Figure adapted from Nguyen et al. [2022].

	Magnetosphere	Magnetosheath	Solar Wind	Total
THEMIS	123,966	86,639	157,731	368,336
Cluster	50,244	76,459	22,011	148,714
Double Star	61,370	48,130	9,263	118,763
MMS	76,833	84,965	56,778	218,576

Table 2.2: Number of labeled points in each region and in total for the different missions.

a comprehensive coverage of the orbits of the other spacecraft within the mission (Fig. 2.5). In contrast, the Cluster labeled dataset includes measurements solely from the C1 probe, since the C3 spacecraft surveys comparable orbits.

Training of the Gradient Boosting Classifier

Gradient Boosting algorithms [Friedman, 2001] are based on the concept of decision trees. These decision trees use a hierarchical sequence of threshold-based tests at various *nodes*, eventually leading to a final decision at one of the *leaves* of the tree. However, unlike the traditional approach of using a single decision tree (i.e. Decision Tree algorithm [Fisher, 1936]) or an ensemble of multiple trees trained on subsets of the dataset – where their individual predictions are combined to form a global prediction – (i.e. Random Forest algorithm [Breiman, 2001]); Gradient Boosting algorithms involve a sequential ensemble of decision trees, where each subsequent tree is trained to correct the errors made by the preceeding one. This characteristic renders Gradient Boosting algorithms especially resilient against common issues such as over-fitting (where the model learns the training data too precisely, capturing noise and outliers, thereby performing poorly on unseen data) and under-fitting (where the model is excessively simplistic and fails to capture the underlying patterns in the training data, leading to poor performance). This quality makes Gradient Boosting algorithms highly popular [Géron, 2017], given that over-fitting and under-fitting are common challenges encountered in many machine learning methods. The Gradient Boosting, like other decision tree based algorithm, are versatile tools that enable both classification and regression (cf Section 2.6.2) tasks.

A comparison was made in Nguyen et al. [2022] between the performance of the Decision Tree, Logistic Regression [Berkson, 1944], and GBC algorithms in identifying the magnetosphere, magnetosheath, and solar wind regions. It revealed that the GBC algorithm outperformed the other two machine learning algorithms.

Normally, the labeled data is randomly split into two sets, with a larger fraction (usually 70%) dedicated to training and a smaller fraction (usually 30%) reserved for testing.

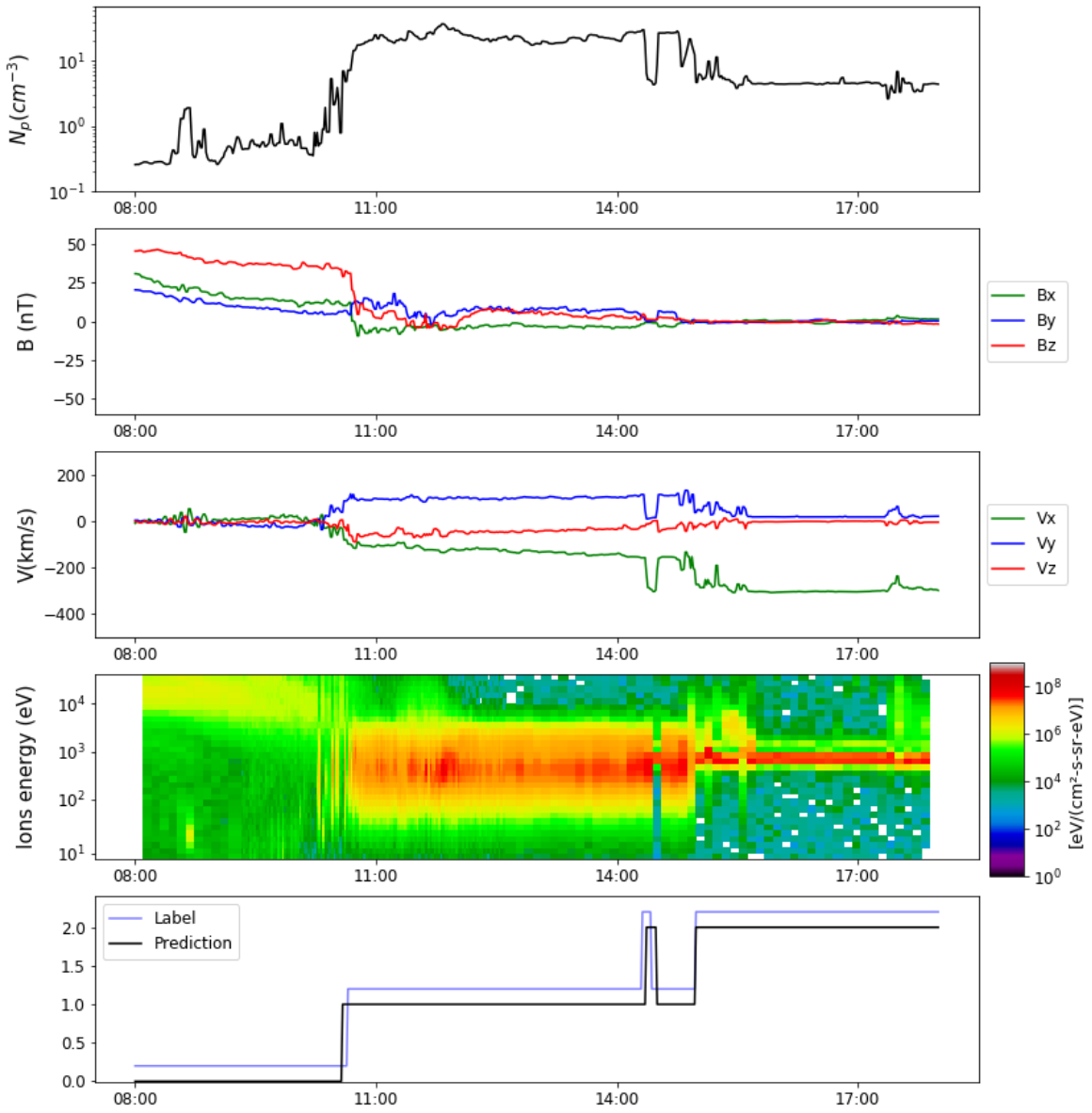

Figure 2.10: In-situ measurements from the THEMIS B spacecraft on May 12th, 2008. The data presented from the top to the bottom panel correspond to: ion density, magnetic field components, velocity components, and omnidirectional differential energy fluxes of ions. The bottom panel displays labels (in blue), intentionally offset for visual purpose, alongside the predictions generated by the GBC algorithm (in black). Figure from Nguyen et al. [2022].

A particular aspect of in-situ spacecraft measurements is the strong temporal correlation between the values of successive data points. Indeed, in a time-series dataset, a data point A measured at t often closely resembles a data point B measured at $t+1$. When the points A and B are randomly assigned to the training and testing sets, respectively, it introduces a lack of independence between the two sets. Consequently, evaluating the model on such a setup does not truly involve unseen data. This bias can be problematic as it hinders the detection of over-fitting, and the resulting model may not perform well on genuinely unseen measurements, contrary to what its evaluation may suggest. A method to circumvent such bias with time-series datasets is to use *time-based splitting* which, instead of randomly splitting the data, splits it in a time-ordered manner.

The time-based splitting approach however, introduces another bias related to the imbalance in the number of labeled points across the different classes (as shown in Table 2.2). Indeed, when using such a splitting method, there is a possibility that the number of points from the different classes in the training and testing sets may not align with the initially desired fraction of data for each dataset. For example, if a class 1 contains significantly fewer data points than class 0, the time-based splitting approach may allocate a majority of the class 1 points to the training set, while only a small number are reserved for the testing set. This could lead to an inaccurate evaluation of the model's performance, especially for the underrepresented class.

To address the aforementioned difficulties, the training and testing sets for each labeled mission dataset have been constructed using the following procedure:

1. Create a separate *region* subset for each class (i.e. magnetosphere, magnetosheath, and solar wind)

2. Truncate each *region* subset into *time-interval* subsets of approximately 5 hours.

3. Randomly allocate the different *time-interval* subsets of each *region* subset into the train/test sets according to the desired fraction of measurements in each dataset.

This approach helps mitigating biases related to time-based splitting and class imbalance, providing a more robust and representative evaluation of the model's performance.

For the training of a Gradient Boosting model, there are four critical hyperparameters that users can fine-tune to optimize performance:

- The *maximum depth*: This parameter sets a limit on the number of nodes in the trees, affecting their complexity

- The *learning rate*: This parameter governs the weight given to the updates provided by each tree during training.

- The *number of trees*: This parameter controls the quantity of decision trees in the ensemble

- The *minimal number of samples* required to split: This parameter determines the minimum number of data points required to split a node in a tree. A lower value can lead to more splits and increased model complexity.

Higher (resp. lower) values of the first three (resp. last) hyperparameters allow for a more detailed analysis but increase the risk of overfitting the data, while lower values reduce training time but may result in underfitting due to model simplicity. Therefore, achieving the right balance among these hyperparameters is essential for obtained a well-generalized gradient boosting model that can provide accurate predictions on new and unseen data. A *grid search* can determine the optimized hyperparameters. This machine learning technique systematically searches for the best combination of hyperparameters for a given model. It automates the process of tuning the hyperparameters to enhance the model's performance.

The first model to be trained is the one of the THEMIS mission because it has the largest labeled dataset and encompasses the most varied orbits (i.e. apogees ranging from 9 to 30 Re, allowing the exploration of various regions of the near-Earth environment). This newly trained model serves as the initial tree upon which subsequent trees are built to correct errors for the training of the model of the other mission (Cluster, Double Star, and MMS). This approach facilitates the transfer of knowledge and adaptation to the specific characteristics of each mission's measurements during training of the other models.

Performance evaluation of the classification models

The subsequent step after training a machine learning model is to evaluate its performance on the test dataset. An example of a prediction made by the THEMIS model is visible in Figure 2.10.

The prediction of a classification model can be categorized into four classes:

- A True Positive (TP) is a data point from a particular class that has been predicted correctly as belonging to that class.
- A True Negative (TN) is a data point not belonging to the class of interest that has been correctly predicted as not belonging to that class.
- A False Negative (FN) is a data point from a certain class that has not been correctly predicted as such, i.e., it was predicted as not belonging to that class when it does.
- A False Positive (FP) is a data point not belonging to the class of interest that has been incorrectly predicted as belonging to that class.

With these categories, two scores can be obtained:

- True Positive Rate (TPR) refers to the percentage of actual positive cases that the model correctly identifies as positive, evaluating the model's capacity to correctly detect positive instances.
- False Positive Rate (FPR) is the percentage of actual negative cases that are incorrectly classified as positive by the model, indicating the model's tendency to produce false instances.

The TPR and FPR can be computed with equations 2.2 and 2.3, respectively, where N_X correspond to the number of points in the X category.

$$TPR = \frac{N_{TP}}{N_{TP} + N_{FN}} \tag{2.2}$$

$$FPR = \frac{N_{FP}}{N_{FP} + N_{TN}} = 1 - TPR \tag{2.3}$$

By calculating the TPR and FPR at different classification thresholds, we can generate a receiver operating characteristic (ROC) curve. This curve is a graphical representation used to evaluate how well a classification model performs. An ideal model would exhibit an ROC curve that rises immediately to a TPR value of 1 in the top-left corner of the graph, demonstrating optimal performance. Alternatively, a random classifier would create a diagonal line from the bottom-left to the top-right, since it has an equal probability of generating true and false positives. Figure 2.11 displays the ROC curves for the THEMIS model in each region, showcasing that the model exhibits high performance.

From the ROC curve, one can derive the Area Under Curve (AUC) score, correspond, as its name indicates, to the area under the ROC curve. The AUC provides a comprehensive evaluation of the model's performance by producing a single numerical value between 0 and 1. It considers

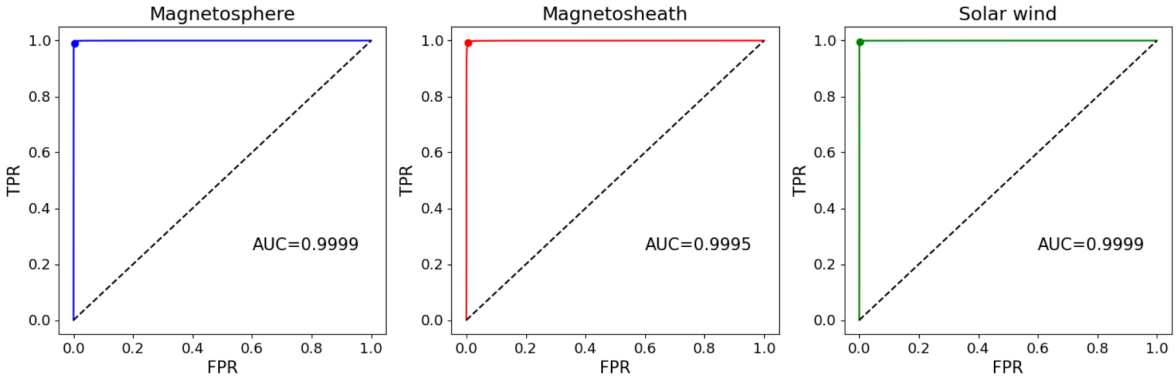

Figure 2.11: The Receiver Operator Curve (ROC) curve for the THEMIS model. The panels from left to right show the ROC curve for the magnetosphere, magnetosheath, and solar wind classifications. The colored point on the curve corresponds to the true positive rate and false positive rate achieved with a decision threshold set at 0.5.

	Magnetosphere	Magnetosheath	Solar Wind
THEMIS	0.9999	0.9995	0.9999
Cluster	0.9952	0.9932	0.9991
Double Star	0.9992	0.9983	0.9995
MMS	0.9993	0.9984	0.9984

Table 2.3: AUC scores for the classification models for the different missions.

the trade-off between the TPR and FPR across different thresholds. An ideal model would obtain a AUC value of 1 while a random classifier would score 0.5. Table 2.3 displays the AUC scores for each region of the different missions, indicating that all models perform extremely highly.

2.4.3 Selected magnetosphere and magnetosheath measurements

Following the validation of the GBC models, the final step consists in making predictions on all the measurements from the previously cited missions. These predictions are generated using datasets from the missions at a 5-second time resolution, which are qualitatively similar to the 1-minute resolution datasets used for training and testing the different models.

	Magnetosphere	Magnetosheath	Solar Wind
THEMIS	64,911,197	26,504,547	1,923,006
Cluster	12,900,629	17,615,497	3,205,215
Double Star	3,705,992	2,496,910	321,368
MMS	2,788,108	4,038,636	2,882,030
Total	84,305,926	50,655,590	17,034,753

Table 2.4: Number of point selected in each region per mission and in total.

Table 2.4 provides information about the number of data points automatically identified in each region for each mission and the total count. Additionally, the spatial coverage of data points in the magnetosphere and magnetosheath is illustrated in Figures 2.12 and 2.13, respectively. The leftmost panels of these figures display a good coverage of the dayside equatorial plane with both magnetospheric and magnetosheath measurements, since most of the missions used in this study have equatorial orbits (see section 2.3). However, the high latitude dayside coverage remains incomplete (middle and rightmost panels of Figures 2.12 and 2.13) as the Cluster is the only mission among the ones we use that has a polar orbit. Additionally, Cluster explores higher latitudes in the southern hemisphere than in the northern hemisphere, resulting in an asymmetry in the spatial

distribution of the measurements between these two regions.

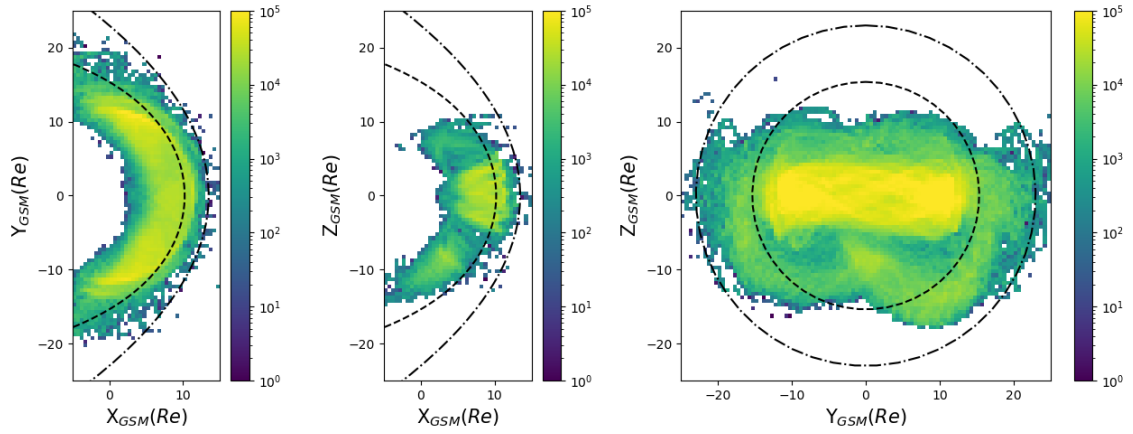

Figure 2.12: Distributions of selected data points in the **magnetosphere** are presented with color-coding indicating the number of points per bin (bin size = 0.5 Re x 0.5 Re). The left panel displays the ($X_{GSM}Y_{GSM}$) plane with data points located within $|Z_{GSM}| \leq 1$ Re. The middle panel shows the ($X_{GSM}Z_{GSM}$) plane with data points located within $|Y_{GSM}| \leq 1$ Re. The right panel shows all data points in the ($Y_{GSM}Z_{GSM}$) plane. The magnetopause [Shue et al., 1998] and bow shock [Jelínek et al., 2012], for average IMF and solar wind conditions, are represented by dashed and dash-dotted black lines, respectively.

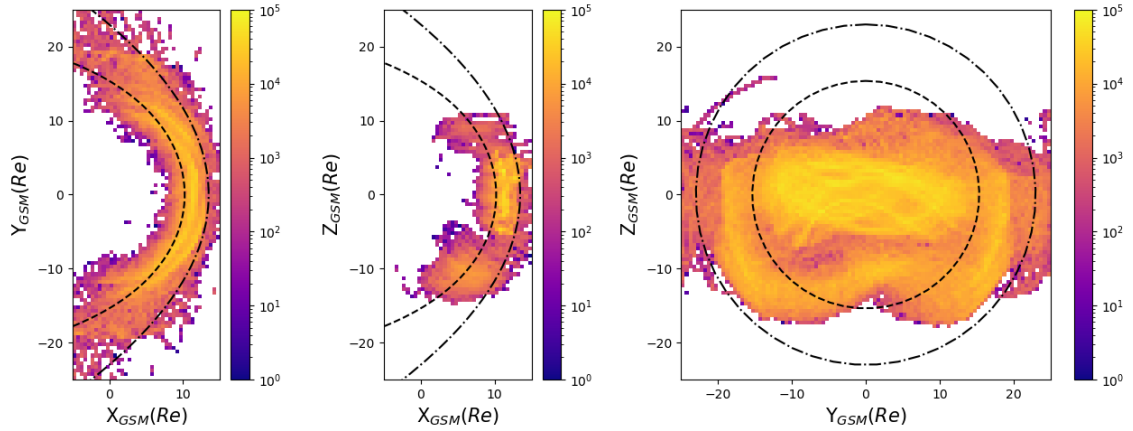

Figure 2.13: Distributions of selected data points in the **magnetosheath** are presented with color-coding indicating the number of points per bin (bin size = 0.5 Re x 0.5 Re). The left panel displays the ($X_{GSM}Y_{GSM}$) plane with data points located within $|Z_{GSM}| \leq 1$ Re. The middle panel shows the ($X_{GSM}Z_{GSM}$) plane with data points located within $|Y_{GSM}| \leq 1$ Re. The right panel shows all data points in the ($Y_{GSM}Z_{GSM}$) plane. The magnetopause [Shue et al., 1998] and bow shock [Jelínek et al., 2012], for average IMF and solar wind conditions, are represented by dashed and dash-dotted black lines, respectively.

2.5 Pairing Measurements with Solar Wind and Magnetospheric Conditions

The state of the magnetosheath is closely tied to the upstream IMF and solar wind conditions. This correlation is not only evident within the measurements themselves, but also extends to their spatial location. Indeed, the position of the magnetopause and bow shock that delineate this region are significantly influenced by these upstream conditions (e.g. Jelínek et al. [2012]; Jeřáb et al. [2005]; Sibeck et al. [1991]). As a result, we not only need the upstream conditions to select subsets of measurements, such as for a specific IMF orientation that we wish to study, but also to

normalize the positions of all data points, as will be explained in Section 2.6.

2.5.1 Solar wind and IMF

Pairing methods in the literature

The simplest method involves using the data from the OMNI database at the time of the spacecraft's measurement. However, this approach neglects to account for the propagation time from the nose of the bow shock, where OMNI database is defined (see section 2.3.5), to the location of the measurements. To reduce the impact of this assumption, Dimmock and Nykyri [2013]; Dimmock et al. [2014, 2016] used a 20-minute average of the OMNI data to accommodate the unknown propagation time to the position of the probe and to minimize the effect of inaccurately timed transient solar wind events.

Another approach is to consider the propagation time within the magnetosheath more directly. For instance, Petrinec [2013] utilized a plasma speed of $V_{SW}/3$, with V_{SW} corresponding to the solar wind velocity, and the distance along the Earth-Sun axis between the bow shock and the spacecraft to calculate the propagation time. Also, Šafránková et al. [2002] employed a two-step propagation technique. First, they determine the time delay associated with propagation in the magnetosheath at average solar wind speed. In a subsequent step, they use the solar wind velocity measurement at the time accounting for this propagation duration to calculate a revised time delay.

A more refined technique for determining the propagation time in the magnetosheath would involve integrating the flow line from the satellite's location to the bow shock. This can be done using an analytical magnetosheath flow models [Génot et al., 2011; Spreiter et al., 1966], or with in-situ measurements. However, it is worth noting that this method, due to its computational cost, is better suited for case studies rather than large statistics.

Lastly, an approach used in Trattner et al. [2021] involves visually inspecting a time interval in the magnetosheath and correlating the magnetic field's components in the measurements with the observed rotations in the IMF. The primary advantages of this method are its accuracy and its ability to consider plasma dilation and compression that can occur during solar wind propagation. However, it is important to note that, even more than for the previous method, this approach is only suited for case studies where a high level of precision is required in determining upstream conditions but is not relevant for a massive dataset.

Pairing method used in this work

The method used for this PhD work is similar to that described in Šafránková et al. [2002]. For each data point in the datasets obtained in Section 2.4, the following steps were applied:

1. Determination of the distance (Δx) along the Earth-Sun axis between the spacecraft and the bow shock nose.
2. Computation of the propagation time ($\Delta t_{\text{average}}$) on the Δx distance at average solar wind speed ($V_{SW_{\text{average}}} \approx -400\ \text{km.s}^{-1}$)
3. Determination of the solar wind velocity $V_{SW}(t - \Delta t_{\text{average}})$ in the OMNI measurements, where t is the time of the spacecraft measurement.
4. Calculation of the propagation time $\Delta t = \Delta x / V_{SW}(t - \Delta t_{\text{average}})$.
5. Pairing of the OMNI data measured at $t - \Delta t$ to the considered data point.

In this method, only the distance Δx along the Earth-Sun axis between the spacecraft and the bow shock nose is considered because the V_x component in the solar wind is vastly predominant (using the OMNI data: $< |V_x|/\|V_{SW}\| >= 0.997 \pm 0.005$). It is worth noting that it is possible to iterate on step 4 (i.e. replacing $\Delta t_{average}$ by the newly computed Δt) until the propagation time converges. However, due to the size of the dataset, conducting these iterations would be computationally intensive and was deemed unnecessary for mainly two reasons: (1) The extensive number of measurements allows for the minimization of noise from erroneous pairings. (2) The resulting reconstruction of the magnetic field in the magnetosheath at the end of this pipeline revealed that the obtained normalized divergence of the magnetic field is quite small for the characteristic scale (see Annex A). This level of accuracy would not have been achievable if the correlation of the measurements with the IMF was not sufficiently precise.

Due to missing data in the OMNI dataset, the measurements selected in Section 2.4 without a solar wind and IMF pairing are eliminated. As a result, the number of magnetosheath and magnetosphere measurements decreases to 46,947,933 and 75,919,506, respectively.

2.5.2 Dipole tilt angle

The dipole tilt angle (Ψ) is the angle between Z_{GSE} axis (cf Sec. 2.7.1) and the Earth's magnetic dipole axis in the ($X_{GSE}Z_{GSE}$) plane. It comprises:

- seasonal variations (Ψ_{year}) produced by the inclination of the rotation axis of the Earth in respect to Z_{GSE} axis as shown in Figure 2.14.a. Ψ_{year} equals 0 degrees during the fall and spring equinoxes due to the Earth's rotation axis being in the plane that is perpendicular to the Earth-Sun axis. In contrast, the inclination in respect to Earth-Sun axis is maximum (resp. minimum) during the summer (resp. winter) solstice with a value of about 23.5° (resp. -23.5°);

- daily variations (Ψ_{day}) produced by the precession of the Earth's magnetic dipole axis around its rotational axis, which is tilted at an angle of approximately 11.5°, as illustrated in Figure 2.14.b. Each day, the values of Ψ_{day} along the Earth-Sun axis are about 0° at 11:00UT and 23:00UT, while being minimum (~-11.5°) and maximum (~11.5°) at 05:00UT and 17:00UT, respectively.

The equations 2.4 to 2.6 [Shue, 1993] allow the computation of the dipole tilt angle for each data point. In these equations *doy* and *ut* correspond to the day of the year (ranging from 0 to 366 days for leap years) and the universal time of the day in hours (ranging from 0 to 24), respectively.

$$\Psi_{year} = 23.4 \cos\left((doy - 172)\frac{2\pi}{365.25}\right) \tag{2.4}$$

$$\Psi_{day} = 11.2 \cos\left((ut - 16.74)\frac{2\pi}{24}\right) \tag{2.5}$$

$$\Psi = \Psi_{year} + \Psi_{day} \tag{2.6}$$

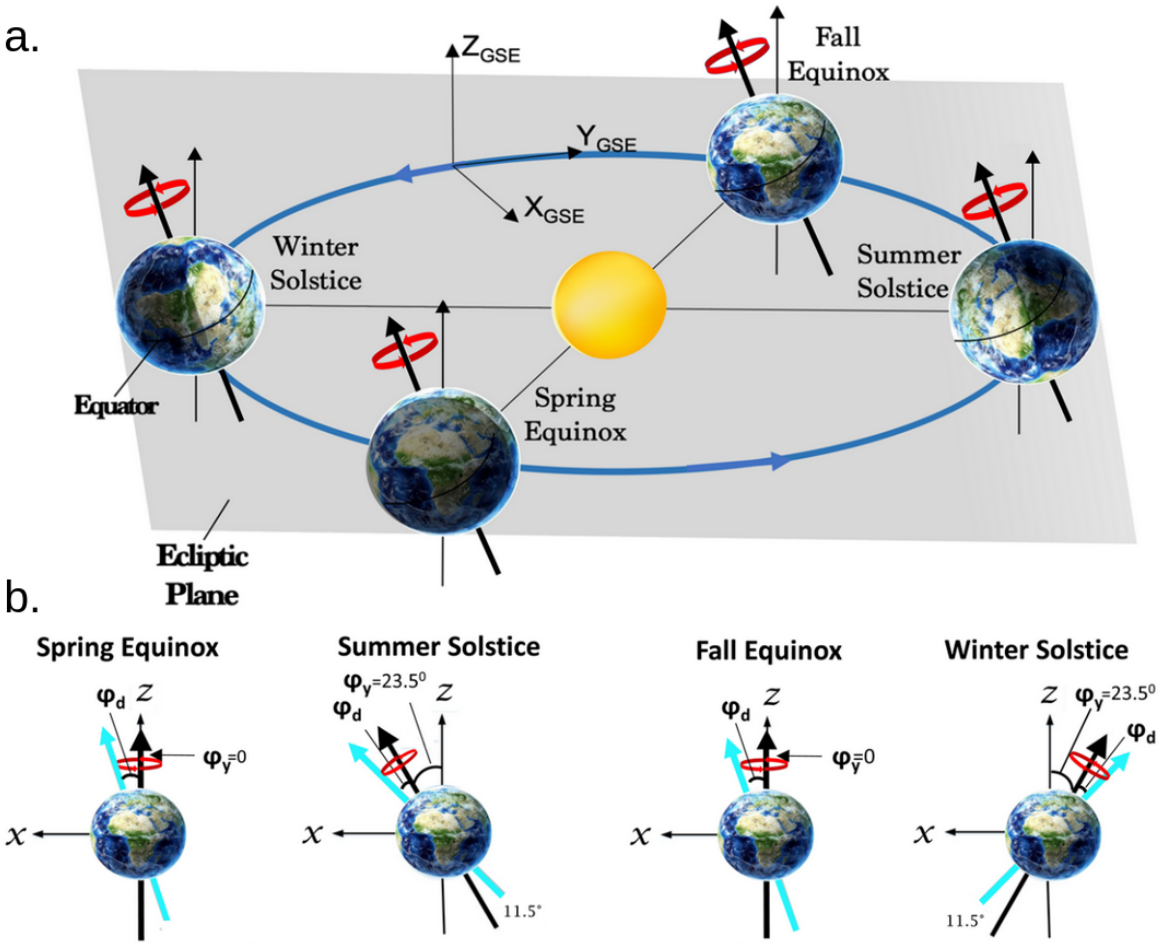

Figure 2.14: Panel a: Illustration of Earth's orbit around the Sun in the ecliptic plane. The black arrow shows the seasonal orientation of the Earth's axis of rotation, and the red circular arrow indicate the precession of the magnetic dipole around it. Panel b: Seasonal (θ_y) and daily (θ_d) of the dipole orientation. The blue arrow shows the maximum tilt of the magnetic dipole at different equinoxes and solstices. Figure adapted from Kavosi et al. [2023]

2.6 Normalization of the Positions

Each data point of the magnetosphere and magnetosheath datasets are measured for different positions of magnetopause and bow shock. Thus, two points measured at the same location can have significantly different relative positions with respect to the boundaries at the time of their measurements. However, it is evident that a measurement taken near the magnetopause would differ significantly from one taken closer to the shock. Without normalizing their positions, the selected data points would not provide an accurate representation of the spatial distribution of magnetic field and plasma properties in the magnetosheath and near the magnetopause. Therefore, the measurements must be repositioned in between a unique pair of magnetopause and bow shock, which requires the determination of their instantaneous distance relative to these boundaries.

2.6.1 Repositioning with analytical models of boundaries

The simplest approach one can think to reposition the measurements involves using analytical models for the position and shape of the magnetopause and bow shock to obtain the positions of the measurements relative to them. In this section, we illustrate why a more advanced and precise approach is necessary to obtain a reliable spatial reconstruction. The radial position of the magnetopause is obtained with the Shue et al. [1998] model noted as $R_{mp\_shue}(\theta, \phi, P_d, B_{z_{imf}})$, where θ and ϕ correspond to the zenith and azimuth angles (see Section 2.7.5). P_d and $B_{z_{imf}}$ correspond to the dynamic pressure of the solar wind and the B_z component of the IMF. This model is selected because it is one of the simplest yet most precise magnetopause models, with an Root Mean Square Error (RMSE) of 1.24 Re [Wang et al., 2013]. The radial position of the bow shock is determined using the Jelínek et al. [2012] model noted as $R_{bs\_jelinek}(\theta, \phi, P_d)$. This model is preferred since it was evaluated to have an average distance ($R_{bs\_observed} - R_{bs\_jelinek}$) of -0.09 Re with a standard deviation of 0.69 Re, which seems low compared to other bow shock models [Merka et al., 2003].

Each data point of the magnetosphere and magnetosheath datasets is repositioned with the following procedure:

1. Determination of the position of the magnetopause model (R_{mp}) and bow shock (R_{mp}). These models are parameterized with the spacecraft's zenith and azimuth angles , and the solar wind and IMF associated with the measurement in Section 2.5.

2. Determine the radial position of the spacecraft ($R_{S/C}$) relative to the boundaries (D_{msp} and D_{msh}) using Equation 2.8 for the magnetosheath and Equation 2.7 for the magnetosphere.

3. Normalize the spacecraft position ($R_{S/C_{normalized}}$) with Equations 2.9 and 2.10 for the magnetosheath and magnetosphere data point, respectively. $R_{mp_{average}}$ and $R_{bs_{average}}$ are the radial position of the *standard* magnetopause and bow shock, respectively, parameterized by average solar wind and IMF (P_d=2 nPa and $B_{z_{imf}}$=0 nT).

$$D_{msp} = \frac{R_{mp} - R_{S/C}}{R_{mp}} \tag{2.7}$$

$$D_{msh} = \frac{R_{S/C} - R_{mp}}{R_{bs} - R_{mp}} \tag{2.8}$$

$$R_{S/C_{normalized}} = R_{mp_{average}} + D_{msh}\left(R_{bs_{average}} - R_{mp_{average}}\right) \tag{2.9}$$

$$R_{S/C_{normalized}} = D_{msp} R_{mp_{average}} \tag{2.10}$$

Figure 2.15 gives an example of why this repositioning method with analytical boundary models is not precise enough to obtain an accurate spatial representation. The figure shows the compression of the magnetic field, also known as magnetic pileup, in the subsolar magnetosheath for

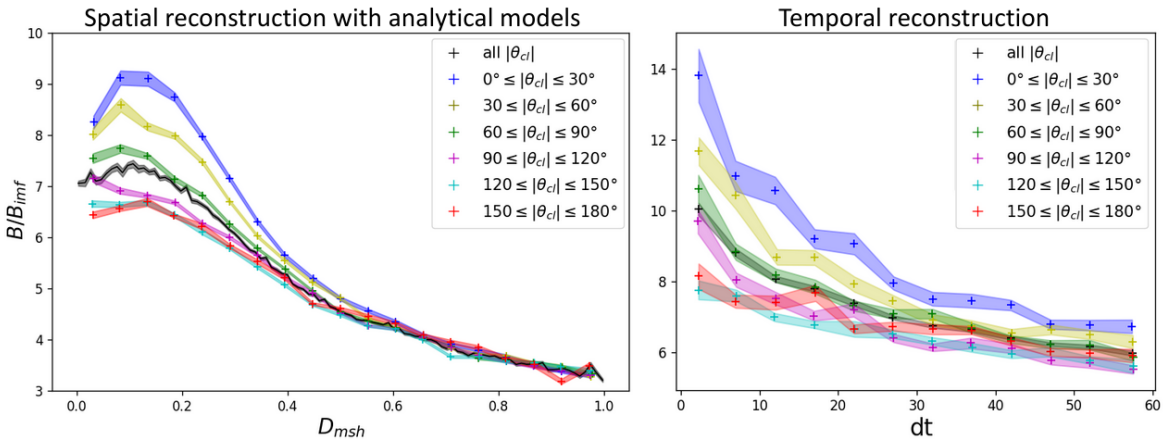

Figure 2.15: Left panel: spatial reconstruction of the magnetic pileup, for different range of IMF clock angles, in the subsolar magnetosheath as function of the relative distance (D_{msh}) to the magnetopause and bow shock obtained with analytical models [Jelínek et al., 2012; Shue et al., 1998]. The magnetopause is located at D_{msh}=0, while the bow shock is at D_{msh}=1. Right panel: temporal reconstruction of the magnetic pileup, for different range of IMF clock angles, in the subsolar magnetosheath as function of duration (dt) in minute spent in this region by the spacecraft before or after crossing the magnetopause (dt=0)

different IMF clock angles (see Section 2.7.5), a phenomenon that will be discussed in more detailed in Chapter 4. The left panel corresponds to the magnetic pileup as a function of the relative distance between the magnetopause (D_{msh}=0) and bow shock (D_{msh}=1) using analytical model prediction. On the other hand, the right panel represents the superposed epoch analysis of magnetic pileup as a function of the time spent by the spacecraft in the magnetosheath before the inward or after the outward crossings the magnetopause (dt=0 min). The decrease in magnetic field amplitude near the magnetopause in the spatial reconstruction is not consistent with the increase observed in the temporal reconstruction. Not only is there no physical explanation for the decrease of the magnetic field amplitude nearby the magnetopause in the spatial reconstruction, but such behavior has never been reported in previous studies [Phan et al., 1994; Pudovkin et al., 2001; Zhang et al., 2019]. Given that we are, above all, interested in the behavior of quantities close by the magnetopause, we concluded that normalizing measurement positions using analytical models of the bow shock and magnetopause is not precise enough. Of course, the temporal reconstruction is only limited to the close spatial vicinity of the magnetopause, thus another way of reconstructing the spatial is needed.

The following section details how the development of more accurate machine-learning models of the magnetopause and bow shock leads to a more accurate spatial representation of the magnetosheath and magnetopause physical properties.

2.6.2 Development of machine learning models of boundaries

The idea is to replace analytical models of boundaries with machine learning models. The development of the boundary models using a machine learning algorithm necessitates an extensive catalog of bow shock and magnetopause crossings. The next section details the method for automatically detecting boundary crossings. The subsequent sections explain the training of the machine learning models, their evaluation and comparison with existing models.

Automatic detection of the boundaries crossings

First, following a similar methodology as in Nguyen et al. [2022], the prediction of the GBC models (see Section 2.4) is used to identify the magnetosphere, magnetosheath, and solar wind measurements of each spacecraft. Subsequently, a rolling window of 10 minutes on the GBC predictions is used to identify:

Probe	Magnetopause	Bow shock
THA	7,477	1,839
THB	398	758
THC	1,098	1,219
THD	7,068	2,251
THE	7,438	2,043
C1	5,333	5,598
C3	3,601	2,880
TC1	1,847	831
MMS	2,280	2,025
Total	36,540	19,444

Table 2.5: Number of magnetopause and bow shock crossings automatically identified per spacecraft and in total.

- magnetopause crossings defined as windows containing 5 minutes of magnetosphere and 5 minutes of magnetosheath data points.

- bow shock crossings defined as windows containing 5 minutes of magnetosheath and 5 minutes of solar wind data points.

Then, it is assessed that each crossing contains only one region transition (e.g., magnetosphere to magnetosheath), if not, the crossing is discarded. This step is important because it will allow to:

- Ensure that the crossing is centered in the 10-minute window and avoid the misidentification of multiple crossings as a single event. For instance, consider a window consisting of 2 minutes in the magnetosheath, followed by 5 minutes in the magnetosphere, and concluding with 3 minutes in the magnetosheath again. This would be incorrectly identified as a single crossing in the magnetosphere (i.e. magnetospheric data points in the center of the window), whereas in reality, it encompasses two distinct magnetopause crossings.

- Ignore errors that may be caused by incorrect predictions during region classification. Although the trained GBC models perform extremely well, they may hesitate in predicting in areas of mixed plasma, such as boundary layers, resulting in rapid transitions between regions that might, therefore, be identified as a boundary crossing.

- Disregard the crossings produced by a fast moving boundary. If the spacecraft crosses the magnetopause or bow shock multiple times in an interval as short as 10 minutes, this could be attributed to rapid changes in solar wind and IMF conditions. We, however, prefer to keep only crossings under relatively stable conditions to facilitate the learning during the training of the models.

Figure 2.16 shows an example of three magnetopause and one bow shock crossings automatically detected with this method. The blue color span provide an example of the 10 minutes window that contains 5 minutes of magnetosheath followed by 5 minutes of magnetosphere data points, with in the middle the magnetopause crossing.

Similar to the magnetosheath and magnetosphere datasets, the causal upstream IMF/solar wind conditions and dipole tilt angle are associated with each crossing using the method described in section 2.5. Crossings that are not paired with upstream conditions due to unavailable OMNI data are excluded.

Table 2.5 provides the specific number of crossings identified for each spacecraft used in this study, as well as the total.

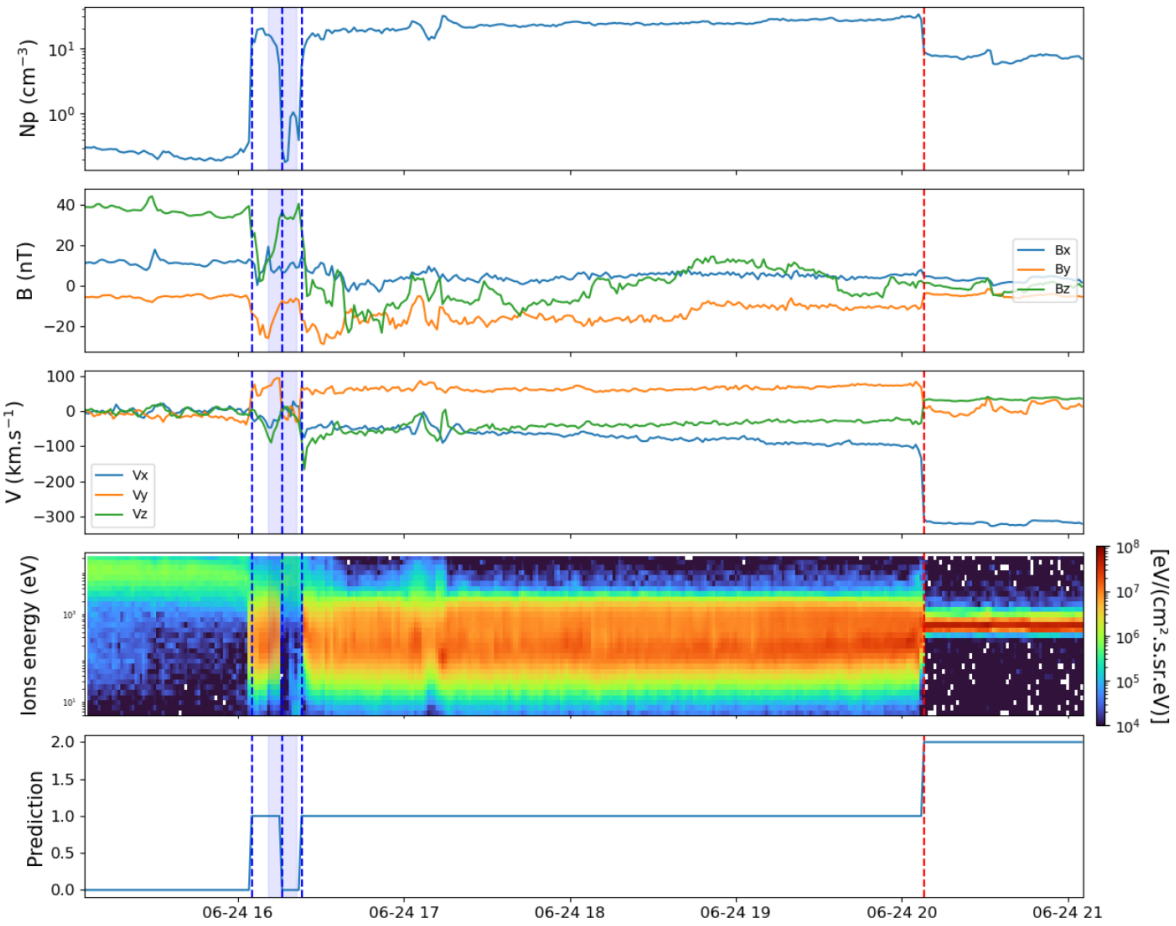

Figure 2.16: In-situ measurements from the THEMIS C spacecraft on June 24th, 2008. The data presented from the top to the bottom panel correspond to: ion density, magnetic field components, velocity components, omnidirectional differential energy fluxes of ions, and the predictions generated by the GBC algorithm. The vertical blue and red lines indicate automatically identified magnetopause and bow shock crossings, respectively. The blue-colored band shows the 10-minutes window used to identify the crossings with the GBC algorithm prediction.

Training of machine learning models of bow shock and magnetopause

Similar to the training of the region classification models (see Section 2.4.2), the initial step in training boundary regression models is to create a training and testing datasets from the set of crossings. When dealing with multiple boundary crossings made by the same spacecraft within a short time frame – such as the magnetopause crossings depicted in Figure 2.16 – splitting data into training and testing sets from random splitting can introduce biases in the evaluation of the algorithm. For instance, if two of the magnetopause crossings in Figure 2.16 are assigned to the training set while the third is placed in the test set, it becomes difficult to determine whether a good prediction on this last crossing stems from the model's generalization ability or from overfitting. Therefore, a time-based splitting approach is required to construct the training and testing datasets. Considering crossing times only is, however, not enough since it is possible for two crossings to occur very close in time but very far apart if they are made with different probes. Hence, including one of them in the test set and the other in the trainset would not cause any bias in the model evaluation but, rather, be a useful to assess the model's generalization ability. Therefore, we opted for what we call a *multi-crossing cluster splitting* to construct the training and testing datasets:

1. group the crossings falling in the same solid angle of 7.5° during the same 30-minute intervals into a *multi-crossing cluster*.

2. randomly assign all crossings of a *multi-crossing cluster* into either test or training set according to the desired fraction of measurements in each datasets to achieve balance between them.

With this method, 17,123 and 8,751 multi-crossing clusters are identified for the magnetopause and the bow shock, respectively. 90% of these clusters are assigned to training set while the remaining 10% are allocated to the test set for each type of boundary.

The machine learning algorithm used to create the magnetopause and bow shock models is a Gradient Boosting Regressor (GBR) Friedman [2001]. While classification algorithms predict discrete values for distinct classes, regression algorithms are employed when the model is expected to produce continuous values. The GBR algorithm was selected due to its robustness against both under- and over-fitting like its classification counterpart (i.e. GBC).

The models are trained using parameters associated with each crossing as described in the previous section: magnetic field and ion bulk velocity components, ion density, ion dynamic pressure, Mach number, magnetic pressure, IMF clock and cone angle (see Section 2.7.5), dipole tilt angle, and spacecraft angular positions (see Section 2.7.5). The target of the models is to predict the radial position of the boundary, given these angular direction and parameters.

Performance evaluation of the magnetopause and shock models

The magnetopause and bow shock regression models are evaluated by calculating the RMSE on the test set, using the observed crossings with the prediction of the models. The RMSE is defined in Equation 2.11, where $\hat{y}_1, \hat{y}_2, \ldots, \hat{y}_n$ are the predicted values, $y_1, y_2, \ldots, y_n$ are the observed values, and n is the number of observations.

$$\text{RMSE} = \sqrt{\frac{1}{n}\sum_{i=1}^{n}(\hat{y}_i - y_i)^2} \tag{2.11}$$

As only 10% of the crossings are included in the testing dataset, we conduct 300 trainings with various random splits of the multi-crossings clusters for a more accurate evaluation of the models. The RMSE of the machine learning models is evaluated for each of these trainings. Additionally, the performance of existing analytical models is computed on the same test set for comparison purposes.

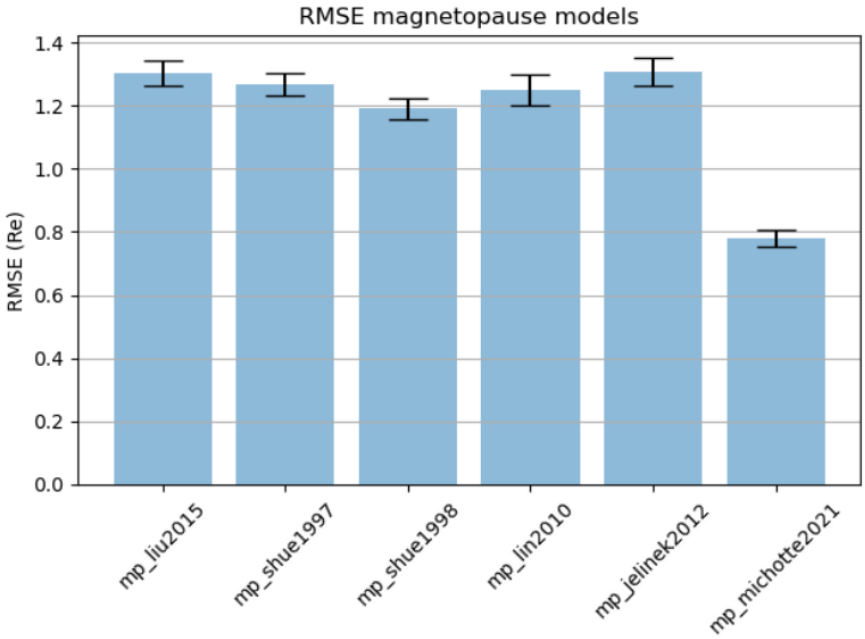

Figure 2.17: RMSE of magnetopause models evaluated on 300 datasets, each consisting of about 3500 crossings. The models evaluated include those of Liu et al. [2015], Shue et al. [1997], Shue et al. [1998], Lin et al. [2010], Jelínek et al. [2012], and lastly the machine learning model for the magnetopause.

Figure 2.17 shows the average RMSE values of various magnetopause models, with their uncertainty determined as the standard deviation of the 300 different test sets, including Liu et al. [2015], Shue et al. [1997], Shue et al. [1998], Lin et al. [2010], Jelínek et al. [2012], and lastly the regression model, respectively. While the tested analytical models of the magnetopause all have a similar RMSE around 1.3 Re, the machine learning model for the magnetopause achieves a smaller error of 0.78 ± 0.03 Re. Additionally, it can be noticed that the RMSE determined for the Shue et al. [1998] model is consistent with the one (i.e. 1.24 Re) obtained in the study of Wang et al. [2013].

Figure 2.18 shows the RMSE values of several analytical bow shock models (Jelínek et al. [2012], Jeřáb et al. [2005], Formisano [1979]) and the GBR bow shock model. The machine learning bow shock model has an RMSE of 0.96 ± 0.06 Re, which is over two-thirds smaller than the values achieved by the analytical models.

The substantial errors in the estimates of the radial position of the Jelínek et al. [2012] and Shue et al. [1998] models (Figures 2.17 and 2.18), when combined, are comparable to the thickness of the magnetosheath [Samsonov et al., 2018]. This suggests that, as suspected, the difference between the spatial reconstruction utilizing these models and the temporal reconstruction (Figure 2.15) is attributable to their lack of accuracy.

In contrast, the magnetic pileup profile in the subsolar region obtained by the spatial reconstruction using the machine learning models of the magnetopause and bow shock, shown in Figure 2.19, is consistent with the temporal reconstruction (right panel of Figure 2.15). Therefore, it can be concluded that the spatial reconstruction using the machine learning model give a reliable representation of the physical properties in the magnetosheath and vicinity of the magnetopause. The profiles of the magnetic pileup in the magnetosheath presented here are not further described in this section, as they will be discussed in more detail in chapter 4.

2.6.3 Normalized positions of the magnetosphere and magnetosheath data

Using the machine learning models of the bow shock and magnetopause, the position of each magnetosheath and magnetosphere measurement is normalized using the method detailed in Section 2.6.1. Some magnetosheath data points are found with a relative distance to these boundaries (Equation 2.8) such that $D_{msh} < -0.1$ and $D_{msh} > 1.1$. These data points were discarded. The magnetosheath measurements with $-0.1 \leq D_{msh} < 0$ and $1 < D_{msh} \leq 1.1$ are repositioned at

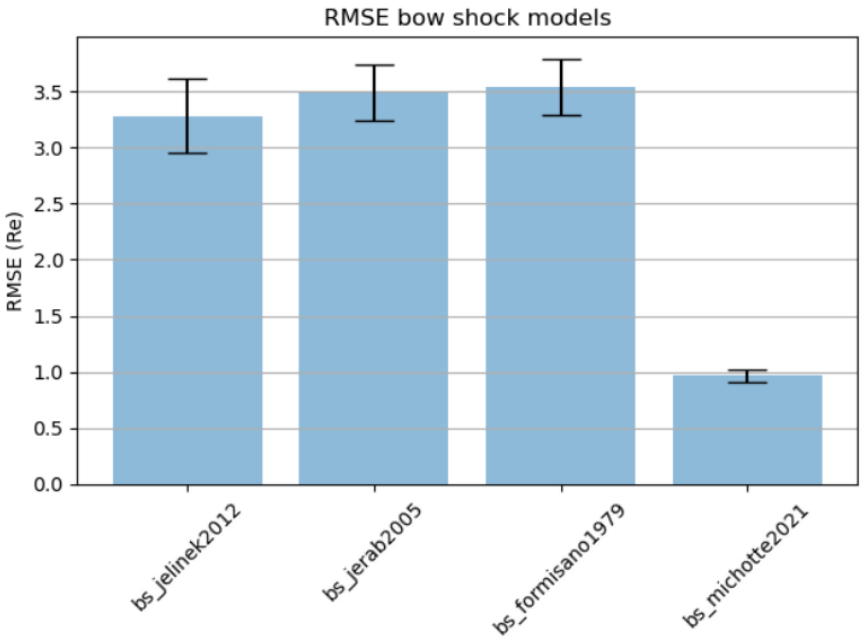

Figure 2.18: RMSE of bow shock models evaluated on 300 datasets, each consisting of about 2000 crossings. The models evaluated include those of Jelínek et al. [2012], Jeřáb et al. [2005], Formisano [1979]), and lastly the machine learning model for the bow shock.

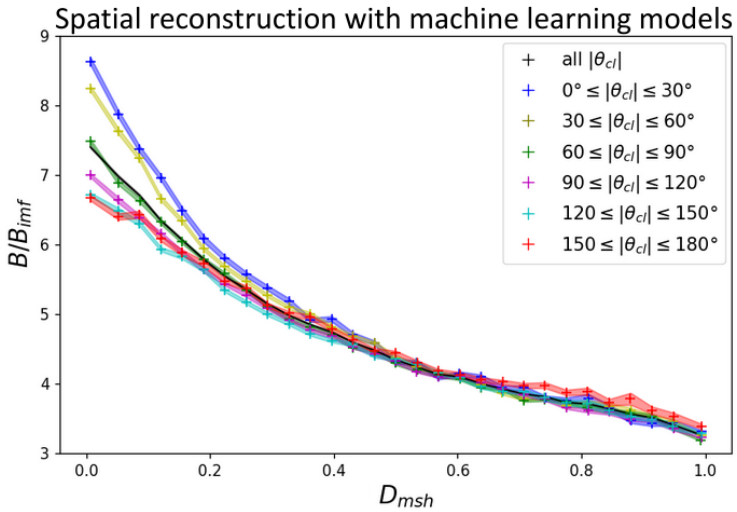

Figure 2.19: Spatial reconstruction of the magnetic pileup, for different range of IMF clock angles, in the subsolar magnetosheath as function of the relative distance (D_{msh}) to the magnetopause and bow shock obtained with the machine learning models. The magnetopause is located at D_{msh}=0, while the bow shock is at D_{msh}=1.

the magnetopause (D_{msh}=0) and at the bow shock (D_{msh}=1), respectively. After this procedure, the final number of magnetosheath measurements decreased from 46,947,933 to 44,897,857 data points.

Similarly, the magnetosphere data point with a relative distance to the magnetopause (Equation 2.7) such as $D_{msp} > 1.1$ are discarded and those with $1 < D_{msp} \leq 1.1$ are repositioned to the magnetopause (D_{msp}=1). Additionally, the measurements with a relative distance $D_{msp} < 0.5$ are eliminated because they are too far from the magnetopause to be of interest in this PhD research. Therefore, the number of magnetosphere data points decreases from 75,919,506 to 54,737,120.

Once their relative position with regard to the system boundaries is known, each point is repositined in between two standard boundaries. These boundaries are chosen among analytical models with the smallest RMSE (i.e. Jelínek et al. [2012] and Shue et al. [1998]) – parameterized by average IMF and solar wind conditions – in respect to which the position of the data points are repositioned.

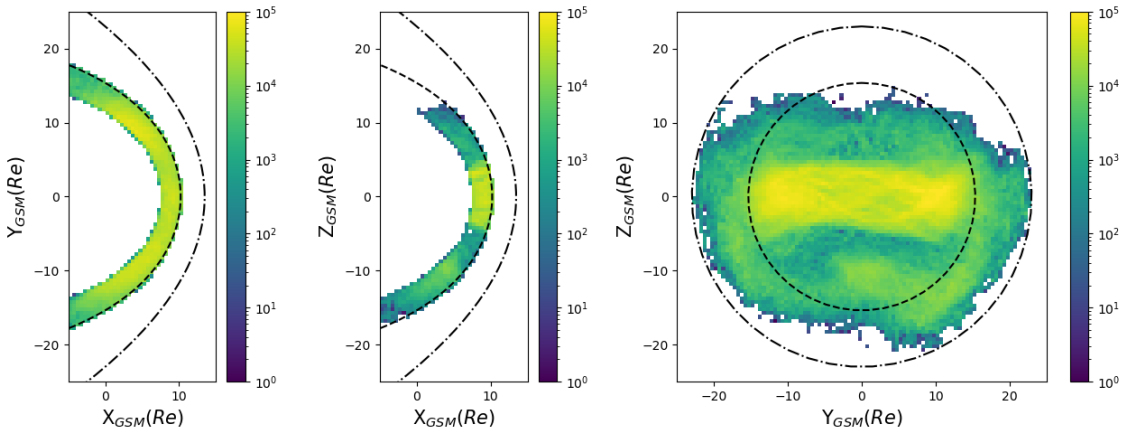

Figure 2.20: Distributions of **magnetosphere** data point renormalized positions are presented through color-coded bins indicating the number of points per bin (bin size = 0.5 Re x 0.5 Re). The left panel displays the ($X_{GSM}Y_{GSM}$) plane with data points located within $|Z_{GSM}| \leq 1$ Re. The middle panel shows the ($X_{GSM}Z_{GSM}$) plane with data points located within $|Y_{GSM}| \leq 1$ Re. The right panel shows all data points in the ($X_{GSM}Z_{GSM}$) plane. The magnetopause [Shue et al., 1998] and bow shock [Jelínek et al., 2012], for average IMF and solar wind conditions, are represented by dashed and dash-dotted black lines, respectively.

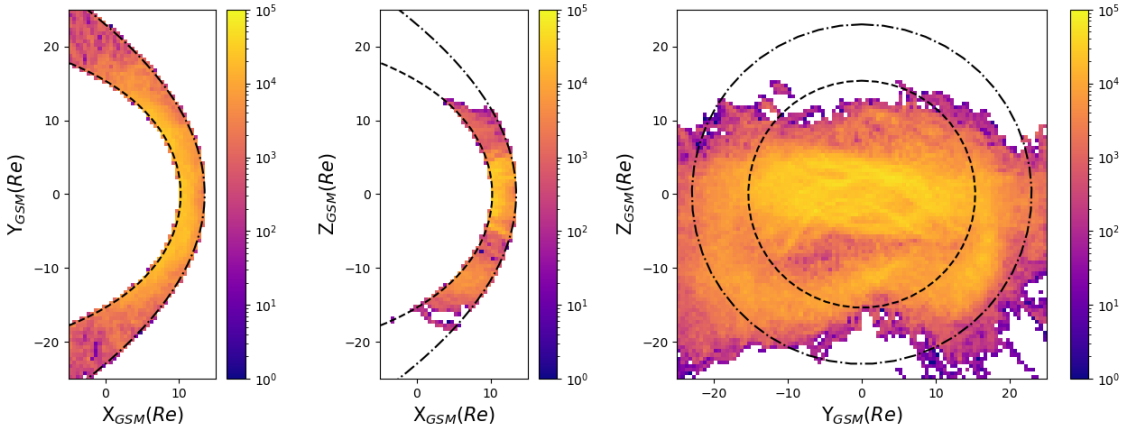

Figure 2.21: Distributions of **magnetosheath** data point renormalized positions are presented through color-coded bins indicating the number of points per bin (bin size = 0.5 Re x 0.5 Re). The left panel displays the ($X_{GSM}Y_{GSM}$) plane with data points located within $|Z_{GSM}| \leq 1$ Re. The middle panel shows the ($X_{GSM}Z_{GSM}$) plane with data points located within $|Y_{GSM}| \leq 1$ Re. The right panel shows all data points in the ($Y_{GSM}Z_{GSM}$) plane. The magnetopause [Shue et al., 1998] and bow shock [Jelínek et al., 2012], for average IMF and solar wind conditions, are represented by dashed and dash-dotted black lines, respectively.

Figures 2.20 and 2.21 show the normalized position of the magnetosphere and magnetosheath data points, respectively. These figures show that, after normalizing the positions, the magnetosphere measurements are all located Earthward of the magnetopause, while the magnetosheath data points are located between the magnetopause and bow shock. If there is good dayside spatial coverage in the equatorial plane (leftmost panels of Figures 2.20 and 2.21), it remains incomplete at high latitudes in the northern hemisphere (middle and rightmost panels).

2.7 Coordinate Systems

This section provides a description of the different coordinate systems and definition of the different angles utilized in this PhD research.

2.7.1 Geocentric Solar Ecliptic (GSE) coordinates

The Geocentric Solar Ecliptic (GSE) coordinate system is the simplest of the orthogonal systems based on the Earth-Sun line. It is an orthogonal coordinate system with its origin at the center of the Earth defined as follows:

- The $\widehat{\mathbf{X}}_{\text{GSE}}$ axis is aligned with the Earth-Sun line and pointing toward the Sun.
- The $\widehat{\mathbf{Z}}_{\text{GSE}}$ axis lies in the plane that is perpendicular to the ecliptic (i.e. the plane of the Earth's revolution around the Sun) and is oriented positively towards the North.
- The $\widehat{\mathbf{Y}}_{\text{GSE}}$ axis close this right-handed system in the aforementioned ecliptic plane.

2.7.2 Geocentric Solar Magnetic (GSM) coordinates

GSM coordinate system is useful for studying quantities and phenomena controlled by the solar wind/IMF and magnetospheric magnetic fields.

It is an orthogonal coordinate system with its origin at the center of the Earth, defined as in the equation system 2.12 [Laundal and Richmond, 2017]:

- The $\widehat{\mathbf{X}}_{\text{GSM}}$ axis is aligned with the Earth-Sun line ($\widehat{\mathbf{s}}$) and pointing toward the Sun.
- The $\widehat{\mathbf{Y}}_{\text{GSM}}$ is perpendicular to the magnetic dipole ($\widehat{\mathbf{m}}$) and to the $\widehat{\mathbf{X}}_{\text{GSM}}$ axis.
- The $\widehat{\mathbf{Z}}_{\text{GSM}}$ axis is along the component of the magnetic dipole perpendicular to the $\widehat{\mathbf{X}}_{\text{GSM}}$ axis and close this right-handed system.

$$\begin{cases} \widehat{\mathbf{X}}_{\text{GSM}} &= \widehat{\mathbf{s}} \\ \widehat{\mathbf{Y}}_{\text{GSM}} &= \frac{\widehat{\mathbf{m}}\times\widehat{\mathbf{X}}_{\text{GSM}}}{\|\widehat{\mathbf{m}}\times\widehat{\mathbf{X}}_{\text{GSM}}\|} \\ \widehat{\mathbf{Z}}_{\text{GSM}} &= \widehat{\mathbf{X}}_{\text{GSM}} \times \widehat{\mathbf{Y}}_{\text{GSM}} \end{cases} \tag{2.12}$$

2.7.3 Solar Wind Interplanetary (SWI) magnetic field coordinate

The Solar Wind Interplanetary magnetic field (SWI) magnetic field coordinate system [Zhang et al., 2019] is convenient for studying quantities in regions strongly governed by the IMF orientation and solar wind such as the magnetosheath. For instance, it enables each data point to fall in either the quasi-parallel or quasi-perpendicular sector of the magnetosheath, with respect to its causal IMF. The quasi-parallel (quasi-perpendicular resp.) of the magnetosheath side lies downstream the part of the bow shock where the IMF is quasi-parallel (quasi-perpendicular resp.) with the shock's normal.

The equation system 2.13 give the unit vectors of the SWI base, such as:

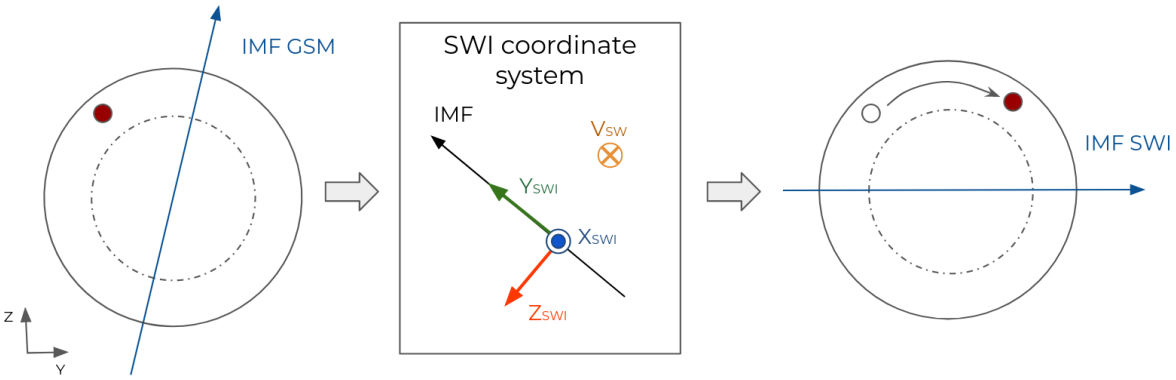

Figure 2.22: Schematic of the coordinate transformation from GSM to SWI. The gray solid and dashed lines correspond to the terminator of the bow shock and magnetopause, respectively. The red point corresponds to the position of a measurement that undergoes the same rotation as the IMF (blue arrow) during the change of coordinate system.

- The $\hat{\mathbf{X}}_{\text{SWI}}$ axis is anti-parallel to the solar wind velocity vector ($\mathbf{V}_{sw}$).
- $\hat{\mathbf{Y}}_{\text{SWI}}$ close this right-handed system and is along the direction of the IMF ($\mathbf{B}_{imf}$) component orthogonal to the $\hat{\mathbf{X}}_{\text{SWI}}$ axis with $\text{B}_{x_{imf}}$ always positive.
- The $\hat{\mathbf{Z}}_{\text{SWI}}$ axis is perpendicular to the $\hat{\mathbf{X}}_{\text{SWI}}$ and to the $\mathbf{B}_{imf}$ vector.

$$\begin{cases} \hat{\mathbf{X}}_{\text{SWI}} & = -\mathbf{V}_{sw} / \|\mathbf{V}_{sw}\| \\ \hat{\mathbf{Y}}_{\text{SWI}} & = \hat{\mathbf{Z}}_{\text{SWI}} \times \hat{\mathbf{X}}_{\text{SWI}} \\ \hat{\mathbf{Z}}_{\text{SWI}} & = \left(\hat{\mathbf{X}}_{\text{SWI}} \times \frac{\text{B}_{x_{imf}}}{|\text{B}_{x_{imf}}|} \mathbf{B}_{imf} \right) / \| \hat{\mathbf{X}}_{\text{SWI}} \times \frac{\text{B}_{x_{imf}}}{|\text{B}_{x_{imf}}|} \mathbf{B}_{imf} \| \end{cases} \tag{2.13}$$

Since the $\hat{\mathbf{Y}}_{\text{SWI}}$ is defined along the magnetic field in the ($\text{Y}_{\text{GSM}}\text{Z}_{\text{GSM}}$) plane, this means that in this coordinate system the IMF clock angle (θ_{cl}) is always 90°. The position of each measurement transformed from the GSM to the SWI coordinate system undergoes a rotation of $\Delta\theta = \pi/2 - \theta_{cl}$ as described in Figure 2.22. The assumption behind the SWI coordinate system is that the pattern of magnetic field draping in the magnetosheath remains the same if rotated by the IMF clock angle around the X axis. Therefore, in this coordinate system, the only dependence on the IMF orientation is on the absolute value of the IMF cone angle, since $\text{B}_{x_{imf}}$ is always positive.

Figure 2.23 shows the distributions of the magnetosheath data points in the SWI coordinate system in the equatorial plane, the noon meridian plane, and in the vicinity of the magnetopause. In this coordinate system, the spatial coverage on the dayside is complete not only at the equatorial plane (left panel), but also at high latitudes (middle and right panels).

2.7.4 Pseudo-Geocentric Solar Magnetic (PGSM) coordinates

The Pseudo-Geocentric Solar Magnetospheric (PGSM) coordinate system was developed during this PhD research and was specifically designed to study the magnetopause with in-situ measurements. The spatial coverage of the magnetopause is optimized by maximizing the amount of measurement with regards to selecting parameters, such as IMF orientation and dipole tilt angle, through the use of symmetries and rotations. The aim of this coordinate system is to reproduce the maps that would be obtained in the GSM coordinate system if the measurements covered the entire dayside magnetopause for all IMF orientations and dipole tilts.

To enhance the spatial coverage of the magnetopause, the assumption of symmetry of the magnetic field with respect to the dipole tilt angle (i.e. $\psi > 0$ transformed in $\psi < 0$ and vice versa) is used for the magnetosphere measurements. In particular, it will allow to complete the spatial coverage of the dayside magnetopause at high latitude which was incomplete in GSM coordinate

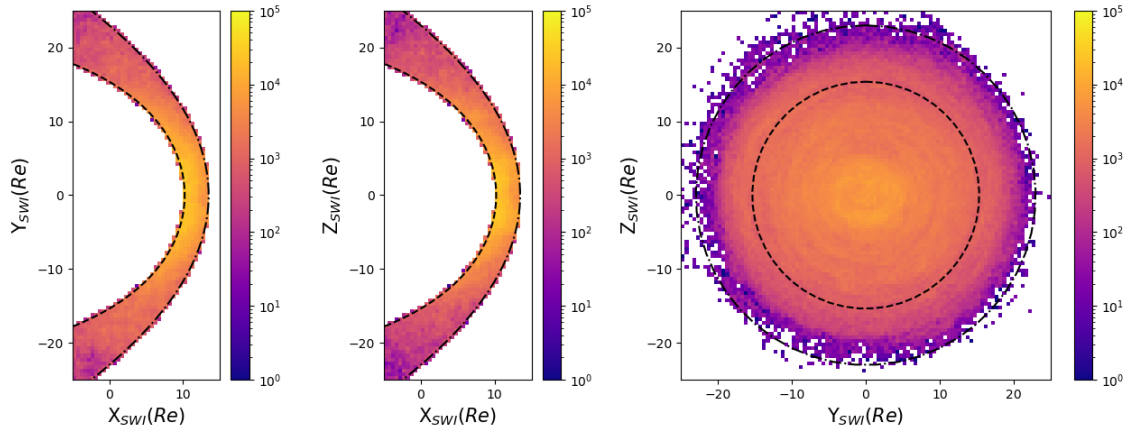

Figure 2.23: **Magnetosheath** data point distributions in SWI coordinates are showcased with color-coded bins that indicate the number of points per bin (bin size = 0.5 Re x 0.5 Re). The left panel displays the ($X_{GSM}Y_{GSM}$) plane with data points located within $|Z_{GSM}| \leq 1$ Re. The middle panel shows the ($X_{GSM}Z_{GSM}$) plane with data points located within $|Y_{GSM}| \leq 1$ Re. The right panel shows data points near the magnetopause ($D_{msh} \leq 0.1$) in the ($Y_{GSM}Z_{GSM}$) plane. The magnetopause [Shue et al., 1998] and bow shock [Jelínek et al., 2012], for average IMF and solar wind conditions, are represented by dashed and dash-dotted black lines, respectively.

(see middle and left panels of Figure 2.20). The symmetry transformations described by the equations in systems 2.14 to 2.16 are applied to each measurement "i" of the magnetosphere dataset.

$$\psi_{PGSM} = \{\psi_{i_{GSM}}, -\psi_{i_{GSM}}\} \tag{2.14}$$

$$\mathbf{X}_{MSP}\begin{cases} X_{PGSM} & = \{X_{i_{GSM}}, X_{i_{GSM}}\} \\ Y_{PGSM} & = \{Y_{i_{GSM}}, -Y_{i_{GSM}}\} \\ Z_{PGSM} & = \{Z_{i_{GSM}}, -Z_{i_{GSM}}\} \end{cases} \tag{2.15}$$

$$\mathbf{B}_{MSP}\begin{cases} B_{x_{PGSM}} & = \left\{B_{i_{x_{GSM}}}, -B_{i_{x_{GSM}}}\right\} \\ B_{y_{PGSM}} & = \left\{B_{i_{y_{GSM}}}, B_{i_{y_{GSM}}}\right\} \\ B_{z_{PGSM}} & = \left\{B_{i_{z_{GSM}}}, B_{i_{z_{GSM}}}\right\} \end{cases} \tag{2.16}$$

Figure 2.24 illustrates the transformation in the PGSM coordinate system for the magnetic field in the magnetosphere nearby the magnetopause. The analytical model of Tsyganenko and Stern [1996] was used in this example. The panels on the left show the three components of the magnetic field with a dipole tilt angle of ψ=24°, while the middle panels display the same components with ψ=-24°. The rightmost panels show that after applying symmetry transformations corresponding to those described by -ψ in the equations in systems 2.14 to 2.16, the transformed magnetic field of ψ=24° is consistent with one obtained for ψ=-24°.

Note that the Solar-Magnetic (SM) coordinate system [Laundal and Richmond, 2017], in which the Z_{SM} axis aligns with the Earth's dipole axis, may appear to be a convenient coordinate system to remove the dependence on the dipole tilt angle. By rotating around the Y_{SM} axis , one can obtain the desired dipole tilt angle without needing to select a subset of measurements surrounding that angle. However, the magnetopause and the nearby magnetic field geometry are not symmetric by rotation around the Y_{SM} axis. Thus, the Solar-Magnetic coordinate system proves unsuitable for studying the magnetic field near the magnetopause.

$$\mathbf{X}_{MSH}\begin{cases} X_{SWI} & = \{X_{i_{SWI}}, X_{i_{SWI}}\} \\ Y_{SWI} & = \{Y_{i_{SWI}}, -Y_{i_{SWI}}\} \\ Z_{SWI} & = \{Z_{i_{SWI}}, Z_{i_{SWI}}\} \end{cases} \tag{2.17}$$

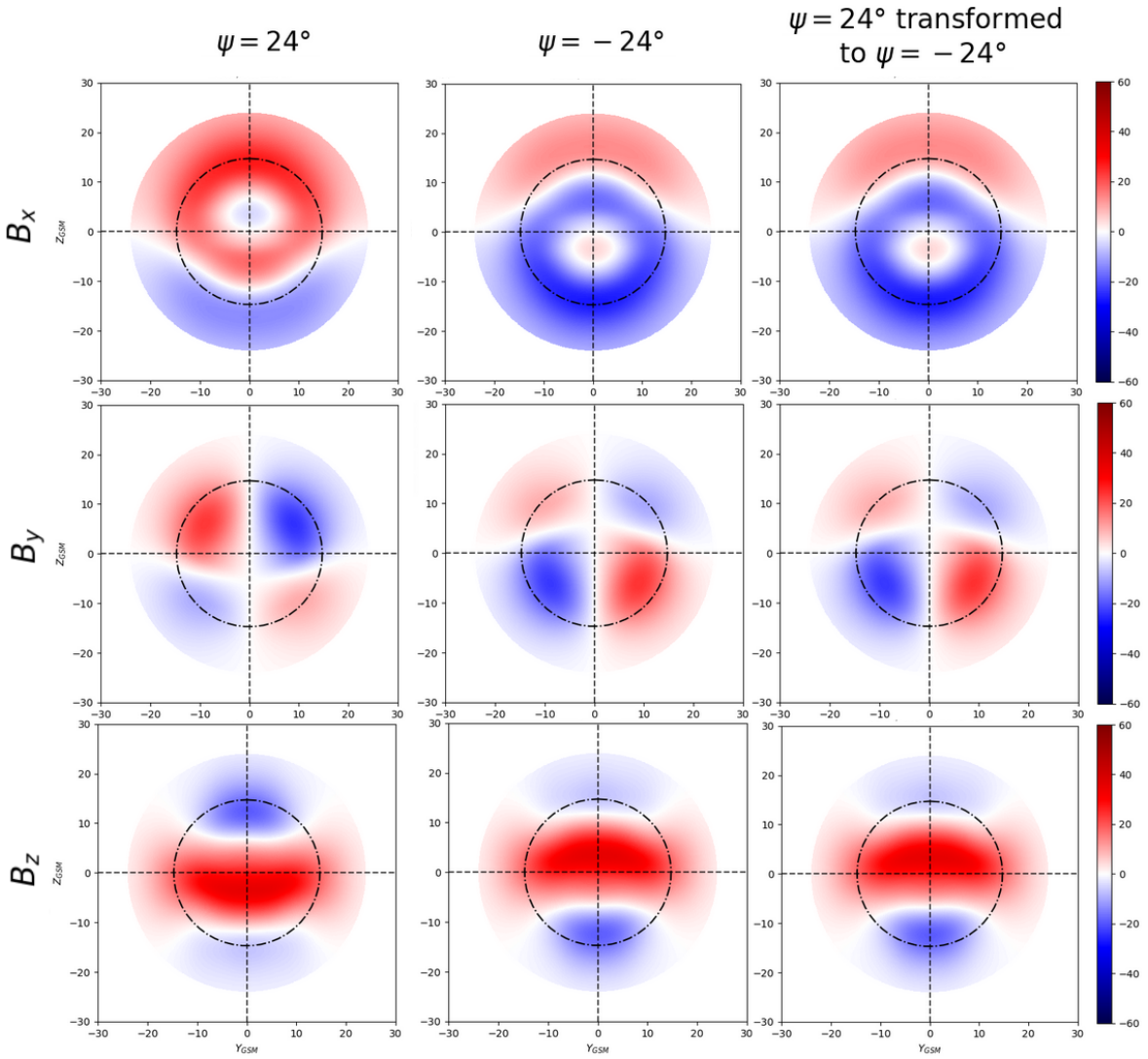

Figure 2.24: Magnetic field nearby the magnetopause on the magnetospheric side, obtained with the Tsyganenko and Stern [1996] model, corresponding to the B_x, B_y, and B_z components in the first, second, and third rows, respectively, for a dipole tilt angle of ψ = 24° and ψ = -24° in the left and middle panels. The right panels correspond to the determined for ψ = 24° transformed into ψ = -24° using the symmetry transformation described by -ψ in the equations found in systems 2.14 through 2.16.

$$\mathbf{B}_{\mathrm{MSH}} \begin{cases} \mathrm{B}_{x_{\mathrm{SWI}}} &= \left\{ \mathrm{B}_{i_{x_{\mathrm{SWI}}}}, \mathrm{B}_{i_{x_{\mathrm{SWI}}}} \right\} \\ \mathrm{B}_{y_{\mathrm{SWI}}} &= \left\{ \mathrm{B}_{i_{y_{\mathrm{SWI}}}}, \mathrm{B}_{i_{y_{\mathrm{SWI}}}} \right\} \\ \mathrm{B}_{z_{\mathrm{SWI}}} &= \left\{ \mathrm{B}_{i_{z_{\mathrm{SWI}}}}, -\mathrm{B}_{i_{z_{\mathrm{SWI}}}} \right\} \end{cases} \tag{2.18}$$

The magnetosheath measurements are first transformed into the SWI coordinate system [Zhang et al., 2019] presented in the previous section, which only depend on the absolute value of the IMF cone angle as IMF clock angle is always of 90°. However, as the number of measurements for absolute values of the IMF cone angle decreases sharply below 45° (see distribution of the IMF cone angle in Figure 2.26), the spatial coverage is not sufficient for relatively radial IMF. Therefore, an additional symmetry with respect to $\mathrm{Y}_{\mathrm{SWI}}$, as described in the equation systems 2.17 and 2.18, is performed at each measurement i to increase the size of the magnetosheath dataset. This symmetry is possible because all measurements are sorted in the SWI coordinate system, so that the quasi-parallel (resp. quasi-perpendicular) side of the magnetosheath is always found for $\mathrm{Y}_{\mathrm{SWI}} \geq 0$ (resp. $\mathrm{Y}_{\mathrm{SWI}} \leq 0$), and with an IMF clock angle of 90° (i.e. along the $\mathrm{Y}_{\mathrm{SWI}}$ axis).

$$\mathbf{X}_{\text{MSH}} \begin{cases} \text{X}_{\text{PGSM}} &= \text{X}_{\text{SWI}} \\ \text{Y}_{\text{PGSM}} &= \sqrt{\text{Y}_{\text{SWI}}^2 + \text{Z}_{\text{SWI}}^2}\sin(\tan^{-1}(\pm\text{Y}_{\text{SWI}}/\text{Z}_{\text{SWI}}) + \Delta\theta_{cl}) \\ \text{Z}_{\text{PGSM}} &= \sqrt{\text{Y}_{\text{SWI}}^2 + \text{Z}_{\text{SWI}}^2}\cos(\tan^{-1}(\pm\text{Y}_{\text{SWI}}/\text{Z}_{\text{SWI}}) + \Delta\theta_{cl}) \end{cases} \quad \text{with} \quad \tan^{-1}\left(\frac{\pm\text{Y}_{\text{SWI}}}{\text{Z}_{\text{SWI}}}\right) \in [-\pi, \pi] \tag{2.19}$$

$$\mathbf{B}_{\text{MSH}} \begin{cases} \text{B}_{x_{\text{PGSM}}} &= \pm\text{B}_{x_{\text{SWI}}} \\ \text{B}_{y_{\text{PGSM}}} &= \sqrt{\text{B}_{y_{\text{SWI}}}^2 + \text{B}_{z_{\text{SWI}}}^2}\sin(\tan^{-1}(\text{B}_{y_{\text{SWI}}}/(\pm\text{B}_{z_{\text{SWI}}})) + \Delta\theta_{cl}) \\ \text{B}_{z_{\text{PGSM}}} &= \sqrt{\text{B}_{y_{\text{SWI}}}^2 + \text{B}_{z_{\text{SWI}}}^2}\cos(\tan^{-1}(\text{B}_{y_{\text{SWI}}}/(\pm\text{B}_{z_{\text{SWI}}})) + \Delta\theta_{cl}) \end{cases} \quad \text{with} \quad \tan^{-1}\left(\frac{\text{B}_{y_{\text{SWI}}}}{\pm\text{B}_{z_{\text{SWI}}}}\right) \in [-\pi, \pi] \tag{2.20}$$

To reconstruct a global distribution of a quantity for a specific IMF orientation as if in GSM coordinates, a subset of the magnetosheath measurements within a specific range of IMF cone angles can be selected and then rotated by an angle of $\Delta\theta_{cl} = \theta_{cl} - \pi/2$, where θ_{cl} is the desired IMF clock angle in radians. This rotation transformation assumes that the pattern of the magnetic field draping in the magnetosheath remains the same if rotated around the X axis by the IMF clock angle, as already assumed when moving into the SWI coordinate system. The equations 2.19 and 2.20 provide the details for this rotation for the measurement position and the magnetic field, respectively. It is performed with taking into account the sign (i.e. $\pm$) of the desired $\text{B}_{x_{imf}}$ component, positive for $\text{B}_{x_{imf}} > 0$ and negative for $\text{B}_{x_{imf}} < 0$.

2.7.5 Angles definitions

Zenith and azimuth angles

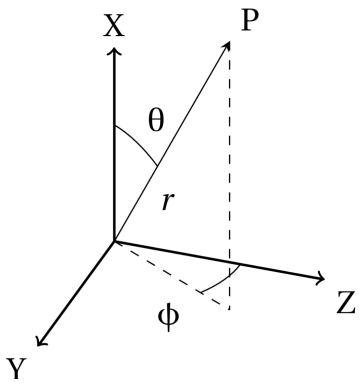

Figure 2.25: Representation of the spherical coordinates used in GSM coordinates in this thesis.

In Figure 2.25, we illustrate the spherical coordinate system employed within the GSM coordinate system with the θ and ϕ corresponding to the zenith and azimuth angle, respectively. Equation 2.21 provides the transformation between Cartesian and spherical coordinates used in this thesis.

$$\begin{cases} \text{X} &= r\cos(\theta) \\ \text{Y} &= r\sin(\theta)\sin(\phi) \\ \text{Z} &= r\sin(\theta)\cos(\phi) \end{cases} \tag{2.21}$$

IMF cone and clock angles

The IMF cone (θ_{co}) and IMF clock (θ_{cl}) angles give the angular orientation of the IMF such as :

- IMF cone angle correspond to the angle between the IMF vector and the Sun-Earth line (i.e. X_{GSM}). A cone angle of 0 degrees indicates that the IMF is aligned with the Sun-Earth line. Conversely, a cone angle of 90 degrees indicates that the IMF lies in a plane perpendicular to the Sun-Earth line.

- IMF clock angle is measured clockwise from the Z_{GSM} in the plane perpendicular to the Sun-Earth line (i.e. $(Y_{GSM}Z_{GSM})$ plane. An IMF clock angle with values of 0°, 90°, -90°, and 180° indicates that the IMF is directed to the north, east, west, and south, respectively.

These angles are computed with the component of the magnetic field in GSM coordinates with the equations 2.22 and 2.23.

$$\theta_{co} = \arctan\left(\frac{\sqrt{B_y^2 + B_z^2}}{B_x}\right) \quad \text{with} \quad \theta_{co} \in [-\pi/2, \pi/2] \tag{2.22}$$

$$\theta_{cl} = \arctan\left(\frac{B_y}{B_z}\right) \quad \text{with} \quad \theta_{cl} \in [-\pi, \pi] \tag{2.23}$$

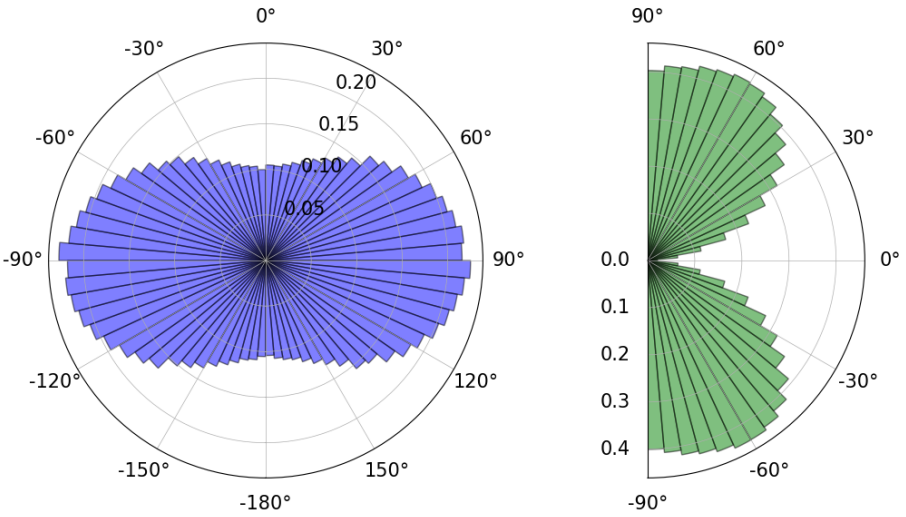

Figure 2.26: The left and right panels display the polar distribution of the IMF clock and cone angles in solar wind, respectively, based on 25 years of OMNI measurements.

Describing the IMF by these angles, rather than by the values of its components, not only makes it easier to visualize it in space, but also decouples its orientation from its amplitude. For instance, Figure 2.26 shows the polar distribution of the clock angle and cone angle of the IMF using OMNI data spanning over more than two decades. It is clear that the dominant orientation of the IMF is in the eastward and westward directions, as shown in the left panel. In the same time, we can see that radial orientations are uncommon in contrast to IMF cone angles of approximately ±60 degrees, as depicted in the right panel. These preferred orientations correspond to the directions of the Parker spiral [Parker, 1958], and they could be easily identified with this representation. Therefore, we will be using these two angles to describe the orientation of the IMF in most of this dissertation.

2.8 Spatial Distribution of a Physical Quantity

Building global and continuous spatial representations of various quantities within the magnetosheath and at the magnetopause from randomly scattered distributions of in-situ measurements is the last step of the methodology that is common to this dissertation.

2.8.1 Classical binning

The simplest way to create a coherent spatial representation from spatially scattered measurements consists in performing a classical statistical binning. This method involves creating a grid across space and calculating the average or median value of the measurements falling within each bin. However, a significant limitation of this approach is that it is not well suited when dealing with non-uniform distributions, such as in-situ measurements (e.g. denser in the subsolar region and sparser towards the flanks, as shown in Figure 2.23). Using a classical binning method often necessitates to choose between achieving a high spatial resolution or reducing statistical noise in areas with a limited amount of data.

For example, the panel a of Figure 2.27 shows that using a small bin size to produce a high spatial resolution results in an important amount of empty bins (i.e. bins without measurements in it) while the bin count remains highly variable from one bin to the next in the comparatively denser subsolar region. Estimating the spatial distribution of a quantity, like the B_x/B_{imf} component, as shown in panel c, with such a refined bin size tends to produce significant noise in addition to empty pixels.

In contrast, a coarser binning like that shown in the panel **b** of Figure 2.27 allows for a greater statistics per bin and, therefore less empty pixel. However, this comes at the expense of lower spatial resolution in regions where there are ample measurements that could offer a better resolution, such as the subsolar magnetopause. If the spatial distribution of the B_x/B_{imf} component provides a clear pattern over most of the dayside, it remains noisy in areas with fewer data points, as shown in panel **d** of Figure 2.27.

Additionally, another drawback of this classical binning method is the built-in assumption that a measurement only contributes to a single bin. As described in Section 2.6, one of the preprocessing steps involves repositioning the measurements relative to a standard magnetopause and bow shock. This repositioning process carries inherent errors due to the uncertainties associated with the GBR magnetopause and bow shock models used for repositioning the measurements. However, this uncertainty is not accounted for in the classical binning method, where a measurement "arbitrarily" participates in the value of single bin. Next section will present a method that allows to address these drawbacks.

2.8.2 K-Nearest Neighbors algorithm

The challenge of handling non-uniform distributions of in-situ measurements can be mitigated with the use of a K-Nearest Neighbors (KNN) regressor algorithm [Kramer, 2013]. For a given location and a considered quantity, the KNN algorithm:

1. computes the Euclidean distance of the considered location to all the point in the dataset
2. identifies the K nearest points in the data to the given position
3. estimates the desired quantity by averaging the values of the K neighboring points, weighted by their distance from the location under consideration.

Equation 2.24 details the computation, by the KNN algorithm, of the average of a quantity Q at the position p from the K neighboring points' values Q_i weighted by their respective distance d_i to p.

$$Q(p) = \frac{\sum_{i=1}^{K} \frac{1}{d_i} Q_i}{\sum_{i=1}^{K} \frac{1}{d_i}} \tag{2.24}$$

This implies that the number of measurement samples used per grid points in the final representation is constant, since the smaller the density the further away the KNN algorithm will look for samples. Nonetheless, even when taking into account more distant data points, the information at a small scale remains preserved because each point's value is weighted by its distance from

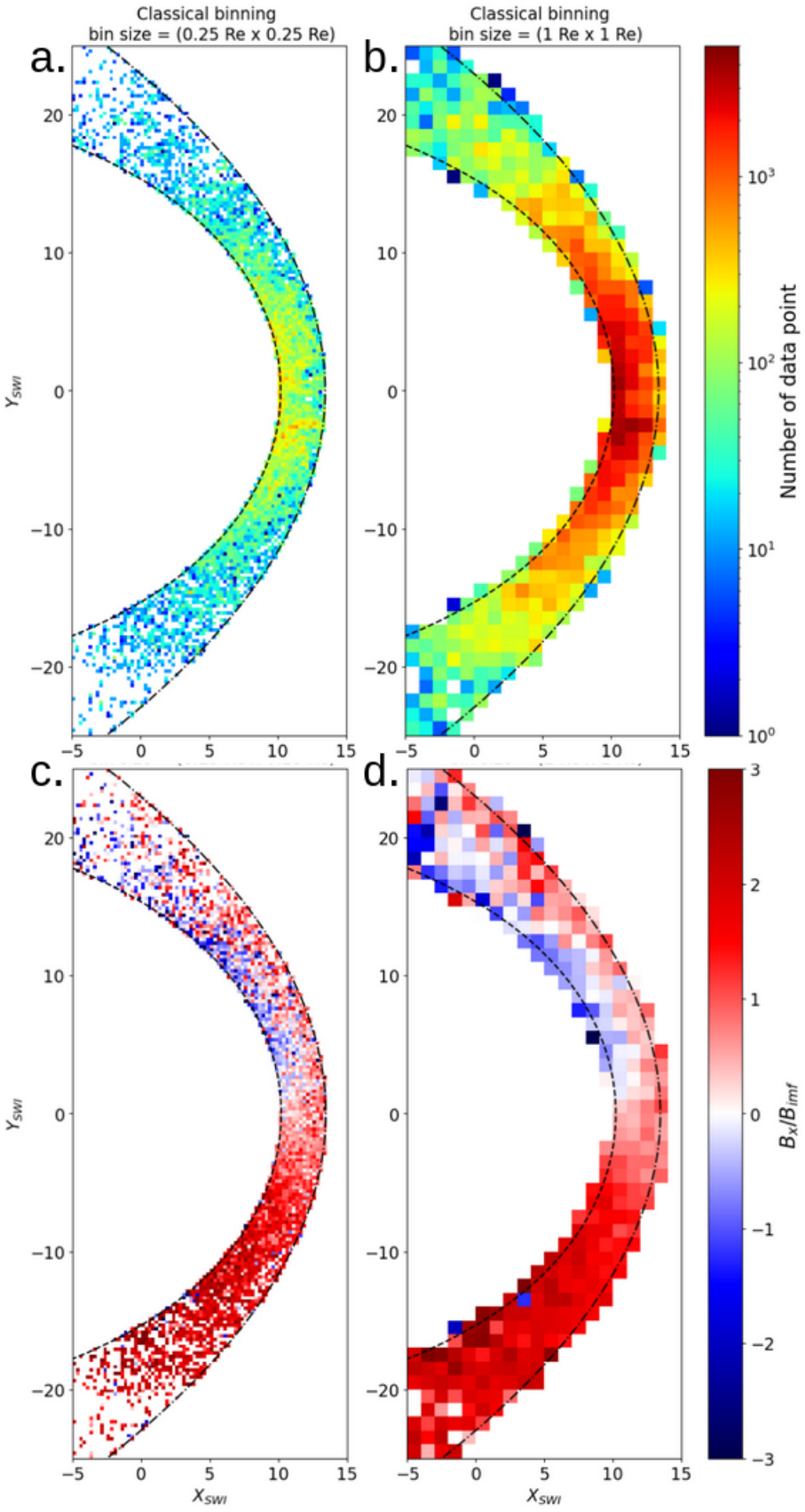

Figure 2.27: Count of the number of point per bin (panels **a** and **b**) and distributions of the B_x/B_{imf} (panels **c** and **d**) in the equatorial plane ($|Z_{SWI}| \leq 0.5$ Re) for measurements falling within $|\theta_{co}|$=25°±5° using the classical binning method for 0.25 Re (panels **a** and **c**) and 1 Re (panels **b** and **d**) square bins.

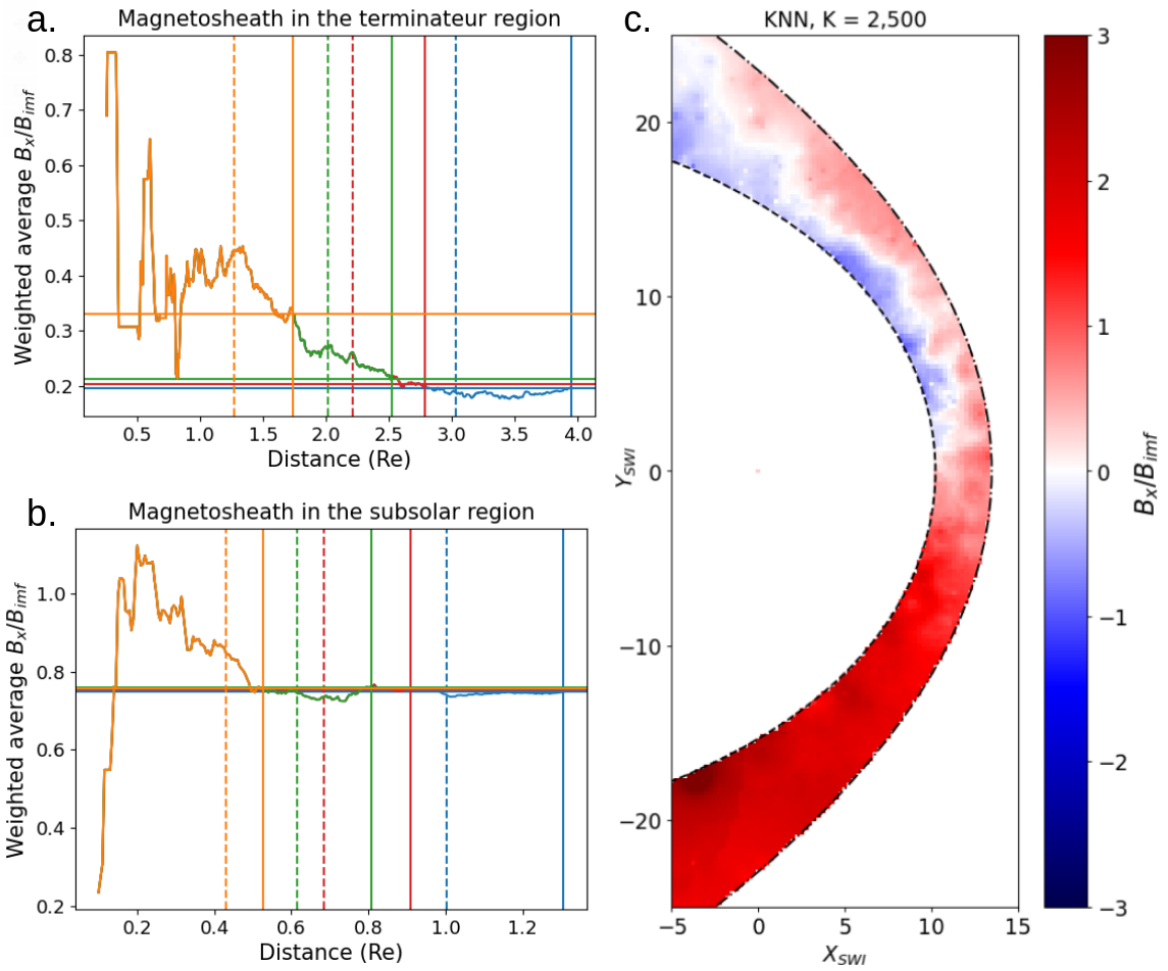

Figure 2.28: Panels **a** and **b** display the predicted B_x/B_{imf} values by the KNN algorithm as a function of the distance for the considered points in the computation, for a location in the terminator and subsolar region, respectively. The K values of 2,500 (orange), 7,500 (green), 10,000 (red), and 25,000 (blue) correspond to the different colors. The colored lines running horizontally correspond to the final obtained values of B_x/B_{imf}. The solid and dashed vertical lines correspond to the maximum and median distance of the points considered for different K, respectively. Panel **c** shows the spatial distribution of B_x/B_{imf} in the equatorial plane for measurements falling within $|\theta_{co}|$=25°±5° using the KNN method.

the desired position. Thus, the farther the data point, the lower its contribution to the final value provided by the KNN. Panels a and b of Figure 2.28 show that the KNN predictions in two different locations (flank and subsolar regions) tend to converge as more distant data points are considered. Panel c in Figure 2.28 shows that the spatial reconstruction of the B_x/B_{imf} component with the KNN algorithm captures the pattern seen in both the fine and coarse bin size of Figure 2.27, while being less noisy.

In addition, the KNN method mitigates the previously mentioned drawback of the classical binning method, in which a point is "arbitrarily" allocated in a specific bin without accounting for uncertainty in the positions' normalization procedure. In contrast, in the KNN method, the same point will be taken into account with different weights in several close locations.

It can be concluded that the KNN method is especially suitable for the reconstruction of the spatial distribution of the quantity with in-situ measurement. In this work, the value of K is typically selected from a range between 7,500 and 10,000, depending on the size of the subset of data under consideration (i.e. measurements with specific upstream conditions).

2.9 Summary

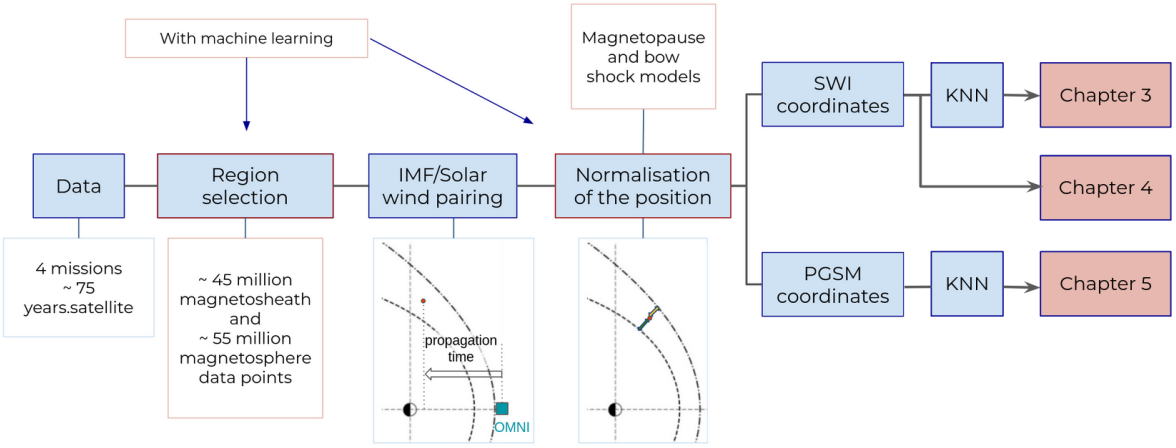

Figure 2.29: Overview of the global methodology used during this PhD research

Figure 2.29 depicts the methodology shared across the various studies conducted in this PhD research. The first step was to collect data from four missions (Cluster, Double Star, THEMIS, MMS), encompassing approximately 75 satellite-years of observations. Then we identified and selected approximately 45 million magnetosheath and 55 million magnetosphere data points using a GBC algorithm. The next phase involved pairing these data points with IMF and solar wind conditions using the OMNI database, considering the propagation time of solar wind parameters to the location of the spacecraft. Subsequently, a normalization step was performed on the position of the measurements to provide a good spatial representation. This step required the development of new models of the bow shock and magnetopause using a GBR algorithm, which allowed a precision not achievable with existing analytical models of these boundaries. The SWI coordinate system was used to reconstruct the magnetosheath properties in chapters 3 and 4, while the PGSM coordinate system is used for the magnetopause study in chapter 5. Finally, the KNN is used in the Chapter 3 and 5 to obtain the spatial distributions of the different quantities in this thesis.

2.10 Bibliography

Alexeev, I. I., Sibeck, D. G., and Bobrovnikov, S. Y.: Concerning the location of magnetopause merging as a function of the magnetopause current strength, , 103, 6675–6684, https://doi.org/10.1029/97JA02863, 1998. 40

Auster, H. U., Glassmeier, K. H., Magnes, W., Aydogar, O., Baumjohann, W., Constantinescu, D., Fischer, D., Fornacon, K. H., Georgescu, E., Harvey, P., Hillenmaier, O., Kroth, R., Ludlam, M., Narita, Y., Nakamura, R., Okrafka, K., Plaschke, F., Richter, I., Schwarzl, H., Stoll, B., Valavanoglou, A., and Wiedemann, M.: The THEMIS Fluxgate Magnetometer, , 141, 235–264, https://doi.org/10.1007/s11214-008-9365-9, 2008. 45

Balogh, A., Carr, C., Acuña, M., Dunlop, M., Beek, T., Brown, P., Fornacon, K.-H., Georgescu, E., Glassmeier, K.-H., Harris, J., Musmann, G., Oddy, T., and Schwingenschuh, K.: The Cluster Magnetic Field Investigation: Overview of in-flight performance and initial results, Annales Geophysicae, 19, https://doi.org/10.5194/angeo-19-1207-2001, 2001. 42

Berkson, J.: Application of the Logistic Function to Bio-Assay, Journal of the American Statistical Association, 39, 357–365, URL http://www.jstor.org/stable/2280041, 1944. 51

Breiman, L.: Random Forests, Mach. Learn., 45, 5–32, https://doi.org/10.1023/A:1010933404324, URL https://doi.org/10.1023/A:1010933404324, 2001. 51

Breuillard, H., Dupuis, R., Retino, A., Le Contel, O., Amaya, J., and Lapenta, G.: Automatic classification of plasma regions in near-Earth space with supervised machine learning: application to Magnetospheric Multi Scale 2016-2019 observation, Frontiers in Astronomy and Space Sciences, 7, 55, https://doi.org/10.3389/fspas.2020.00055, 2020. 49

Carr, C., Brown, P., Zhang, T. L., Gloag, J., Horbury, T., Lucek, E., Magnes, W., O'Brien, H., Oddy, T., Auster, U., Austin, P., Aydogar, O., Balogh, A., Baumjohann, W., Beek, T., Eichelberger, H., Fornacon, K. H., Georgescu, E., Glassmeier, K. H., Ludlam, M., Nakamura, R., and Richter, I.: The Double Star magnetic field investigation: instrument design, performance and highlights of the first year's observations, Annales Geophysicae, 23, 2713–2732, https://doi.org/10.5194/angeo-23-2713-2005, 2005. 44

Dimmock, A. P. and Nykyri, K.: The statistical mapping of magnetosheath plasma properties based on THEMIS measurements in the magnetosheath interplanetary medium reference frame, Journal of Geophysical Research (Space Physics), 118, 4963–4976, https://doi.org/10.1002/jgra.50465, 2013. 48, 57

Dimmock, A. P., Nykyri, K., and Pulkkinen, T. I.: A statistical study of magnetic field fluctuations in the dayside magnetosheath and their dependence on upstream solar wind conditions, Journal of Geophysical Research (Space Physics), 119, 6231–6248, https://doi.org/10.1002/2014JA020009, 2014. 48, 57

Dimmock, A. P., Pulkkinen, T. I., Osmane, A., and Nykyri, K.: The dawn-dusk asymmetry of ion density in the dayside magnetosheath and its annual variability measured by THEMIS, Annales Geophysicae, 34, 511–528, https://doi.org/10.5194/angeo-34-511-2016, 2016. 48, 57

Dimmock, A. P., Hietala, H., and Zou, Y.: Compiling Magnetosheath Statistical Data Sets Under Specific Solar Wind Conditions: Lessons Learnt From the Dayside Kinetic Southward IMF GEM Challenge, Earth and Space Science, 7, 01 095, https://doi.org/10.1029/2020EA001095, 2020. 49

Dunlop, M. W., Zhang, Q. H., Bogdanova, Y. V., Lockwood, M., Pu, Z., Hasegawa, H., Wang, J., Taylor, M. G. G. T., Berchem, J., Lavraud, B., Eastwood, J., Volwerk, M., Shen, C., Shi, J. K., Constantinescu, D., Frey, H., Fazakerley, A. N., Sibeck, D., Escoubet, P., Wild, J. A., and Liu, Z. X.: Extended Magnetic Reconnection across the Dayside Magnetopause, , 107, 025004, https://doi.org/10.1103/PhysRevLett.107.025004, 2011. 40

Eggington, J. W. B., Eastwood, J. P., Mejnertsen, L., Desai, R. T., and Chittenden, J. P.: Dipole Tilt Effect on Magnetopause Reconnection and the Steady-State Magnetosphere-Ionosphere System: Global MHD Simulations, Journal of Geophysical Research (Space Physics), 125, e27510, https://doi.org/10.1029/2019JA027510, 2020. 40

Farris, M. H. and Russell, C. T.: Determining the standoff distance of the bow shock: Mach number dependence and use of models, , 99, 17 681–17 690, https://doi.org/10.1029/94JA01020, 1994. 48

Fisher, R. A.: The use of multiple measutements in taxonomic problems, Annals of Eugenics, 7, 179–188, https://doi.org/10.1111/j.1469-1809.1936.tb02137.x, URL https://onlinelibrary.wiley.com/doi/abs/10.1111/j.1469-1809.1936.tb02137.x, 1936. 51

Formisano, V.: The three-dimensional shape of the bow shock., Nuovo Cimento C Geophysics Space Physics C, 2C, 681–692, https://doi.org/10.1007/BF02558125, 1979. 65, 66

Friedman, J. H.: Greedy function approximation: A gradient boosting machine., Ann. Statist., 29, 1189–1232, https://doi.org/10.1214/aos/1013203451, URL https://doi.org/10.1214/aos/1013203451, 2001. 51, 64

Génot, V., Broussillou, L., Budnik, E., Hellinger, P., Trávníček, P. M., Lucek, E., and Dandouras, I.: Timing mirror structures observed by Cluster with a magnetosheath flow model, Annales Geophysicae, 29, 1849–1860, https://doi.org/10.5194/angeo-29-1849-2011, 2011. 57

Glocer, A., Dorelli, J., Toth, G., Komar, C. M., and Cassak, P. A.: Separator reconnection at the magnetopause for predominantly northward and southward IMF: Techniques and results, Journal of Geophysical Research (Space Physics), 121, 140–156, https://doi.org/10.1002/2015JA021417, 2016. 40

Géron, A.: Hands-on machine learning with Scikit-Learn and TensorFlow : concepts, tools, and techniques to build intelligent systems, O'Reilly Media, Sebastopol, CA, 2017. 51

Jelínek, K., Němeček, Z., and Šafránková, J.: A new approach to magnetopause and bow shock modeling based on automated region identification, Journal of Geophysical Research (Space Physics), 117, A05208, https://doi.org/10.1029/2011JA017252, 2012. 49, 56, 60, 61, 65, 66, 67, 70

Jeřáb, M., Němeček, Z., Šafránková, J., Jelínek, K., and Měrka, J.: Improved bow shock model with dependence on the IMF strength, Planetary and Space Science, 53, 85–93, https://doi.org/10.1016/j.pss.2004.09.032, 2005. 51, 56, 65, 66

Kavosi, S., Raeder, J., Johnson, J. R., Nykyri, K., and Farrugia, C. J.: Seasonal and diurnal variations of Kelvin-Helmholtz Instability at terrestrial magnetopause, Nature Communications, 14, 2513, https://doi.org/10.1038/s41467-023-37485-x, 2023. 59

Kaymaz, Z., Siscoe, G., and Luhmann, J. G.: IMF draping around the Geotail: IMP 8 observations, , 19, 829–832, https://doi.org/10.1029/92GL00403, 1992. 48

King, J. H. and Papitashvili, N. E.: Solar wind spatial scales in and comparisons of hourly Wind and ACE plasma and magnetic field data, Journal of Geophysical Research (Space Physics), 110, A02104, https://doi.org/10.1029/2004JA010649, 2005. 48

Komar, C. M., Fermo, R. L., and Cassak, P. A.: Comparative analysis of dayside magnetic reconnection models in global magnetosphere simulations, Journal of Geophysical Research (Space Physics), 120, 276–294, https://doi.org/10.1002/2014JA020587, 2015. 40

Kramer, O.: K-Nearest Neighbors, pp. 13–23, Springer Berlin Heidelberg, Berlin, Heidelberg, https://doi.org/10.1007/978-3-642-38652-7_2, URL https://doi.org/10.1007/978-3-642-38652-7_2, 2013. 74

Laundal, K. M. and Richmond, A. D.: Magnetic Coordinate Systems, , 206, 27–59, https://doi.org/10.1007/s11214-016-0275-y, 2017. 68, 70

Lin, R. L., Zhang, X. X., Liu, S. Q., Wang, Y. L., and Gong, J. C.: A three-dimensional asymmetric magnetopause model, Journal of Geophysical Research (Space Physics), 115, A04207, https://doi.org/10.1029/2009JA014235, 2010. 51, 65

Liu, Z. Q., Lu, J. Y., Wang, C., Kabin, K., Zhao, J. S., Wang, M., Han, J. P., Wang, J. Y., and Zhao, M. X.: A three-dimensional high Mach number asymmetric magnetopause model from global MHD simulation, Journal of Geophysical Research (Space Physics), 120, 5645–5666, https://doi.org/10.1002/2014JA020961, 2015. 65

McFadden, J. P., Carlson, C. W., Larson, D., Ludlam, M., Abiad, R., Elliott, B., Turin, P., Marckwordt, M., and Angelopoulos, V.: The THEMIS ESA Plasma Instrument and In-flight Calibration, Scientific Studies of Reading, 141, 277–302, https://doi.org/10.1007/s11214-008-9440-2, 2008. 45

Merka, J., Szabo, A., Narock, T. W., King, J. H., Paularena, K. I., and Richardson, J. D.: A comparison of IMP 8 observed bow shock positions with model predictions, Journal of Geophysical Research (Space Physics), 108, 1077, https://doi.org/10.1029/2002JA009384, 2003. 49, 60

Moore, T. E., Fok, M. C., and Chandler, M. O.: The dayside reconnection X line, Journal of Geophysical Research (Space Physics), 107, 1332, https://doi.org/10.1029/2002JA009381, 2002. 40

Nguyen, G., Aunai, N., Michotte de Welle, B., Jeandet, A., Lavraud, B., and Fontaine, D.: Massive Multi-Mission Statistical Study and Analytical Modeling of the Earth's Magnetopause: 1. A Gradient Boosting Based Automatic Detection of Near-Earth Regions, Journal of Geophysical Research (Space Physics), 127, e29773, https://doi.org/10.1029/2021JA029773, 2022. 49, 50, 51, 52, 61

Olshevsky, V., Khotyaintsev, Y. V., Lalti, A., Divin, A., Delzanno, G. L., Anderzén, S., Herman, P., Chien, S. W. D., Avanov, L., Dimmock, A. P., and Markidis, S.: Automated Classification of Plasma Regions Using 3D Particle Energy Distributions, Journal of Geophysical Research (Space Physics), 126, e29620, https://doi.org/10.1029/2021JA029620, 2021. 49

Parker, E. N.: Dynamics of the Interplanetary Gas and Magnetic Fields., The Astrophysical Journal, 128, 664, https://doi.org/10.1086/146579, 1958. 73

Petrinec, S. M.: On the Magnetic Field Configuration of the Magnetosheath, Terrestrial, Atmospheric and Oceanic Sciences, 24, 265, https://doi.org/10.3319/TAO.2012.10.17.02(SEC), 2013. 48, 57

Phan, T., Frey, H. U., Frey, S., Peticolas, L., Fuselier, S., Carlson, C., Rème, H., Bosqued, J. M., Balogh, A., Dunlop, M., Kistler, L., Mouikis, C., Dandouras, I., Sauvaud, J. A., Mende, S., McFadden, J., Parks, G., Moebius, E., Klecker, B., Paschmann, G., Fujimoto, M., Petrinec, S., Marcucci, M. F., Korth, A., and Lundin, R.: Simultaneous Cluster and IMAGE observations of cusp reconnection and auroral proton spot for northward IMF, , 30, 1509, https://doi.org/10.1029/2003GL016885, 2003. 40

Phan, T. D. and Paschmann, G.: The Magnetosheath Region Adjacent to the Dayside Magnetopause, Geophysical Monograph Series, 90, 115, https://doi.org/10.1029/GM090p0115, 1995. 48

Phan, T. D., Paschmann, G., Baumjohann, W., Sckopke, N., and Luehr, H.: The magnetosheath region adjacent to the dayside magnetopause: AMPTE/IRM observations, , 99, 121–142, https://doi.org/10.1029/93JA02444, 1994. 61

Pollock, C., Moore, T., Jacques, A., Burch, J., Gliese, U., Saito, Y., Omoto, T., Avanov, L., Barrie, A., Coffey, V., Dorelli, J., Gershman, D., Giles, B., Rosnack, T., Salo, C., Yokota, S., Adrian, M., Aoustin, C., Auletti, C., Aung, S., Bigio, V., Cao, N., Chandler, M., Chornay, D., Christian, K., Clark, G., Collinson, G., Corris, T., De Los Santos, A., Devlin, R., Diaz, T., Dickerson, T., Dickson, C., Diekmann, A., Diggs, F., Duncan, C., Figueroa-Vinas, A., Firman, C., Freeman, M., Galassi, N., Garcia, K., Goodhart, G., Guererro, D., Hageman, J., Hanley, J., Hemminger, E., Holland, M., Hutchins, M., James, T., Jones, W., Kreisler, S., Kujawski, J., Lavu, V., Lobell, J., LeCompte, E., Lukemire, A., MacDonald, E., Mariano, A., Mukai, T., Narayanan, K., Nguyan, Q., Onizuka, M., Paterson, W., Persyn, S., Piepgrass, B., Cheney, F., Rager, A., Raghuram, T., Ramil, A., Reichenthal, L., Rodriguez, H., Rouzaud, J., Rucker, A., Saito, Y., Samara, M., Sauvaud, J. A., Schuster, D., Shappirio, M., Shelton, K., Sher, D., Smith, D., Smith, K., Smith, S., Steinfeld, D., Szymkiewicz, R., Tanimoto, K., Taylor, J., Tucker, C., Tull, K., Uhl, A., Vloet, J., Walpole, P., Weidner, S., White, D., Winkert, G., Yeh, P. S., and Zeuch, M.: Fast Plasma Investigation for Magnetospheric Multiscale, Scientific Studies of Reading, 199, 331–406, https://doi.org/10.1007/s11214-016-0245-4, 2016. 47

Pudovkin, M. I., Besser, B. P., Zaitseva, S. A., Lebedeva, V. V., and Meister, C. V.: Magnetic barrier in case of a southward interplanetary magnetic field, Journal of Atmospheric and Solar-Terrestrial Physics, 63, 1075–1083, https://doi.org/10.1016/S1364-6826(01)00023-2, 2001. 61

Rème, H., Aoustin, C., Bosqued, J. M., Dand ouras, I., Lavraud, B., Sauvaud, J. A., Barthe, A., Bouyssou, J., Camus, T., Coeur-Joly, O., Cros, A., Cuvilo, J., Ducay, F., Garbarowitz, Y., Medale, J. L., Penou, E., Perrier, H., Romefort, D., Rouzaud, J., Vallat, C., Alcaydé, D., Jacquey, C., Mazelle, C., D'Uston, C., Möbius, E., Kistler, L. M., Crocker, K., Granoff, M., Mouikis, C., Popecki, M., Vosbury, M., Klecker, B., Hovestadt, D., Kucharek, H., Kuenneth, E., Paschmann, G., Scholer, M., Sckopke (), N., Seidenschwang, E., Carlson, C. W., Curtis, D. W., Ingraham, C., Lin, R. P., McFadden, J. P., Parks, G. K., Phan, T., Formisano, V., Amata, E., Bavassano-Cattaneo, M. B., Baldetti, P., Bruno, R., Chionchio, G., di Lellis, A., Marcucci, M. F., Pallocchia, G., Korth, A., Daly, P. W., Graeve, B., Rosenbauer, H., Vasyliunas, V., McCarthy, M., Wilber, M., Eliasson, L., Lundin, R., Olsen, S., Shelley, E. G., Fuselier, S., Ghielmetti, A. G., Lennartsson, W., Escoubet, C. P., Balsiger, H., Friedel, R., Cao, J. B., Kovrazhkin, R. A., Papamastorakis, I., Pellat, R., Scudder, J., and Sonnerup, B.: First multispacecraft ion measurements in and near the Earth's magnetosphere with the identical Cluster ion spectrometry (CIS) experiment, Annales Geophysicae, 19, 1303–1354, https://doi.org/10.5194/angeo-19-1303-2001, 2001. 42

Rème, H., Dandouras, I., Aoustin, C., Bosqued, J. M., Sauvaud, J. A., Vallat, C., Escoubet, P., Cao, J. B., Shi, J., Bavassano-Cattaneo, M. B., Parks, G. K., Carlson, C. W., Pu, Z., Klecker, B., Moebius, E., Kistler, L., Korth, A., and Lundin, R.: The HIA instrument on board the Tan Ce 1 Double Star near-equatorial spacecraft and its first results, Annales Geophysicae, 23, 2757–2774, URL https://hal.archives-ouvertes.fr/hal-00329440, 2005. 43, 44

Retinò, A., Bavassano Cattaneo, M. B., Marcucci, M. F., Vaivads, A., André, M., Khotyaintsev, Y., Phan, T., Pallocchia, G., Rème, H., Möbius, E., Klecker, B., Carlson, C. W., McCarthy, M., Korth, A., Lundin, R., and Balogh, A.: Cluster multispacecraft observations at the high-latitude duskside magnetopause: implications for continuous and component magnetic reconnection, Annales Geophysicae, 23, 461–473, https://doi.org/10.5194/angeo-23-461-2005, 2005. 40

Russell, C. T., Anderson, B. J., Baumjohann, W., Bromund, K. R., Dearborn, D., Fischer, D., Le, G., Leinweber, H. K., Leneman, D., Magnes, W., Means, J. D., Moldwin, M. B., Nakamura, R., Pierce, D., Plaschke, F., Rowe, K. M., Slavin, J. A., Strangeway, R. J., Torbert, R., Hagen, C., Jernej, I., Valavanoglou, A., and Richter, I.: The Magnetospheric Multiscale Magnetometers, Scientific Studies of Reading, 199, 189–256, https://doi.org/10.1007/s11214-014-0057-3, 2016. 47

Samsonov, A. A., Sibeck, D. G., Dmitrieva, N. P., Semenov, V. S., Slivka, K. Y., Å afránkova, J., and Němeček, Z.: Magnetosheath Propagation Time of Solar Wind Directional Discontinu-

ities, Journal of Geophysical Research (Space Physics), 123, 3727–3741, https://doi.org/10.1029/2017JA025174, 2018. 65

Shue, J.-H.: Dependence of the Ionospheric Convection Pattern on the Conductivity and the Southward IMF., Ph.D. thesis, University of Alaska, Fairbanks, 1993. 58

Shue, J. H., Chao, J. K., Fu, H. C., Russell, C. T., Song, P., Khurana, K. K., and Singer, H. J.: A new functional form to study the solar wind control of the magnetopause size and shape, , 102, 9497–9512, https://doi.org/10.1029/97JA00196, 1997. 65

Shue, J. H., Song, P., Russell, C. T., Steinberg, J. T., Chao, J. K., Zastenker, G., Vaisberg, O. L., Kokubun, S., Singer, H. J., Detman, T. R., and Kawano, H.: Magnetopause location under extreme solar wind conditions, JGR, 103, 17 691–17 700, https://doi.org/10.1029/98JA01103, 1998. 50, 56, 60, 61, 65, 67, 70

Sibeck, D. G., Lopez, R. E., and Roelof, E. C.: Solar wind control of the magnetopause shape, location, and motion, , 96, 5489–5495, https://doi.org/10.1029/90JA02464, 1991. 56

Spreiter, J. R., Alksne, A. Y., and Abraham-Shrauner, B.: Theoretical proton velocity distributions in the flow around the magnetosphere, , 14, 1207–1220, https://doi.org/10.1016/0032-0633(66)90033-X, 1966. 57

Trattner, K. J., Mulcock, J. S., Petrinec, S. M., and Fuselier, S. A.: Location of the reconnection line at the magnetopause during southward IMF conditions, , 34, L03108, https://doi.org/10.1029/2006GL028397, 2007. 40

Trattner, K. J., Petrinec, S. M., and Fuselier, S. A.: The Location of Magnetic Reconnection at Earth's Magnetopause, , 217, 41, https://doi.org/10.1007/s11214-021-00817-8, 2021. 57

Tsyganenko, N. A. and Stern, D. P.: Modeling the global magnetic field of the large-scale Birkeland current systems, , 101, 27 187–27 198, https://doi.org/10.1029/96JA02735, 1996. 70, 71

Verigin, M. I., Tátrallyay, M., Erdős, G., and Kotova, G. A.: Magnetosheath Interplanetary medium reference frame: Application for a statistical study of mirror type waves in the terrestrial plasma environment, Advances in Space Research, 37, 515–521, https://doi.org/10.1016/j.asr.2005.03.042, 2006. 48

Šafránková, J., Přech, L., Němeček, Z., and Sauvaud, J. A.: Density profile in the magnetosheath adjacent to the magnetopause, Advances in Space Research, 30, 1693–1703, https://doi.org/10.1016/S0273-1177(02)00438-6, 2002. 57

Wang, Y., Sibeck, D. G., Merka, J., Boardsen, S. A., Karimabadi, H., Sipes, T. B., Šafránková, J., Jelínek, K., and Lin, R.: A new three-dimensional magnetopause model with a support vector regression machine and a large database of multiple spacecraft observations, Journal of Geophysical Research (Space Physics), 118, 2173–2184, https://doi.org/10.1002/jgra.50226, 2013. 48, 60, 65

Zhang, H., Fu, S., Pu, Z., Lu, J., Zhong, J., Zhu, C., Wan, W., and Liu, L.: Statistics on the Magnetosheath Properties Related to Magnetopause Magnetic Reconnection, , 880, 122, https://doi.org/10.3847/1538-4357/ab290e, 2019. 48, 61, 68, 71

Chapter 3

Magnetic Draping in the Magnetosheath

Contents

3.1 Introduction

The angular shear of magnetic field lines perhaps is the most important aspect of a reconnecting system. The magnetopause itself, is mainly defined as the boundary where the magnetic field is sheared between its orientation in magnetosphere, and the draped IMF in the magnetosheath. The main source of variability in the magnetospheric field is the temporal evolution of the dipole tilt due to the Earth rotation and its revolution around the Sun. This effect is rather well accounted for in analytical models such as Tsyganenko and Stern [1996]. On the other hand, the IMF in the magnetosheath is much more complex. First, the interplanetary medium is inhomogeneous and non steady, then, the IMF drapes around the magnetosphere in a non-trivial way. The focus of this chapter thus consists in better characterizing and understanding the way the IMF drapes around the Earth's magnetopause, in order to better constrain this aspect of the boundary condition to magnetic reconnection therein.

Magnetic field draping is a universal phenomenon in highly conducting magnetized astrophysical plasmas. It is known to occur around induced [Bertucci et al., 2011; Delva et al., 2017; McComas et al., 1986; Rong et al., 2014; Zhang et al., 2022] and intrinsic planetary magnetospheres [Behannon and Fairfield, 1969; Fairfield, 1967; Kaymaz et al., 1996], comets [Koenders et al., 2016; Reidler et al., 1986], solar ejecta in the IMF [Jones et al., 2002; Kaymaz and Siscoe, 2006; McComas et al., 1988], the heliosphere in the interstellar field [Opher et al., 2007; Pogorelov et al., 2021], galaxies in the intergalactic field [Pfrommer and Dursi, 2010]. Magnetic field draping is key in understanding how plasma environments couple with their surroundings. In particular, it is of pivotal importance in determining the location, triggering and efficiency of magnetic reconnection at magnetic boundaries [Cassak and Fuselier, 2016; Trattner et al., 2021].

The closest example of magnetic field draping is found in the Earth's magnetosheath, where the IMF drapes around the magnetopause. This region thus constitutes a unique observatory for in-situ measurements of this ubiquitous plasma process. Predicted theoretically from the transport of field lines in gas dynamics models [Spreiter et al., 1966], the magnetic draping was first evidenced in the magnetosheath the following couple of years [Behannon and Fairfield, 1969; Fairfield, 1967] in spacecraft in-situ measurements, although only a few data points were available at the time. Increasingly more detailed observations were subsequently performed [Coleman, 2005; Crooker et al., 1985; Kaymaz, 1998; Kaymaz et al., 1992; Longmore et al., 2006; Ohtani and kokubun, 1991; Petrinec, 2016], confirming the draping of the IMF and comparing the orientation of the magnetic field locally measured in the magnetosheath, to that predicted by models. These observations were, however, restricted to coarse angular sectors of the IMF orientations and to particular orbital planes. Our current understanding of how the magnetic field drapes around the magnetosphere in a global and three-dimensional manner and as a function of the IMF orientation thus only comes from analytical [Kallio and Koskinen, 2000; Kobel and Fluckiger, 1994; Vandas and Romashets, 2019] and numerical modeling [Kaymaz, 1998; Turc et al., 2014]. Half a century after the first models of the magnetic field draping in the magnetosheath [Spreiter et al., 1966], there is still so far no consistent equivalent from a purely observational standpoint. This is the goal of this study.

This Chapter offers a global and detailed three-dimensional statistical representation of the magnetic field draping around the magnetosphere, as a function of the IMF orientation, using only in-situ measurements. The statistical representation of the observed draping will be compared to the one obtained by a magnetostatic model [Kobel and Fluckiger, 1994]. This comparison is made not because such a model can be considered as realistic as, say, the result of a global MHD numerical model. But, assuming the draping occurs in vacuum, this model offers an interesting contrast we use to emphasize the key role played by the magnetosheath flow in structuring the draping for various IMF orientations. Moreover, owing to its relative simplicity, this draping model is broadly used by researchers and has been at the root of studies of the dynamics of cosmic dust [Juhász and Horányi, 1999], spacecraft fine debris [Juhász and Horányi, 1997] and many other plasma processes occurring not only in the Earth's magnetosheath (e.g. Génot et al. [2011]), but also in that of other planets such as Mercury [Schmid et al., 2021a,b], Jupiter [Masters, 2017], Saturn Su-

laiman et al. [2014], Uranus [Masters, 2014] and Neptune [Masters, 2015]. It is, furthermore, a key ingredient in how researchers nowadays predict where magnetic reconnection may occur at the magnetopause for a given upstream IMF orientation [Trattner et al., 2021]. Very recently, the same analytical approach has been undertaken with more realistic boundary geometries [Romashets and Vandas, 2019; Vandas and Romashets, 2019] and compared to THEMIS observations [Vandas et al., 2020], but still without coupling the magnetic field to the flow.

Section 3.2 describes the methodology used to reconstruct the magnetic draping in three dimensions. Section 3.3 compares the draping produced using in-situ measurements to that based on Kobel and Fluckiger [1994]'s magnetostatic model. Finally, in Section 3.4, we demonstrate quantitatively that the detailed structure of the observed draping results from the magnetic field being frozen in the deflected magnetosheath flow.

3.2 Method

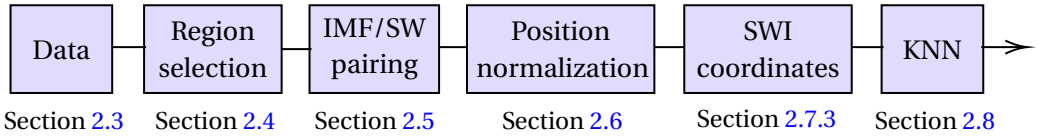

Figure 3.1: Overview of the global methodology detailed in Chapter 2.

Most of the processing pipeline used in this chapter corresponds to what is explained in Chapter 2. Before explaining in the following subsections the aspects specific to this chapter, let us first briefly recall the different steps of this global methodology, represented on Figure 3.1. Almost all magnetosheath measurements are identified using a trained Gradient Boosting Classifier [Nguyen et al., 2022] (see Section 2.4) from data collected by the Cluster, Double Star, THEMIS, and MMS missions (see Section 2.3). Reconstructing the magnetic draping as a function of the IMF orientation requires pairing each measurement with the properties of its causal IMF and solar wind using OMNI data [King and Papitashvili, 2005] and a transport method [Šafránková et al., 2002] (see Section 2.5). To obtain a fair spatial representation, the position of each data point relative to the bow shock and the magnetopause at the time of the measurement is estimated using Gradient Boosting Regression models of the boundaries, parameterized with solar wind and IMF conditions (see Section 2.6). Using these relative distances to the magnetopause and bow shock, all points are re-positioned between a standard couple of boundaries [Jelínek et al., 2012; Shue et al., 1998] parameterized with average solar wind conditions (i.e. dynamic pressure of 2nPa and $B_{z_{imf}}$ = 0 nT). Then all measurements are converted from GSM to SWI coordinates (see Section 2.7.3). Subsequently, the KNN algorithm is used to compute the distance-weighted average of the K closest measurements to a desired position (see Section 2.8). The KNN is applied to a meshed surface obtained with the magnetopause model [Shue et al., 1998] parameterized with average solar wind and IMF conditions. This enables the determination of spatial distributions for quantities, such as, in this study, the magnetic field B_x component.

3.2.1 From discrete scattered samples to 3D continuous magnetic field lines

At this point of the processing pipeline, we have a collection of measurements at discrete positions scattered in a standard magnetosheath. We now need a method to construct field lines from this discrete collection of magnetic data points. Magnetic field lines can be obtained by three-dimensional integration, using a KNN algorithm (see Section 2.8) to locally estimate the magnetic field components from the discrete samples, at each step of the integration. In practice we use the Backward Differentiation Formula (BDF) implicit integration solver.

The draping we aim at constructing assumes the IMF entirely slips on the magnetopause and no reconnection occurs. In practice, each magnetic field measurement, in the magnetosheath and magnetosphere, has a small component normal to the meshed magnetopause surface. Such

a small normal component may be due to magnetic reconnection. But more probably, it arises from the local inconsistency between the smooth magnetopause surface we use for representation purposes, and the real magnetopause close to which measurements were made. A small normal component can also arise from the statistical noise produced during the position normalization process (Section 2.6). Consequently, the normal components of the magnetic field are gradually decreased, within a distance of approximately 0.30 Re from the magnetopause, until the magnetic field becomes tangential to the boundary surface, as described in Equation 3.1. $\mathbf{B}_{\text{integration}}$, $\mathbf{B}_{\text{KNN}}$, r, r_{mp}, and $\mathbf{N}_{\text{mp}}$ correspond to the magnetic field used in the field lines integration, the magnetic field values predicted by the KNN (K=7,500 or 10,000 depending on the size of the considered subset), the positional radius, the magnetopause radius, and the unit vector normal to the magnetopause surface, respectively.

$$\mathbf{B}_{\text{integration}} = \mathbf{B}_{\text{KNN}} - \left(0.5\left(1 - \tanh\left(\frac{(r - r_{\text{mp}}) - 0.15}{0.1}\right)\right)\right)(\mathbf{B}_{\text{KNN}} \cdot \mathbf{N}_{\text{mp}})\mathbf{N}_{\text{mp}} \tag{3.1}$$

Finally, when a field line crosses the bow shock outwards, it is prolonged in the solar wind by a straight line inclined with respect to the X_{SWI} axis by an angle corresponding to the average value of the IMF cone angle θ_{co} (see Section 2.7.5) for the considered subset.

3.2.2 The magnetostatic model of Kobel and Fluckiger 1994

The Kobel and Fluckiger [1994] model can in principle be used to determine the magnetic field vector anywhere in our standard magnetosheath for comparison with the field reconstructed from observations. However, if used as is, the comparison would not be very fair, since the difference between the two not only stands in one being a model and the other measurements, but also in the fact that former is known everywhere given a specific IMF orientation, while the latter needs the whole repositioning procedure and a finite range of IMF orientations for statistical reasons. We therefore choose to compute the model at the position of measurements, with their paired IMF and solar wind conditions, to focus only on the difference arising from the model's assumptions. Annex B details how the model is designed and used to obtain a magnetic field value at a given position.

Therefore, for each selected magnetosheath data point:

1. compute the standoff distances (x_0 and x_1) predicted by the machine learning models of magnetopause and bow shock (Section 2.6.2) parametrized by the paired properties of the solar wind, IMF, and dipole tilt angle (Section 2.5).

2. Normalize the position of the data point between the confocal and parabolic approximation of the magnetopause and the bow shock determined with x_0 and x_1 (see Equation B.9 and method of Section 2.6).

3. Compute the magnetic field predicted by the Kobel and Fluckiger [1994] model using the normalized position, x_0, x_1, and the IMF components.

4. Normalize the position of all the points between the same pair of shock and magnetopause [Jelínek et al., 2012; Shue et al., 1998] parametrized by average solar wind and IMF (see Section 2.6).

5. Transformation from GSM to SWI coordinate system (see Section 2.7.3).

The amplitude of the magnetic field predicted by the Kobel and Fluckiger [1994] model depends on the positions of the magnetopause and bow shock, in particular of the thickness of the enclosed magnetosheath. Considering the regression models we have constructed to predict these boundaries' positions result in smaller errors than analytical models, we decided to use them in the computation of the parabolic and confocal approximations used in KF94.

Finally, the spatial distribution of the magnetostatic magnetic field and its field lines are estimated using the KNN as for the case of the in-situ measurements.

3.2.3 Time integration of the plasma flow lines

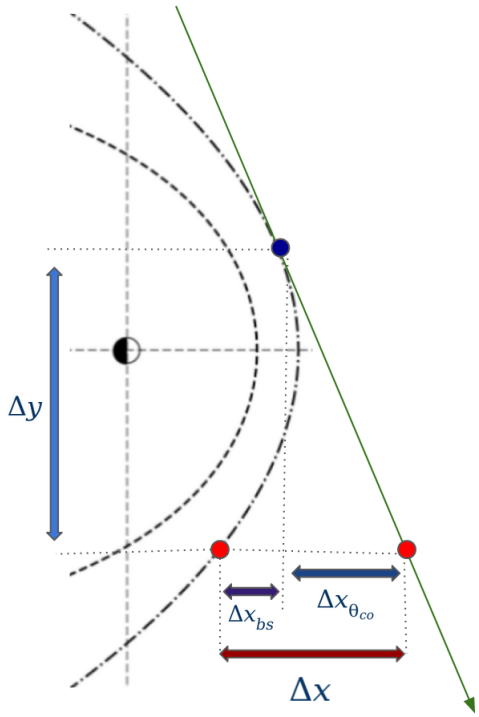

Figure 3.2: Determination of the integration time of the flow lines. The streamline is integrated from the blue point. This point is magnetically connected to the red point. The streamline is integrated during the time taken for the red point to reach the bow shock, estimated via Eq. 3.2 . $\Delta X_{co} = \Delta Y / \tan\theta_{co}$ is the distance produced by the inclination of the IMF in respect of the X axis and ΔX_{bs} is the additional distance produced by the shock's shape.

In this study, we aim to demonstrate that the specific geometry of the magnetic draping in the magnetosheath arises from the magnetic field lines being frozen in the plasma flow. This can also be considered as a sanity check proving our magnetic field lines are reconstructed correctly. To achieve this, we integrate a magnetic field line from an arbitrary location, such as the red point at the bow shock in Figure 3.2. We then determine the propagation duration Δt of fluid elements magnetically connected to this magnetic field line that entered the magnetosheath prior to the red point reaching the bow shock, such as the blue point. This duration Δt can be estimated with Equation 3.2 under two simple assumptions:

- The solar wind velocity is constant.
- The IMF orientation is steady.

$$\Delta t = \frac{\frac{\Delta Y}{\tan\theta_{co}} + \Delta X_{bs}}{V_{sw}} \tag{3.2}$$

In Equation 3.2, Δ_Y corresponds to the distance along the Y axis between the starting points of the magnetic field at the bow shock and the flow lines represented by the red and blue points in Figure 3.2. ΔX_{bs} is the distance along the X axis between those start points produced by the bow shock shape, as shown in Figure 3.2. θ_{co} corresponds to the median value of the IMF cone angle in the subset range chosen for a specific reconstruction. The solar wind velocity V_{sw} is equal to 1 because each magnetosheath velocity measurement is normalized by its causal solar wind speed.

Finally, we integrate plasma flow lines from various seed points on the bow shock like the blue point, for a time interval given by the Δt duration associated with their position, with the in-situ velocity measurements. The integration is perfomed the same way as for the magnetic field lines

(see Section 3.2.1). The KNN algorithm is thus used to predict the values of the velocity components at each step of the integration. Since all 45 million magnetosheath velocity measurements are used to determine the streamlines, the value in KNN is set to K= 45,000, which still allows the median distances of the considered K points to be lower than 0.5 Re.

The uncertainties of the flow lines are dominated by the dependence of Equation 3.2 to the IMF cone angle range being used. Therefore, the first and third quartiles of this angle range are used to calculate the longest and shortest integration times, respectively, and used to represent the uncertainty for the tip of the flow line.

3.3 Draping Structure: Model versus Measurements

The draping will now be reconstructed for a given IMF cone angle. We will split our analysis into three different ranges of IMF cone angle corresponding empirically to three significantly different structures of the draping on the dayside. Before delving into the results, it should be remained that in the SWI coordinates, the quasi-parallel side of the magnetosheath (i.e., the side where the orientation of the IMF is the most parallel to the normal to the bow shock surface) is always $Y_{SWI} > 0$, whereas the quasi-perpendicular side is found for $Y_{SWI} < 0$. In addition, by convention of the SWI system, the B_x and B_y components of the IMF are always positive, while the B_z is equal to zero.

3.3.1 Magnetic draping for large IMF cone angles

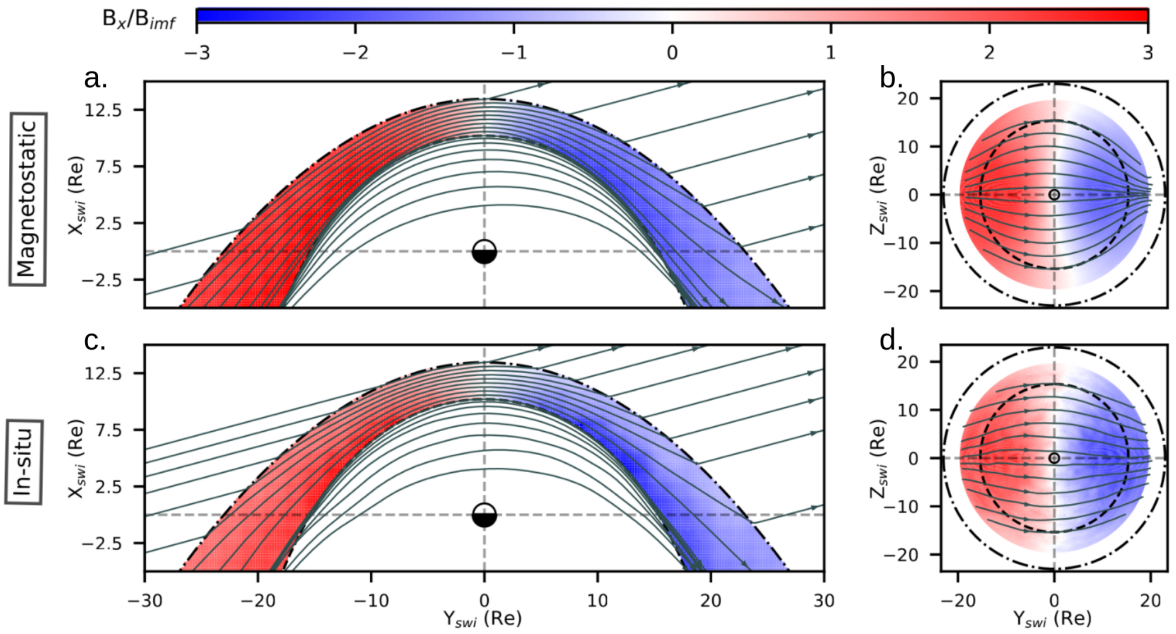

Figure 3.3: Large IMF cone angle draping corresponding to the subset of measurements falling within $70° \leq |\theta_{co}| \leq 80°$. Panels (**a**, **b**) and (**c**, **d**) correspond respectively to magnetostatic Kobel and Fluckiger [1994] and in-situ data magnetic field. The color maps correspond to B_x/B_{imf}. The grey arrowed lines correspond to the magnetic field lines integrated in 3D (see section 3.2.1). Panels a and c correspond to the data close to the $Z_{SWI} = 0$ plane. Panels **b** and **c** correspond to the data close to the magnetopause.

The first comparison between the draping reconstructed from in-situ measurements and the Kobel and Fluckiger [1994] model, shown in Figures 3.3 and 3.4, is made for the subset of the measurements associated with an IMF cone angle falling within the range $70° \leq |\theta_{co}| \leq 80°$. At such a large cone angle, the IMF is almost perpendicular to the Sun-Earth axis, as can be seen in the two left panels of Figure 3.3, representing the system in the plane containing the IMF. A quick glance at Figure 3.3 reveals that the draping obtained with the magnetostatic model (upper panels a and b) is strikingly similar to the one obtained from in-situ data (lower panels c and d)).

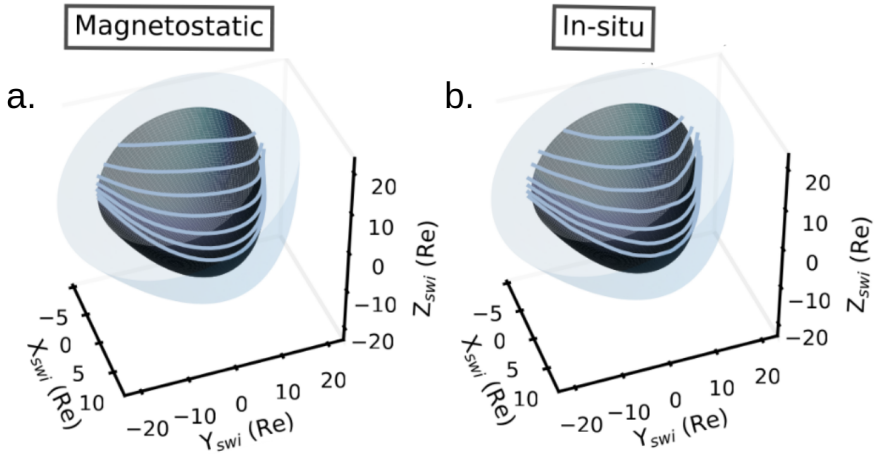

Figure 3.4: Large IMF cone angle draping, Subset $70° \leq |\theta_{co}| \leq 80°$. Panel a and b shows the three-dimension views of the magnetic field lines close to the magnetopause for the magnetostatic model [Kobel and Fluckiger, 1994] and in-situ magnetic field measurement, respectively.

Consistently, the B_x component, positive in the quasi-perpendicular side, goes through zero around the subsolar region and becomes negative in the quasi-parallel region. The amplitude of the B_x values are reasonably similar between the model and the observation. The in-situ values seem a bit lower than those of the model but it is unclear to what extent this difference is physical, considering the model does not account for the magnetic flux pile up on the magnetopause and primarily depends on the distance between the two boundaries. The field lines that appear to cross the magnetopause actually do not, but rise in the third dimension, above the $Z_{SWI} = 0$ plane to circumvent the magnetopause. This is better seen from the right panels which represent the field lines close to the magnetopause surface as seen from the Sun vantage point. Initially contained in the ($X_{SWI}Y_{SWI}$) plane upstream of the bow shock, the field lines bend in the Z_{SWI} direction to wrap the magnetopause. Figure 3.4 offer a complementary 3D view of the field lines close to the magnetopause. The great similarity between the modeled draping and the observed one hides that the former is only constrained by the boundary conditions at the shock and magnetopause boundaries while the latter also is constrained by the structure of the magnetosheath flow. When considered, these different constraints explain the subtle differences seen in this large IMF cone angle limit between lower and upper panels of Figure 3.3 such as the more pronounced equatorward convergence of field lines in the model (seen on panels b and d). These different constraints are at the root of a much more pronounced disagreement between the two draping patterns at smaller cone angles, as will be explained in the following.

In the model (resp. the in-situ measurements), field lines must meet the imposed IMF orientation at the bow shock and must be exactly (resp. almost) tangential to the magnetopause. In the magnetostatic case where no electrical current flows within the magnetosheath volume, the magnetic field lines wrap the magnetopause like paper wraps a candy and diverge from two singular points at the magnetopause along the normal to the shock where it is parallel to the IMF. Without any other constraint, field lines just diverge away from these two singularities as prescribed by the magnetic potential function. This behavior explains the convergence of the field lines easily seen on the two flanks if looked at from the Sun standpoint in panel b of Figure 3.3. In a perfect 90° IMF cone angle condition, the two singularities would be perfectly symmetric with respect to $Y_{SWI} = 0$. Here, however, the singularity in the quasi-parallel region is closer to the subsolar region due to the slight radial component of the IMF, resulting in slightly more pronounced apparent convergence of the field lines in the quasi-parallel region of Figure 3.3.b.

In contrast, magnetic field lines in reality must also comply with the frozen-in condition, imposing that magnetically connected solar wind fluid elements must remain so during the draping. The temporal aspect of the draping then becomes important, and in the large IMF cone angle limit, follows the schematic of Figure 3.5. Among the represented connected points, the red one

is the first to meet the shock surface. In the subsolar region, that element will be strongly decelerated while other connected points remain in motion at the solar wind speed. Because the IMF cone angle is large, connected fluid elements are not far apart from one another along the Sun-Earth axis. The element arrived at the shock in the subsolar region (red dot) is thus still lagging in the slow stagnation flow region when other connected elements make contact with the shock. Together with the curved shape of the magnetopause and shock, this gives the observed bow shape to the field line, reminiscent of the one obtained in the magnetostatic model. Field lines close to the magnetopause are deflected around it and thus also bend in the Z directions like in the model, as seen from the Sun vantage point in Figure 3.4.b. Coincidentally, field lines appear to converge more on the quasi-parallel side than in the quasi-perpendicular side as in the modeled draping. However, the reason here has nothing to do with topological singularities but is again found in the temporal sequence of the draping. Parts of the field lines that crossed the shock in the quasi-perpendicular region did so earlier than those in the quasi-parallel side. Consequently, they had more time to rise away from the $Z_{SWI} = 0$ plane and are thus found slightly more spread apart than their counterparts in the quasi-parallel side, but in a way that is slightly different than for the modeled field.

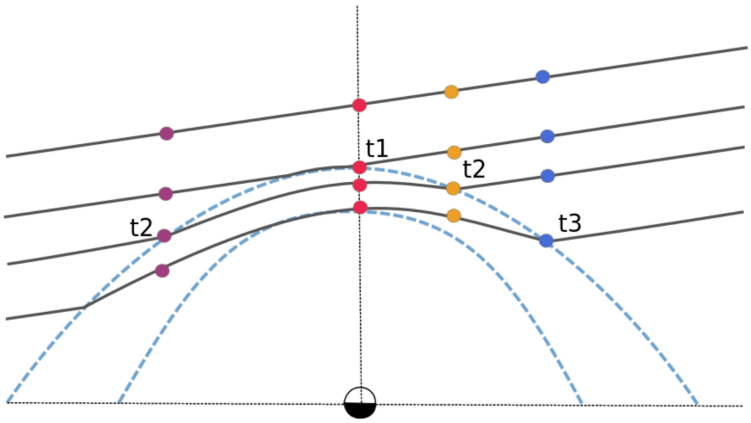

Figure 3.5: Schematic of the draping mechanism for the large cone angle regime. $t1$ to $t3$ represent the arrival time at the bow shock of the different fluid elements (purple, red, orange and blue points) connected by the same magnetic field line.

3.3.2 Magnetic draping for intermediate IMF cone angles

Differences between the model and data become more drastic as the IMF cone angle decreases. As it does so, the parallel shock region moves closer to the subsolar region. The previously discussed magnetic singularity of the model is now found closer to the subsolar region as well, as seen in Figure 3.6a. Clearly, this singularity is not seen in the in-situ measurements Figure 3.6.c. In contrast, all the field lines obtained from in-situ data, no matter how far from the subsolar region on the quasi-parallel side, eventually connect to more sunward regions. Consequently, B_x takes negative values all along the magnetopause on the quasi-parallel side, exactly as it did for large IMF cone angles, and thus opposed to what the model predicts. This important difference with the magnetostatic model again results from the magnetic field being frozen in the magnetosheath flow. Therefore, the magnetostatic model, which assumes a draping in vacuum, cannot account for this effect unlike MHD models [Alksne, 1967; Romanelli et al., 2014].

As before, the part of the field line entered in the subsolar region does not have the time to re-accelerate before other parts arrive at the shock in the quasi-parallel region. Field lines entering the quasi-parallel region must thus again connect to the subsolar region. It is interesting to note, however, that the field lines do not immediately turn towards the dayside as soon as they cross the shock as they do for the large IMF cone angle regime. The key is that for lower IMF cone angle,

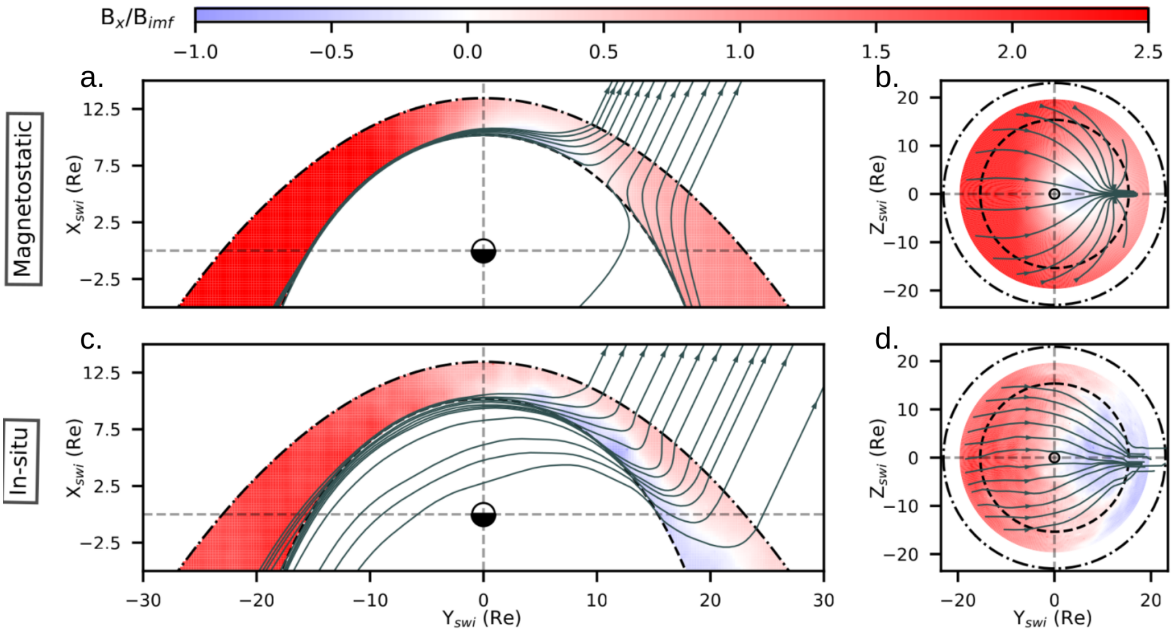

Figure 3.6: Intermediate IMF cone angle draping corresponding to the subset of measurements falling within $20° \leq |\theta_{co}| \leq 30°$. Panels (a, b) and (c, d) correspond respectively to magnetostatic Kobel and Fluckiger [1994] and in-situ data magnetic field. The color maps correspond to B_x/B_{imf}. The grey arrowed lines correspond to the magnetic field lines integrated in 3D (see section 3.2.1). Panels a and c correspond to the data close to the $Z_{SWI} = 0$ plane. Panels b and d correspond to the data close to the magnetopause.

connected elements are now further apart along X_{SWI} in the solar wind, as can be seen on Figure 3.8. They are close enough for the subsolar part of the line to still lag behind by the time they arrive at the shock. However, they are too far apart for elements entering the magnetosheath at any point of the quasi-parallel region to pass ahead of connected elements previously entered, as in the large cone angle regime. Upon crossing the bow shock in the quasi-parallel region, field lines thus must continue nightward over some distance before turning back towards the dayside. The sign of B_x is thus necessarily reversed across the magnetosheath in the quasi-parallel side, and an associated steady current sheet exists in the central magnetosheath over a significant portion of the dayside. This electrical current in the magnetosheath volume is the consequence of the transport of the magnetic field in the plasma flow.

As previously noticed in the regime of large IMF cone angles (panels b and d of Figure 3.3), an asymmetry is visible in the orientation of field lines between the quasi-parallel/perpendicular sides of the magnetosheath as viewed from the Sun (panels b and d of Figure 3.6). However, here the asymmetry is much more pronounced (Figure 3.6.b). In the modeled draping (Figure 3.6.b), this strong asymmetry simply relates to the singularity being now located closer to the subsolar region, towards which field lines must converge. In reality (Figure 3.6.d), the asymmetry still relates to the temporal aspect of the draping. For these lower IMF cone angles, connected fluid elements are more separated along X_{SWI}. The delay between their arrival at the shock in the quasi-parallel and quasi-perpendicular is thus significantly longer. As a result, field lines in the quasi-perpendicular region have a much longer time to leave the plane $Z = 0$, but they need to remain connected to parts arrived near $Z_{SWI} = 0$, leading to the observed asymmetry. The 3D plots on the rightmost panels offer a clear complementary overview of the fundamental difference between the two draping patterns.

3.3.3 Magnetic draping for small IMF cone angles

An important question at this point is to what extent the model and data keep exhibiting these distinct patterns as the IMF cone angle decreases even further down to zero. For symmetry reasons, it is clear that for an exactly radial IMF, field lines must spread equally around from the subsolar

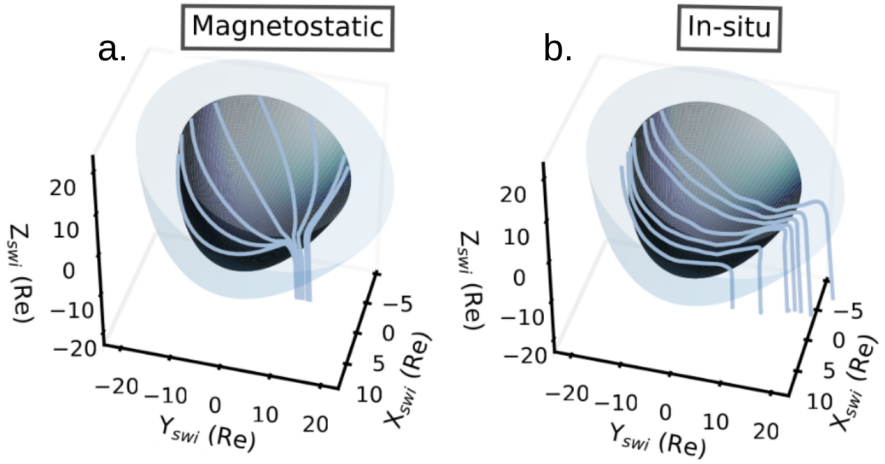

Figure 3.7: Intermediate IMF cone angle draping. Subset $20° \leq |\theta_{co}| \leq 30°$. Panel a and b shows the three-dimension views of the magnetic field lines close to the magnetopause for the magnetostatic model [Kobel and Fluckiger, 1994] and in-situ magnetic field measurement, respectively.

point. In both the model and data $\theta_{co} = 0$ must thus lead to a null point in that region, as it does only for the model for other IMF orientations on the quasi-parallel side. It is unclear at this point, however, whether data only shows this divergent pattern for a zero degree IMF cone angle or not.

The answer is clearly seen on Figure 3.9, which represents both modeled and observed draping for a very small but non-zero IMF cone angle. In that regime, it is unsurprising to see that the modeled draping only differs from previous ones by the position of the magnetic singularity, now much closer to the subsolar point. It is, however, interesting to notice that the observed draping now also exhibits a similar structure, with an apparent divergence of the field lines originating approximately from the same location as in the model.

It can be noticed that the pattern obtained with in-situ data (e.g. 3.9.d) within this low IMF cone angle regime is very noisy, due to the limited amount of data (see Figure 2.26) and the likely presence of enhanced fluctuations in that region downstream of the foreshock. However, the results appear again consistent with the dominant effect of the magnetosheath flow in which the magnetic field is frozen, and in particular with the temporal aspect of the draping, represented in Figure 3.11. For such a low, yet non-zero, IMF cone angle, connected fluid elements are now so far from each other along X_{SWI} that their arrival time at the shock is significantly longer than the time it takes for the red element to leave the flow stagnation region. The part of the field line entering the subsolar region thus no longer acts as a bottleneck as it did for the two preceding regimes. Fluid elements arriving at the shock in the quasi-parallel region ($Y_{SWI} \geq 0$) are now connected to elements that have traveled a long distance in the magnetosheath and are located much further nightward. As a result, the draping pattern is again close to the one obtained in the model, since like in the large cone angle regime, the magnetosheath flow does not lead to the existence of a current sheet in the magnetosheath volume, which the model ignores.

Although the model and data representations broadly agree again in this very low IMF cone angle regime, some subtle differences still reveal that the magnetic field is frozen in the flow in reality while the modeled field ignores this constraint. The field lines obtained from in-situ data (Figure 3.9.c) in the quasi-parallel region indeed appear to go back towards the magnetopause, consistently with the idea that they should still remain connected to their previously entered counterpart in the quasi-perpendicular side. In contrast, the magnetostatic field lines (Figure 3.9.a), ignoring the frozen-in constraint, have a completely uncorrelated behavior on both side of the singularity. This difference in behavior between the magnetostatic model and the in-situ measurements can also be seen in the 3D representation of the magnetic field lines in Figure 3.10.

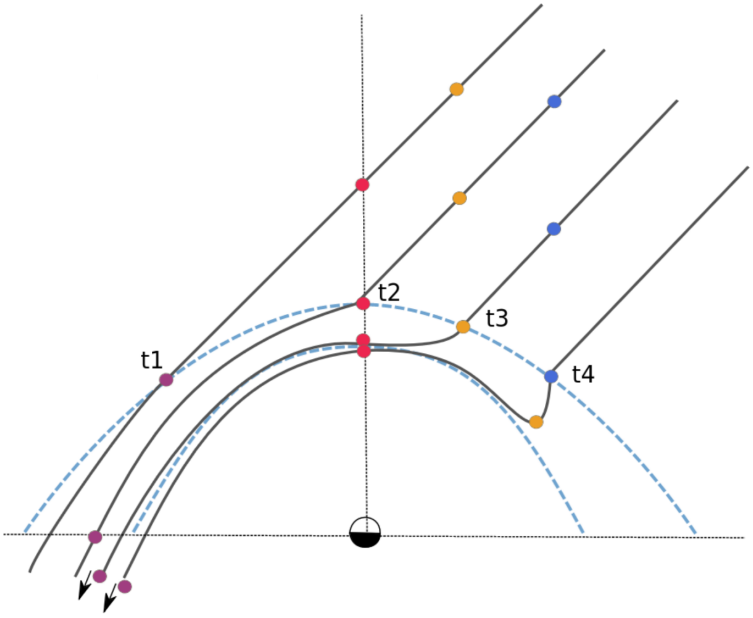

Figure 3.8: Schematic of the draping mechanism for the intermediate IMF cone angle regimes. $t1$ to $t4$ represent the arrival time at the bow shock of the different fluid elements (purple, red, orange and blue points) connected by the same magnetic field line.

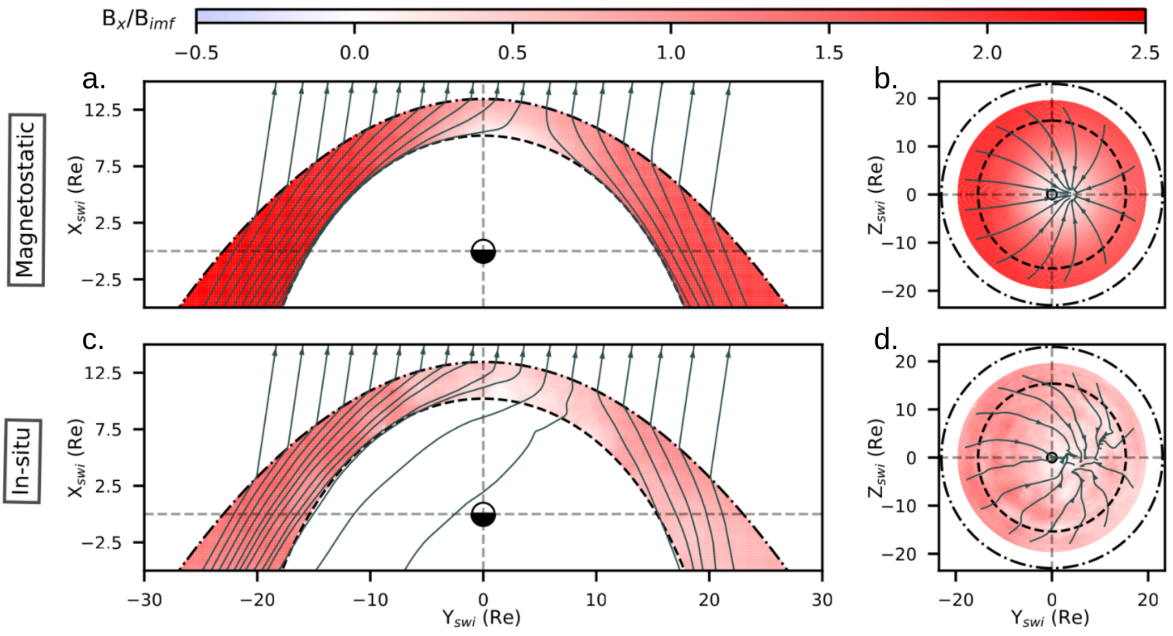

Figure 3.9: Small IMF cone angle draping corresponding to the subset of measurements falling within $0° \leq |\theta_{co}| \leq 12.5°$. Panels (a, b) and (c, d) correspond respectively to magnetostatic Kobel and Fluckiger [1994] and in-situ data magnetic field. The color maps correspond to B_x/B_{imf}. The grey arrowed lines correspond to the magnetic field lines integrated in 3D (see section 3.2.1). Panels a and c correspond to the data close to the $Z_{SWI} = 0$ plane. Panels b and d correspond to the data close to the magnetopause.

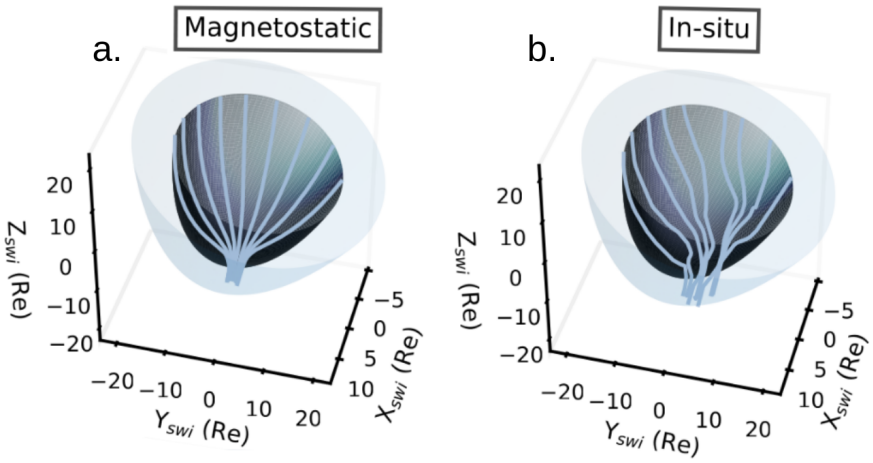

Figure 3.10: Small IMF cone angle draping. Subset $0° \leq |\theta_{co}| \leq 12.5°$. Panel a and b shows the three-dimension views of the magnetic field lines close to the magnetopause for the magnetostatic model [Kobel and Fluckiger, 1994] and in-situ magnetic field measurement, respectively.

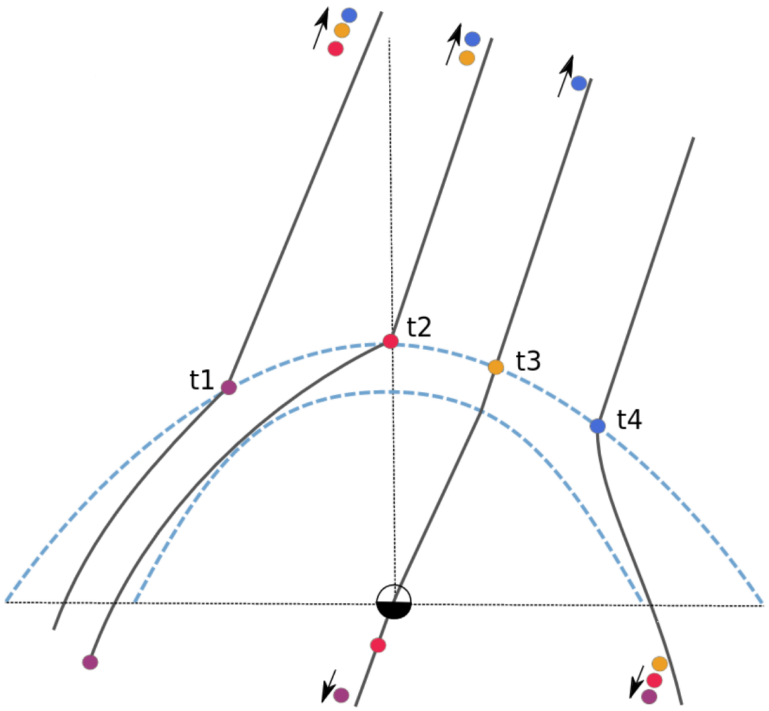

Figure 3.11: Schematic of the draping mechanism for the low IMF cone angle regime. $t1$ to $t4$ represent the arrival time at the bow shock of the different fluid elements (purple, red, orange and blue points) connected by the same magnetic field line.

3.4 Role of the Magnetosheath Flow in Structuring the Draping

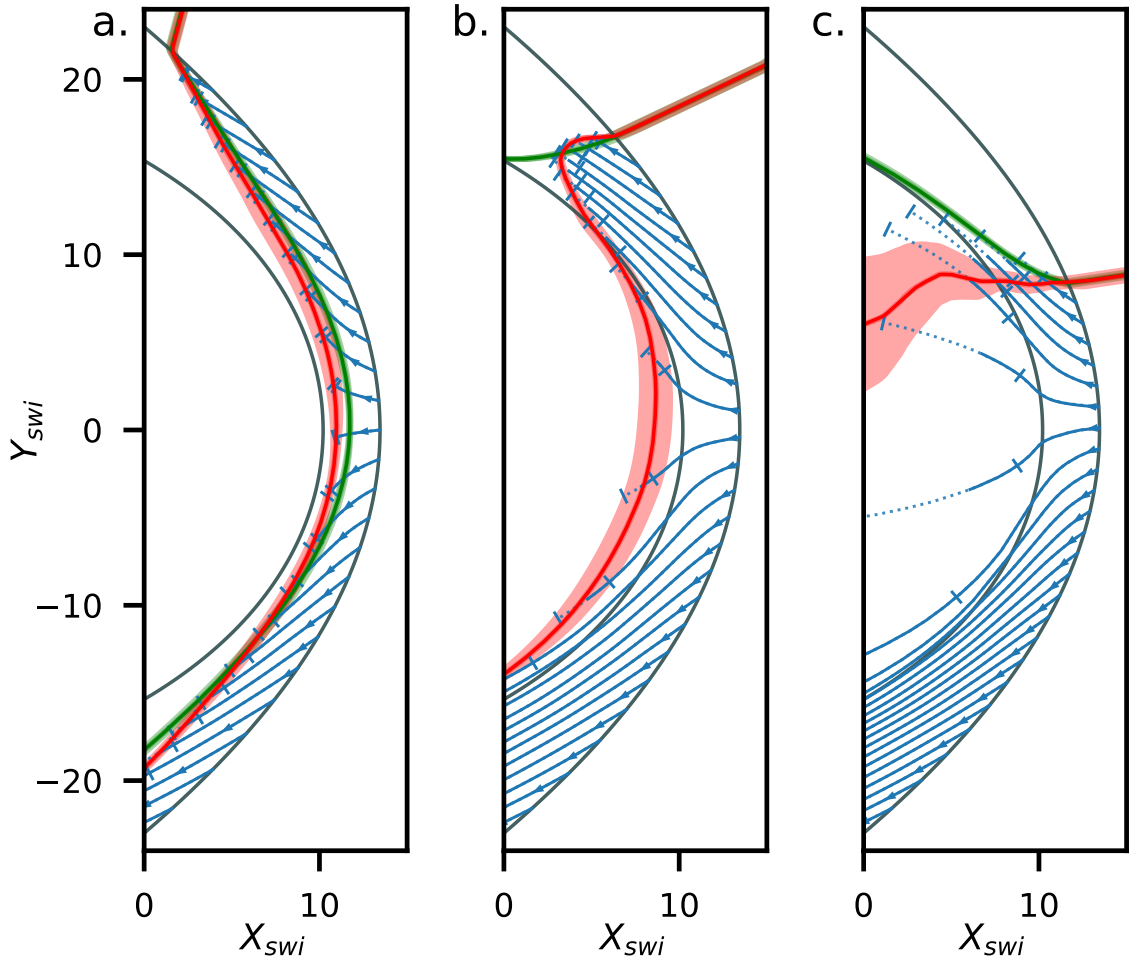

Figure 3.12: Quantitative estimate of the flux freezing condition. Panels a, b and c are associated with the large, intermediate and small IMF cone angle regimes, respectively. The red and green lines represent the magnetic field lines obtained from in-situ data and the magnetostatic model Kobel and Fluckiger [1994], respectively. The uncertainty on the position of these magnetic field lines is represented with the shaded area and is determined by the integrating 1500 magnetic field lines with starting points in a sphere of 0.5 Re of diameter. The solid blue lines correspond to the plasma streamlines integrated in 3D with in-situ measurements of the velocity (see 3.2.3). The error bars are determined for each line by calculating the integration times corresponding to the first and third quartile of the distribution of the IMF cone angle in each subset.

Previous figures gave us a qualitative and consistent picture of the importance of the frozen-in behavior for understanding the structure of the field line draping around the magnetopause. The following analysis now tests this interpretation in a more quantitative way. We focus on Figure 3.12, where each panel represents the dayside magnetosphere in the ($X_{SWI}Y_{SWI}$) plane for each of the three draping regimes previously identified. Each panel shows green and red magnetic field lines, obtained from the magnetostatic model and in-situ data, respectively. Ion flow streamlines, obtained from in-situ data in a similar way as for the magnetic field, are also represented. Each line is again the result of a three-dimensional integration. The red and green magnetic field lines are chosen to intersect the bow shock at an arbitrary but identical position, located in the quasi-parallel side of the system. Knowing the point at which the magnetic field line intersects the bow shock, the IMF cone angle, and given a solar wind velocity assumed steady, it is easy to compute the time delay between the time of the representation and that at which the field line crossed the bow shock at any other point corresponding to the time during which it has propagated into the

magnetosheath (see Section 3.2.3). Multiple points are thus chosen on the bow shock as starting points of flow lines.

The three-dimensional flow lines, integrated during the time delay associated to their starting point, stop right on top of the magnetic field line obtained from data for the large and intermediate IMF cone angle regimes (panels a and b of Figure 3.12), as expected from the frozen-in condition. The agreement is remarkable, considering that the integration time only assumes a constant solar wind velocity, a steady IMF orientation, and, above all, knowing that the magnetic field and velocity are two independent in-situ measurements. The flow line integration also agrees better with the magnetic field data than with that of the model in the large cone angle one, despite their very close behavior. This analysis clearly confirms previous qualitative interpretations in each of the IMF cone angle regimes. In the very IMF low cone angle limit (Figure 3.12.c), the results remain consistent, even if the scarcity of the data increases a lot the uncertainty associated with the field line integration. In addition, the large delay between arrival times at the shock, of the different part of the magnetic field line, leaves room for many processes to invalidate the steady state assumption our study is based on.

3.5 Conclusion

It has been known for decades that the interplanetary magnetic field drapes around the magnetosphere of the Earth as it crosses the bow shock. However, until now, only global MHD numerical models have provided a complete, global and three-dimensional structure of the draping for a given IMF orientation. These numerical results have so far remained unchallenged by observations. Through the use of innovative machine learning based data processing, this study offers such a global view from a purely observational standpoint. To emphasize the role of the magnetosheath flow, the observed draping is compared to that predicted by the magnetostatic model of Kobel and Fluckiger [1994], where the plasma is absent, and therefore the frozen-in constraint irrelevant. For large ($|\theta_{co}| > 45° \pm 5°$) or small ($12.5° \pm 2.5° < |\theta_{co}|$) IMF cone angles, the global draping is found to be qualitatively consistent with a magnetostatic draping assuming no current in the magnetosheath volume [Kobel and Fluckiger, 1994]. In contrast, data clearly and fundamentally disagree with the magnetostatic draping in the intermediate cone angle regime ($12.5° \pm 2.5° < |\theta_{co}| < 45.0° \pm 5°$) and angular deviations can be as high as about 180° in some portions of the quasi-parallel magnetosheath. In the data, field lines fold onto the magnetopause surface and are constrained to remain frozen in solar wind fluid elements. This folding is associated to a large scale current sheet at mid-depth in the quasi-parallel magnetosheath. This scenario is further quantitatively validated by mapping magnetic field lines with the 3D integration of the independently measured flow velocity. The detailed structure of the magnetic field draping, shown in our study to be intrinsically linked to the plasma flow in the magnetosheath, constitutes the immediate boundary condition for the magnetosphere system. It is in particular relevant to where magnetic reconnection occurs and operate, and thus how the Earth system couples to its environment. Our study also shows how having decades of data from multiple missions enables the assessment of global yet detailed and quantitative properties of the Earth magnetosphere despite the fundamentally local character of in-situ measurements. Although considerably less data exists, these results are also relevant to the case of other planets and obstacles to magnetized plasma flows.

This chapter presents the first significant outcome of this thesis work, demonstrating the effectiveness of the employed methodology and paving the way for further research in the magnetosheath volume and in the vicinity of the magnetopause.

3.6 Bibliography

Alksne, A. Y.: The steady-state magnetic field in the transition region between the magnetosphere and the bow shock, , 15, 239–245, https://doi.org/10.1016/0032-0633(67)90192-4, 1967. 90

Behannon, K. W. and Fairfield, D. H.: Spatial variations of the magnetosheath magnetic field, Planetary and Space Science, 17, 1803–1816, https://doi.org/10.1016/0032-0633(69)90056-7, 1969. 84

Bertucci, C., Duru, F., Edberg, N., Fraenz, M., Martinecz, C., Szego, K., and Vaisberg, O.: The Induced Magnetospheres of Mars, Venus, and Titan, Space Science Reviews, 162, 113–171, https://doi.org/10.1007/s11214-011-9845-1, 2011. 84

Cassak, P. A. and Fuselier, S. A.: Reconnection at Earth's Dayside Magnetopause, in: Magnetic Reconnection: Concepts and Applications, edited by Gonzalez, W. and Parker, E., vol. 427 of *Astrophysics and Space Science Library*, p. 213, https://doi.org/10.1007/978-3-319-26432-5_6, 2016. 84

Coleman, I. J.: A multi-spacecraft survey of magnetic field line draping in the dayside magnetosheath, Annales Geophysicae, 23, 885 – 900, https://doi.org/10.5194/angeo-23-885-2005, 2005. 84

Crooker, N. U., Luhmann, J. G., Russell, C., Smith, E. J., Spreiter, J. R., and Stahara, S. S.: Magnetic field draping against the dayside magnetopause, Journal of Geophysical Research (Space Physics), 90, 3505 – 3510, https://doi.org/10.1029/ja090ia04p03505, 1985. 84

Delva, M., Volwerk, M., Jarvinen, R., and Bertucci, C.: Asymmetries in the Magnetosheath Field Draping on Venus' Nightside, Journal of Geophysical Research: Space Physics, 122, 10,396–10,407, https://doi.org/10.1002/2017ja024604, 2017. 84

Fairfield, D. H.: The ordered magnetic field of the magnetosheath, vol. 72 of *Journal of Geophysical Research*, https://doi.org/10.1029/jz072i023p05865, 1967. 84

Génot, V., Broussillou, L., Budnik, E., Hellinger, P., Trávníček, P. M., Lucek, E., and Dandouras, I.: Timing mirror structures observed by Cluster with a magnetosheath flow model, Annales Geophysicae, 29, 1849–1860, https://doi.org/10.5194/angeo-29-1849-2011, 2011. 84

Jelínek, K., Němeček, Z., and Šafránková, J.: A new approach to magnetopause and bow shock modeling based on automated region identification, Journal of Geophysical Research (Space Physics), 117, A05208, https://doi.org/10.1029/2011JA017252, 2012. 85, 86

Jones, G. H., Rees, A., Balogh, A., and Forsyth, R. J.: The draping of heliospheric magnetic fields upstream of coronal mass ejecta, Geophysical Research Letters, 29, 15–1–15–4, https://doi.org/10.1029/2001gl014110, 2002. 84

Juhász, A. and Horányi, M.: Dynamics of charged space debris in the Earth's plasma environment, Journal of Geophysical Research: Space Physics, 102, 7237–7246, https://doi.org/10.1029/96ja03672, 1997. 84

Juhász, A. and Horányi, M.: Magnetospheric screening of cosmic dust, Journal of Geophysical Research: Space Physics, 104, 12 577–12 583, https://doi.org/10.1029/1999ja900091, 1999. 84

Kallio, E. J. and Koskinen, H. E. J.: A semiempirical magnetosheath model to analyze the solar wind-magnetosphere interaction, JGR, 105, 27 469–27 480, https://doi.org/10.1029/2000JA900086, 2000. 84

Kaymaz, Z.: IMP 8 magnetosheath field comparisons with models, Annales Geophysicae, 16, 376 – 387, https://doi.org/10.1007/s00585-998-0376-3, 1998. 84

Kaymaz, Z. and Siscoe, G.: Field-Line Draping Around ICMES, Solar Physics, 239, 437–448, https://doi.org/10.1007/s11207-006-0308-x, 2006. 84

Kaymaz, Z., Siscoe, G., and Luhmann, J. G.: IMF draping around the Geotail: IMP 8 observations, Geophysical Research Letters, 19, 829–832, https://doi.org/10.1029/92gl00403, 1992. 84

Kaymaz, Z., Luhmann, J. G., Fedder, J. A., Lyon, J. G., Spreiter, J. R., and Stahara, S. S.: Evidence for reverse draping of magnetosheath field around the magnetosphere in IMP 8 observations for northward interplanetary magnetic field, Journal of Geophysical Research (Space Physics), 101, 13 321 – 13 326, https://doi.org/10.1029/96ja00509, 1996. 84

King, J. H. and Papitashvili, N. E.: Solar wind spatial scales in and comparisons of hourly Wind and ACE plasma and magnetic field data, Journal of Geophysical Research (Space Physics), 110, A02104, https://doi.org/10.1029/2004JA010649, 2005. 85

Kobel, E. and Fluckiger, E. O.: A model of the steady state magnetic field in the magnetosheath, , 99, 23 617–23 622, https://doi.org/10.1029/94JA01778, 1994. 84, 85, 86, 88, 89, 91, 92, 93, 94, 95, 96

Koenders, C., Goetz, C., Richter, I., Motschmann, U., and Glassmeier, K.-H.: Magnetic field pile-up and draping at intermediately active comets: results from comet 67P/Churyumov–Gerasimenko at 2.0 AU, Monthly Notices of the Royal Astronomical Society, 462, S235–S241, https://doi.org/10.1093/mnras/stw2480, 2016. 84

Longmore, M., Schwartz, S. J., and Lucek, E. A.: Rotation of the magnetic field in Earth's magnetosheath by bulk magnetosheath plasma flow, Annales Geophysicae, 24, 339–354, https://doi.org/10.5194/angeo-24-339-2006, 2006. 84

Masters, A.: Magnetic reconnection at Uranus' magnetopause, Journal of Geophysical Research: Space Physics, 119, 5520–5538, https://doi.org/10.1002/2014ja020077, 2014. 85

Masters, A.: Magnetic reconnection at Neptune's magnetopause, Journal of Geophysical Research: Space Physics, 120, 479–493, https://doi.org/10.1002/2014ja020744, 2015. 85

Masters, A.: Model-Based Assessments of Magnetic Reconnection and Kelvin-Helmholtz Instability at Jupiter's Magnetopause, Journal of Geophysical Research (Space Physics), 122, 11, https://doi.org/10.1002/2017ja024736, 2017. 84

McComas, D. J., Spence, H. E., Russell, C. T., and Saunders, M. A.: The average magnetic field draping and consistent plasma properties of the venus magnetotail, , 91, 7939–7953, https://doi.org/10.1029/JA091iA07p07939, 1986. 84

McComas, D. J., Gosling, J. T., Winterhalter, D., and Smith, E. J.: Interplanetary magnetic field draping about fast coronal mass ejecta in the outer heliosphere, Journal of Geophysical Research: Space Physics, 93, 2519–2526, https://doi.org/10.1029/ja093ia04p02519, 1988. 84

Nguyen, G., Aunai, N., Michotte de Welle, B., Jeandet, A., Lavraud, B., and Fontaine, D.: Massive Multi-Mission Statistical Study and Analytical Modeling of the Earth's Magnetopause: 1. A Gradient Boosting Based Automatic Detection of Near-Earth Regions, Journal of Geophysical Research (Space Physics), 127, e29773, https://doi.org/10.1029/2021JA029773, 2022. 85

Ohtani, S. K. S. and kokubun: Magnetic properties of the high-latitude tail boundary: Draping of magnetosheath field lines and tail-aligned current, JGR, 96, 1 – 10, https://doi.org/10.1029/91ja00570, 1991. 84

Opher, M., Stone, E. C., and Gombosi, T. I.: The Orientation of the Local Interstellar Magnetic Field, Science, 316, 875–878, https://doi.org/10.1126/science.1139480, 2007. 84

Petrinec, S. M.: Draping of strongly flow-aligned interplanetary magnetic field about the magnetopause, Advances in Space Research, 58, 175–180, https://doi.org/10.1016/j.asr.2015.10.001, 2016. 84

Pfrommer, C. and Dursi, J.: Detecting the orientation of magnetic fields in galaxy clusters, Nature Physics, 6, 520–526, https://doi.org/10.1038/nphys1657, 2010. 84

Pogorelov, N. V., Fraternale, F., Kim, T. K., Burlaga, L. F., and Gurnett, D. A.: Magnetic Field Draping of the Heliopause and Its Consequences for Radio Emission in the Very Local Interstellar Medium, The Astrophysical Journal Letters, 917, L20, https://doi.org/10.3847/2041-8213/ac14bd, 2021. 84

Reidler, W., Schwingenschuh, K., Yeroshenko, Y. G., Styashkin, V. A., and Russell, C. T.: Magnetic field observations in comet Halley's coma, Nature, 321, 288–289, https://doi.org/10.1038/321288a0, 1986. 84

Romanelli, N., Gómez, D., Bertucci, C., and Delva, M.: Steady-state Magnetohydrodynamic Flow around an Unmagnetized Conducting Sphere, , 789, 43, https://doi.org/10.1088/0004-637X/789/1/43, 2014. 90

Romashets, E. P. and Vandas, M.: Analytic Modeling of Magnetic Field in the Magnetosheath and Outer Magnetosphere, Journal of Geophysical Research (Space Physics), 124, 2697–2710, https://doi.org/10.1029/2018JA026006, 2019. 85

Rong, Z. J., Barabash, S., Futaana, Y., Stenberg, G., Zhang, T. L., Wan, W. X., Wei, Y., Wang, X. D., Chai, L. H., and Zhong, J.: Morphology of magnetic field in near-Venus magnetotail: Venus express observations, Journal of Geophysical Research (Space Physics), 119, 8838–8847, https://doi.org/10.1002/2014JA020461, 2014. 84

Schmid, D., Narita, Y., Plaschke, F., Volwerk, M., Nakamura, R., and Baumjohann, W.: Magnetosheath plasma flow model around Mercury, Annales Geophysicae, 39, 563–570, https://doi.org/10.5194/angeo-39-563-2021, 2021a. 84

Schmid, D., Narita, Y., Plaschke, F., Volwerk, M., Nakamura, R., and Baumjohann, W.: Pick-Up Ion Cyclotron Waves Around Mercury, Geophysical Research Letters, 48, https://doi.org/10.1029/2021gl092606, 2021b. 84

Shue, J. H., Song, P., Russell, C. T., Steinberg, J. T., Chao, J. K., Zastenker, G., Vaisberg, O. L., Kokubun, S., Singer, H. J., Detman, T. R., and Kawano, H.: Magnetopause location under extreme solar wind conditions, JGR, 103, 17 691–17 700, https://doi.org/10.1029/98JA01103, 1998. 85, 86

Spreiter, J. R., Summers, A. L., and Alksne, A. Y.: Hydromagnetic flow around the magnetosphere, Planetary and Space Science, 14, 223–253, https://doi.org/10.1016/0032-0633(66)90124-3, 1966. 84

Sulaiman, A. H., Masters, A., Dougherty, M. K., and Jia, X.: The magnetic structure of Saturn's magnetosheath, Journal of Geophysical Research (Space Physics), 119, 5651 – 5661, https://doi.org/10.1002/2014ja020019, 2014. 84

Trattner, K. J., Petrinec, S. M., and Fuselier, S.: The Location of Magnetic Reconnection at Earth's Magnetopause, Space Science Reviews, 217, 1 – 47, https://doi.org/10.1007/s11214-021-00817-8, 2021. 84, 85

Tsyganenko, N. A. and Stern, D. P.: Modeling the global magnetic field of the large-scale Birkeland current systems, , 101, 27 187–27 198, https://doi.org/10.1029/96JA02735, 1996. 84

Turc, L., Fontaine, D., Savoini, P., and Kilpua, E. K. J.: A model of the magnetosheath magnetic field during magnetic clouds, Annales Geophysicae, 32, 157–173, https://doi.org/10.5194/angeo-32-157-2014, 2014. 84

Vandas, M. and Romashets, E. P.: Modeling of magnetic field in the magnetosheath using elliptic coordinates, Planetary and Space Science, 178, 104 692, https://doi.org/10.1016/j.pss.2019.07.007, 2019. 84, 85

Vandas, M., Nemecek, Z., Safrankova, J., Romashets, E. P., and Hajoš, M.: Comparison of Observed and Modeled Magnetic Fields in the Earth's Magnetosheath, Journal of Geophysical Research (Space Physics), 125, e27 705, https://doi.org/10.1029/2019ja027705, 2020. 85

Šafránková, J., Přech, L., Němeček, Z., and Sauvaud, J. A.: Density profile in the magnetosheath adjacent to the magnetopause, Advances in Space Research, 30, 1693–1703, https://doi.org/10.1016/S0273-1177(02)00438-6, 2002. 85

Zhang, C., Rong, Z., Klinger, L., Nilsson, H., Shi, Z., He, F., Gao, J., Li, X., Futaana, Y., Ramstad, R., Wang, X., Holmström, M., Barabash, S., Fan, K., and Wei, Y.: Three-Dimensional Configuration of Induced Magnetic Fields Around Mars, Journal of Geophysical Research (Planets), 127, e07334, https://doi.org/10.1029/2022JE007334, 2022. 84

Chapter 4

Magnetic Pileup and Plasma Depletion Layer in the Magnetosheath

Contents

4.1 Introduction

Chapter 3 focused on examining the draping of the IMF around the magnetopause. We now have a better understanding of the orientation of the magnetic field on the most variable side of the magnetopause. This magnetic geometry plays a crucial role in how reconnection occurs at this boundary. This chapter now focuses on how the amplitude of the magnetic field and the plasma density, equally important for reconnection [Borovsky, 2013; Cassak and Shay, 2007; Swisdak and Drake, 2007], vary in the magnetosheath as a function of the IMF orientation.

Upon arriving onto the Earth's magnetosphere, the solar wind slows down, to a subsonic speed, and piles up onto the magnetopause along with the magnetic field. The magnetic field amplitude and plasma density sharply increase through the bow shock according to the well known Rankine-Hugoniot conditions, and then slowly increase up to the magnetopause. This spatial variation and its dependence on the IMF orientation is still not well constrained from an observational standpoint for the same reason than for the draping geometry studied in Chapter 3. Although the plasma piles up onto the magnetopause obstacle, the concomitant increase in the magnetic pressure will counter the increase of the plasma density and even possibly lead to its local decrease to maintain pressure balance [Anderson et al., 1997; Paschmann et al., 1993; Phan et al., 1994]. The decrease of the plasma density in the vicinity of the magnetopause is called the Plasma Depletion Layer (PDL) The magnetic pileup and PDL were first predicted analytically [Lees, 1964; Zwan and Wolf, 1976] and latter observed with in-situ measurements [Crooker et al., 1979; Fuselier et al., 1991; Hall et al., 1990; Paschmann et al., 1978; Song et al., 1990]. It is expected that the level of magnetic flux pileup and plasma depletion both depend on the IMF orientation and constitute the boundary condition to magnetopause reconnection. But they should also be the consequence of reconnection itself, whose rate regulates the fraction of the flow and magnetic flux that goes through the boundary or has to circumvent it [Anderson et al., 1997; Phan et al., 1994]. The magnetic pileup and the PDL furthermore are universal phenomena and have been observed upstream of other planetary magnetospheres, such as the one of Mercury [Gershman et al., 2013] and Saturn [Masters et al., 2014], as well as at the heliopause [Cairns and Fuselier, 2017].

Anderson and Fuselier [1993] observed a PDL for all IMF orientations, and noted a smaller depletion with an increasing IMF clock angle. Phan et al. [1994] found that PDLs are only present for low magnetic shear angles (smaller than 60°) at the magnetopause but are absent for higher values of magnetic shear angles. However, Paschmann et al. [1993] reported the observation of magnetic pileup and PDL in less than half of 22 magnetopause crossings at low magnetic shear angles (smaller or equal to 30°). Šafránková et al. [2002] analyzed three magnetopause crossings and observed a PDL in the subsolar region for an IMF clock angle of approximately 90° and in the flank region for anti-parallel magnetic fields, but did not detect a plasma depletion for low magnetic shear angles. Pudovkin et al. [2001] suggested that magnetic pileup and PDL are present for all magnetic shears, but the magnetic field and density could plateau in the vicinity of the magnetopause, and that if the time interval considered is too short, it could give the appearance of an absence of pileup/PDL. Using data from the THEMIS and Cluster missions, [Zhang et al., 2019] reconstructed the profile of the magnetic field amplitude and plasma density in the subsolar region. They found that a magnetic pileup and a plasma depletion layer (PDL) were present for all IMF orientations. The authors found profiles not influenced by the variation of the IMF clock angle but only by the IMF cone angle. This is somewhat surprising since, if true, it would imply reconnection, which depends on the clock angle, has no effect on the amount of flux that piles up onto the magnetopause. The formation of the magnetic pileup and PDL, and their dependence on the IMF orientation is therefore still poorly understood.

Walters [1964] theorized, based on the Rankine-Hugoniot equations, that there exists an asymmetry in plasma quantities (density, pressure, temperature) between the quasi-parallel and quasi-perpendicular sides of the magnetosheath, relative to the bow shock. Given that the Parker spiral imparts a preferred orientation to the IMF,the quasi-perpendicular and quasi-parallel sides of the bow shock are preferentially positioned on the dawn and dusk sides of the magnetosheath, respectively. Several studies have investigated asymmetries in the magnetosheath, with a particular

focus on the plasma density.

Paularena et al. [2001] studied the asymmetry in the plasma density between the dawn and dusk sides during different solar cycle periods. Slightly larger densities were found on the dawn side during solar maxima, but not during minima. This asymmetry, however, did not appear to be correlated with the IMF orientation. Němeček et al. [2002] observed a dawn-dusk asymmetry of ion fluxes with a larger density on the dawn side, but concluded that it was not caused by the orientation of the IMF and the localization of the quasi-parallel/quasi-perpendicular regions of the bow shock. Longmore et al. [2005], using the Cluster measurements, found lower densities measured on the dawn side of the magnetosheath in the Northern Hemisphere and did also not find a correlation between the IMF orientation on the observed asymmetry. Walsh et al. [2012] proposed that the asymmetry in the plasma quantities is caused by an asymmetry in the position and shape between the dawn and dusk sides of the bow shock. This asymmetry in the bow shock location would be correlated with the solar wind Mach number and would therefore be influenced by the solar cycle [Walsh et al., 2014].

It is puzzling that, in all of the above results, the asymmetry of plasma quantities was not found to depend on IMF orientation, since this orientation is the very reason why an asymmetry was theorized downstream of the shock in the first place.

We now have an vast amounts of data at our disposal. Following our statistical approach, this chapter aims at improving our understanding of the magnetic and density pileup onto the magnetopause, by reconstructing spatial variations throughout the entire magnetosheath for various IMF orientations

4.2 Method

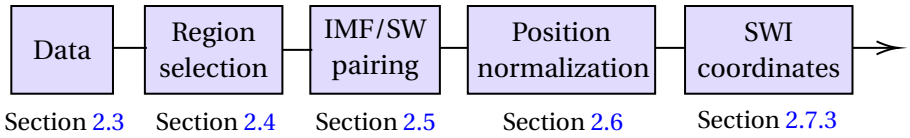

Figure 4.1: Overview of the global methodology detailed in Chapter 2.

Figure 4.1 summarizes the different steps of the global methodology, detailed in the Chapter 2, used in this chapter.

As in the previous work, we use data collected by the Cluster, Double Star, THEMIS, and MMS missions (see Section 2.3) from which almost all magnetosheath measurements are identified using a trained Gradient Boosting Classifier [Nguyen et al., 2022] (see Section 2.4). As previously done in Chapter 3 and explained in Chapter 2, each measurement is paired with the properties of its causal IMF and solar wind using OMNI data [King and Papitashvili, 2005] and a transport method [Šafránková et al., 2002] (see Section 2.5). The position of each data point relative to the bow shock and the magnetopause at the time of the measurement is estimated using Gradient Boosting Regression models of the boundaries, parameterized with solar wind and IMF conditions (see Section 2.6). Using these relative distances to the magnetopause and bow shock, all points are repositioned between a standard couple of boundaries [Jelínek et al., 2012; Shue et al., 1998] parameterized with average solar wind conditions (i.e. dynamic pressure of 2nPa and $B_{z_{imf}}$ = 0 nT). Then all measurements were converted from GSM to SWI coordinates (see Section 2.7.3).

4.2.1 Reconstructed profiles through the subsolar magnetosheath

The first part of this study focuses on the variation of the magnetic field and density in the subsolar region. This region is of particular interest due to the dominant radial plasma flow, which transports magnetic field lines directly from the bow shock to the magnetopause. In this study, we define the subsolar region as a region within a radius of 5 Re of the subsolar point ($\sqrt{Y_{SWI}^2 + Z_{SWI}^2} \leq$ 5 Re), corresponding to the red area depicted in the left panel of Figure 4.2.

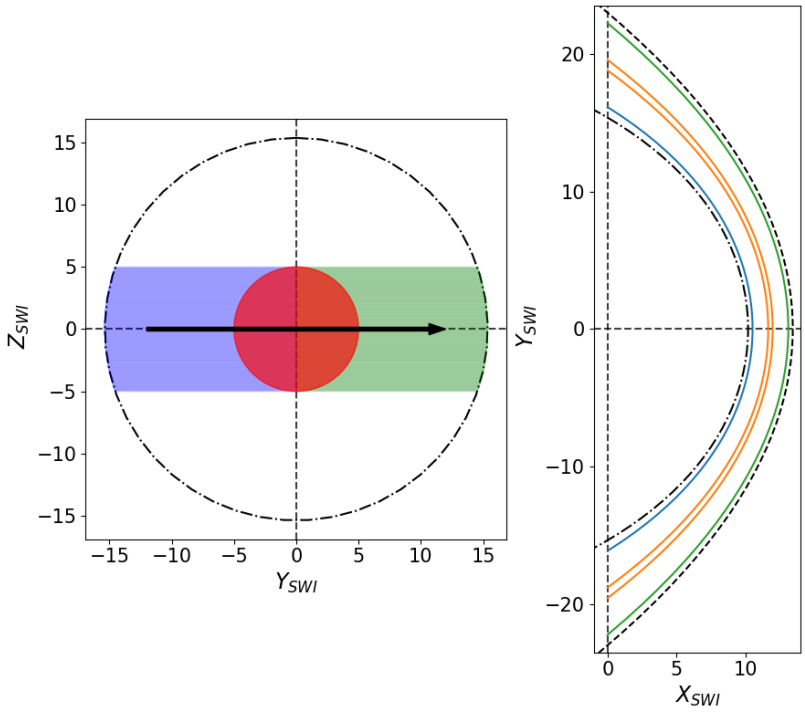

Figure 4.2: In the left panel, the red, blue, and green shaded areas correspond to the considered subsolar, quasi-perpendicular, and quasi-parallel region, respectively. The dashed-dotted line circle correspond to the terminator of the magnetopause. In the right panel, the green, orange, and blue lines correspond to shell of ΔD_{msh}=0.1 near the bow shock (dashed line), in the middle of the magnetosheath, and near the magnetopause (dashed-dotted line), respectively.

The variation of the magnetic field and density are represented as a function of the position D_{msh} in the magnetosheath relative to the magnetopause and bow shock, given by equation 4.1, where R, R_{mp}, R_{bs} correspond to the radial positions of the data point, magnetopause, and bow shock respectively. Additionally, we will examine the variation of the magnetic field and density in the vicinity of the magnetopause ($D_{msh} \leq 0.1$) as a function of both the IMF cone and clock angles.

$$D_{msh} = \frac{R - R_{mp}}{R_{bs} - R_{mp}} \tag{4.1}$$

The uncertainty in the obtained values is probably dominated by two factors. The first one is the repositioning of the measurements between a standard bow shock and magnetopause. This processing step comes with a substantial uncertainty caused by the error in the GBR bow shock and magnetopause model (see Section 2.6.2). This will tend to mix the measurement of different location hindering the spatial reconstruction of the profile. The second major source of error arises from incorrect pairing of magnetosheath measurements with their causal solar wind and IMF conditions. As these upstream conditions are used to obtain normalized data, mis-pairing can introduce significant noise in the obtained distributions. In practice, employing the standard deviation (σ) as a measure of uncertainty results in values that seem excessively large, particularly given the level of detail in our study that aligns with known physical processes. Conversely, when using the standard error $\sigma/\sqrt{N}$, where N represents the number of points selected by the Nearest Neighbors algorithm, the resulting measure of uncertainty appears too small and seems to fail to adequately reflect the variation observed for the different distributions. Therefore, it was finally decided not to represent the error bars on the obtained distributions while being careful not to over-interpret the results.

4.2.2 Asymmetries between the quasi-parallel and quasi-perpendicular sides

The SWI coordinate system (see Section 2.7.3) is particularly useful for studying the asymmetries between the quasi-parallel and quasi-perpendicular sides of the magnetosheath.

We evaluate the Equation 4.2 to estimate the asymmetry A for a quantity Q (the magnetic field amplitude or plasma density) between the quasi-perpendicular and quasi-parallel sides of the magnetosheath as a function of Y_{SWI}. Positive values of the asymmetry A indicate that larger values of Q in the quasi-perpendicular side of the magnetosheath represented by the blue shaded area in the left panel of Figure 4.2. Conversely, negative values of the asymmetry A indicate larger values of Q in the quasi-parallel side of the magnetosheath represented by the green shaded area in the same panel. For the sake of simplicity of the representation, and because it is enough to demonstrate the point, we will focus on estimating the asymmetry in the equatorial plane ($(|Z_{SWI}| \leq 5)$).

$$A(Y_{SWI}) = 100\left(\frac{Q(-Y_{SWI})}{Q(Y_{SWI})} - 1\right) \quad \text{with} \quad Y_{SWI} \geq 0 \tag{4.2}$$

This study will examine the asymmetry of the magnetic field and density within the magnetosheath at three distinct distances: near the magnetopause, at the center of the magnetosheath, and close to the bow shock. These regions are illustrated in the right panel of Figure 4.2.

Additionally, the variation of the asymmetry throughout the magnetosheath will be studied by averaging it over all Y_{SWI} for different relative distances from the shock to the magnetopause.

4.3 Magnetic Amplitude and Plasma Density through the Subsolar Magnetosheath

4.3.1 Variability of the magnetic pileup with the IMF orientation

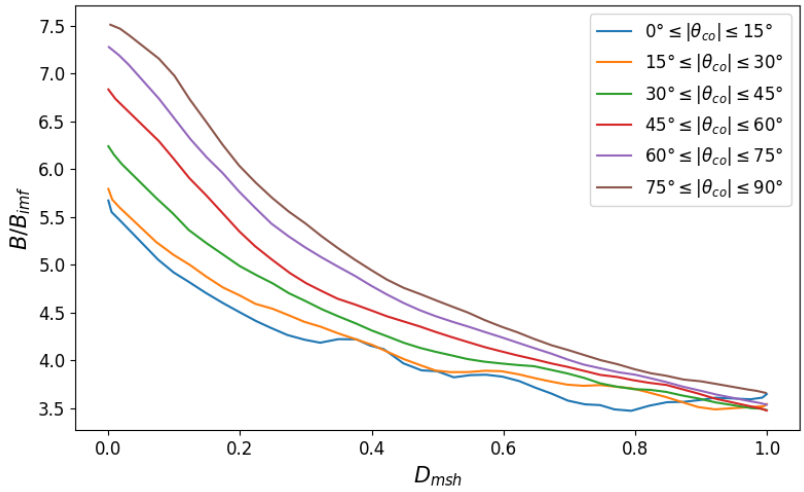

Figure 4.3: Magnetic field amplitude in the subsolar magnetosheath ($\sqrt{Y^2+Z^2} \leq 5$ Re) normalized by the IMF amplitude (B_{imf}) as a function of the position in the magnetosheath D_{msh} relative to the magnetopause and bow shock. The magnetopause and bow shock are positioned at D_{msh}=0 and D_{msh}=1, respectively. The different colored lines represent the normalized magnetic field amplitude for different absolute value of IMF cone angles ($|\theta_{co}|$).

Figure 4.3 presents the profile of the magnetic field amplitude as a function of the relative position in the magnetosheath (D_{msh}) in the subsolar region for various IMF cone angles ($|\theta_{co}|$). It reveals the presence of a magnetic pileup for all IMF cone angles. Furthermore, we observe that the pileup is more pronounced as the IMF cone angle increases. This leads to a difference of approximately 2 between the nearly radial and large IMF cone angles. Downstream of the shock, the magnetic field amplitude shows relatively similar values for all IMF cone angles.

The difference in the pileup profiles for different IMF cone angle probably results from the magnetosheath plasma flowing more freely along the the magnetic field lines as the IMF cone angle decreases. As shown in Figure 4.4, downstream of the shock, $|V_x|/V_{sw}$ velocity diminishes with decreasing IMF cone angles. Simultaneously, the amplitudes of V_{yz}/V_{sw} ($V_{yz} = \sqrt{V_y^2 + V_z^2}$) exhibits higher values with decreasing IMF cone angles. This suggests that as the IMF becomes more radial, the plasma is more effectively able to circumvent the magnetopause, thereby inducing less compression of the magnetic field at the magnetopause. Furthermore, the amplitude of the velocity V/V_{sw} appears to be smaller for large IMF cone angles in most of the magnetosheath than for intermediate and small IMF cone angles (i.e. $|\theta_{co}| \leq 45°$). This is consistent with the observation that the magnetic flux accumulates in the magnetosheath for large IMF cone angles producing a more effective compression of the magnetic field. A slight increase of the velocity amplitude near the magnetopause ($D_{msh} \leq 0.2$) at large IMF cone angle (i.e. $|\theta_{co}| \geq 45°$) can be observed. This acceleration could be produced by the magnetic pressure force resulting from the larger pileup occurring in these conditions.

Let us now focus on how the magnetic field piles up as a function of the IMF clock angle, whatever the IMF cone angle. Figure 4.5 shows the profile of the magnetic field amplitude as a function of the relative position throughout the magnetosheath (D_{msh}) in the subsolar region for various IMF clock angles ($|\theta_{cl}|$). It is immediately visible that the magnetic field amplitudes increases from the bow shock to the magnetopause, whatever the value of the IMF clock angle. The amplitude of the magnetic field just downstream of the shock, down to the middle of the magnetosheath, is remarkably independent of the IMF clock angle. From the middle of the magnetosheath down to the magnetopause, the amplitude of the field clearly reveals a clock angle dependence. Near the magnetopause, the magnetic pileup increases as the IMF clock angles decrease, with a difference of B/B_{imf} of approximately 1 at the boundary between the most northward and southward IMF conditions. Interestingly, the decrease of the magnetic pileup when the IMF turns from northward to southward is not linear with the clock angle, but rather abruptly changes for IMF clock angles greater than 60° ($|\theta_{cl}| \geq 60°$). This nonlinear shift distinguishes northward with $|\theta_{cl}| \leq 60°$ conditions from southward IMF ($|\theta_{cl}| \geq 90°$), where the magnetic pileup amplitudes remain relatively similar. Only a slight decrease in the magnetic pileup occurs when the IMF changes from an eastward to a southward orientation. The decrease in the magnetic field amplitude with increasing IMF clock angles is consistent with the expected effect of magnetic reconnection eroding the magnetic flux at the magnetopause.

If magnetic reconnection is at the root of the pileup reduction observed in Figure 4.5, a consistent signature should be seen in the velocity field. We therefore plot on Figure 4.6, the velocity $|V_x|/V_{sw}$ as a function of the relative position and for different values of the IMF clock angle. $|V_x|/V_{sw}$ shows a linear decrease from the shock to the magnetopause, whatever the value of the clock angle, as expected from the slow down of the plasma piling-up against the obstacle. We note, furthermore, that $|V_x|/V_{sw}$ is slightly higher throughout the whole thickness of the magnetosheath when the IMF has a southward component than when it is oriented northward. This clock angle dependence is consistent with reconnection operating at the magnetopause and effectively letting some of the solar wind penetrating across it rather than going around in the magnetosheath. While the V_{yz}/V_{sw} velocity profiles do not exhibit a clear dependence on the IMF clock angle until the middle of the magnetosheath, they do show larger values for southward IMF conditions. This observation seems consistent with the acceleration of plasma in reconnection outflows, which are expected to be tangential to the magnetopause. In addition, the amplitude of the velocity profiles V/V_{sw} generally increases with the increase of the IMF clock angle. This trend is similar to that visible in the magnetic amplitude profile, with an abrupt change near the magnetopause for predominantly eastward IMF ($|\theta_{cl}| \geq 60°$).

Since we are interested in magnetic reconnection operating at the magnetopause, let us now focus on how the magnetic field amplitude values varies as a function of both the IMF clock and cone angles, but only near the subsolar magnetopause. Figure 4.7 show the values taken by the magnetic field in the subsolar region near the magnetopause ($D_{msh} \leq 0.1$) as a function of both IMF

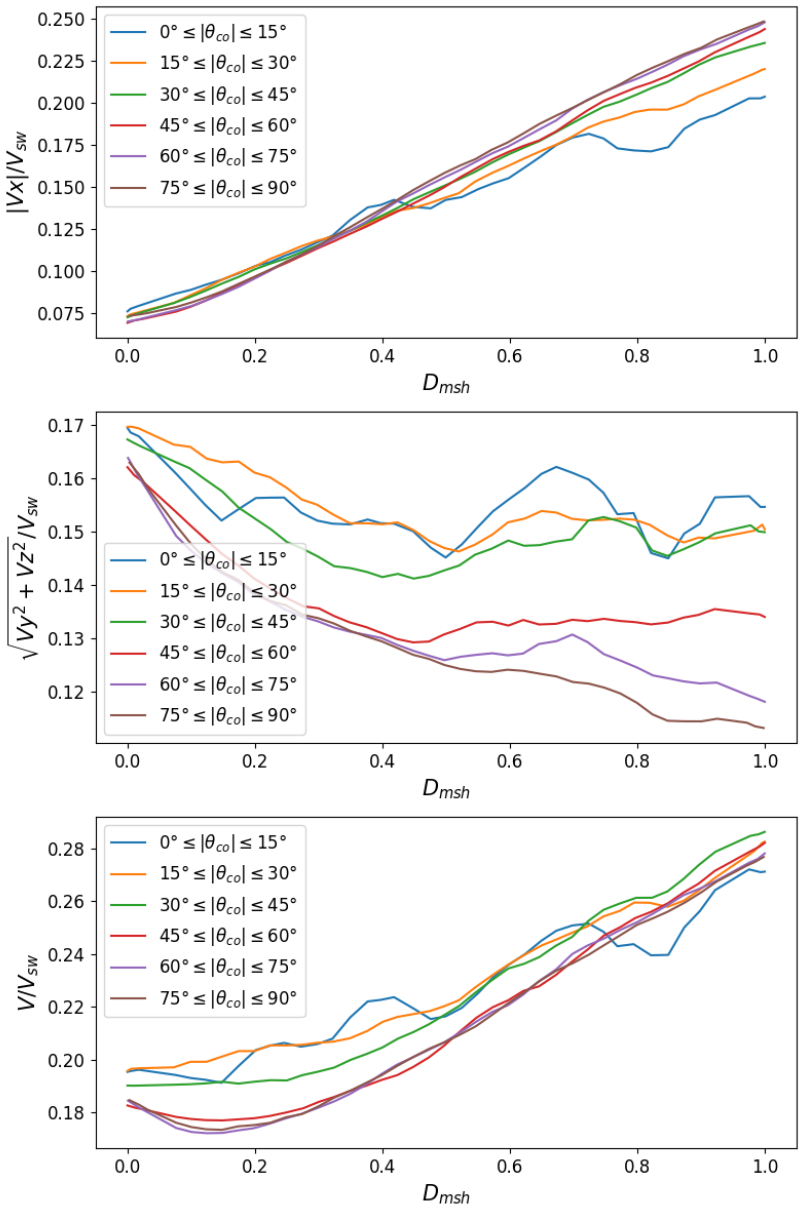

Figure 4.4: Velocity profiles in the subsolar magnetosheath ($\sqrt{Y^2+Z^2} \leq 5$ Re) normalized by the solar wind velocity as a function of the position in the magnetosheath D_{msh} relative to the magnetopause and bow shock. From top to bottom panel is represented: V_x/V_{sw}, $V_{yz} = \sqrt{V_y^2+V_z^2}/V_{sw}$ and V/V_{sw}. The magnetopause and bow shock are positioned at D_{msh}=0 and D_{msh}=1, respectively. The different colored lines represent the velocity profiles for different absolute value of IMF cone angles ($|\theta_{co}|$).

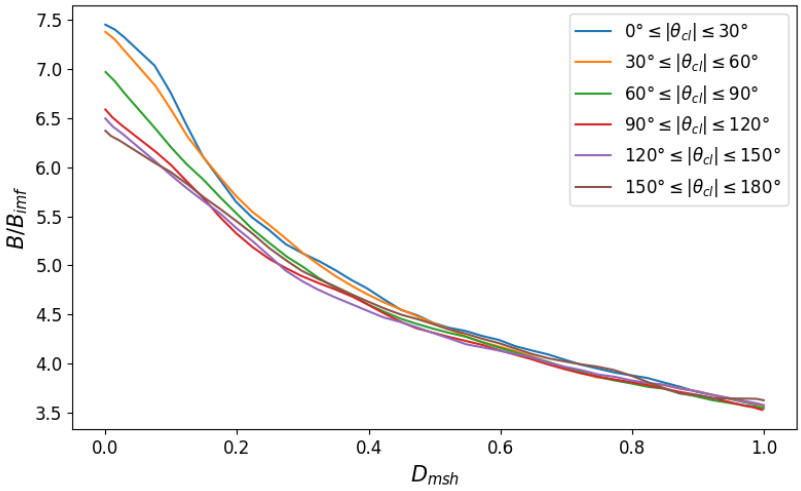

Figure 4.5: Magnetic field amplitude in the subsolar magnetosheath ($\sqrt{Y^2+Z^2} \leq 5$ Re) normalized by the IMF (B_{imf}) as a function of the position in the magnetosheath D_{msh} relative to the magnetopause and bow shock. The magnetopause and bow shock are positioned at D_{msh}=0 and D_{msh}=1, respectively. The different colored lines represent the normalized magnetic field amplitude for different absolute value of IMF clock angles ($|\theta_{cl}|$).

clock and cone angles. Overall, the observed variation in magnetic amplitude, ranging from about 5 in southward and low IMF cone angle, to about 8-9 in northward and large cone angle conditions, support previous findings. We can also see that for IMF cone angles smaller than 20°, the magnetic pileup does not appear to decrease as the IMF turns southward. This may suggest that, for such a low IMF cone angle, magnetic reconnection may not be operating at the magnetopause or so little that it does not impact how the magnetic field piles up. In contrast, for IMF cone angles greater than 60°, the magnetic pileup decreases rapidly when the IMF clock angle is between 60° and 90°, and appears to be almost constant for more southward IMF.

4.3.2 The plasma depletion layer for various IMF orientations

We now repeat the same procedure as previous sections but now for the plasma density across the magnetosheath, in particular focusing in the possible depletion layer nearby the magnetopause. We start by investigating the profile of the particle density as a function of the relative position across the subsolar magnetosheath, and for different IMF cone angles, all clock angles considered, shown in Figure 4.8. Near the bow shock, the density ratio increases with increasing IMF cone angle, reaching a maximum compression of approximately 4 when the IMF is almost perpendicular to the shock ($|\theta_{co}| \geq 60°$). For almost radial IMF conditions ($|\theta_{co}| \leq 30°$), the density ratio exhibits an almost continuous increase up to the magnetopause, where no depletion is observed. In contrast, a PDL near the magnetopause is observed for IMF with cone angles greater than 30°. The density ratios increases up to approximately $D_{msh} = 0.4$, after which it decreases up to the magnetopause. Interestingly, for IMF cone angles greater than 60°, the density ratio at the magnetopause is even lower than at the bow shock. The magnitude of the depletion of plasma nearby the magnetopause increases with the IMF cone angle. This is consistent with the concomitant increase of the magnetic field amplitude seen in Figure 4.3 and previously discussed.

Similarly to what we did for the magnetic amplitude, we now turn on investigating how the density profile changes for different IMF clock angles. Figure 4.9 presents the density profile as a function of the relative position throughout the subsolar magnetosheath (D_{msh}) for various IMF clock angles (θ_{cl}). We observe a PDL for each of the IMF clock angle, and there is no clear dependence on the IMF clock angle throughout most of the magnetosheath. Near the magnetopause ($D_{msh} \leq 0.2$), however, the density appears to be lower for lower IMF clock angles. The deepening of the depletion seems to predominantly occur as soon as the IMF clock angle passes 60°. This

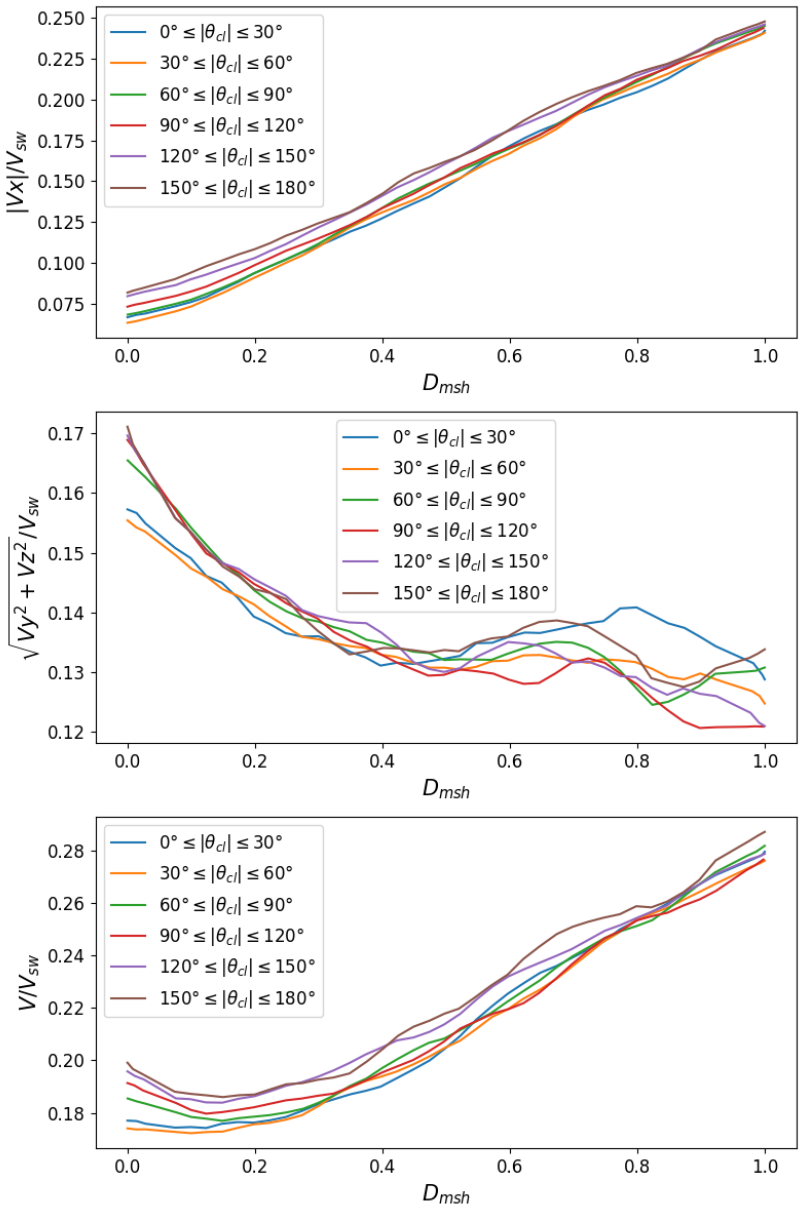

Figure 4.6: Velocity profiles in the subsolar magnetosheath ($\sqrt{Y^2+Z^2} \leq 5$ Re) normalized by the solar wind velocity as a function of the position in the magnetosheath D_{msh} relative to the magnetopause and bow shock. From top to bottom panel is represented: V_x/V_{sw}, $V_{yz} = \sqrt{V_y^2+V_z^2}/V_{sw}$ and V/V_{sw}. The magnetopause and bow shock are positioned at D_{msh}=0 and D_{msh}=1, respectively. The different colored lines represent the velocity profiles for different absolute value of IMF clock angles ($|\theta_{cl}|$).

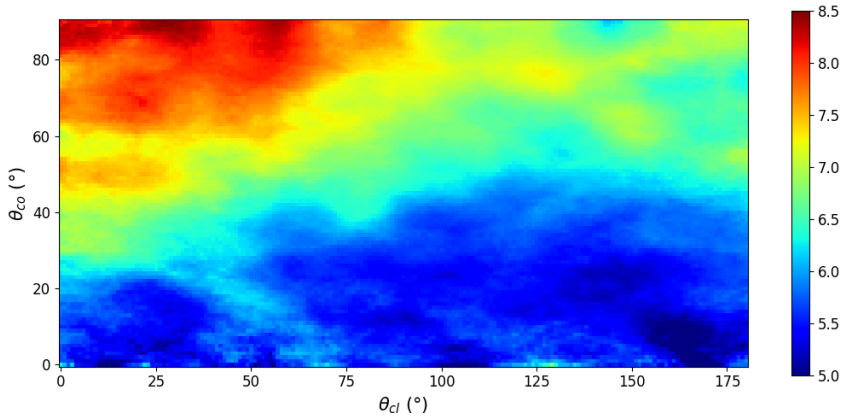

Figure 4.7: Magnetic pileup (B/B_{imf}) near the magnetopause (D_{msh} ≤0.1) in the subsolar magnetosheath ($\sqrt{Y^2+Z^2} \leq 5$ Re) as a function of the IMF clock ($|\theta_{cl}|$)and cone ($|\theta_{co}|$) angles.

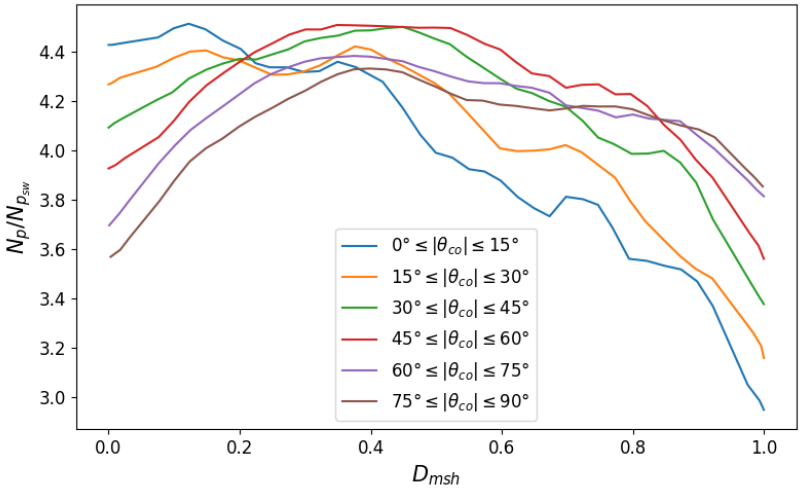

Figure 4.8: Ion density ratio ($N_p/N_{p_{sw}}$) in the subsolar magnetosheath ($\sqrt{Y^2+Z^2} \leq 5$ Re) as a function of the position in the magnetosheath D_{msh} relative to the magnetopause and bow shock. The magnetopause and bow shock are positioned at D_{msh}=0 and D_{msh}=1, respectively. The different colored lines represent the plasma density profiles for different absolute value of IMF cone angles ($|\theta_{co}|$).

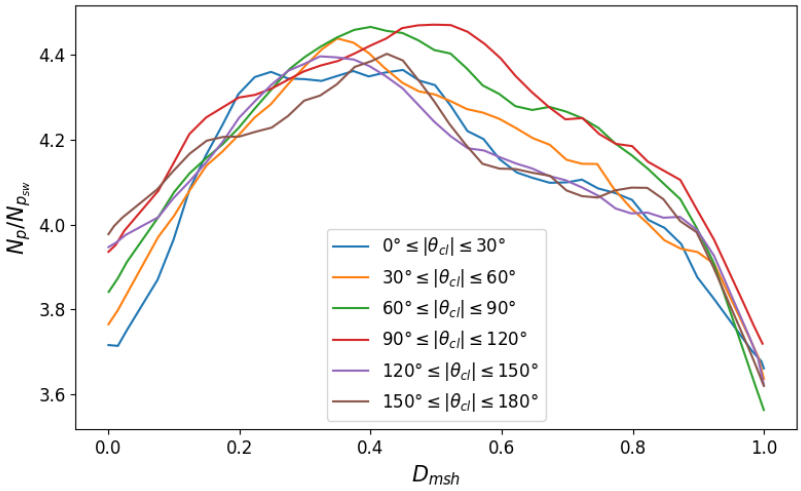

Figure 4.9: Ion density ratio ($N_p/N_{p_{sw}}$) in the subsolar magnetosheath ($\sqrt{Y^2+Z^2} \leq 5$ Re) as a function of the position in the magnetosheath D_{msh} relative to the magnetopause and bow shock. The magnetopause and bow shock are positioned at D_{msh}=0 and D_{msh}=1, respectively. The different colored lines represent the plasma density profiles for different absolute value of IMF clock angles ($|\theta_{cl}|$).

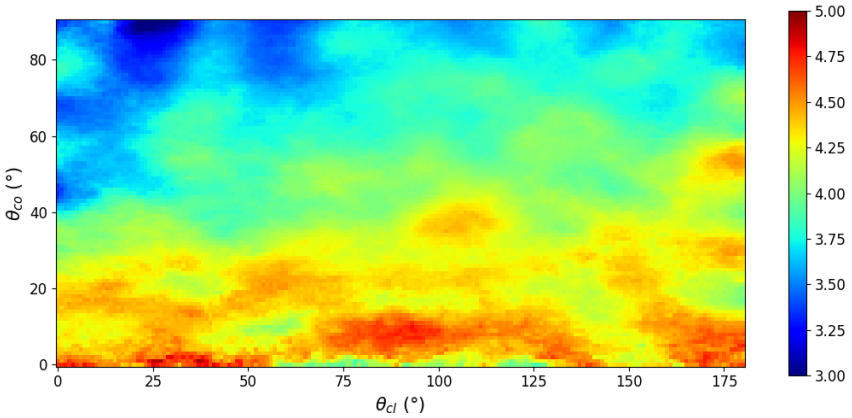

Figure 4.10: Density ratio ($N_p/N_{p_{sw}}$) near the magnetopause ($D_{msh} \leq 0.1$) in the subsolar magnetosheath ($\sqrt{Y^2+Z^2} \leq 5$ Re) as a function of the IMF clock ($|\theta_{cl}|$)and cone ($|\theta_{co}|$) angles.

pattern is consistent with the observed increase in magnetic pileup, as shown in Figure 4.5. Together, the magnetic field amplitude and plasma density, in their dependence on the IMF clock angle, seem to be consistent with magnetic reconnection eroding the pileup and the PDL as the IMF turns southward.

Let us now focus on the region nearby the magnetopause and observe in more details how the density varies with both the IMF cone and clock angles. Figure 4.10 shows the density ratio in the subsolar region close to the magnetopause ($D_{msh} \leq 0.1$) as a function of both IMF clock and cone angles. The density ratio increases as the IMF cone angle decreases. Consistently with the magnetic field amplitude (Figure 4.7), the density does not seem to have a clear dependence on the IMF clock angle for IMF cone under 20°. The density ratio is the smallest for northward IMF ($|\theta_{cl}| \leq 25°$) at large IMF cone angle ($|\theta_{co}| \geq 45°$) where the magnetic pileup is maximum. In contrast, as the IMF turns southward, its value rapidly increases. Once the IMF becomes eastward ($|\theta_{cl}| \geq 60°$), the density values do not seem to exhibit a strong dependence on the IMF clock angle but only on the IMF cone angle. Overall, the observed variation of the density ratio is consistent with the variation of the magnetic field and the effect of magnetic reconnection.

4.4 Asymmetry of the Equatorial Magnetosheath

4.4.1 Asymmetry of the magnetic field amplitude

It is well known from the Rankine Hugoniot jump conditions, that the magnetic field should be more compressed behind a quasi-perpendicular shock than a quasi-parallel one. In this section, we shall investigate, first, to what extent this asymmetry is seen in the data just downstream of the shock, and then to what extent it persists as one gets closer to the magnetopause.

Figure 4.11 presents the magnetic field amplitude normalized by that of the IMF and its asymmetry (Equation 4.2) between the quasi-parallel ($Y_{SWI} \geq 0$) and quasi-perpendicular ($Y_{SWI} \leq 0$) sides of the equatorial region of the magnetosheath.

For all IMF cone angles (left panels), the magnetic field amplitude increases as the magnetopause is approached, with a more pronounced enhancement in the subsolar region ($|Y_{SWI}| \leq 5$ Re) than in the flanks.

For IMF cone angles greater than 80° ($|\theta| \geq 80°$), the left upper panel reveals no significant asymmetry in the magnetic field ratio for any magnetopause distance. The corresponding asymmetry plot (right upper panel) confirms the absence of an asymmetry, with values close to zero across the magnetosheath. This absence of asymmetry is expected for IMF conditions with a predominantly perpendicular orientation.

For IMF cone angles of $50° \leq |\theta| \leq 60°$, the left middle panel shows relatively similar asymmetries between the quasi-parallel and quasi-perpendicular sides near the bow shock and in the middle of the magnetosheath. However, the asymmetry seems to have almost disappeared near the magnetopause. The middle panel on the right shows that the asymmetry is relatively similar near the bow shock and in the middle of the magnetosheath, increasing from the subsolar region to the terminator ($X_{SWI} = 0$), reaching values about 20% higher in the quasi-perpendicular side. Near the magnetopause, the asymmetry shows significant variability and is perhaps a little bit positive in the quasi-perpendicular region if not zero.

Finally, for IMF cone angles of $20° \leq |\theta| \leq 30°$, the left bottom panel reveals higher values in the magnetic field ratio on the quasi-perpendicular throughout the magnetosheath thickness. The asymmetry plot in the bottom right panel shows that the asymmetry near the shock and in the middle of the magnetosheath increases from the subsolar region to the terminator similarly. At the terminator, it reaches approximately 30% higher values in favor of the quasi-perpendicular side. In contrast, the asymmetry near the magnetopause appears to remain relatively constant with the quasi-perpendicular side exhibits magnetic field values approximately 10% stronger.

Figure 4.12 shows the average asymmetry in the magnetic field amplitude between the quasi-parallel and quasi-perpendicular sides in the equatorial region as a function of distance in the magnetosheath thickness (D_{msh}). For IMF cone angles greater than 80° ($|\theta| \geq 80°$), the average asymmetry remains relatively constant, with values close to zero, indicating a lack of distinct asymmetry throughout the magnetosheath. For IMF cone angles between 50° and 60° ($50° \leq |\theta| \leq 60°$), the average asymmetry indicates that the quasi-perpendicular side of the magnetosheath has higher values of about 8% from the shock to the middle of the magnetosheath, and then decreases to 2.5% near the magnetopause. For IMF cone angles between 20° and 30° ($20° \leq |\theta| \leq 30°$), the average asymmetry remains relatively constant throughout most of the magnetosheath, with values approximately 15% higher on the quasi-perpendicular side. However, this asymmetry decreases closer to the magnetopause ($D_{msh} \leq 0.2$) to about 6%.

Overall, the asymmetry in the magnetic field amplitude between the quasi-perpendicular and quasi-parallel sides of the magnetosheath decreases as the IMF cone angle increases and presents smaller values at the magnetopause than in the rest of the magnetosheath. It should be noted that no clear effect of the IMF clock angle on the magnetic field asymmetry was observed.

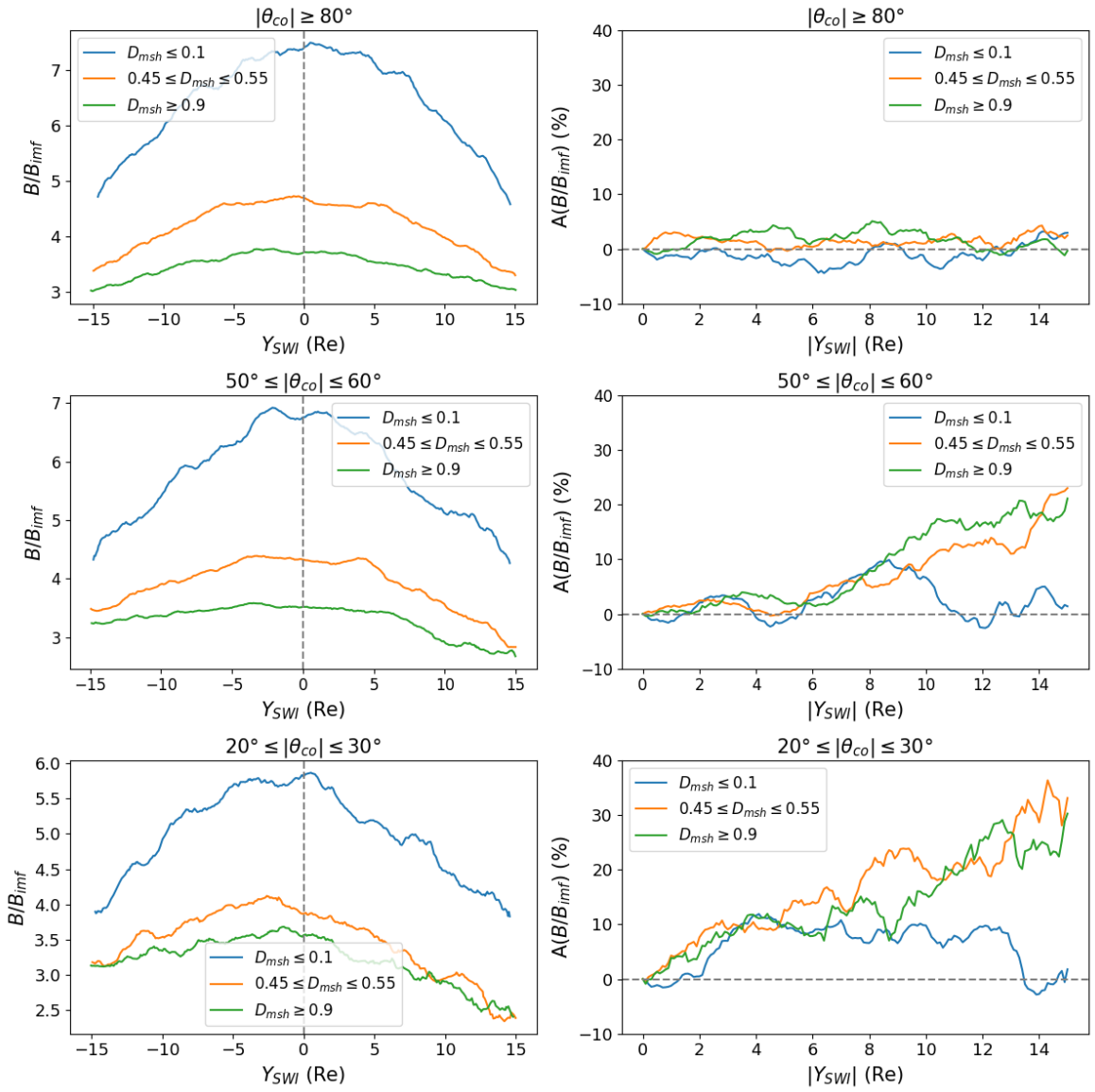

Figure 4.11: The left panels shows the distribution of the magnetic field amplitude as a function of Y_{SWI}. The right panels show the asymmetry $A(B/B_{imf})$ (Equation 4.2) between the quasi-parallel and quasi-perpendicular side of the magnetosheath. The top, middle, and last row correspond to IMF cone angles of $|\theta| \geq 80°$, $50° \leq |\theta| \leq 60°$, $20° \leq |\theta| \leq 30°$, respectively. The green, orange, and blue lines correspond to the magnetic field amplitude or asymmetry near the bow shock ($D_{msh} \geq 0.9$), in the center of the magnetosheath ($0.45 \leq D_{msh} \leq 0.55$), and near the magnetopause ($D_{msh} \leq 0.1$), respectively.

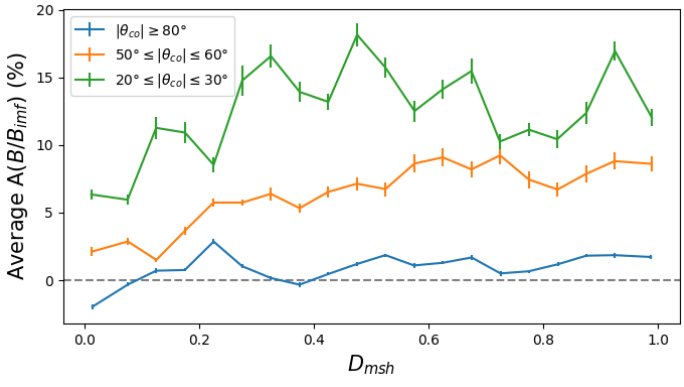

Figure 4.12: Average asymmetry $A(B/B_{imf})$ (Equation 4.2) in the magnetic field amplitude between the quasi-parallel and quasi-perpendicular as a function of the magnetosheath distance (D_{msh})

4.4.2 Asymmetry in the plasma density

Figure 4.13 presents the ratio of the plasma density and its asymmetry between the quasi-parallel ($Y_{SWI} \geq 0$) and quasi-perpendicular ($Y_{SWI} \leq 0$) sides of the equatorial region of the magnetosheath.

For all IMF cone angles (left panels), the density in the flanks ($|Y_{SWI}| \geq 5$ Re) at the magnetopause is smaller than in the center of the magnetosheath, indicating the presence of a PDL in these regions. Interestingly, the presence of these flank PDLs seems to be relatively independent of magnetic field amplitude and IMF cone angle.

For IMF cone angles greater than 80° ($|\theta| \geq 80°$), the density values are the highest in the middle of the magnetosheath, and the density ratio near the magnetopause is smaller than in proximity to the bow shock, confirming, for different Y positions, what was already seen in the subsolar region in Figure 4.8. The profiles do not show any asymmetries between the quasi-parallel and quasi-perpendicular sides of the magnetosheath. This is confirmed in the corresponding asymmetry plot (right upper panel) where the values remains close to zero from the shock to the magnetopause. The absence of asymmetry in the density ratio for such IMF cone angles is consistent with the lack of asymmetry observed in the magnetic field amplitude (upper panels of Figure 4.11).

For IMF cone angles between 50° and 60° ($50° \leq |\theta| \leq 60°$), the density ratio (left middle panel) is slightly higher in the subsolar magnetopause than near the bow shock, while remaining maximum in the middle of the magnetosheath, again consistently with Figure 4.8. The density ratio profile in the equatorial region does not exhibit a clear asymmetry between the quasi-perpendicular and quasi-parallel sides of the magnetosheath near the bow shock. However, at greater distances, in the center of the magnetosheath and near the magnetopause, the quasi-parallel side shows higher values than the quasi-perpendicular side. In the right middle panel, the values of the asymmetry near the bow shock vary around zero, indicating no distinct asymmetry in this region. In contrast, in the center of the magnetosheath and near the magnetopause, the asymmetry increases from the subsolar region to the terminator, reaching values about 15% higher in the quasi-parallel side. Note that in contrast to the magnetic field (middle panels of Figure 4.11), the asymmetry in the density ratio seems to increase from the shock to the magnetopause.

The left bottom panel shows the density profile for IMF cone angles between 20° and 30° ($20° \leq |\theta| \leq 30°$). The density ratio profile in the vicinity of the bow shock shows higher values in the quasi-perpendicular than in the quasi-parallel side of the magnetosheath. In contrast, in the middle of the magnetosheath this asymmetry seems to have disappeared, and near the magnetopause the asymmetry seems to have shifted in favor of the quasi-parallel side. This reversal of the asymmetry is shown clearly in the right middle panel. Near the bow shock side , the density values are about 10% higher on the quasi-perpendicular side than in the quasi-parallel. Conversely, near the magnetopause, the density ratio, while being more variable, is approximately 10% higher on the quasi-parallel side of the magnetosheath. And in between, no clear asymmetry is distinguishable in the middle of the magnetosheath. The reversal of the asymmetry between the quasi-perpendicular and quasi-parallel sides can be attributed to the combined effects of the compression downstream of the bow shock and the magnetic pileup near the magnetopause. The plasma is more compressed downstream of the quasi-perpendicular shock (see Figure 4.8). In contrast, the magnetic pileup, which is stronger on the quasi-perpendicular side near the magnetopause (bottom panels of Figure 4.11), induces a more significant depletion of plasma in this region, resulting in a higher density on the quasi-parallel side.

Figure 4.14 presents the asymmetry in the density ratio between the quasi-parallel and quasi-perpendicular sides in the equatorial region, averaged over Y_{SWI} and as a function of the position throughout the magnetosheath (D_{msh}). For IMF cone angles greater than 80° ($|\theta| \geq 80°$), the average asymmetry remains relatively constant, with values close to zero, indicating a lack of distinct asymmetry throughout the magnetosheath. For IMF cone angles between 50° and 60° ($50° \leq |\theta| \leq 60°$), the average asymmetry decrease from the values close to zero in proximity of the bow shock to approximately -8% near the magnetopause, indicating that the plasma density is larger in the quasi-parallel than in the quasi-perpendicular side of the magnetosheath. For IMF cone angles between 20° and 30° ($20° \leq |\theta| \leq 30°$), the average asymmetry decreases from approx-

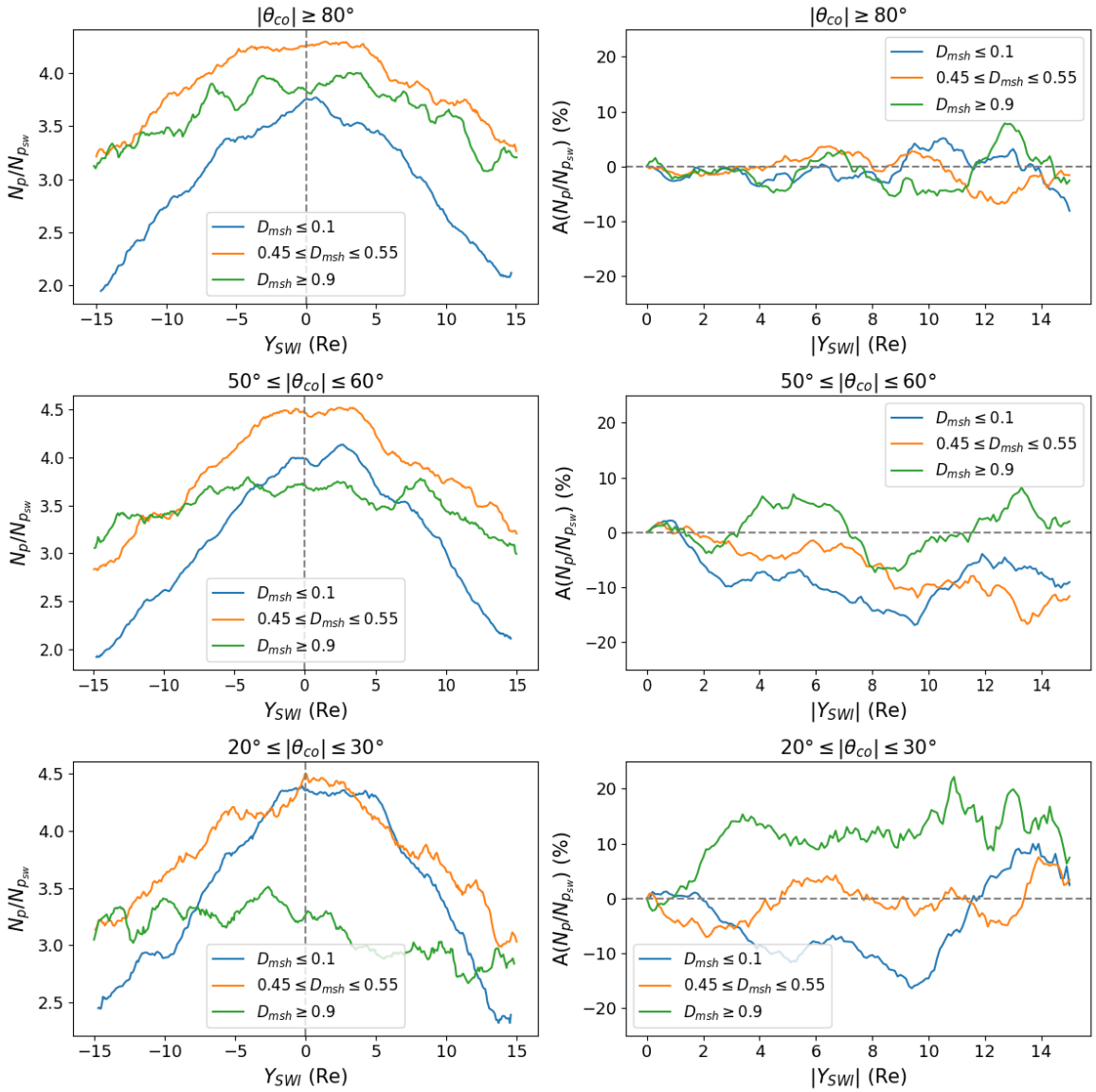

Figure 4.13: The left panels shows the distribution of the density ratio as a function of Y_{SWI}. The right panels show the asymmetry $A(N_p/N_{p_{sw}})$ (Equation 4.2) between the quasi-parallel and quasi-perpendicular side of the magnetosheath. The top, middle, and last row correspond to IMF cone angles of $|\theta| \geq 80°$, $50° \leq |\theta| \leq 60°$, $20° \leq |\theta| \leq 30°$, respectively. The green, orange, and blue lines correspond to the magnetic field amplitude or asymmetry near the bow shock ($D_{msh} \geq 0.9$), in the center of the magnetosheath ($0.45 \leq D_{msh} \leq 0.55$), and near the magnetopause ($D_{msh} \leq 0.1$), respectively.

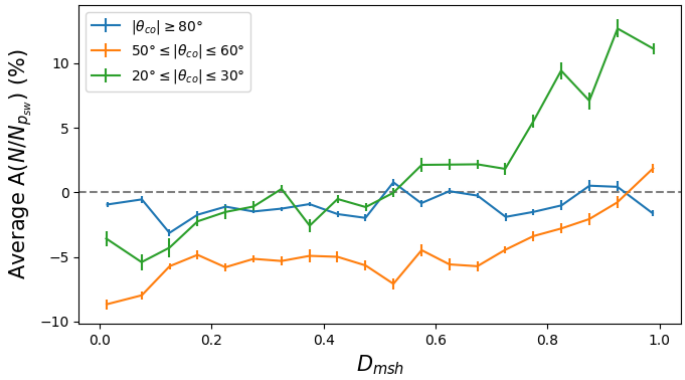

Figure 4.14: Average asymmetry A($N_p/N_{p_{sw}}$) (Equation 4.2) in the plasma density between the quasi-parallel and quasi-perpendicular as a function of the magnetosheath distance (D_{msh}).

imately 10% (i.e. higher density on the quasi-perpendicular side) to -5% (i.e. higher density on the quasi-parallel side) from the shock to the magnetopause. As mentioned above, this reversal of the density asymmetry between the quasi-perpendicular and quasi-parallel sides of the magnetosheath is attributed to the combined effects of the bow shock and magnetic pileup.

It should be noted that similarly to the magnetic field, no clear effect of the IMF clock angle on the density asymmetry was observed.

4.5 Discussion and Conclusion

The objective of this study was to investigate how the orientation of the IMF influences the formation and properties of the magnetic pileup and the PDL, as well as their interrelationships.

It was observed that the magnetic pileup decreases with the IMF cone angle. The velocity distribution in the magnetosheath suggests that a more radial orientation facilitates the circumvention of the magnetopause by the plasma, resulting in less magnetic compression at the boundary. Near the magnetopause, the magnetic pileup decreases as the IMF clock angle increases, which is consistent with the effect of magnetic reconnection eroding the magnetic pileup. This is supported by the increased velocity, suggesting more transport across the boundary and the presence of a tangential flows possibly related to reconnection outflows. Interestingly, this decrease of the magnetic pileup occurs rather abruptly when the IMF clock angle reaches on average (over IMF cone angles) a value of 60°. After this sudden change, the pileup appears to be almost constant with only a slight decrease. It is interesting to note that this angle of 60° is also reported by Phan et al. [1994] as a critical angle above which they observe no PDL.

The clock angle dependence of the magnetic pileup profile was not seen in Zhang et al. [2019]. The consistency of the signatures we observed also in the density and velocity let us think this is a real property of the near-magnetopause region, but one that can easily be missed if not carefully classifying, pairing and repositioning data points as we do in our methodology.

The decrease of the IMF cone angle induces a shallower PDL to the point where it even ceases to exists, for radial IMF conditions, as expected theoretically [Lees, 1964]. Interestingly, for large IMF cone angles, the plasma density at the magnetopause is found to be lower than at the bow shock. In most of the magnetosheath, no clear dependence of the plasma density on the IMF clock angle was observed but near the magnetopause the plasma depletion layers becomes less pronounced as the IMF clock angle increases. This is consistent with the effect of magnetic reconnection decreasing the magnetic pileup, thereby progressively removing the source of plasma depletion. Overall, there is an anti-correlation between the variation of the PDL and the amplitude of the magnetic field in the subsolar region. It should be noted that a PDL is seen in the flanks whose properties appear relatively independent of the IMF orientation.

Previous works, mentioned in the introduction, were mostly addressing the problem from a

local point of view, i.e. through the analysis of the data in the form of time series measured near magnetopause crossings. Consequently, previous results were mainly presenting the properties of flux pileup and plasma depletion as a function of the local magnetic shear. However, as we have seen in Chapter 3, the magnetic orientation in the magnetosheath (therefore the magnetic shear) is quite inhomogeneous on the magnetopause surface, whatever the orientation of the upstream IMF, thereby leaving the understanding of what happens in the global magnetosheath as a function of the IMF orientation relatively unclear. In contrast, this study offers a global, average, and consistent overview of the state of the magnetosheath, and in particular in the way the magnetic field and density behave in the dayside.

Above findings are then complemented by the investigation of magnetosheath asymmetries in the magnetic field amplitude and density, as well as their evolution from the bow shock to the magnetopause.

The magnetic field strength exhibits an asymmetry between the quasi-perpendicular and quasi-parallel sides of the magnetosheath, with higher values observed on the quasi-perpendicular side. This asymmetry decreases with the increase of the IMF cone angle with no clear asymmetry at large IMF cone angle. The asymmetry and the effect of the IMF cone angle seem to be consistent with the a larger compression of the magnetic field on the quasi-perpendicular side of the bow shock. The asymmetry between the quasi-parallel and quasi-perpendicular sides of the magnetosheath was found to decrease from the shock to the magnetopause. The origin of the isotropization of the pileup is at the moment still unclear but it is already quite important to report that magnetopause reconnection does not see the well known asymmetry downstream of the shock, as one could probably have thought. Finally, no clear effect of the IMF clock angle on the magnetic field asymmetry was observed.

The plasma density asymmetry exhibits more complex variations than that of the magnetic field. When the IMF is almost perpendicular to the Sun-Earth axis, no clear asymmetry is visible. For IMF cone angles in the range of the Parker spiral orientation ($50° \leq |\theta| \leq 60°$), the asymmetry is found to increase from the bow shock to the magnetopause, exhibiting larger values on the quasi-parallel side of the magnetosheath. However, when the IMF cone angle decreases ($20° \leq |\theta| \leq 30°$), such as at the quasi-parallel bow shock localizes in the dayside, there is a reversal of the asymmetry between the quasi-perpendicular and quasi-parallel sides of the magnetosheath. This reversal can be attributed to the combined effects of the bow shock and magnetic pileup. Near the bow shock, larger density values are found on the quasi-perpendicular side as expected. Conversely, near the magnetopause, larger density values are found on the quasi-parallel side because of the less pronounced PDL therein. Similarly to the asymmetry in the magnetic field strength, no clear effect of the IMF clock angle on the density asymmetry was observed.

To conclude this last part of our work, we can say that, as previous studies, we do not notice an influence of the IMF clock angle on the asymmetry of the magnetoseath. However we do notice an influence of the IMF cone angle that previous studies did not report. We think the reversal of the asymmetry we observe at mid-magnetosheath is key to explain why previous works, focused on asymmetries integrated throughout the magnetosheath thickness, could not detect this asymmetry.

This study calls for several future investigations. First, the state of the magnetosheath is only looked through its dependency on the IMF orientation. Although critical, this parameter is, by far, not the only one to be important. Future works should focus on the dependence on the upstream Mach number or plasma beta and its relationship with the diamagnetic suppression of reconnection at the magnetopause Swisdak et al. [2003], among others. Future work should also focus on conducting a more thorough analysis of the coupling between reconnection at the magnetopause and the observed properties of the pileup and depletion layer. In particular it could be important to investigate to what extent the reconnection rate somehow saturates for IMF clock angles above 90° and/or is not large enough to prevent further reduction of the pileup as we observed. It could also be interesting to relate the magnetic field variation to the total plasma pressure instead of just the density. Using the temperature statistically as we do in the thesis is, however, more subject to

caution as data products for this second order moments show more heterogeneity across missions and instruments.

Through Chapters 3 and 4, we now have a much better understanding of the properties of the orientation and amplitude of the magnetic throughout the magnetosheath, as well as for the plasma density. The following Chapter will move on with using these results, along with similar processing on the magnetospheric side, to reconstruct the state of the magnetopause itself, as a function of the IMF orientation, in order to better constrain, from an observational standpoint, how reconnection occurs there.

4.6 Bibliography

Anderson, B. J. and Fuselier, S. A.: Magnetic pulsations from 0.1 to 4.0 Hz and associated plasma properties in the Earth's subsolar magnetosheath and plasma depletion layer, , 98, 1461–1480, https://doi.org/10.1029/92JA02197, 1993. 102

Anderson, B. J., Phan, T. D., and Fuselier, S. A.: Relationships between plasma depletion and subsolar reconnection, , 102, 9531–9542, https://doi.org/10.1029/97JA00173, 1997. 102

Borovsky, J. E.: Physical improvements to the solar wind reconnection control function for the Earth's magnetosphere, Journal of Geophysical Research (Space Physics), 118, 2113–2121, https://doi.org/10.1002/jgra.50110, 2013. 102

Cairns, I. H. and Fuselier, S. A.: The Plasma Depletion Layer Beyond the Heliopause: Evidence, Implications, and Predictions for Voyager 2 and New Horizons, , 834, 197, https://doi.org/10.3847/1538-4357/834/2/197, 2017. 102

Cassak, P. A. and Shay, M. A.: Scaling of asymmetric magnetic reconnection: General theory and collisional simulations, Physics of Plasmas, 14, 102114, https://doi.org/10.1063/1.2795630, 2007. 102

Crooker, N. U., Eastman, T. E., and Stiles, G. S.: Observations of plasma depletion in the magnetosheath at the dayside magnetopause, , 84, 869–874, https://doi.org/10.1029/JA084iA03p00869, 1979. 102

Fuselier, S. A., Klumpar, D. M., Shelley, E. G., Anderson, B. J., and Coates, A. J.: He^{2+} and H^+ dynamics in the subsolar magnetosheath and plasma depletion layer, , 96, 21 095–21 104, https://doi.org/10.1029/91JA02145, 1991. 102

Gershman, D. J., Slavin, J. A., Raines, J. M., Zurbuchen, T. H., Anderson, B. J., Korth, H., Baker, D. N., and Solomon, S. C.: Magnetic flux pileup and plasma depletion in Mercury's subsolar magnetosheath, Journal of Geophysical Research (Space Physics), 118, 7181–7199, https://doi.org/10.1002/2013JA019244, 2013. 102

Hall, D. S., Hapgood, M. A., and Bryant, D. A.: The transition from the magnetosheath to the magnetosphere, , 17, 2039–2042, https://doi.org/10.1029/GL017i011p02039, 1990. 102

Jelínek, K., Němeček, Z., and Šafránková, J.: A new approach to magnetopause and bow shock modeling based on automated region identification, Journal of Geophysical Research (Space Physics), 117, A05208, https://doi.org/10.1029/2011JA017252, 2012. 103

King, J. H. and Papitashvili, N. E.: Solar wind spatial scales in and comparisons of hourly Wind and ACE plasma and magnetic field data, Journal of Geophysical Research (Space Physics), 110, A02104, https://doi.org/10.1029/2004JA010649, 2005. 103

Lees, L.: Interaction between the solar plasma wind and the geomagnetic cavity, AIAA Journal, 2, 1576–1582, 1964. 102, 116

Longmore, M., Schwartz, S. J., Geach, J., Cooling, B. M. A., Dandouras, I., Lucek, E. A., and Fazakerley, A. N.: Dawn-dusk asymmetries and sub-Alfvénic flow in the high and low latitude magnetosheath, Annales Geophysicae, 23, 3351–3364, https://doi.org/10.5194/angeo-23-3351-2005, 2005. 103

Masters, A., Phan, T. D., Badman, S. V., Hasegawa, H., Fujimoto, M., Russell, C. T., Coates, A. J., and Dougherty, M. K.: The plasma depletion layer in Saturn's magnetosheath, Journal of Geophysical Research (Space Physics), 119, 121–130, https://doi.org/10.1002/2013JA019516, 2014. 102

Nguyen, G., Aunai, N., Michotte de Welle, B., Jeandet, A., Lavraud, B., and Fontaine, D.: Massive Multi-Mission Statistical Study and Analytical Modeling of the Earth's Magnetopause: 1. A Gradient Boosting Based Automatic Detection of Near-Earth Regions, Journal of Geophysical Research (Space Physics), 127, e29773, https://doi.org/10.1029/2021JA029773, 2022. 103

Němeček, Z., Šafránková, J., Zastenker, G. N., Pišoft, P., and Paularena, K. I.: Spatial distribution of the magnetosheath ion flux, Advances in Space Research, 30, 2751–2756, https://doi.org/10.1016/S0273-1177(02)80402-1, 2002. 103

Paschmann, G., Sckopke, N., Haerendel, G., Papamastorakis, J., Bame, S. J., Asbridge, J. R., Gosling, J. T., Hones, E. W., J., and Tech, E. R.: ISEE Plasma Observations near the Subsolar Magnetopause (Article published in the special issues: Advances in Magnetospheric Physics with GEOS- 1 and ISEE - 1 and 2.), , 22, 717–737, https://doi.org/10.1007/BF00212620, 1978. 102

Paschmann, G., Baumjohann, W., Sckopke, N., Phan, T. D., and Luehr, H.: Structure of the dayside magnetopause for low magnetic shear, , 98, 13 409–13 422, https://doi.org/10.1029/93JA00646, 1993. 102

Paularena, K. I., Richardson, J. D., Kolpak, M. A., Jackson, C. R., and Siscoe, G. L.: A dawn-dusk density asymmetry in Earth's magnetosheath, , 106, 25 377–25 394, https://doi.org/10.1029/2000JA000177, 2001. 103

Phan, T. D., Paschmann, G., Baumjohann, W., Sckopke, N., and Luehr, H.: The magnetosheath region adjacent to the dayside magnetopause: AMPTE/IRM observations, , 99, 121–142, https://doi.org/10.1029/93JA02444, 1994. 102, 116

Pudovkin, M. I., Besser, B. P., Zaitseva, S. A., Lebedeva, V. V., and Meister, C. V.: Magnetic barrier in case of a southward interplanetary magnetic field, Journal of Atmospheric and Solar-Terrestrial Physics, 63, 1075–1083, https://doi.org/10.1016/S1364-6826(01)00023-2, 2001. 102

Shue, J. H., Song, P., Russell, C. T., Steinberg, J. T., Chao, J. K., Zastenker, G., Vaisberg, O. L., Kokubun, S., Singer, H. J., Detman, T. R., and Kawano, H.: Magnetopause location under extreme solar wind conditions, JGR, 103, 17 691–17 700, https://doi.org/10.1029/98JA01103, 1998. 103

Song, P., Russell, C. T., Gosling, J. T., Thomsen, M., and Elphic, R. C.: Observations of the density profile in the magnetosheath near the stagnation streamline, , 17, 2035–2038, https://doi.org/10.1029/GL017i011p02035, 1990. 102

Swisdak, M. and Drake, J. F.: Orientation of the reconnection X-line, , 34, L11106, https://doi.org/10.1029/2007GL029815, 2007. 102

Swisdak, M., Rogers, B. N., Drake, J. F., and Shay, M. A.: Diamagnetic suppression of component magnetic reconnection at the magnetopause, Journal of Geophysical Research (Space Physics), 108, 1218, https://doi.org/10.1029/2002JA009726, 2003. 117

Šafránková, J., Přech, L., Němeček, Z., and Sauvaud, J. A.: Density profile in the magnetosheath adjacent to the magnetopause, Advances in Space Research, 30, 1693–1703, https://doi.org/10.1016/S0273-1177(02)00438-6, 2002. 102, 103

Walsh, A. P., Haaland, S., Forsyth, C., Keesee, A. M., Kissinger, J., Li, K., Runov, A., Soucek, J., Walsh, B. M., Wing, S., and Taylor, M. G. G. T.: Dawn-dusk asymmetries in the coupled solar wind-magnetosphere-ionosphere system: a review, Annales Geophysicae, 32, 705–737, https://doi.org/10.5194/angeo-32-705-2014, 2014. 103

Walsh, B. M., Sibeck, D. G., Wang, Y., and Fairfield, D. H.: Dawn-dusk asymmetries in the Earth's magnetosheath, Journal of Geophysical Research (Space Physics), 117, A12211, https://doi.org/10.1029/2012JA018240, 2012. 103

Walters, G. K.: Effect of Oblique Interplanetary Magnetic Field on Shape and Behavior of the Magnetosphere, , 69, 1769–1783, https://doi.org/10.1029/JZ069i009p01769, 1964. 102

Zhang, H., Fu, S., Pu, Z., Lu, J., Zhong, J., Zhu, C., Wan, W., and Liu, L.: Statistics on the Magnetosheath Properties Related to Magnetopause Magnetic Reconnection, , 880, 122, https://doi.org/10.3847/1538-4357/ab290e, 2019. 102, 116

Zwan, B. J. and Wolf, R. A.: Depletion of solar wind plasma near a planetary boundary, , 81, 1636, https://doi.org/10.1029/JA081i010p01636, 1976. 102

Chapter 5

Global Contraints on Magnetic Reconnection at the Magnetopause

Contents

5.1 Introduction

In the chapter 3, we reconstructed in detail the magnetic draping of the IMF in the magnetosheath. The study showed that it is possible to globally access the orientation of the magnetic field, critical in the reconnection process [Hesse et al., 2013; Moore et al., 2002], on the most variable side of the magnetopause using only in-situ measurement. The chapter 4 focused on the spatial variation of the equally important [Borovsky, 2013; Cassak and Shay, 2007; Swisdak and Drake, 2007] magnetic field amplitude and density throughout the dayside magnetosheath. The objective of this chapter is to reconstruct the spatial distribution of quantities relevant to the reconnection process on the magnetopause. Furthermore, we will examine the implications of these spatial distributions on the location of magnetic reconnection.

On the magnetopause, observational evidence indicate it could occur along an extended line [Dunlop et al., 2011; Phan et al., 2000, 2001, 2006; Walsh et al., 2017; Zhou et al., 2017]. Such a long X-line has also been seen in global magnetohydrodynamic (MHD) simulations [Eggington et al., 2020; Glocer et al., 2016; Komar et al., 2015; Souza et al., 2017]. However, its precise location on the magnetopause, as a function of solar wind and interplanetary magnetic field (IMF) conditions remains a challenging open question. Determining that location is crucial, as the efficiency of reconnection strongly depends on the local properties of the plasma and the magnetic field [Axford, 1969; Borovsky and Birn, 2014; Borovsky et al., 2008; Cassak and Shay, 2007; Vasyliunas, 1975], which significantly vary along the magnetopause surface [Dimmock and Nykyri, 2013; Dimmock et al., 2014, 2016; Zhang et al., 2019]. Historically, the X-line was considered to locate only in regions separating anti-parallel magnetic fields [Crooker et al., 1979; Dungey, 1961; Luhmann et al., 1984]. Numerous observations (e.g. Daly et al. [1984]; Pu et al. [2005]; Scurry et al. [1994]) of reconnection signatures consistent with the merging of only components of the field, however, later favored the alternative idea of possible non-coplanar merging [Cooling et al., 2001; Cowley and Owen, 1989; Gonzalez and Mozer, 1974; Hill, 1975; Moore et al., 2002; Sonnerup, 1974]. The reconnection of non-coplanar magnetic fields, however, vastly complicates the problem of locating the X-line, enabling it to explore much wider range of conditions and locations on the magnetopause surface. Several studies have then be dedicated to finding physical effects and observational evidence that would help narrowing down the possible regions where X-lines could be found on the magnetopause.

Observations and analysis of low-speed cutoff in cusp ion distributions [Onsager et al., 1991], and later of ion flow reversals [Trattner et al., 2017, 2021], were found to correlate well with regions on the magnetopause where analytical models predict a large magnetic shear. This led to the empirical proposition that, given a global map of the magnetic shear for some IMF orientation and dipole tilt angle, the X-line is a global line traversing regions maximizing the shear angle. More specifically, the so-called *Maximum Magnetic Shear model*, predicts that, for strongly southward IMF ($155^\circ < \theta_{cl} \equiv \tan^{-1}(B_y/B_z) < 205^\circ$ with $\theta_{cl} \in [0, 2\pi]$) or for a dominant B_x component ($B_x/\|\mathbf{B}\| > 0.7$), the X-line would be localized in anti-parallel regions. For other conditions, the X-line would mostly traverse the dayside magnetopause where the shear is maximum to join anti-parallel regions in the flanks [Trattner et al., 2016, 2021].

The maximum shear model has difficulties explaining reconnection signatures observed at times where the IMF shows a dominant B_x component (typically when the IMF cone angle $\theta_{co} = \tan^{-1}\left(\sqrt{B_y^2 + B_z^2}/B_x\right)$ is less than 45°) Trattner et al. [2021]. A possible explanation for these difficulties stands in the inacurate draping predicted by the Kobel & Fluckiger current-free magnetostatic model [Kobel and Fluckiger, 1994], hereafter noted as KF94, at the root of the shear maps used to compute the X-line location [Trattner et al., 2012b, 2021]. Chapter 3 revealed that the 3D magnetic draping reconstructed from in-situ measurements indeed significantly differs from the magnetostatic predictions for conditions where the IMF cone angle $|\theta_{co}|$ is comprised between $12.5^\circ \pm 2.5^\circ$ and $45.0^\circ \pm 5^\circ$, owing to the important role of the plasma flow in the magnetosheath.

Besides observational evidence at the root of the model, maximizing the magnetic shear also makes sense from a theoretical perspective if considering reconnection lies in regions that are the

most favorable for either its onset or fast reconnection rates, and if maximum magnetic shear regions are seen as a good proxy of these locations. However, both the onset via the tearing instability [Daughton and Karimabadi, 2005; Drake and Lee, 1977], and fast reconnection rates in the nonlinear regime, more fundamentally depend on other quantities such as the current Alexeev et al. [1998] and plasma densities and the magnetic field amplitude jump across the magnetopause [Birn and Priest, 2007]. These parameters, despite their obvious correlation with the magnetic shear, have, a priori, no reason to be distributed along the magnetopause surface exactly the same way. In other words, regions maximizing the magnetic shear may not be those where the current density or the reconnection rate are the most favorable for either the onset or a fast reconnection rate. Realistic spatial distributions of these more fundamental quantities are, however, more difficult to obtain than that of the magnetic shear. Today, such global distributions are obtained from global MHD simulations. A study based on global MHD simulations [Komar et al., 2015] have shown that the self consistent topological separator along which reconnection occurs often correlates well with the maximization of the current density, the magnetic shear or reconnection rate [Borovsky, 2013] and outflow speed scaling laws [Swisdak and Drake, 2007]. However, the IMF and dipole configurations that were used did not result in significant differences among the various theoretical predictions. Results also showed cases, such as for northward IMF with an important dipole tilt angle, where none of the lines maximizing the above quantities were consistent with the topological separator obtained in the simulation. Finding conditions where the maximization of the above quantities leads to well-differentiated predictions will require computationally heavy parametric studies, with a deeper exploration of the role of the IMF cone angle and the tilt of the geomagnetic dipole, which are still poorly understood despite their likely importance.

It is important to note that the above ideas, consisting in the construction of an X-line on the magnetopause surface from the maximization of a specific quantity, given its spatial distribution on the magnetopause, *de facto* also imposes the local orientation of that X-line with respect to the magnetic field on each side of the boundary at that location. In this paradigm, that we shall identify as the *global approach* to the localization problem, the local orientation of an X-line, can thus only be determined with the knowledge of the global state of the magnetopause. Interestingly, however, simulations of isolated asymmetric current sheets separating magnetic field sheared by some arbitrary but uniform angle [Aunai et al., 2016; Hesse et al., 2013; Liu et al., 2015a, 2018; Swisdak et al., 2003], still end up with an X-line aligned with a specific orientation, which, in this case, can only result from local physics, which is, moreover, often neglected in global MHD models. The mechanisms imagined to constrain the local orientation of an X-line in this approach incidentally also follow the idea consisting in maximizing the efficiency of the process. Several effects have been considered, which are not mutually exclusive, such as the diamagnetic drift of the X-line [Swisdak et al., 2003], the importance of the "magnetic energy" available in the reconnecting components [Hesse et al., 2013], the preferred orientation of tearing modes [Liu et al., 2015a, 2018], or maximizing the outflow velocity [Swisdak and Drake, 2007]. These studies can be gathered into what we shall call the *local approach* to the localization problem, for which a global line would result from following local orientations determined by such local effects. This local approach has already been considered in a previous work [Moore et al., 2002] where a global line results from following the local bisector of analytical models of the magnetic field in the magnetosheath and magnetosphere. Interestingly, the orientation of the bisection, followed somewhat arbitrarily in the aforementioned study, has later been found in several self consistent 2D and 3D full and hybrid PIC simulations as the one favoring the fastest rate of all orientations [Aunai et al., 2016; Hesse et al., 2013; Liu et al., 2015a, 2018].

Whether it concerns the local or the global approach, the spatial distribution of key quantities on the magnetopause usually emanates from analytical or numerical models and remains largely unknown from an observational standpoint. The reconstruction of the magnetic field draping throughout the global magnetosheath in chapter 3, and in particular adjacent to the magnetopause, from large statistical analysis of multi-mission data, has opened up an opportunity for investigating the detailed spatial distributions of these quantities and their dependence on the

IMF orientation and dipole tilt angle. This study therefore aims to revisit the problem of localizing the reconnection X-line on the magnetopause, this time from in-situ measurements only, following this large-scale, multi-mission statistical analysis methodology.

The second section of this chapter explains the different steps to reconstruct the global constraints on the magnetopause. We then start by investigating to what extent magnetic shear maps obtained from magnetic field models, often used today to predict the location of X-lines, resemble those reconstructed from in-situ measurements. Section 5.3 establishes this comparison, for typical large, intermediate and low IMF cone angle conditions. To go beyond the sole usage of the magnetic shear, section 5.4 presents magnetopause maps of the current density and of what we call the *potential reconnection rate*, i.e. the rate at which reconnection would locally proceed if it was occurring there, based on the evaluation of an MHD scaling law [Cassak and Shay, 2007]. These quantities are chosen for their very basic and general role in magnetic reconnection, and because they have been among the most discussed so far in the aforementioned literature. Other quantities, such as the density of cold and heavy ions populations [Toledo-Redondo et al., 2021], the plasma beta [Phan et al., 2013; Swisdak et al., 2003], the solar wind Mach number, etc. are also known to impact dayside reconnection. Taking them into account, however, shall come in a more refined version of this work at later times not to complicate the already many outcomes of this study. A possible way to include these effects while keeping the same driving idea, would be to include their impact in the reconnection rate estimate. These global maps are then analyzed for various IMF orientations and dipole tilt angles. In each of these configurations, we compute and show the X-line that maximizes the distribution of the magnetic shear, the current density and potential reconnection rate, following the global approach. We discuss how the produced X-lines vary across the various quantities, and also how they evolve with the changing of the IMF orientation and dipole tilt. Lastly, section 5.5 examines to what extent following the local approach results in different X-lines than the global approach. The results are then summarized and discussed in section 5.6.

5.2 Method

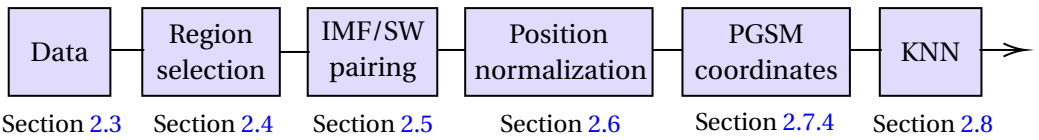

Figure 5.1: Overview of the global methodology detailed in Chapter 2.

This work relies on the different steps of the global methodology, detailed in the Chapter 2, synthesized in Figure 5.1. This method entails utilizing data collected by the Cluster, Double Star, THEMIS, and MMS missions (see Section 2.3) from which almost all magnetosheath and magnetosphere measurements are identified using a trained Gradient Boosting Classifier [Nguyen et al., 2022a] (see Section 2.4). Studying the global constraint on magnetic reconnection as a function of the IMF orientation requires pairing each measurement with the properties of its causal IMF and solar wind using OMNI data [King and Papitashvili, 2005] and a transport method [Šafránková et al., 2002] (see Section 2.5). Two points close spatially may be at different distances from the magnetopause and bow shock for their respective solar wind and IMF conditions. Therefore, to give a fair spatial representation of spatial physical properties near the magnetopause, it is necessary to re-position each data point relatively to the same bow shock and magnetopause. The position of each data point relative to the bow shock and the magnetopause at the time of the measurement is estimated using Gradient Boosting Regression models of the boundaries, parameterized with solar wind and IMF conditions (see Section 2.6). Using these relative distances to the magnetopause and bow shock, all points are re-positioned between a standard couple of boundaries [Jelínek et al., 2012; Shue et al., 1998] parameterized with average solar wind conditions (i.e. dynamic pressure of

2nPa and $B_{z_{imf}}$ = 0 nT). Then all measurements were converted from GSM to PGSM coordinates. The PGSM coordinate system was specifically designed in this PhD study to obtain good spatial coverage of the spatial distributions of the physical properties at the magnetopause using in-situ data (see Section 2.7.4). Subsequently, KNN algorithm is used to compute the distance-weighted average of the K closest measurements to a desired position (see Section 2.8). The KNN is thus used to predict the value of the considered quantity at each node of a meshed surface obtained with the magnetopause model [Shue et al., 1998] parameterized with average solar wind and IMF conditions. This enables the determination of spatial distributions for quantities, such as magnetic field or ion density, at the magnetopause.

From there, we determine the global distributions of the magnetic shear angle, current density, and reconnection rate asymmetric MHD scaling law estimate at the magnetopause using the method detailed in Section 5.2.1. The magnetic shear angle at the magnetopause is also computed using models of magnetic field (i.e. Tsyganenko and Stern [1996] (T96) and Kobel and Fluckiger [1994] (KF94)), as described in Section 5.2.2, to be compared to the maps of the same quantity obtained with in-situ measurements. Finally, Section 5.2.3 describes the determination of candidate X-lines that maximize each of the above quantities.

5.2.1 Global distributions at the magnetopause using in-situ measurements

Magnetic shear angle spatial distribution

The magnetic shear angle is determined by using the global distributions of the magnetic fields on both sides of the magnetopause. The KNN algorithm is used with data subsets selected based on a range of dipole tilt and IMF cone angles for the magnetosphere and the magnetosheath, respectively. Each magnetic field measurement, on the magnetosheath and magnetosphere, has a small component normal to the magnetopause surface used in our maps. Such a small normal component may be due to magnetic reconnection. But more probably, it arises from the local inconsistency between the smooth magnetopause surface we use for representation purposes, and the real magnetopause close to which measurements were made. For consistency with previous work, and because we aim at understanding how pristine magnetosheath and magnetosphere configurations could constrain reconnection at the magnetopause, we assume that the magnetic fields are tangential to the magnetopause surface. We thus remove from the magnetic field vectors obtained at each node of the meshed boundary surface, the small component locally normal to the surface. Finally, computing the line that maximizes the shear angle requires a smooth spatial distribution, so a gaussian filter with a standard deviation of about 2 Re is applied to both magnetic fields ($\mathbf{B}_{\mathrm{MSP}}$ and $\mathbf{B}_{\mathrm{MSH}}$) before calculating the magnetic shear angle with equation 5.1.

$$\theta = \cos^{-1}\left(\frac{\mathbf{B}_{\mathrm{MSP}} \cdot \mathbf{B}_{\mathrm{MSH}}}{\|\mathbf{B}_{\mathrm{MSP}}\| \|\mathbf{B}_{\mathrm{MSH}}\|}\right) \tag{5.1}$$

Current density spatial distribution

The global distribution of the current density **J** is calculated using the Ampere equation (Eq. 5.2) and the magnetic fields on each side of the magnetopause determined in the section 5.2.1. The calculation is done in a basis with one unit vector, $\widehat{\mathbf{N}}$, along the local normal to the magnetopause surface, and the other two unit vectors, $\widehat{\mathbf{L}}$ and $\widehat{\mathbf{M}}$, chosen such that the first one is along the magnetospheric magnetic field and the second completes the basis. It is necessary to make an assumption about the thickness of the magnetopause (d_{mp}) when calculating the current density. For simplicity, we used a uniform value of 800 km, which is consistent with the median magnetopause thickness [Haaland et al., 2020] ranging from 734±19 km in the dayside to 858±41 km and 927±53 km in the dusk and dawn flanks, respectively, as shown in Figure 5.2. It should be noticed that the current density we compute is the one associated with the large scale variation of the magnetic field across the magnetopause (i.e. it is not associated with local processes such as magnetic reconnection).

$$\mathbf{J} = \frac{\nabla \times \mathbf{B}}{\mu_0} = \mathrm{J}_l \widehat{\mathbf{L}} + \mathrm{J}_m \widehat{\mathbf{M}} \quad \text{with} \quad \begin{cases} \widehat{\mathbf{L}} & = \mathbf{B}_{\mathrm{MSP}} / \|\mathbf{B}_{\mathrm{MSP}}\| \\ \widehat{\mathbf{M}} & = \widehat{\mathbf{N}} \times \widehat{\mathbf{L}} \end{cases} \quad \text{and} \quad \begin{cases} \mathrm{J}_l & \approx \frac{-(\mathrm{B}_{m_{\mathrm{MSH}}} - \mathrm{B}_{m_{\mathrm{MSP}}})}{d_{\mathrm{mp}} \mu_0} \\ \mathrm{J}_m & \approx \frac{\mathrm{B}_{l_{\mathrm{MSH}}} - \mathrm{B}_{l_{\mathrm{MSP}}}}{d_{\mathrm{mp}} \mu_0} \end{cases} \tag{5.2}$$

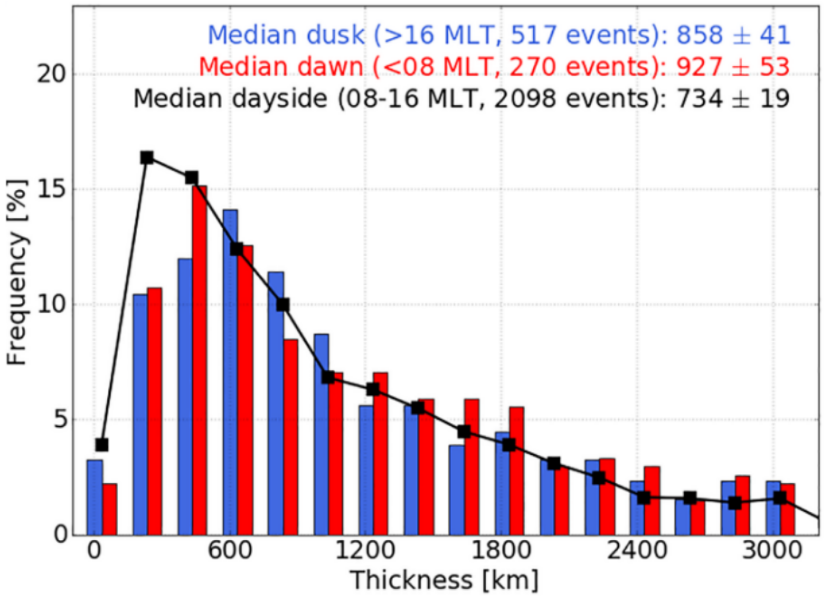

Figure 5.2: Histograms of the thickness in units of kilometers for the dayside, dawn and dusk magnetopause flanks. The Magnetic Local Time (MLT) coordinates correspond to the hour angle formed by the meridional plane that contain the subsolar point with the meridional plane of the considered position. Figure adapted from Haaland et al. [2020].

Reconnection rate spatial distribution

The reconnection rate (Equation 5.3) is determined using the Cassak-Shay scaling law for asymmetric upstream conditions [Cassak and Shay, 2007]. Additionally to the magnetic fields, it requires the global distribution of the particles density (ρ_{MSP} and ρ_{MSH}) on both side of the magnetopause. These densities are obtained using again the KNN algorithm on each node of the meshed magnetopause and then smoothed with a gaussian filter (see section 5.2.1). The Cassak-Shay scaling law was developed for anti-parallel magnetic fields. However, in general, the magnetic fields on each side of the magnetopause are not coplanar. In this study, we evaluate the Cassak-Shay equation using the reconnecting components of each fields. To proceed, we thus need to assume what they are, knowing the total magnetic field on both sides. Here, we assume the merging components are such that they maximize the prediction of the Cassak-Shay rate. More specifically, for an angle α between the X-line and the magnetospheric magnetic field such that the reconnection rate satisfies $\partial R/\partial\alpha = 0$ [Komar et al., 2015]. This choice is somewhat arbitrary. Tests were done if choosing components perpendicular to the local bisection of the magnetic fields and led to very similar results. In Equation 5.3, the aspect ratio δ/Δ is taken equal to 0.1 [Liu et al., 2017], θ is the magnetic shear angle (Equation 5.1) used with the angle α to determine the reconnected components of the magnetic fields on each side of the magnetopause.

$$R = \frac{2\delta}{\Delta} \frac{(\|\mathbf{B}_{\mathrm{MSP}}\| \sin(\alpha) \|\mathbf{B}_{\mathrm{MSH}}\| \sin(\theta - \alpha))^{3/2}}{\sqrt{\mu_0 (\|\mathbf{B}_{\mathrm{MSP}}\| \sin(\alpha) + \|\mathbf{B}_{\mathrm{MSH}}\| \sin(\theta - \alpha))(\rho_{\mathrm{MSH}} \|\mathbf{B}_{\mathrm{MSP}}\| \sin(\alpha) + \rho_{\mathrm{MSP}} \|\mathbf{B}_{\mathrm{MSH}}\| \sin(\theta - \alpha))}} \tag{5.3}$$

5.2.2 Modeled magnetic shear spatial distribution

Magnetic shear maps are also computed with modeled magnetic fields to compare to maps obtained with in-situ measurements. The magnetic field on the magnetosphere side of the mag-

netopause is calculated by combining the International Geomagnetic Reference Field (IGRF) and Tsyganenko and Stern [1996] models, noted as T96. This model predicts the presence in the dayside of open magnetic field lines produced by magnetic reconnection, as shown in the left panel of Figure 5.3. These open field lines result in a magnetic field non-tangential to the surface of the magnetopause and therefore in a magnetic shear out of the boundary plane. To be consistent with the assumption of tangential magnetopause made in the reconstruction of the shear angle distribution from in-situ data, we need to setup the T96 so to obtain closed field lines only. To do so, the IMF B_y and B_z components –B_x is not a parameter of the model– required in the T96 model are set to zero as shown in right panel of Figure 5.3. It should be noted that even when all the IMF components are set to zero, a few magnetic field lines may remain open in the northern cusp region (not shown in the right panel of Figure 5.3). Nevertheless, these magnetic field lines do not alter the local magnetic shear. The T96 model defines the magnetopause location based on the Sibeck et al. [1991] (S91) model, with modifications. Instead of having different parameterizations depending on the range of dynamic pressure (P_d), it only uses the parameters defined for $P_d \in [1.47, 2.60]$ nPa. This is the modified version of S91 that we used to mesh the magnetopause surface and determine the magnetospheric magnetic field.

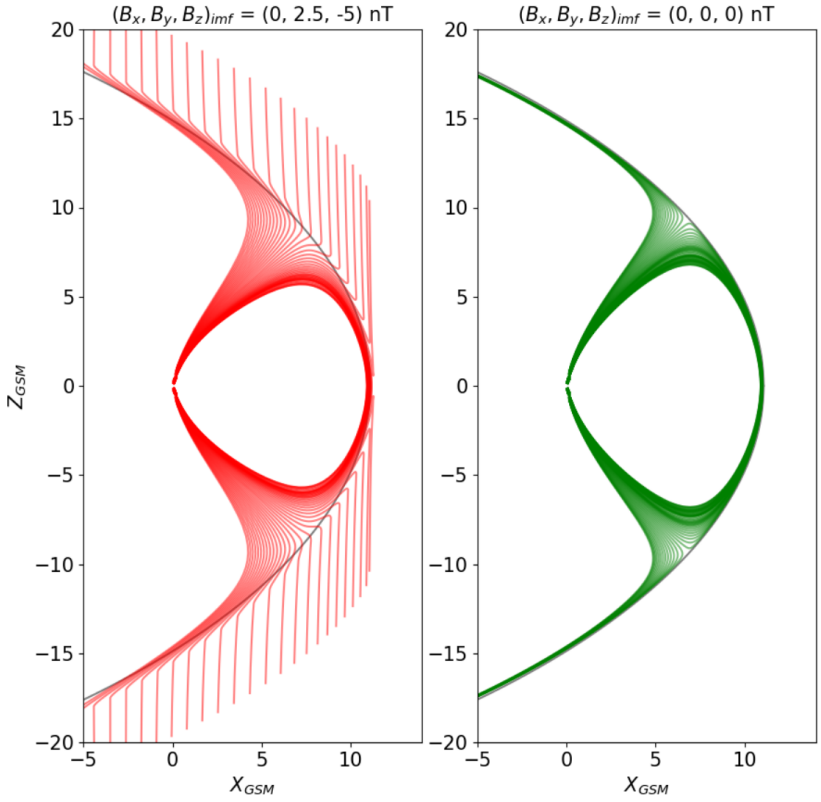

Figure 5.3: Magnetic field lines near the magnetopause obtained with the Tsyganenko and Stern [1996] model. In the left panel, the T96 model is parametrized with non-nul B_y and B_z components of the IMF, resulting in open magnetic field lines. In contrast, the right panel shows closed magnetic field lines when the B_y and B_z components of the IMF are set to zero.

Regarding the magnetosheath side of the magnetopause, the draped magnetic field is obtained using the Kobel and Fluckiger [1994] (KF94). As detailed in Annex B, it is defined by a magnetic potential valid between parabolic and confocal approximation of the magnetopause and bow shock. The modified version of the S91 model and the Jelínek et al. [2012] bow shock model are used to determine the parabolic and confocal approximation of the boundaries. However, this results in a magnetopause with a slightly different shape than that used to obtained the magnetospheric magnetic field. Therefore, to align the magnetic fields on both sides of the magnetopause, the magnetosheath magnetic field is estimated where the normal to the S91 surface intersects its parabolic approximation.

5.2.3 Line maximizing the global distribution of a quantity

Maximum magnetic shear lines

We start by explaining how to obtain a global line maximizing the distribution of the magnetic shear on the magnetopause that we shall call the Maximum Magnetic Shear Line (MSL). Figure 5.4 shows an example of the distribution of shear angle for an IMF clock angle of 130° and a cone angle pf 85° with no dipole tilt angle. Qualitatively, the MSL is line joining the anti-parallel regions by following the ridge of the shear angle distribution through the dayside subsolar region.

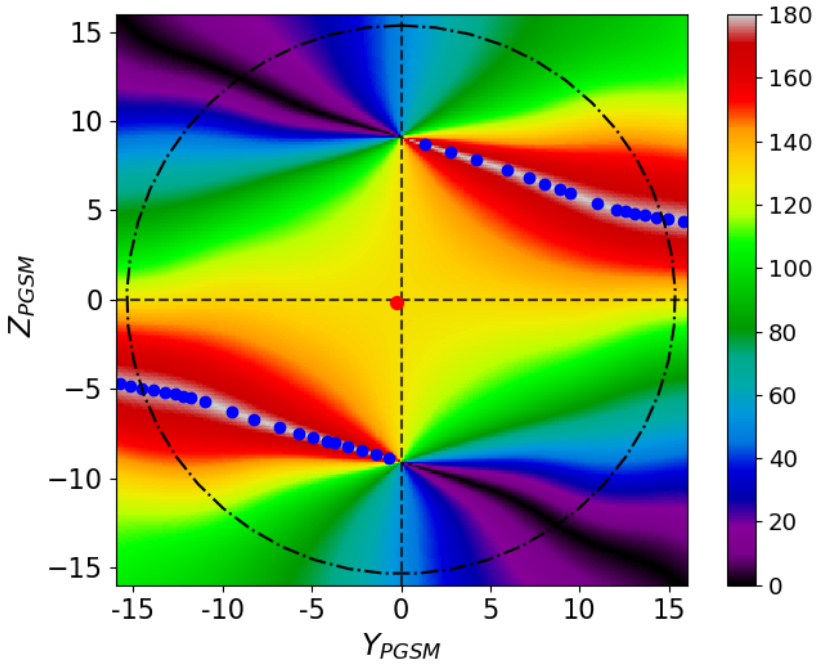

Figure 5.4: Magnetic shear angle obtained for in-situ measurements falling within the IMF cone angle range of $|\theta_{co}|$=85°±5° and dipole tilt angle of ψ=0°±2.5°. The IMF clock angle is set to 130° in the PGSM coordinate system (see Section 2.7.4). The blue and red points correspond to local maxima and the saddle point, respectively. The magnetopause terminator is represented by the dashed-dotted circle.

The component reconnection part of the MSL is obtained by integrating the magnetic shear gradient from the saddle point between the two anti-parallel branches. Following the gradient from the saddle point between two maxima enables obtaining the shortest line that maximizes a quantity.

A saddle point is a critical point (derivative is zero) that is not an extremum (minimum or maximum) and is located where the gradient of the distribution has positive values in certain directions and negative values in others. Therefore, a saddle point can be identified by the presence of eigenvalues of the Hessian matrix (square matrix of second-order partial derivatives) with opposite signs, indicating opposite signs of curvatures. For instance, the saddle point in the magnetic shear angle map of Figure 5.4 is marked with the red point.

At the saddle point, where the gradient is zero, the initial step of the integration follows the eigenvector corresponding to the largest eigenvalue of the Hessian matrix. When used from a saddle point, this eigenvector gives the direction of the maximum curvature. The next integrating steps follow the magnetic shear gradient until the component reconnection part of the MSL reaches the anti-parallel regions, where the integration stops as the gradient there is zero.

The anti-parallel branches are obtained using a local maxima detection algorithm [van der Walt et al., 2014] to find the points along anti-parallel magnetic shear regions, such as the blue points in Figure 5.4. These points are interpolated into the two anti-parallel branches, which are then added to the component reconnection part of the MSL.

The MSLs are not determined for absolute values of IMF clock angles below 25° and above 155°

because the such cases most of the dayside magnetopause is almost parallel or anti-parallel.

Maximum current density and reconnection rate lines

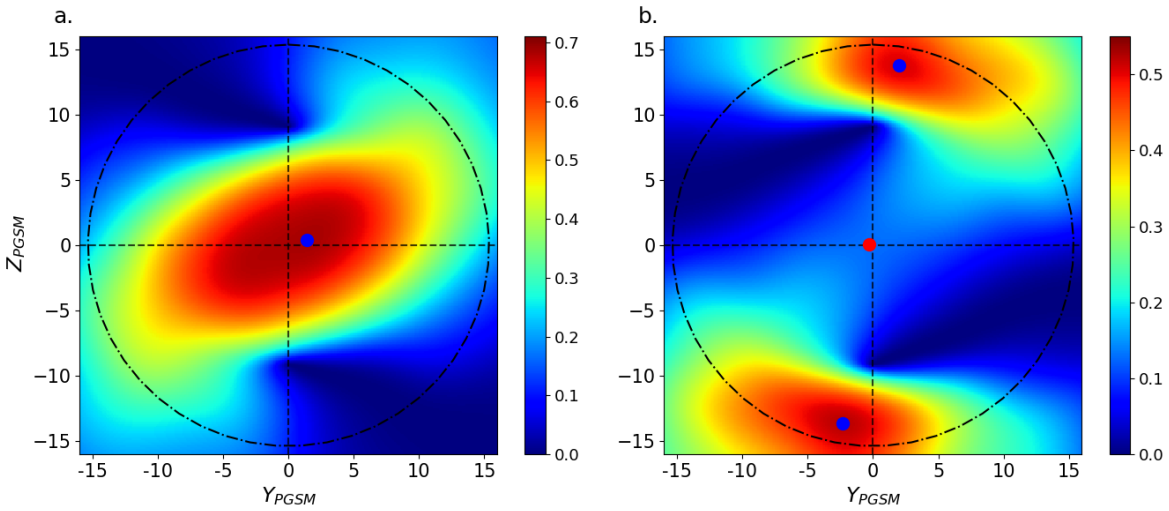

Figure 5.5: Reconnection rate for an IMF cone angle range of $|\theta_{co}|$=85°±5° and dipole tilt angle of ψ=0°±2.5°. In the PGSM coordinate system (see Section 2.7.4), the IMF clock angle is set to 130° and 30° in panel a and b, respectively. The blue and red points correspond to local maxima and a saddle point, respectively. The magnetopause terminator is represented by the dashed-dotted circle.

We now proceed with determining the lines maximizing the distribution of the current density and reconnection rate, we shall call Maximum Current Density Line (MCL) and a Maximum Reconnection Rate Line (MRL), respectively.

Obtaining a MCL and a MRL is a more complex process than for a MSL. Indeed, unlike the global distribution of the magnetic shear, which has a single saddle point, we have found that the distributions of the current density and reconnection rate sometimes have more than one saddle points and/or maxima. This complexity requires decisions to be made about the starting points of the lines to maximize the considered quantity, since the outcome of the integration process depends on these starting points. Our driving idea is to compute X-lines that explore the dayside magnetopause, i.e. that pass equatorwards of the cusps, a reasonable choice considering this is were the IMF first touches the magnetopause. To satisfy this last constraint, after identifying the local maxima of the global distribution (see section 5.2.3), two different techniques of line integration are used, as described below.

The first technique is used when the global maximum of the distribution lies between the polar cusps ($\sqrt{Y_{PGSM}^2 + Z_{PGSM}^2} \leq 7$ Re), such as in the left panel of Figure 5.5. The desired line departing from the maximum (i.e. the blue point in Figure 5.5.a) is the one keeping the highest possible values. Thus, the line is integrated by following the eigenvector corresponding to the smallest negative eigenvalue of the Hessian matrix.

The second technique is applied when the maximum of the global distribution is found at higher latitudes than the polar cusps ($\sqrt{Y_{PGSM}^2 + Z_{PGSM}^2} \geq 7$ Re), such as in the right panel of Figure 5.5. Our goal is that the line passes by the maxima that can be found in one or both lobes (example the blue points in Figure 5.5.b). The possible existence of a (smaller) local maximum in the subsolar region, indicates one or more saddle points in the dayside (such as the red point in Figure 5.5.b), in which case several line portions are computed and eventually merged into a single global one.

5.3 Comparison of Observed and Modeled Magnetic Shear Spatial Distributions

This section aims at comparing magnetic shear maps produced using magnetic field models for the magnetosheath (KF94) and the magnetosphere (T96), with those made using only in-situ measurements. It is important to evaluate the validity of the modeled shear maps, as they are often used to predict the location of magnetic reconnection and other phenomena at the magnetopause [Petrinec et al., 2022; Sun et al., 2022; Trattner et al., 2017]. We saw in Chapter 3 that the magnetic field draping in the magnetosheath can be classified into three regimes as a function of the IMF cone angle : large ($(|\theta_{co}| \geq 45° \pm 5°$), intermediate ($45° \pm 5° \geq |\theta_{co}| \geq 12.5° \pm 2.5°$), and low ($|\theta_{co}| \leq 12.5° \pm 2.5°$) values. Correspondingly, this section will be divided into three subsections for each of the identified IMF cone angle regime. Note that the maps obtained studied in these subsections will reproduce cases published in the literature, when available, in order to show the validity of our method to reconstruct the modeled magnetic shear maps (see section 5.2.2).

5.3.1 Large IMF cone angles

The large IMF cone angle regime, as defined in Chapter 3, corresponds to orientations within $|\theta_{co}| \geq 45° \pm 5°$, which represents about 70% of the IMF orientations measured at 1 AU. Figure 5.6 shows maps of the magnetic shear angle at the magnetopause as viewed from the Sun assuming steady state. The Figure 5.6.b reproduces the modeled magnetic shear map of Trattner et al. [2021] (Figure 13) on the 20 September 1997 at 07:34 UT with a dipole tilt of -6.6°, an IMF cone angle of -80.7°, and an IMF clock angle of 130°. The magnetic shear map in Figure 5.6.a is obtained from in-situ data only. The magnetic field on the magnetosheath side of the magnetopause is made for the subset of the data associated with an IMF cone angle falling within the range $76° \leq |\theta_{co}| \leq 86°$, and with an IMF clock angle set to 130° in the PGSM coordinate system. The in-situ measurements on the magnetospheric side are selected for a dipole tilt of ψ = - 6.6°±2.5°.

The modeled shear map (Figure 5.6.b) exhibits a high similarity with the one obtained using in-situ data (Figure 5.6.a). This outcome could be anticipated since the KF94 magnetic draping is very similar to the observed one for large IMF cone angles (see Section 3.3.1). The shape of the anti-parallel areas is the most noticeable difference between the two magnetic shear maps (Figure 5.6.a, b). In the map made with magnetic field models, they are bending to become nearly parallel to the equator. In contrast, in the map made from in-situ measurements, they remain almost straight. To investigate the origin of this difference, we computed magnetic shear maps made using in-situ measurements on one side of the magnetopause and a magnetic field model (either T96 or KF94) on the other side (Figure 5.6.c and d). The magnetic shear map using in-situ magnetospheric measurements and the KF94 model (Figure 5.6.d) displays anti-parallel areas similar to the observed map. On the other hand, the map made with T96 and magnetosheath data (Figure 5.6.c) shows patterns comparable to figure 5.6.b, we conclude that the discrepancy arises from the magnetospheric field being different in observations than the one predicted by T96. A possible explanation for these differences is that the T96 model uses a magnetopause model (S91) independent of the dipole tilt angle, whereas the shape of the magnetopause is actually affected by it [Lin et al., 2010; Liu et al., 2015b; Nguyen et al., 2022b]. Since the T96 model magnetic field must remain tangent to the magnetopause surface, this could result in a slight difference in curvature between the modeled (Figure 5.6.c) and observed (Figure 5.6.d) magnetic field lines. Additionally, a part of these discrepancies may arise from the slight difference of shape between the magnetopause models used in the observed [Shue et al., 1998] and modeled [Sibeck et al., 1991] maps. Further investigation is required to understand these details but this is beyond the scope of this study.

The Maximum Shear Line (MSL), which maximizes locally the magnetic shear angle on the magnetopause surface, is often used to predict the location of the X-line [Trattner et al., 2007]. On average, observed and modeled MSLs (Figure 5.6.a and b) are about 1 Re apart. It should be noted that the component reconnection part of the modeled MSL is more inclined toward the equator

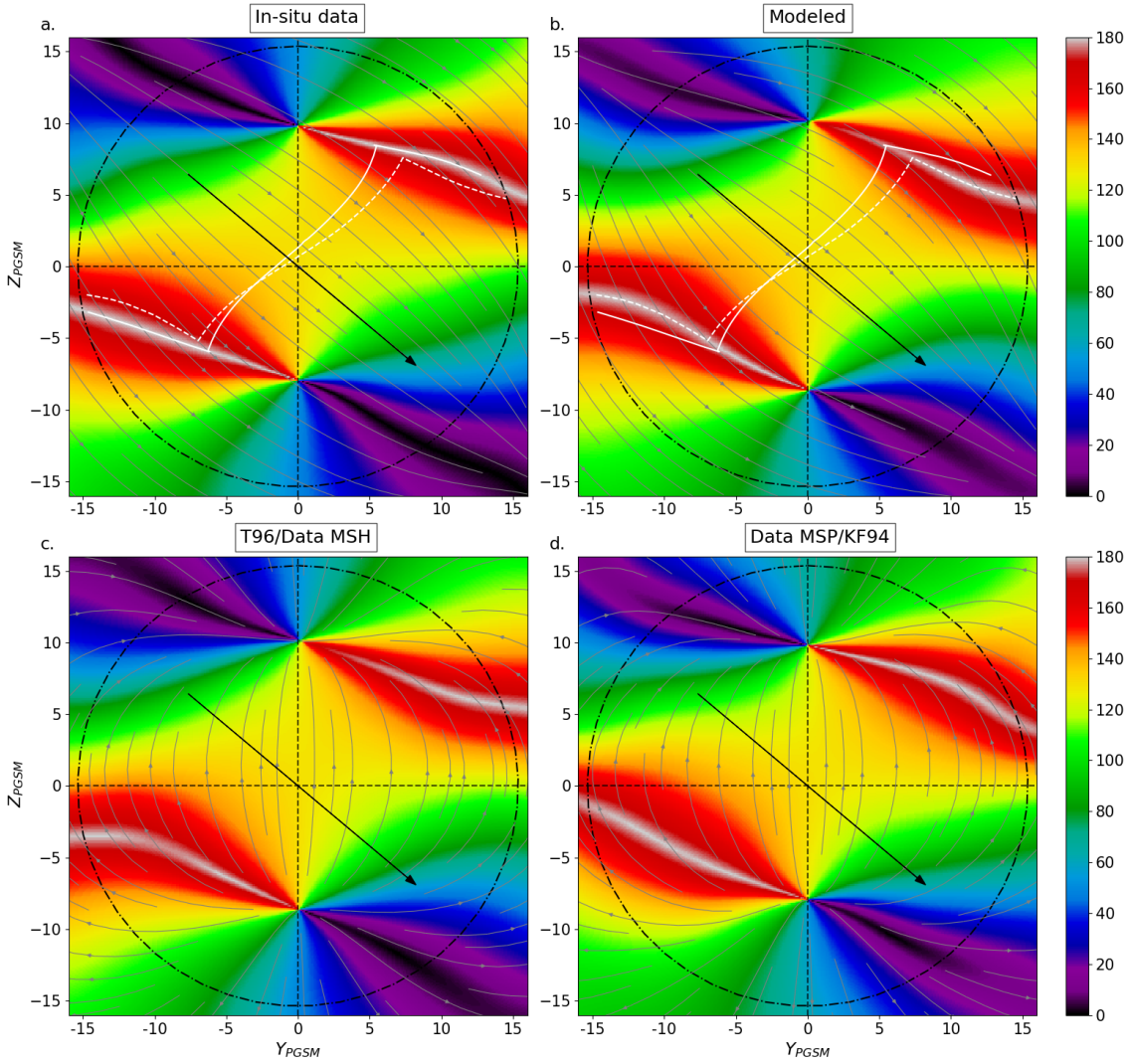

Figure 5.6: **Magnetic shear maps at large IMF cone angle.** Panels a and b correspond to the magnetic shear angle maps using only in-situ measurements and magnetic field models [Kobel and Fluckiger, 1994; Tsyganenko and Stern, 1996], respectively. The magnetic shear map on panel b correspond to the one presented in Trattner et al. [2021] (Figure13) on 20 September 1997 at 07:34 UT. The map in panel c is made with the T96 model and the magnetosheath in-situ measurements. The map in panel d is made with the magnetosphere in-situ measurements and the KF94 model. The subset of in-situ magnetosheath measurements used in panels a and c is $76^\circ \leq |\theta_{co}| \leq 86^\circ$ and turned to an IMF clock angle of 130°. The subset of in-situ magnetosphere measurements used in panels a and d is $|\psi| = 6.6^\circ \pm 2.5^\circ$. The value of dipole tilt of modeled magnetospheric magnetic field (T96) used in the panels b and c is -6.6°. The modeled magnetosheath magnetic field (KF94) in the panels b and d is made with ($B_{x_{imf}}$,$B_{y_{imf}}$,$B_{z_{imf}}$)=(-0.7,3.8,-3.2). The grey arrowed lines in the panels a and b (resp. c and d) represent magnetic field lines of the observed and modeled magnetosheath (resp. magnetosphere), respectively. The solid and dashed white lines maximize the observed and modeled magnetic shear, respectively. The black arrows correspond to IMF orientation in the ($Y_{PGSM}Z_{PGSM}$) plane. The magnetopause terminator is represented by the dashed-dotted circle.

than the one from observations (Figure 5.6.a and b). And while the maps obtained with the T96 /KF94 models in the large IMF cone angle regime provide a reliable qualitative estimate of the magnetic shear at the magnetopause, we will see later (section 5.4.1) that the discrepancy in the orientation of the MSL actually shows a significant difference in term of its dependence on the IMF direction, between the modeled and observed maps.

5.3.2 Intermediate IMF cone angle

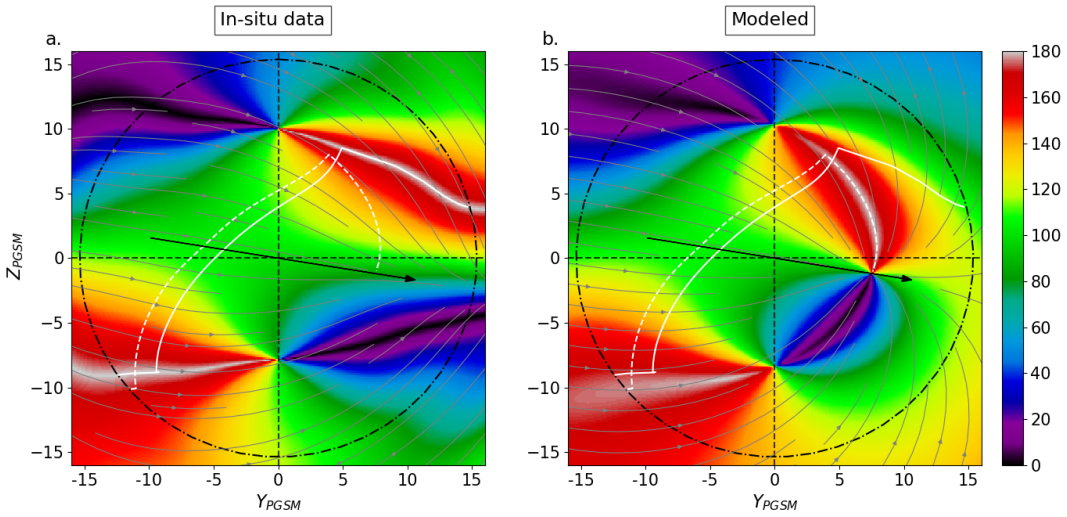

Figure 5.7: Magnetic shear maps at intermediate IMF cone angle. Subsets $13.5° \leq |\theta_{co}| \leq 23°$ and $|\psi|$ = 8.2°±2.5°. Panels a and b correspond to the magnetic shear angle maps made using only in-situ measurements and magnetic field models [Kobel and Fluckiger, 1994; Tsyganenko and Stern, 1996], respectively. The magnetic shear map on panel b correspond to the one presented in Trattner et al. [2012a] (Figure 4) on the 22 Mars 1996 at 02:40 UT. The grey arrowed lines represent in the panels a and b represent magnetic field lines of the observed and modeled magnetosheath draping, respectively. The solid and dashed white lines maximize the observed and modeled magnetic shear (MSL), respectively. ($Y_{PGSM}Z_{PGSM}$) plane. The magnetopause terminator is represented by the dashed-dotted circle.

Figure 5.7 shows an observed (panel a) and modeled (panel b) shear map for an IMF cone angle in the intermediate regime (i.e. $45° \pm 5° \geq |\theta_{co}| \geq 12.5° \pm 2.5°$), which represents about 28% of the IMF. Figure 5.7.b reproduces the modeled magnetic shear map of Trattner et al. [2012a] (Figure4) on 22 Mars 1996 at 02:40 UT with a dipole tilt of -8.2°, an IMF cone angle of 18.5°, and an IMF clock angle of 99°. The observed magnetic shear map in Figure 5.7.a is made with the subset of the magnetosheath measurements for which the IMF cone angle lies within $13.5° \leq |\theta_{co}| \leq 23°$ and an IMF clock angle set to 99° in the PGSM coordinate system. The in-situ measurements on the magnetospheric side are selected for a dipole tilt of ψ = -8.2°±2.5°.

In the modeled shear map (Figure 5.7.b), parallel and anti-parallel magnetic shear areas join on the dayside of the quasi-parallel magnetopause. This pattern results from the convergence (or divergence, depending on the sign of $B_{x_{imf}}$) of the magnetosheath field lines predicted by the KF94 model towards a topological singularity ($Y_{PGSM} \approx 7.5$ Re and $Z_{PGSM} \approx -1.5$ Re) aligned with the parallel bow shock. In contrast, in the observed shear map (Figure 5.7.a), the parallel and anti-parallel magnetic shear areas do not connect on the quasi-parallel magnetopause, but instead extend towards the nightside. This difference results from the absence of the aforementioned singularity in the observed magnetic field draping for such an IMF cone angle (see Section 3.3.2). As seen with the solid and dashed white lines, throughout most of the dayside, the observed and modeled MSLs are approximately 2 Re apart, but this distance significantly increases up to around 8 Re on the quasi-parallel side of the magnetopause at dusk.

The absence of a divergent pattern in the observed magnetosheath draping leads to unex-

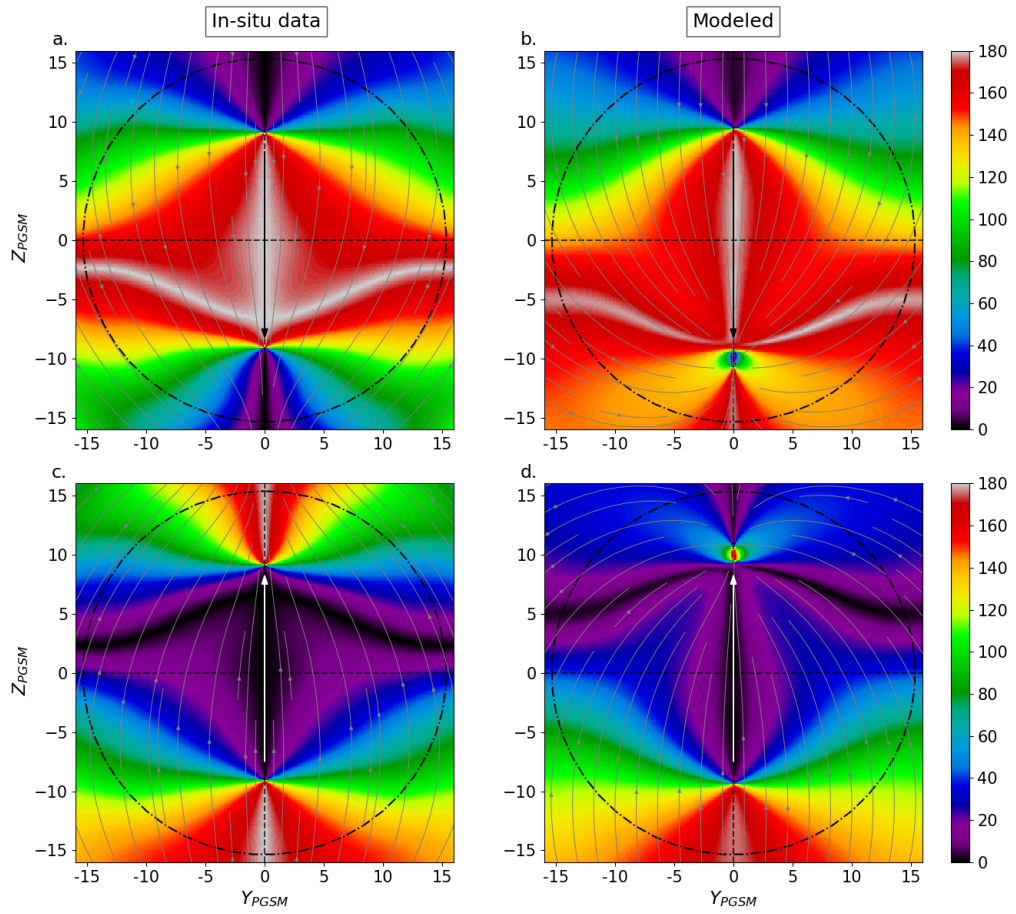

Figure 5.8: Magnetic shear maps at intermediate IMF cone angle. Subsets θ_{co} =25°±5° and |ψ| = 0°±2.5° with θ_{cl} =180° (Panel a and b) and θ_{cl} =0° (Panel c and d). Panels (a and c) and (b and d) correspond to the magnetic shear angle maps made using only in-situ measurements and magnetic field models [Kobel and Fluckiger, 1994; Tsyganenko and Stern, 1996], respectively. The grey arrowed lines represent in the panels (a and c) and (b and d) represent magnetic field lines of the observed and modeled magnetosheath draping, respectively. The black or white arrows correspond to IMF orientation in the ($Y_{PGSM}Z_{PGSM}$) plane. The magnetopause terminator is represented by the dashed-dotted circle.

pected effects when the region of the magnetosheath behind the quasi-parallel shocks is located on one of the lobes, as shown in Figure 5.8 for an IMF clock angle of 180° (panels a, b) or of 0° (panels c, d). For an IMF clock angle of 180°, both observed and modeled maps exhibit the majority of the dayside magnetopause at high magnetic shear, with an anti-parallel area in the southern hemisphere due to asymmetry in the magnetosheath draping. However, the modeled map (Figure 5.8.b) predicts that most of the southern lobe has a high magnetic shear because the divergent pattern predicted by the KF94 model is located equatorward of the southern cusp. In contrast, without this singularity, the observed map (Figure 5.8.a) displays low shear angles across the entire south lobe. The situation for an IMF clock angle of 0° is similar but reversed, with the observed map (Figure 5.8.c) showing high magnetic shear in both lobes, while only in the southern lobe for the modeled map (Figure 5.8.d). An important conclusion from this comparison is that if only considering the magnetic shear for determining the location of magnetic reconnection, both lobes are equally important in observations while they are significantly different in the modeled map.

In general, the magnetic shear maps derived from the T96 /KF94 models do not provide a reliable estimate of the observed shear angle at the magnetopause in the intermediate IMF cone angle regime.

5.3.3 Low IMF cone angle

The low IMF cone angle regime (i.e $|\theta_{co}| \leq 12.5° \pm 2.5°$) represents less than 2% of the IMF data. The maps in Figure 5.9 display the magnetic shear for a due east IMF (i.e. $\theta_{cl} = 90°$) and a dipole tilt of 0° in the case of low IMF cone angle. The observed map (Figure 5.9.a) is made using magnetosheath measurements within $|\theta_{co}| \leq 12.5°$ and a dipole tilt angle of $\psi = 0° \pm 2.5°$ for the magnetosphere side. Since we did not find in the literature a case of a modeled magnetic shear map at a low IMF cone angle, the one of Figure 5.9.b was made for an IMF cone angle of 8.3°, corresponding to the average IMF cone angle for the selected subset of magnetosheath measurements.

The two maps generally agree, as both the modeled and observed magnetosheath magnetic draping display a divergent pattern (see Section 3.3.3), connecting the parallel and anti-parallel areas on the dayside magnetopause. However, in the observed map (Figure 5.9.a), these areas have a slightly rounder shape on the quasi-parallel side ($Y_{PGSM} \geq 0$) and are located at lower latitudes on the quasi-perpendicular side ($Y_{PGSM} \leq 0$) of the magnetopause than in the modeled map (Figure 5.9.b). These differences arise from subtle discrepancies between the modeled and observed magnetic fields in the magnetosheath. In reality, the field lines on the quasi-parallel side remain connected to their quasi-perpendicular counterparts because they are frozen in the magnetosheath plasma flow (see Section 3.3.3). In contrast, this effect is not seen in the field lines predicted by the KF94 model, which leads to the shape of the magnetic field lines in Figure 5.9.b, that tends to be less curved toward the $Y_{PGSM} < 0$ side than in the observed draping (Figure 5.9.a).

On average, the MSLs are approximately 1 Re apart and located slightly more towards the anti-parallel regions. As in the large IMF cone angle regime, the modeled shear maps can provide a relatively good estimate of the magnetic shear angle at the magnetopause in the low IMF cone angle regime.

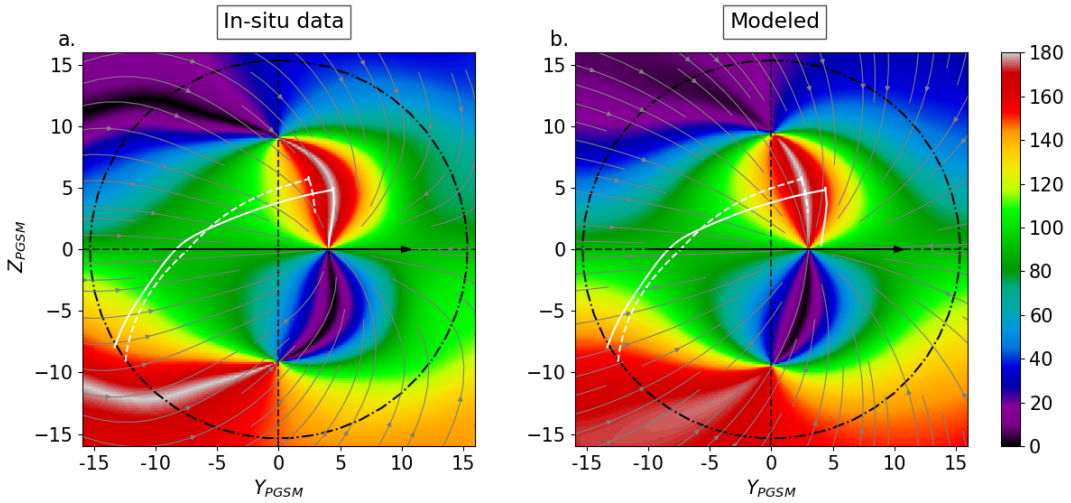

Figure 5.9: Magnetic shear maps at low IMF cone angle. Subsets $|\theta_{co}| \leq 12.5°$ and $|\psi| = 0° \pm 2.5°$ with $\theta_{cl} = 90°$. Panels a and b correspond to the magnetic shear angle maps made using only in-situ measurements and magnetic field models [Kobel and Fluckiger, 1994; Tsyganenko and Stern, 1996], respectively. The magnetic shear map on panel b correspond to the one presented in Trattner et al. [2012a] (Figure4) on the 22 Mars 1996 at 02:40 UT. The grey arrowed lines represent in the panels a and b represent magnetic field lines of the observed and modeled magnetosheath draping, respectively. The solid and dashed white lines maximize the observed and modeled magnetic shear (MSL), respectively. ($Y_{PGSM}Z_{PGSM}$) plane. The magnetopause terminator is represented by the dashed-dotted circle.

5.4 Global Distribution of the Magnetic Shear, Current Density, and Reconnection Rate

Although the orientation of the magnetic fields on both sides of the magnetopause, as studied in the previous section, plays a crucial role in magnetic reconnection, other quantities are also important in this process, among which in particular the current density [Alexeev et al., 1998] and the reconnection electric field [Borovsky, 2013], etc. However, knowledge of their global distribution at the magnetopause comes only from modeling, usually numerical. In this study, in addition to the magnetic shear, we also obtained the current density and the Cassak-Shay asymmetric reconnection rate from an observational standpoint. In this section, we will first compare the global distribution of these quantities obtained with in-situ measurements with those obtained in published MHD simulation studies. Then, in the following subsections, we examine the variations of these quantities with respect to IMF orientation and dipole tilt angle.

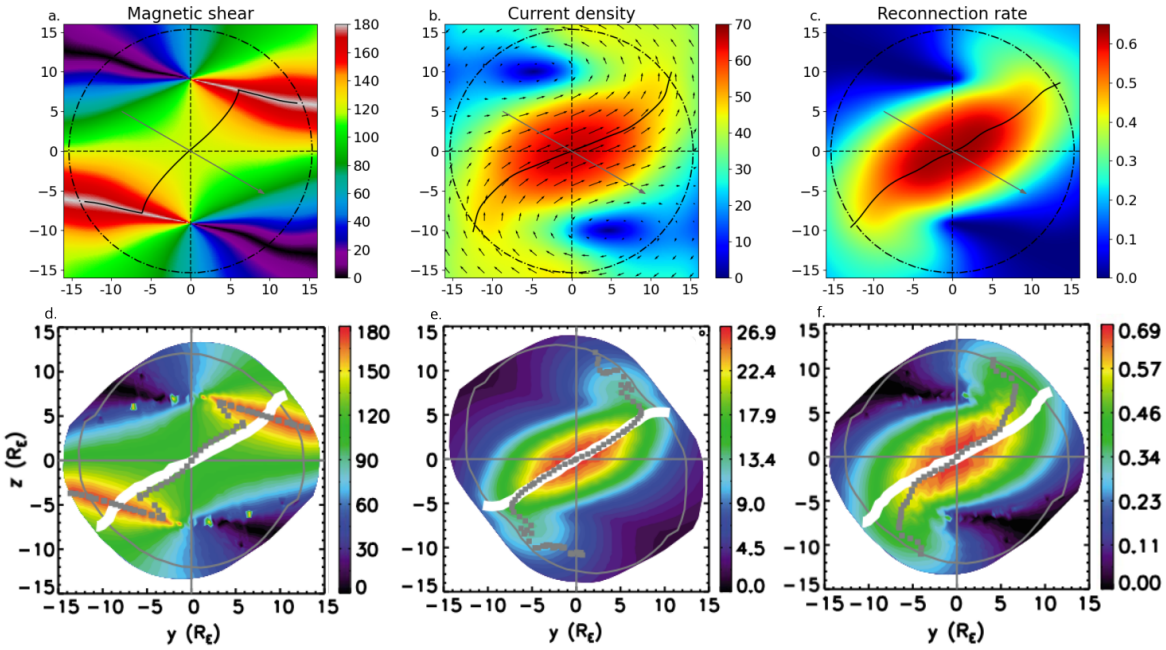

Figure 5.10: Panels a, b, and c show the global distributions of magnetic shear, current density, and reconnection rate, respectively, obtained from in-situ measurements for IMF cone angles in the range of $80° \leq |\theta_{co}| \leq 90°$, a dipole tilt angles of $\psi = 0° \pm 2.5°$, and an IMF clock angle of 120°. The black lines maximize the quantities represented in each panel. The gray arrows correspond to IMF orientation in the (YZ) plane. The terminator is represented by the dashed circle. Panels d, e, and f show the corresponding quantities obtained from a global MHD simulation in the study of Komar et al. [2015] for similar IMF and dipole tilt orientations. The dotted gray line maximize the quantities and the white line correspond to the separator.

Figure 5.10 shows the magnetic shear, current density, and reconnection rate at the magnetopause using in-situ measurements in panels a to c, respectively. These maps are made using measurements with IMF cone angles in the range of $80° \leq |\theta_{co}| \leq 90°$ and a dipole tilt angle of $\psi = 0° \pm 2.5°$. Panels d to f show the corresponding quantities obtained from a global MHD simulation in the study of Komar et al. [2015]. For all these maps the IMF clock angle has a value of 120°.

The observed magnetic shear angle pattern (Figure 5.10.a) closely resembles the one obtained in the global MHD simulation of Komar et al. [2015] (Figure 5.10.d). Interestingly, the MHD shear map, with an IMF orientation close to that in Figure 5.6, displays straight anti-parallel areas, consistent with observations from section 5.3.1. The observed MSL is consistent with the one obtained in the MHD simulation.

Figure 5.10.b shows a map of the current density at the magnetopause, where the direction of the current, indicated by black arrows, aligns with expectations for the given IMF orientation. The

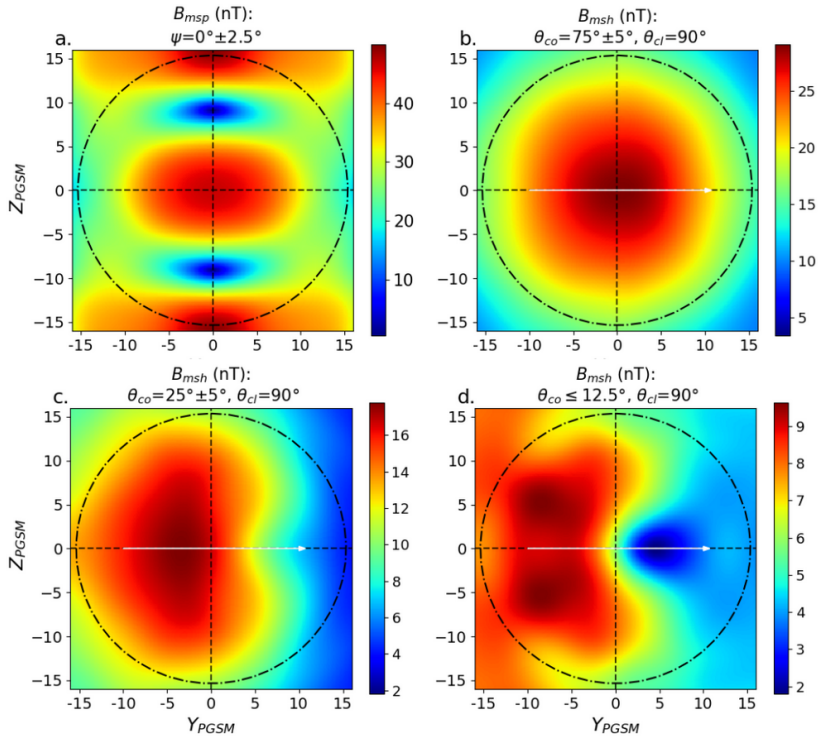

Figure 5.11: Amplitude of the magnetic fields at the surface of the magnetopause. Panel a shows the distribution of the magnetospheric magnetic field strength for a dipole tilt angle of $\psi = 0°\pm2.5°$. Panels b, c, and d show the amplitude of the magnetosheath magnetic field for large ($70° \leq |\theta_{co}| \leq 80°$), intermediate ($20° \leq |\theta_{co}| \leq 30°$), and small ($|\theta_{co}| \leq 12.5°$) IMF cone angle and an IMF clock angle of 90°, respectively.

amplitude of the current density is maximum in the subsolar region, where the amplitude of the magnetic field magnitude on each side of the magnetopause (Figure 5.11.a and 5.11.b) and the magnetic shear angle are highest. This amplitude remains large in both lobes due to the large differences in magnetic field strength between the magnetosphere and the magnetosheath. Finally, the current density amplitude is low in regions where the magnetic shear and the differences of strengths between the magnetic fields are small. The observed current density pattern remains consistent with MHD simulations (not shown) across different IMF orientations and dipole tilt angles found in published studies [Komar et al., 2015; Souza et al., 2017]. The MHD current density amplitude, being of the same order of magnitude, is consistent with the observed map. The difference of amplitude between the two maps may arises from the resistivity set in the global simulation, which significantly impacts current density values [Glocer et al., 2016]. In addition, if the orientation of the IMF is similar between the simulation and the measurements, it is not the case of other physical parameters that could influence the thickness of the magnetopause, which is assumed to be constant (800 km) in the observed map, but also the magnetic pileup, etc. The observed current density amplitude is remarkably consistent with studies using in-situ measurement. For instance, recent studies found median values of 62.1±1.5 nA/m^2 for the dayside and about 47±3.2 nA/m^2 for the flanks [Haaland et al., 2020]; a current density distribution mostly between 10 nA/m^2 and 150 nA/m^2 [Lukin et al., 2020]; and a median amplitude of the current density in the dayside magnetopause of 67.7±5.6 nA/m^2 [Beedle et al., 2022]. It is worth noting that Figure 5.10.b represents the macroscopic current density at the magnetopause, but locally, the current can be highly inhomogeneous and exhibit stronger amplitudes. The Maximum Current density Line (MCL) that maximizes the current density is consistent with the one determined in the MHD simulation.

The reconnection rate in Figure 5.10.c shows a pattern and amplitude very similar to that of the global MHD simulation of Komar et al. 2015 (Figure 5.10.f). The highest values of the reconnection rate are in the subsolar region, where the high values of the magnetic pileup in the

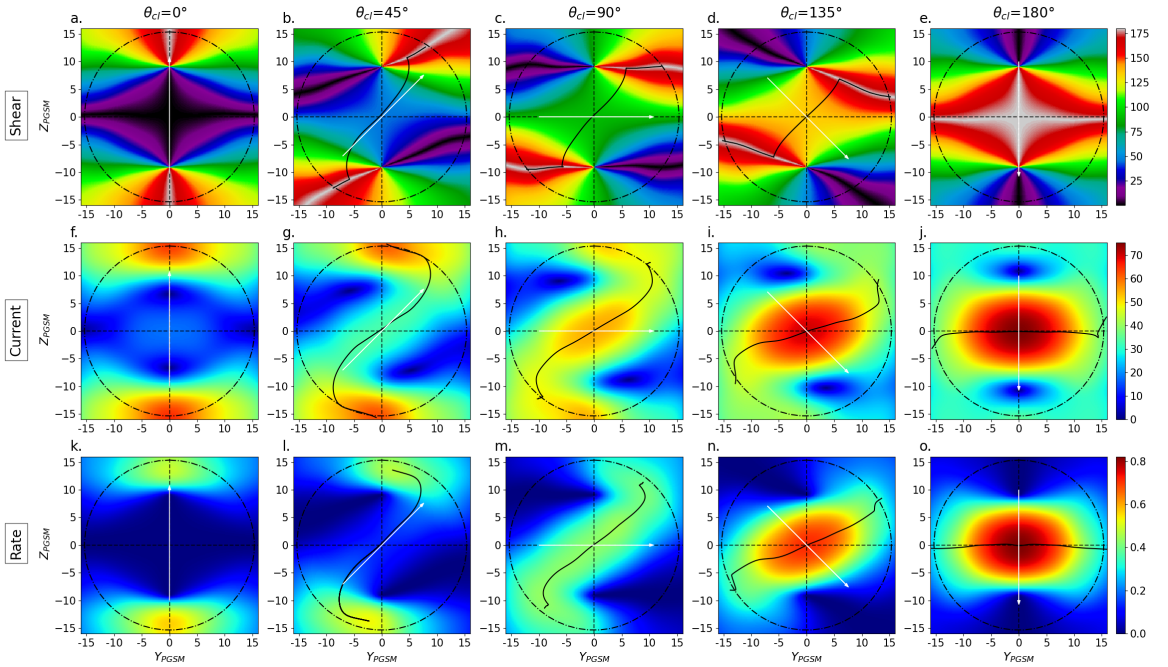

Figure 5.12: Global distributions of magnetic shear, current density, and reconnection rate at the surface of the magnetopause at Large IMF cone angles. Subsets of the measurement for IMF cone angles in the range $70° \leq |\theta_{co}| \leq 80°$ and dipole tilt angles of $|\psi| = 0° \pm 2.5°$. The magnetic shear (panels a to e), the current density (panels f to j), and the reconnection rate (panels k to o) for IMF clock angle 0° (panels a, f, and k), 45° (panels b, g, and l), 90° (panels c, h, and m), 135° (panels d, i, and n), and 180° (panels e, j, and o). The black lines maximize the quantities represented in each panel. The white arrows correspond to IMF orientation in the (YZ) plane. The terminator is represented by the dashed circle.

magnetosheath coincide with large magnetic shear (Figure 5.10.a). The lowest reconnection rate values are found in regions of low magnetic shear, because the reconnected components of the magnetic fields would be extremely small. However, unlike the current density, a large difference in magnetic field amplitude between the magnetosphere and the magnetosheath (Figure 5.11.a and b) does not increase the rate. As a result, the reconnection rate at high latitudes experiences a rapid decline due to the decrease of the magnetic pileup in the magnetosheath. The similarity of the global pattern of the reconnection rate to MHD simulations remains consistent (not shown) across different IMF orientations and dipole tilt angles found in Komar et al. [2015]. The Maximum Rate Line (MRL) obtained from in-situ measurements appears straighter and more tilted toward the equator compared to that in Figure 5.10, yet remains consistent with it. In line with the observations made by Komar et al. (2015) for southward IMF, incorporating velocity shear (not shown) into the calculations of the reconnection rate [Cassak and Otto, 2011] has a negligible impact on its magnitude. Indeed, the correction is about one to two orders of magnitude smaller compared to the reconnection rate without velocity shear.

Overall, the global distribution of magnetic shear, current density, and reconnection rate obtained using only in-situ measurements agrees with numerical simulations.

5.4.1 Dependence on the IMF clock angle

We will now investigate the influence of the IMF clock angle on the distribution of the magnetic shear, the current density, and the reconnection rate on the magnetopause. This subsection is divided into three parts, corresponding to the different draping regimes, similar to the section 5.3.

Large IMF cone angle

Figure 5.12 shows the magnetic shear (panels a to e), the current density (panels f to j), and the reconnection rate (panels k to o) for a large IMF cone angle ($70° \leq |\theta_{co}| \leq 80°$) for a dipole tilt of 0° ($|\psi| = 0° \pm 2.5°$) as a function of the IMF clock angle (0°, 45°, 90°, 135°, and 180°).

For an IMF clock angle of 0° (Figure 5.12.a), the magnetic shear is anti-parallel in both lobes, with most of the dayside magnetopause exhibiting low shear angle values. As the IMF shifts southward (Figure 5.12.b,c,d), the magnetic shear angle on the dayside increases, with the anti-parallel (resp. parallel) shear regions moving closer to (resp. further from) the equator. Surprisingly, while the anti-parallel portion of the MSLs gets closer to the equator axis as the IMF clock angle increases, the global orientation of the component reconnection part of the lines appears to remain constant. In fact, when plotted together (Figure 5.13.a), most of the component reconnection part of these MSLs overlap and remain close at high latitudes. This behavior has already been observed in a global MHD simulation study [Komar et al., 2015], which also found that the MSLs have a fixed orientation at the subsolar magnetopause and do not rotate for the different IMF clock angles. In contrast, the slopes of the modeled MSLs (Figure 5.13.b) decrease with increasing IMF clock angle, resulting in a distance of about 5 Re at high latitude between the southernmost and northernmost lines. Further investigation revealed that the independence of the observed MSLs to the IMF clock angle is due to the magnetosheath magnetic field lines being less curved than those predicted by the KF94 model. This would result in a flatter gradient of the observed magnetic shear map than that produced by the models. Therefore, the component reconnection portion of the observed MSLs, following this gradient, would pass at roughly the same location in the component reconnection region and separate at higher latitudes where the magnetosheath field lines are more curved. The curvature differences between the modeled and observed draping could be explained by magnetic reconnection which affects the bending of the field lines by altering the global magnetosheath plasma flow. This effect would be observable only in in-situ measurements and MHD simulations, but not in the KF94 model that assumes draping in vacuum and thus does not account for magnetic reconnection. Finally, for an IMF clock angle of 180° (Figure 5.12.e) most of the dayside magnetopause exhibits a high magnetic shear and parallel shear angle in both lobes.

For an IMF clock angle of 0° (Figure 5.12.f), the current density is maximum and exhibits similar amplitudes in both lobes. As the IMF clock angle increases (Figure 5.12.g,h,i), the amplitude decreases in the lobes and increases in the subsolar region as the magnetic shear angle increases in this region. The magnitude is maximum in the subsolar region for an IMF clock angle of 180° (Figure 5.12.j) as the magnetic pileup (Figure 5.11.b) coincides with the anti-parallel region (Figure 5.12.e). In contrast to the MSLs, the MCLs show a clear dependence on the IMF clock angle. The lines become more inclined toward the equator as the IMF clock angle increases, until they align with the equator for an IMF clock angle of 180° (Figure 5.12.j).

The reconnection rate exhibits a pattern similar to that of the current density, with high values in the lobes for northward IMF (Figure 5.12.k), shifting towards the subsolar region as the IMF turns southward (Figure 5.12.l,m,n), and peaking in the subsolar region for an IMF clock angle of 180° (Figure 5.12.o). Like the MCLs, but unlike the MSLs, the MRLs become more inclined towards the equator as the IMF clock angle increases.

Intermediate IMF cone angle

Figure 5.14 shows the magnetic shear (panels a to e), current density (panels f to j), and the reconnection rate (panels k to o) at intermediate IMF cone angle ($20° \leq |\theta_{co}| \leq 30°$) and for a dipole tilt of 0° ($|\psi| = 0° \pm 2.5°$) as a function of the IMF clock angle (0°, 45°, 90°, 135°, and 180°).

For an IMF clock angle of 0° (Figure 5.14.a), the pattern of the magnetic shear is similar to that seen for a large IMF cone angle (Figure 5.12.a), but with a thinner (resp. larger) high shear region in the northern (resp. southern) lobe due to the asymmetry of the magnetosheath draping between the quasi-parallel and the quasi-perpendicular sides of the magnetopause. However, unlike the case of a large IMF cone angle, the MSLs exhibit a dependence on the IMF clock angle as the IMF

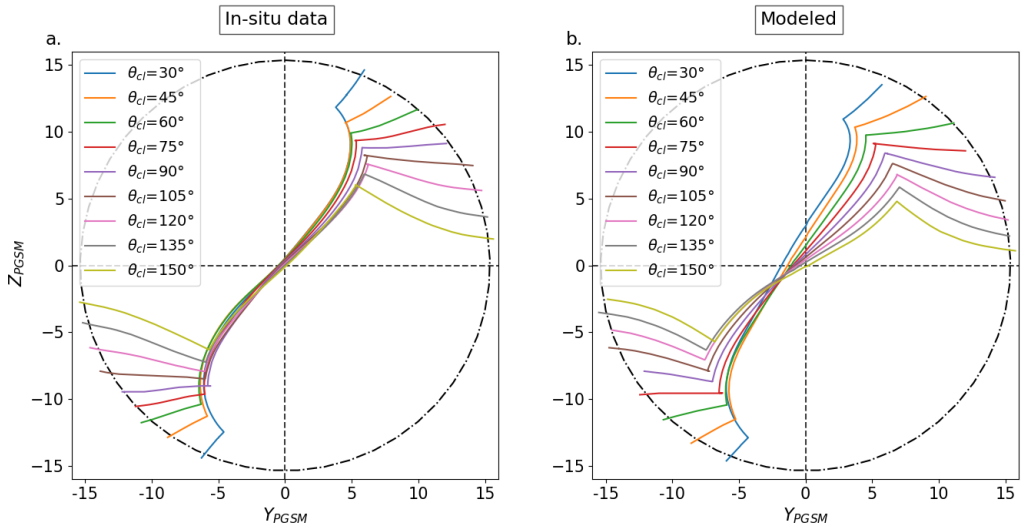

Figure 5.13: Maximum magnetic Shear Line (MSL) as a function of the IMF clock angle made from global distribution of the magnetic shear made obtained with in-situ measurements ($70° \leq |\theta_{co}| \leq 80°$ and $|\psi| = 0° \pm 2.5°$) and analytical models of magnetic fields (T96 ans KF94) in panels a and b, respectively.

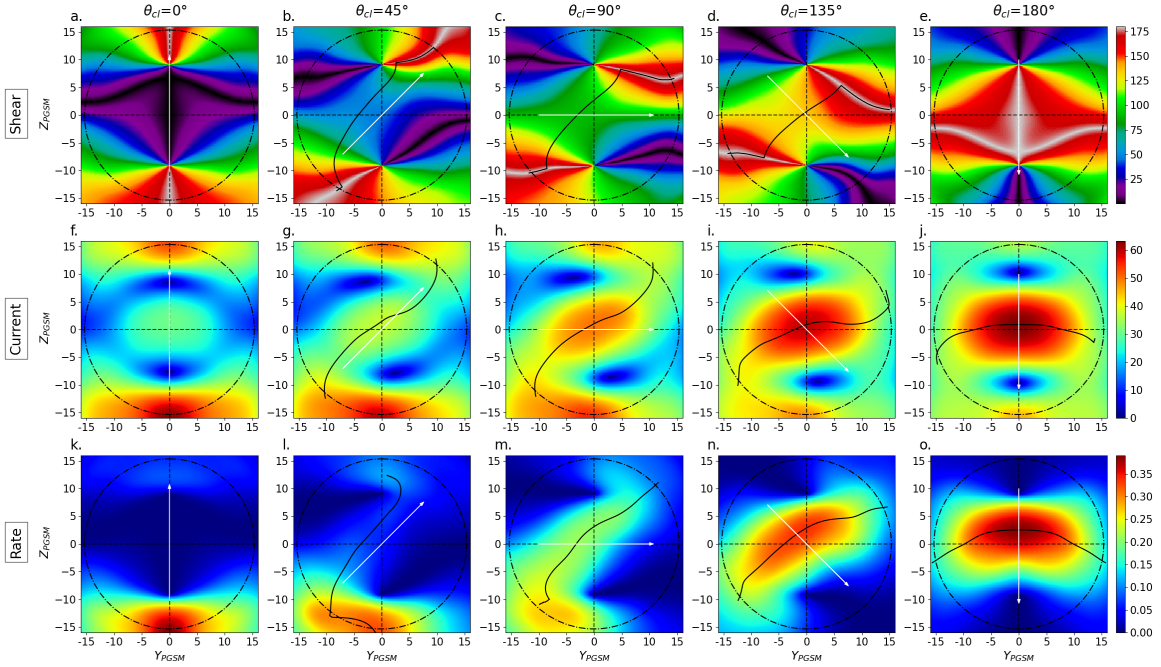

Figure 5.14: Global distributions of magnetic shear, current density, and reconnection rate at the surface of the magnetopause at intermediate IMF cone angles. Subsets of the measurement for IMF cone angles in the range $20° \leq |\theta_{co}| \leq 30°$ and dipole tilt angles of $|\psi| = 0° \pm 2.5°$. The legend is the same as Figure 5.12.

turns towards the south (Figure 5.14.b-d). This is because asymmetry in the magnetic field draping between the quasi-parallel and quasi-perpendicular side of the magnetopause (see Figure 5.7.a) affects the spatial variation of the magnetic shear gradient, which is therefore more dependent on the value of the IMF clock angle. Finally, for an IMF clock angle of 180° (Figure 5.14.e), the dayside mostly exhibits high magnetic shear but the geometry of the anti-parallel region (along the noon meridian and in the southern hemisphere) prevents the definition of a MSL.

The current density for an IMF clock angle of 0° (Figure 5.14.f) exhibits a small asymmetry between the north and south lobes, with the latter showing higher values, due to the asymmetry in magnetic strength between the quasi-parallel and quasi-perpendicular sides of the magnetopause (Figure 5.11.c). The amplitude of the current density in the subsolar region is higher than for large IMF cone angles because of the larger difference in magnitude between the magnetosheath and the magnetospheric magnetic fields, which tends to increase the current density at low magnetic shear. As the IMF turns southward (Figure 5.14.g-i), the current density decreases in the lobes and increases in the subsolar region, eventually reaching its maximum value in this region for an IMF clock angle of 180° (Figure 5.14.j). At intermediate IMF cone angles, the MCLs seem to overlap for north to pure east IMF (Figure 5.14.g,h), and incline towards the equator for southward IMF (Figure 5.14i,j). The MCL for an IMF clock angle of 180° extends into the southern hemisphere on the flanks because of the magnetosheath draping asymmetry.

At intermediate IMF cone angles, the global reconnection rate amplitude is about half that of the large IMF cone angle, due to the decrease in magnetic field strength in the magnetosheath between these two regimes (Figure 5.11 b and c). The reconnection rate for an IMF clock angle of 0° (Figure 5.14.k) shows a strong asymmetry between the north and south lobes, despite both having a high magnetic shear, due to the difference in amplitude between the quasi-parallel/quasi-perpendicular sides of the magnetic pileup (Figure 5.11.c). This is interesting because when magnetic shear is considered as the only parameter determining the location of magnetic reconnection, both lobes are equally important, while when reconnection rate is considered, only the south lobe is significant. When the IMF turns southward (Figure 5.14.l-n), the reconnection rate remains larger on the quasi-perpendicular part of the magnetopause, resulting, for an IMF clock angle of 180° (Figure 5.14.o), in higher values in the northern hemisphere. The MRLs tend to become more curved and inclined towards the equator as the IMF turns toward south.

Low IMF cone angle

Figure 5.15 shows the magnetic shear (panels a to e), the current density (panels f to j), and the reconnection rate (panels k to o) at low IMF cone angle ($|\theta_{co}| \leq 12.5°$) and for a dipole tilt of 0° ($|\psi|$ = 0°±2.5°) as a function of the IMF clock angle (0°, 45°, 90°, 135°, and 180°).

As described in section 5.3.3, when the IMF cone angle is low, the areas of anti-parallel and parallel magnetic shear join together at the dayside magnetopause. For an IMF clock angle of 0° (Figure 5.15.a), most of the dayside magnetopause exhibits low shear values that increase as the IMF turns towards southward (Figure 5.15.b,c,d,e). Due to the positive sign of the B_x component of the IMF, the southern (resp. northern) lobe remains at high (resp. low) shear for all IMF clock angles. The location of the MSLs changes slightly as the IMF clock angle increases.

At low IMF cone angles, the global current density pattern (Figure 5.15.f-j) is only weakly affected by the IMF clock angle, since the main contribution to its amplitude comes from the difference in strength between the magnetospheric and magnetosheath magnetic fields. Another consequence of this difference in strength is that for an IMF clock angle of 0°, the subsolar region (Figure 5.15.f) has the highest current density values of all IMF cone regimes (Figure 5.12.f, 5.14.f). As the IMF turns southward, there is a slight increase in the current density in the subsolar region due to an increase in magnetic shear, and a slight decrease in both lobes due to the magnetic pileup in the quasi-perpendicular magnetosheath shifting towards the north lobe at low shear. The change in the shape of the MCLs seems to be due only to the difference in the integration technique, gradient (Figure 5.15.g and h) and eigenvector of the Hessian matrix (Figure 5.15i and j), used to obtain these lines (see section 5.2.3). It should also be noted that the MCL for an IMF

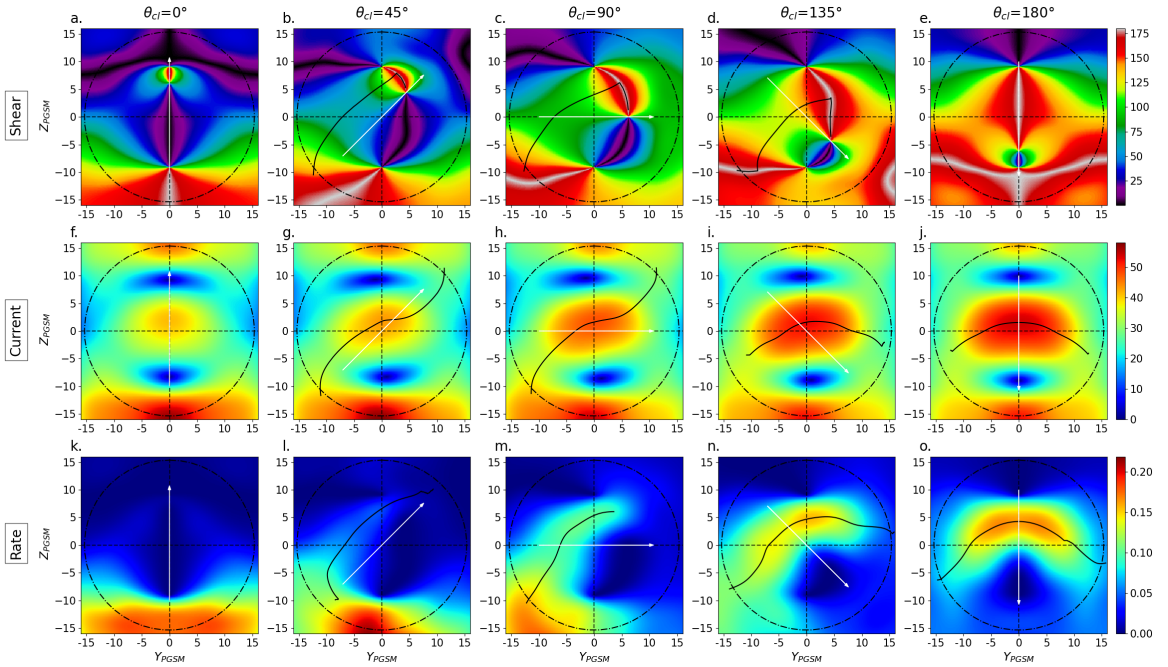

Figure 5.15: Global distributions of magnetic shear, current density, and reconnection rate at the surface of the magnetopause at small IMF cone angles. Subsets of the measurement for IMF cone angles in the range $|\theta_{co}| \leq 12.5°$ and dipole tilt angles of $|\psi| = 0° \pm 2.5°$. The legend is the same as Figure 5.12.

clock angle of 45° (Figure 5.15.g) passes through a region of parallel magnetic fields (Figure 5.15.b) where reconnection is impossible, and this would be the same for all IMF clock angles below about 60°.

At low IMF cone angles, the reconnection rate is approximately half that of the intermediate IMF cone angle consistently, again, with the decrease of the magnetic field strength in the magnetosheath between these two regimes (Figure 5.11 c and d). In contrast with the current density, the pattern of the reconnection rate is significantly impacted by the IMF clock angle, presenting a strong asymmetry between the quasi-parallel and quasi-perpendicular side of the magnetopause. When the IMF is northward (Figure 5.15.k,l), the reconnection rate is highest in the southern lobe, where both the magnetic amplitude (Figure 5.11.d) and magnetic shear (Figure 5.15.a) are also at their highest. Since the magnetic shear in the northern lobe remains low for all IMF clock angles, the reconnection rate in this region remains extremely small. When the IMF turns southward (Figure 5.15.l,m,n), the reconnection rate increases on the dayside due to an increase in magnetic shear, and it decreases in the southern lobe as the magnetic pileup in the magnetosheath shifts towards the north lobe. For a pure south IMF (Figure 5.15.o), the reconnection rate shows the highest values in the northern hemisphere due to the strong asymmetry in the magnetic pileup. However as the high shear areas do not coincide with the magnetic pileup, these reconnection rate values remain smaller than those obtained for northward IMF in the southern lobe. This is interesting because it suggests that for small IMF cone angles, magnetic reconnection is more efficient for northward than for the southward IMF. In contrast to the MCLs, the MRLs appear to show a dependence on the IMF clock angle (Figure 5.15.k-o). They tend to tilt toward the equator as the IMF turns southward, resulting in a curved line that is mainly in the northern hemisphere for an IMF clock angle of 180°.

5.4.2 Dependence on the dipole tilt angle

The previous subsection discussed the influence of the IMF clock and cone angles on the global distribution of magnetic shear, current density, and reconnection rate. We now examine how the dipole tilt angle affects the lines that maximize these quantities.

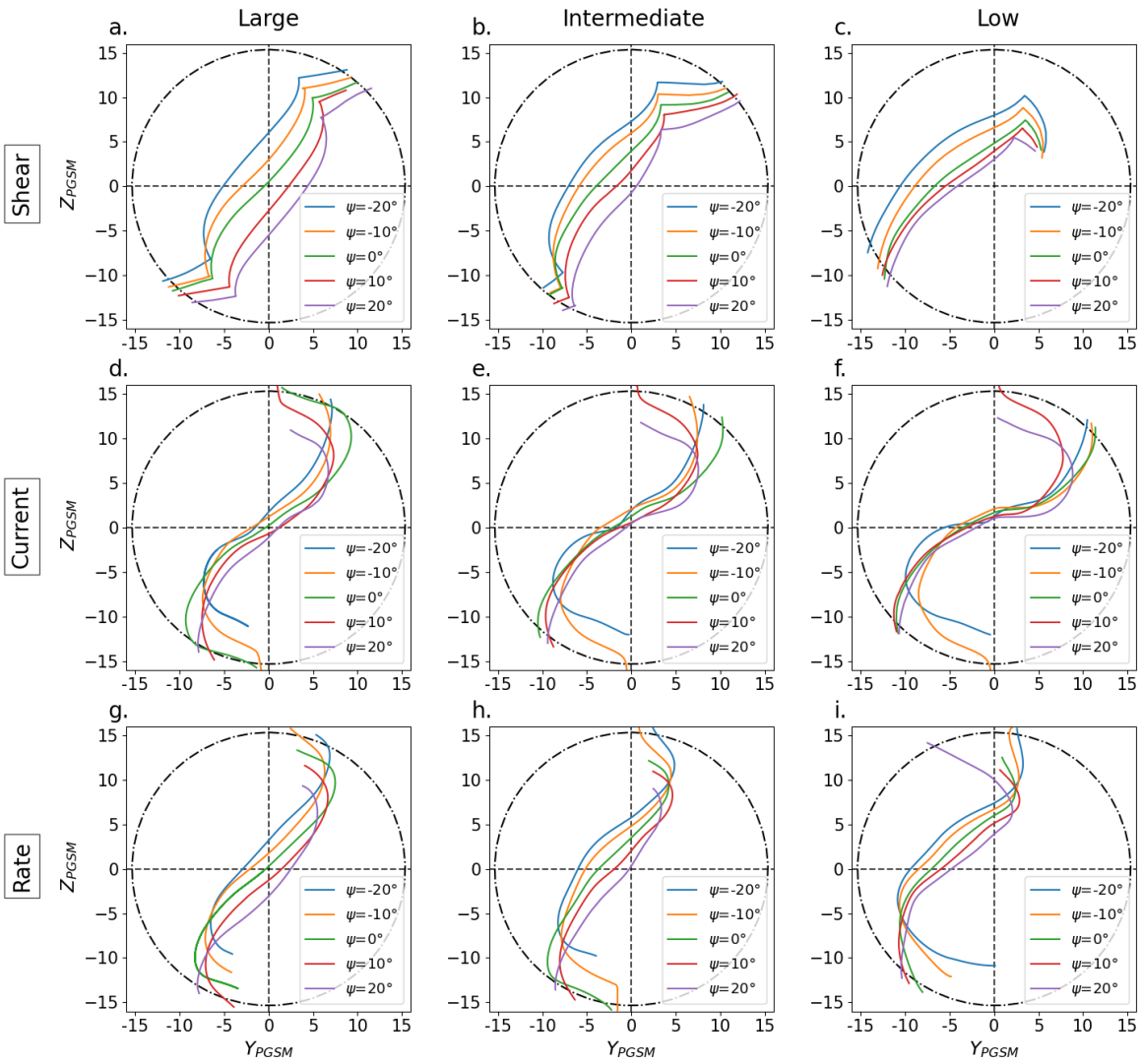

Figure 5.16: Lines maximizing the magnetic shear (panels a, b, c), the current density (panels d, e, f), and reconnection rate (panels g, h, i) at large (panels a, d, g), intermediate (panels b, e, h) and low (panels c, f, i) IMF cone angle and for an IMF clock angle of 60° as a function of the dipole tilt angle (-20°, -10°, 0°, 10°, and 20°). The dashed-dotted circle represents the terminator.

Northward IMF

Figure 5.16 shows the MSLs (panels a, b, c), MCLs (panels d, e, f), and the MRLs (panels g, h, i) at large (panels a, d, g), intermediate (panels b, e, h) and low (panels c, f, i) IMF cone angle and for an IMF clock angle of 60° as a function of the dipole tilt angle (-20°, -10°, 0°, 10°, and 20°). The global distributions of the quantities used to obtain each of these lines can be found in the supplementary material.

The MSLs exhibit a strong dependence on the dipole tilt angle at large IMF cone angles (Figure 5.16.a), shifting from a predominantly northern hemisphere location to a southern hemisphere location as the tilt angle increases. In line with expectations, the MSL with a dipole tilt angle of 0° passes through the subsolar point. The same dependence on the dipole tilt angle is observed at intermediate IMF cone angles (Figure 5.16.b). However, due to the asymmetry in the draping between the quasi-parallel/quasi-perpendicular sides of the magnetopause, the MSLs are shifted towards the northern hemisphere in comparison with the large IMF cone angle case, with the MSL at ψ=20° passing near the subsolar point. This shift is even more pronounced at low IMF cone angles (Figure 5.16.c), where all MSLs cross the noon meridian far northward of the subsolar point.

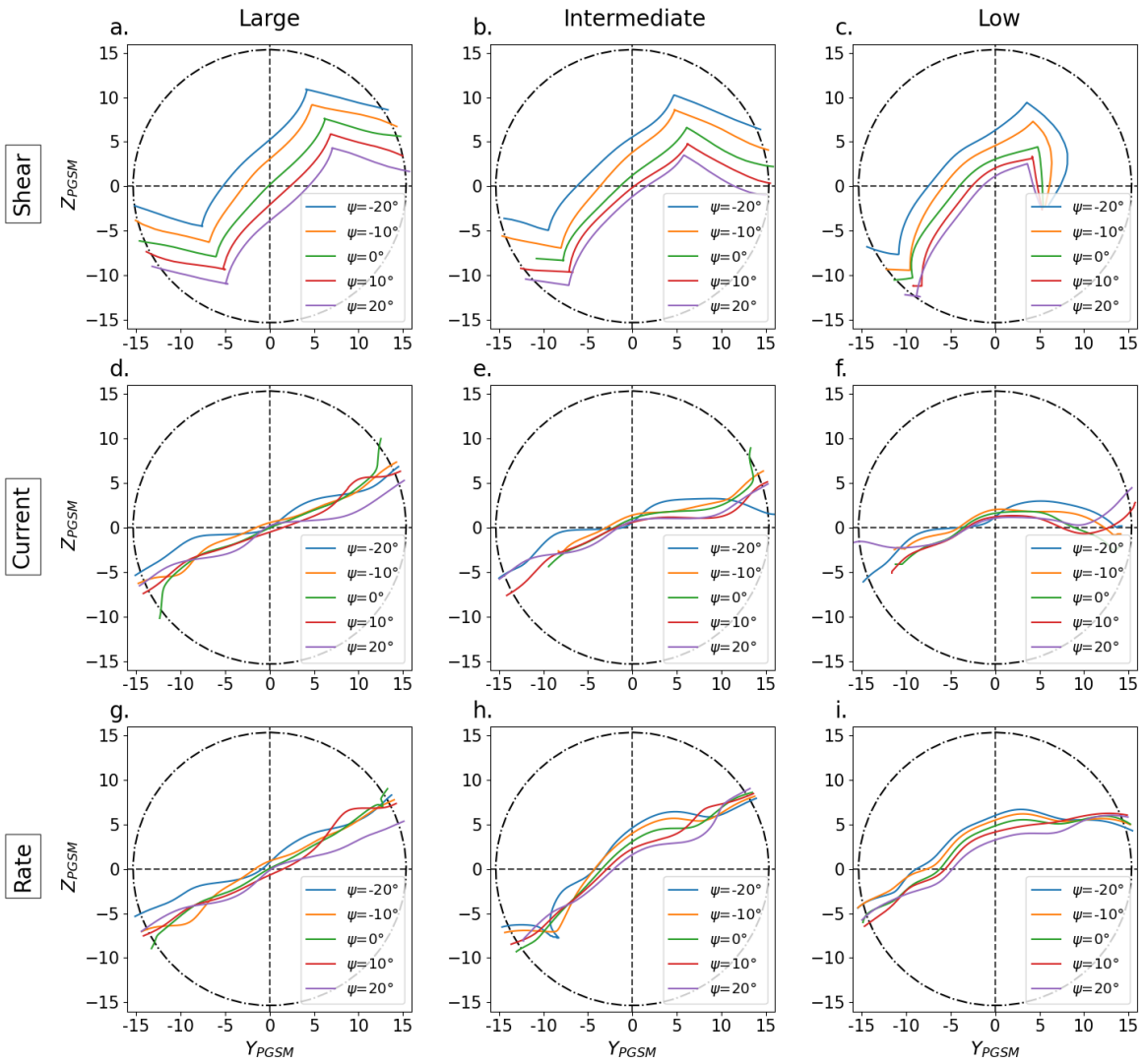

Figure 5.17: Lines maximizing the magnetic shear (panels a, b, c), the current density (panels d, e, f), and reconnection rate (panels g, h, i) at large (panels a, d, g), intermediate (panels b, e, h) and low (panels c, f, i) IMF cone angles and for an IMF clock angle of 120° as a function of the dipole tilt angle (-20°, -10°, 0°, 10°, and 20°). The dashed-dotted circle represents the terminator.

The MCLs show a small dependence on dipole tilt angle at large IMF cone angles (Figure 5.17.d), crossing the noon meridian in the northern and southern hemispheres for negative and positive dipole tilt angles, respectively. The dependence on the dipole tilt angle appears to decrease as the IMF cone angle decreases in the intermediate and low regimes (Figure 5.17.e and f). This is because the difference in magnetic field strength between the magnetosphere and the magnetosheath becomes the main contributor to the current density amplitude. The influence on the dipole tilt angle seems to be visible only at higher latitudes in the northern and southern hemispheres for positive and negative dipole tilt values, respectively.

Similarly to the MSLs, the MRLs show a dependence to dipole tilt angle across all the IMF cone angles regimes (Figure 5.17.g, h, and i) as expected given the strong dependence of the reconnection rate on the magnetic shear.

Southward IMF

Figure 5.17 shows the MSLs (panels a, b, c), MCLs (panels d, e, f), and MRLs (panels g, h, i) at large (panels a, d, g), intermediate (panels b, e, h) and low (panels c, f, i) IMF cone angle and for an IMF clock angle of 120° as a function of the dipole tilt angle (-20°, -10°, 0°, 10°, and 20°).

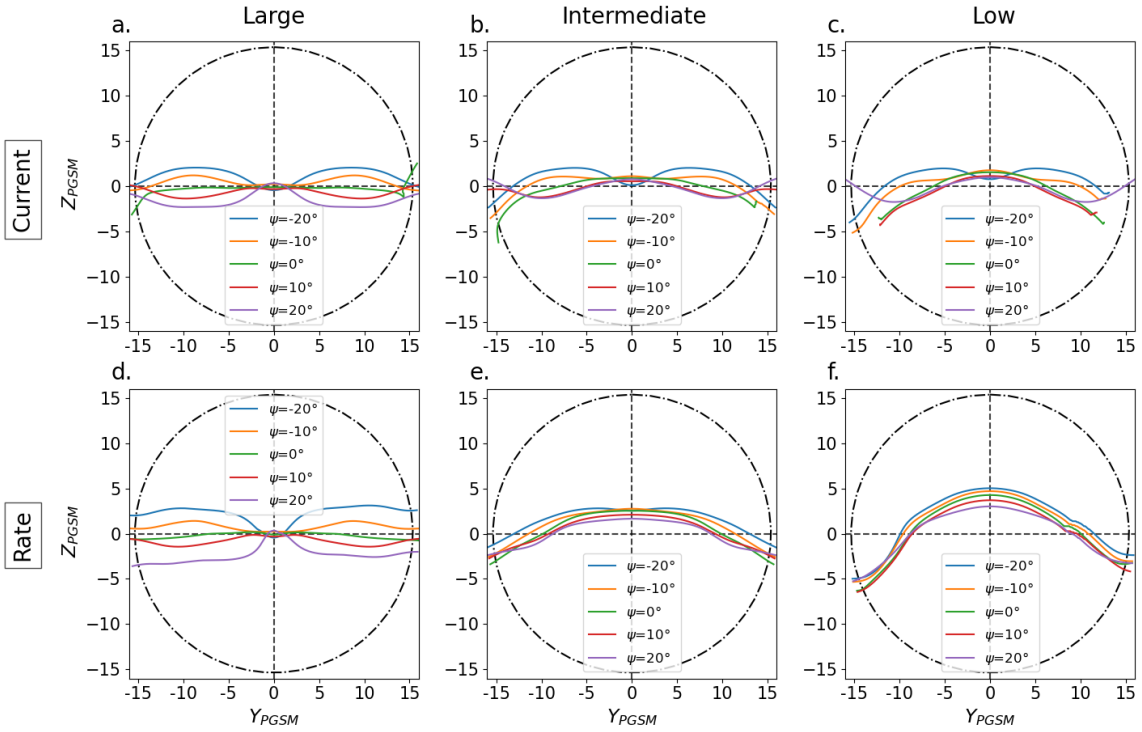

Figure 5.18: Lines maximizing the current density (panels a, b, c), the reconnection rate (panels d, e, f), at large (panels a, d), intermediate (panels b, e) and low (panels c, f) IMF cone angles and for an IMF clock angle of 180° as a function of the dipole tilt angle (-20°, -10°, 0°, 10°, and 20°). The dashed-dotted circle represents the terminator.

The MSLs (Figure 5.17.a, b, and c) show the same strong dependence on the dipole tilt angle as in the northward case.

In contrast with the northward IMF case, the MCLs do not seem to exhibit a clear dependence on the dipole tilt angle at large IMF cone (Figure 5.17.d). In fact, the maximum values of the current change position slightly as the dipole tilt angle varies (see Supplementary Material). However, these maxima are shifted along the average orientation of the MCLs. This keeps the lines relatively close to each other. Similar to the northward IMF case, the significant amplitude difference in magnetic field strength diminishes the influence of the dipole tilt angle as the IMF cone angle decreases in the intermediate and low regimes (Figure 5.17.e and f).

Similar to the current density, the shift of the global pattern (see Supplementary Materials) along the average orientation of the MRLs (Figure 5.17.g) leaves them unaffected by the dipole tilt angle variation for large IMF cone angles. As the IMF cone decreases into the intermediate and low regimes (Figure 5.17.h and g), the influence of the dipole tilt angle becomes apparent due to the asymmetry in magnetic field amplitude between the quasi-parallel and quasi-perpendicular sides of the magnetosheath.

Figure 5.18 shows the MCLs (panels a, b, c), and the MRLs (panels d, e, f) at large (panels a, d,), intermediate (panels b, e) and low (panels c, f) IMF cone angle and for an IMF clock angle of 180° as a function of the dipole tilt angle (-20°, -10°, 0°, 10°, and 20°). The global distributions of the quantities used to obtain each of these lines can be found in the supplementary material. Figure 5.18 does not show MSLs because, as mentioned in the method section 5.2.3, we do not determine them for an IMF clock angle of 180°. However, the spatial distribution of the magnetic shear can be found in supplementary materials.

The MCLs for large IMF cone angle (Figure 5.18.a) show a dependence on the dipole tilt angle in the flanks but converge toward the equator in the subsolar region. The behavior of the MCLs in the subsolar region is influenced by three factors. First, for an IMF clock angle of 180°, the noon meridian displays anti-parallel magnetic shear between the cusps (Figure 5.12.e). Second, the values of the magnetospheric magnetic field strength at the subsolar point remain maximum (47.4

nT ± 1.6 nT) regardless of the dipole tilt angles. Lastly, the magnetic pileup in the magnetosheath peaks near the subsolar point (Figure 5.11.b). Therefore the current is also maximum near the subsolar point and the effect of the dipole tilt angle is only visible on the flanks. As the IMF cone angle decreases into the intermediate and low regimes (Figure 5.18.b and c), the dependence of the MCLs on the dipole tilt angle becomes less clear for $\psi \geq 0°$.

The MRLs for large IMF cone angles (Figure 5.18.d) show a strong dependence on the dipole tilt angle in the flanks but come back toward the equator in the subsolar region for the reasons detailed above for the MCLs (Figure 5.18.a). Interestingly, their shape seem quite consistent with separators obtained with global MHD simulations in a study of the effect of dipole tilt on magnetic reconnection (Eggington et al. 2020 [Eggington et al., 2020]). The location of the MRLs show only a small dependence on the dipole tilt angle in the intermediate and low IMF cone angle regimes (Figure 5.18.e and f). Their shape, which favors the northern hemisphere (i.e. aligned with the quasi-perpendicular bow shock) for all tilt angle values, seems surprising. Even more so since the draping asymmetry between the quasi-parallel/quasi-perpendicular side of the magnetopause tends to produce the highest magnetic shears in the southern hemisphere (Figure 5.14.e and Figure 5.15.e). However, their shape and location result from the large amplitude of the magnetosheath magnetic field in the northern hemisphere (here quasi-perpendicular side of the magnetosheath). The overall evolution of the location, shape, and ordering of the MRLs (subsolar region in panel d; panels e and f) shows that the reconnection rate, once the magnetic shear is sufficiently high, is primarily controlled by the amplitude of the magnetosheath magnetic field, and secondarily by the magnetospheric magnetic strength. However, when the variation amplitude of the magnetosheath magnetic field is relatively isotropic (Figure 5.11.b), a small difference in magnetic shear and amplitude of the magnetospheric magnetic field seems to have a strong effect on the location of the MRLs (away of subsolar region in Figure 5.18.d).

5.5 Global and local approaches on magnetic reconnection

Section 5.4 explored the influence of the IMF orientation and dipole tilt angle on the global distribution of the magnetic shear angle, current density, and reconnection rate and on the lines maximizing these quantities. Such maximization can be considered a global approach, as it requires knowledge of the global spatial variation of a quantity to identify a possible X-line. Thus, the underlying idea would be that the localization of the magnetic reconnection is controlled by global constraints at the magnetopause. In parallel, several numerical modeling studies [Aunai et al., 2016; Hesse et al., 2013; Liu et al., 2015a, 2018; Schreier et al., 2010] focused on determining the orientation of reconnection lines with an initially homogeneous current sheet, which can therefore be characterized as a local approach to determining how X-line develop. For most of the local studies [Aunai et al., 2016; Hesse et al., 2013; Liu et al., 2015a, 2018], the X-line is found to bisect the magnetic fields on each side of the magnetopause. Although it can be expected that global and local approaches will results in different X-line orientations, the extent of these difference is unknown. This is the aim of this section, in which we compare the line maximizing magnetic shear used in the Maximum Magnetic Shear model [Trattner et al., 2007] with the line following the bisection from the subsolar point.

Figure 5.19.a shows the color coded spatial distribution of the magnetic shear angle for a IMF cone angle of $80° \leq |\theta_{co}| \leq 90°$, an IMF clock angle of 130°, and a dipole tilt angle of $\psi = 0° \pm 2.5°$ for the magnetosphere. Along the MSL is represented the local and bisecting orientations (small black lines) of the magnetic field vector on each side of the magnetopause (green and blue arrows for the magnetic field of the magnetosphere and magnetosheath, respectively). As expected, the magnetic field vectors are in agreement with the shear angle map, exhibiting anti-parallel behavior in white regions and forming an angle of approximately 130° in the subsolar region. It is important to notice that the bisection orientations are not aligned with the local tangents of the MSL which demonstrates that the global and local approaches are not consistent with each other. The angular differences are large in the anti-parallel region, where the local bisections are nearly perpendicular

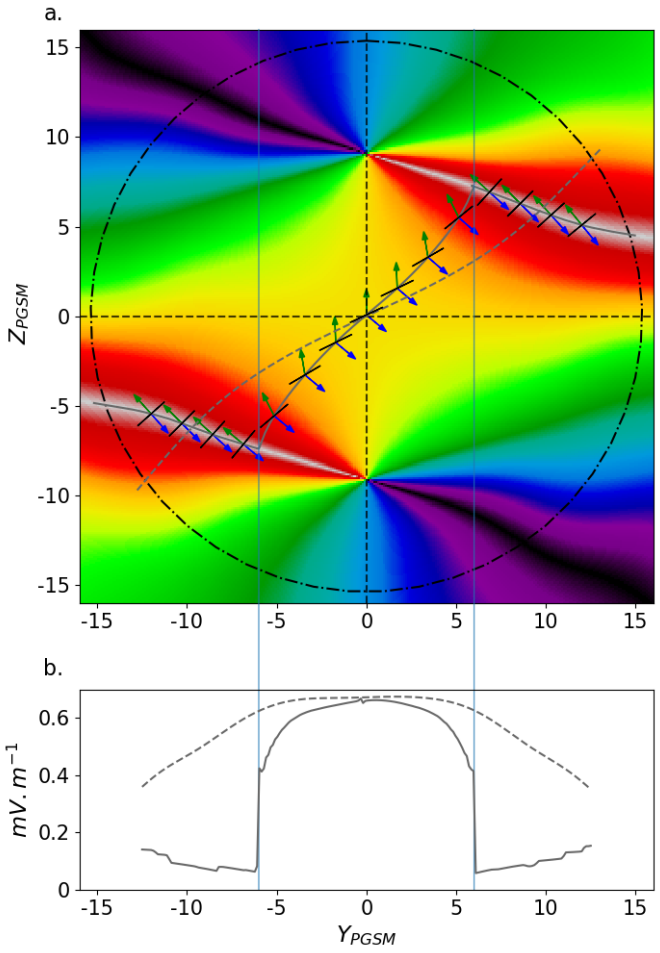

Figure 5.19: Global distribution of the magnetic shear represented in panel a, using in-situ measurements for a IMF cone angle of $80° \leq |\theta_{co}| \leq 90°$, an IMF clock angle has a value of 130°, and a dipole tilt angle of ψ = 0°±2.5° for the magnetosphere. The solid gray line is the MSL, along which the orientation of the magnetospheric and magnetosheath magnetic fields are indicated by the green and blue arrows, respectively. The small black lines correspond to the local bisections of the magnetic fields. The dashed gray line follow the local bisection of the magnetic fields, as integrated from the subsolar point. In panel b, the reconnection rate along the MSL and the bisection line are shown as solid and dashed lines, respectively. The vertical blue lines mark where the component reconnection part of the MSL joins the anti-parallel branches.

to the MSL, and smaller in the subsolar region. However, a global X-line obtained by following the local bisections from this region gives a prediction significantly different from the MSL. More than the distance between the lines, the fundamental difference between these two candidate X-lines is that the bisection line cannot align with the anti-parallel regions for any IMF orientation, except for IMF clock angle of 180°. However, observations of accelerated cusp ions [Trattner et al., 2007, 2021] and MHD simulations for northward IMF [Komar et al., 2015] show that magnetic reconnection occurs along the anti-parallel regions.

Figure 5.19.b shows the reconnection rate along the MSL and the bisection line if magnetic merging were to occurs there. In contrast to the reconnection rate discussed in the previous section, for which the merging components are determined by maximizing its values (section 5.2.1), here these components are those which are perpendicular to the local tangents of the two candidate X-lines. If the reconnection rate for these lines is similar at the subsolar point, the one associated with the MSL decreases to approximately 0.4 mV/m before the component reconnection part of the MSL joins the anti-parallel branches (vertical blue lines). A discontinuity is present at the junction to the anti-parallel branches, where the reconnection rate suddenly drops to 0.06 mV/m before slowly increasing to approximately 0.15 mV/m in the flanks. This drastic reduction of the reconnection rate in the anti-parallel magnetic shear region results from the orientation of the MSL is associated with really small reconnecting component. In contrast, the reconnection rate along the bisection line remains almost constant with a value of about 0.61 mV/m until the line reaches the anti-parallel regions, and then decreases to 0.34 mV/m. The decrease in the reconnection rate occurs where the magnetic shear along the bisection line is the highest. An increase in the magnetic shear should increase the amplitude of the reconnected components (Eq. 5.3). However, the reconnection rate decreases due to the reduction in the amplitude of the magnetic field in the magnetosphere and magnetosheath (Figure 5.11.a and b).

5.6 Discussion and Conclusion

Both numerical simulations and observations support the existence of extended reconnection lines on the magnetopause surface. Their location, as a function of the IMF orientation and dipole tilt angle, constitutes a long standing question in magnetospheric physics. Historically, the spatial distribution of the shear angle between the draped magnetosheath magnetic field and the magnetospheric field, has been the primary parameter used to build models predicting the location of such global X-lines. Besides the obvious importance of the magnetic shear in the reconnection process, other quantities such as the current density and the reconnection rate, could be thought as equally determinant for localizing the reconnection line. Especially, since these quantities strongly depend on the magnetic shear, but also on the plasma density and/or the amplitude of magnetic fields. However, until now, the spatial distribution of these quantities on the magnetopause and their dependence on the IMF orientation and dipole tilt are still poorly understood. Furthermore, these spatial distributions, including that of the magnetic shear angle, have so far only been obtained from analytical or numerical models, and never entirely constrained by observational means.

In this study, we proposed the first global reconstruction of the spatial distribution of magnetic shear, current density, and an MHD reconnection rate scaling law on the dayside magnetopause from in-situ spacecraft measurements only. These distributions and their dependence on the IMF orientation and dipole tilt angle have been analyzed. A line maximizing the considered quantity has been computed and discussed as a possible X-line candidate.

5.6.1 Spatial distributions of the magnetic shear, current density, and reconnection rate

The first outcome of this study concerns the distribution of the magnetic shear angle. A comparison between the magnetic shear maps obtained with in-situ measurements and those ob-

tained with models showed that there is a relatively good agreement between the two for large ($|\theta_{co}| \geq 45° \pm 5°$) and small ($|\theta_{co}| \leq 12.5° \pm 2.5°$) IMF cone angles. However, significant differences were found at intermediate IMF cone angles ($12.5° \pm 2.5° \leq |\theta_{co}| \leq 45° \pm 5°$) because the KF94 model predicts invalid magnetosheath field draping for such IMF orientations. Despite their qualitative agreement, the maximum shear maps obtained from models and observations lead to maximum shear lines that differ in their response to varying IMF clock angles. In contrast to those obtained from models, maximum shear lines at large IMF cone angles obtained from observations are found to be relatively independent of the IMF clock angle in the component reconnection region. This behavior appears consistent with results from global MHD simulations performed in similar IMF conditions [Komar et al., 2015]. The dependence of maximum shear lines with the dipole tilt angle is important and similar to that already reported in previous studies [Trattner et al., 2021], with a shift to northern (resp. southern) latitudes for negative (resp. positive) tilt angles.

A drawback of considering only the magnetic shear is that it disregards the impact of the magnetic field amplitude on reconnection, although it is well known to be important in reconnection physics. The distribution of the magnetic amplitude on the magnetopause and its jump across the layer is, however, considered in the current density and the reconnection rate scaling laws. The reconstructed distributions of the current density and the reconnection rate were found to be consistent with those obtained from published MHD simulations results [Glocer et al., 2016; Komar et al., 2015; Souza et al., 2017]. The current density amplitude is also found to be consistent with that observed in-situ [Beedle et al., 2022; Haaland et al., 2020; Lukin et al., 2020]. Although the current density and reconnection rate scaling law both factor in the magnetic shear, their distributions are found to be very different from that of the magnetic shear. They are, however, relatively similar to each other. This similarity between the current and reconnection rate distributions, and their respective maximum line, is more pronounced for large IMF cone angles, and fades away as the IMF becomes increasingly radial due to their different dependence on the amplitude of the magnetic field. Indeed the current density becomes primarily results from the difference in the amplitude of the upstream magnetic fields for increasingly radial IMF conditions, whereas the reconnection rate depends on the magnetic shear and the absolute amplitude of reconnecting magnetic components rather than their difference. One of the important consequences for the current density is that its distribution becomes weakly dependent on the IMF clock angle and dipole tilt angle as the IMF becomes more radial, in contrast to the distribution of the reconnection rate. Contrary to the lines obtained from maximizing the magnetic shear, those obtained from the current density or the reconnection rate do not present sharp turns, which is a specificity of the maximum shear model.

The spatial distributions of the current density and reconnection rate were found to be more complex than that of the shear angle. In particular, in the case of the current density, we observed the possible appearance of several local maxima originating from the fact that the current can be large either because of a large jump in the magnetic amplitude or in the magnetic orientation, whose behaviors are relatively independent. This results in a necessary choice among different maximization lines for which a physical constraint would remain to be found. We also found that certain configurations unfavorable to the merging process, such as those with low magnetic shear and strong asymmetry between magnetospheric and magnetosheath magnetic field strengths, can still result in significant current density. Furthermore, some IMF orientations results in lines maximizing the current density passing through regions of parallel magnetic fields, where reconnection is *de facto* impossible. Therefore, even though the current density is an important feature of the magnetopause and could also be important for aspects of reconnection such as its onset and/or propagation, it seems unlikely that a global X-line can be determined by the sole maximization of the current density distribution.

5.6.2 Discriminating between the X-line candidates

The three quantities analyzed in this study display distinct characteristics and dependence on the IMF orientation and dipole tilt angles. Therefore observations of magnetic reconnection in cer-

tain ranges of these parameters should allow to discriminate between the different X-line models (if any applies). For instance, observations made for intermediate and low IMF cone angles should allow us to distinguish between the lines maximizing the current density and those maximizing the magnetic shear or the reconnection rate. Indeed, the dependence of current density on IMF clock and dipole tilt angle decreases when the IMF cone angle decreases, which is not true for the other two quantities. In contrast, the lines maximizing the magnetic shear and the reconnection rate are relatively similar, except for strongly southward IMF, at intermediate and low IMF cone angle. This would make them difficult to distinguish from each other, especially considering the uncertainty in the determination of the causal IMF. However, for large IMF cone angles, the maximum reconnection rate lines incline towards the equator as the IMF clock angle increases, which fact does not occur for the component reconnection part of the maximum magnetic shear lines. Thus, observations of magnetic reconnection at high latitudes or in the magnetopause flanks should allow to discriminate between these two X–line candidates. Furthermore, at large IMF cone angles, some IMF clock angles produce reconnection rate distributions resulting in lines that are mostly independent of the dipole tilt angle, while the lines maximizing the magnetic shear remains strongly dependent on it. Finally, a unique feature distinguishes the lines maximizing magnetic shear from those maximizing other quantities is that it follows the region of anti-parallel shear, provided that the IMF clock angle is not strongly southward.

5.6.3 Global and local approaches of an X-line

No matter which quantity is considered, X-lines were obtained by maximizing a quantity defined on a global scale. The physics underlying the formation of such extended X-lines remains, however, unclear. In one scenario, these regions could be those of preferred reconnection onset, resulting from the global scale interaction of the solar wind and IMF with the magnetosphere. In another, extended X-lines could result from a localized onset followed by X-line spreading governed by local plasma mechanisms.

In this study, we have shown the X-line built from maximizing a given quantity distributed on the magnetopause is locally oriented along directions disagreeing with predictions suggested by local physics, and therefore these two scenarios are not consistent with each other.

Local studies [Aunai et al., 2016; Hesse et al., 2013; Liu et al., 2015a, 2018] tend to agree that magnetic reconnection appears to be oriented along the bisection of the upstream magnetic fields. However, the construction of a global X-line following this local approach critically depend on the onset location of magnetic reconnection, and therefore requires further constraints to be defined. For instance, the onset location could be situated at point of first contact of the IMF with the magnetopause as used in this study, it can also be where the reconnecting component are the greatest [Moore et al., 2002], or it might be located elsewhere. More importantly, since following the bisection does not take into account the spatial variation of physical quantities such as magnetic shear or magnetic field amplitude, it can produce X-lines located where reconnection is unlikely or even impossible, such as in regions of parallel magnetic fields.

An X-line following the global approach, such as the maximum magnetic shear model [Trattner et al., 2007], can result in local merging orientation producing small reconnecting component of the magnetic fields, and therefore, small reconnection rate. Indeed, except for strongly southward IMF, the parts of the MSL along the anti-parallel branches are often close to being parallel to the magnetic field orientation on both sides of the magnetopause. More importantly, an abrupt change in orientation of an X-line, such as the junction between the component and anti-parallel parts of the MSL, tends to produce discontinuities in the reconnection rate along the X-line, and is not seen in other X-line scenarios.

5.6.4 Limitations and perspectives

For reconstructing the spatial distributions of quantities such as the magnetic field, this study assumes that the influence of magnetic reconnection can be neglected on a large scale, therefore

subsets of magnetosheath measurements were selected based solely on the IMF cone angle values and maps for specific clock angles were thus produced in the PGSM coordinate system. However, studies tend to show that magnetic reconnection could have a global effect on the ion density and magnetic field [Anderson et al., 1997; Kaymaz, 1998; Phan et al., 1994]. Such an effect could marginally change the distributions of quantities such as magnetic shear, current density, and reconnection rate. Investigations (not included in this report) revealed minor alterations, such as the detailed curvature of magnetic field lines in the magnetosheath, that do not affect the findings of this study but call for more detailed and future work.

Estimating the potential reconnection rate on the magnetopause surface, leading to a solid X-line candidate, is not easy and the distributions proposed in this study should be considered carefully. In this study, the reconnection rate was estimated from an MHD scaling law designed for asymmetric conditions but antiparallel field lines. Global MHD simulations seems to indicate [Komar and Cassak, 2016] that this law generally under-estimates the measured reconnection rate in conditions different than due southward IMF. Furthermore, it has also been shown that the reconnection rate in asymmetric and non-coplanar current sheets critically depends on ion kinetic effects [Hesse et al., 2013]. More work is thus needed to improve the prediction of the potential reconnection rate on the magnetopause surface.

This study has brought new constraints to where reconnection could be located on the magnetopause, from an observational standpoint. Although also generally the case in other studies, we feel an important limitation of our results comes from assuming steady upstream conditions. Work is being done to reconstruct the time dependent distribution of a given quantity on the magnetopause in varying upstream conditions accounting for the propagation in the magnetosheath, and will be the focus of a forthcoming study.

Although they are among the main parameters conditioning reconnection at the magnetopause, we have here only considered a dependency on the IMF orientation and dipole tilt. The role of other parameters, such as the solar wind Mach number, should be investigated in the future. Also, we assumed the state of the magnetopause only depends on upstream conditions in the solar wind. In reality, the location of X-lines may also depend on the system's more or less recent history, and this should also be investigated.

In addition to addressing the limitations mentioned above, future work should focus on gathering statistical evidence from reconnection signatures to discriminate among all possible scenarios. This could be achieved by extracting reconnection signatures massively from decades of data from multiple spacecraft missions, and correlating them with environmental maps such as those used in this study. Work is currently being undertaken in that regard.

5.7 Bibliography

Alexeev, I. I., Sibeck, D. G., and Bobrovnikov, S. Y.: Concerning the location of magnetopause merging as a function of the magnetopause current strength, , 103, 6675–6684, https://doi.org/10.1029/97JA02863, 1998. 125, 137

Anderson, B. J., Phan, T. D., and Fuselier, S. A.: Relationships between plasma depletion and subsolar reconnection, , 102, 9531–9542, https://doi.org/10.1029/97JA00173, 1997. 152

Aunai, N., Hesse, M., Lavraud, B., Dargent, J., and Smets, R.: Orientation of the X-line in asymmetric magnetic reconnection, Journal of Plasma Physics, 82, 535820401, https://doi.org/10.1017/S0022377816000647, 2016. 125, 147, 151

Axford, W. I.: Magnetospheric convection., Reviews of Geophysics and Space Physics, 7, 421–459, https://doi.org/10.1029/RG007i001p00421, 1969. 124

Beedle, J. M. H., Gershman, D. J., Uritsky, V. M., Phan, T. D., and Giles, B. L.: A Systematic Look at the Temperature Gradient Contribution to the Dayside Magnetopause Current, , 49, e97547, https://doi.org/10.1029/2021GL097547, 2022. 138, 150

Birn, J. and Priest, E. R.: Reconnection of magnetic fields : magnetohydrodynamics and collisionless theory and observations, 2007. 125

Borovsky, J. E.: Physical improvements to the solar wind reconnection control function for the Earth's magnetosphere, Journal of Geophysical Research (Space Physics), 118, 2113–2121, https://doi.org/10.1002/jgra.50110, 2013. 124, 125, 137

Borovsky, J. E. and Birn, J.: The solar wind electric field does not control the dayside reconnection rate, Journal of Geophysical Research (Space Physics), 119, 751–760, https://doi.org/10.1002/2013JA019193, 2014. 124

Borovsky, J. E., Hesse, M., Birn, J., and Kuznetsova, M. M.: What determines the reconnection rate at the dayside magnetosphere?, Journal of Geophysical Research (Space Physics), 113, A07210, https://doi.org/10.1029/2007JA012645, 2008. 124

Cassak, P. A. and Otto, A.: Scaling of the magnetic reconnection rate with symmetric shear flow, Physics of Plasmas, 18, 074501, https://doi.org/10.1063/1.3609771, 2011. 139

Cassak, P. A. and Shay, M. A.: Scaling of asymmetric magnetic reconnection: General theory and collisional simulations, Physics of Plasmas, 14, 102114, https://doi.org/10.1063/1.2795630, 2007. 124, 126, 128

Cooling, B. M. A., Owen, C. J., and Schwartz, S. J.: Role of the magnetosheath flow in determining the motion of open flux tubes, , 106, 18 763–18 776, https://doi.org/10.1029/2000JA000455, 2001. 124

Cowley, S. W. H. and Owen, C. J.: A simple illustrative model of open flux tube motion over the dayside magnetopause, , 37, 1461–1475, https://doi.org/10.1016/0032-0633(89)90116-5, 1989. 124

Crooker, N. U., Eastman, T. E., and Stiles, G. S.: Observations of plasma depletion in the magnetosheath at the dayside magnetopause, , 84, 869–874, https://doi.org/10.1029/JA084iA03p00869, 1979. 124

Daly, P. W., Saunders, M. A., Rijnbeek, R. P., Sckopke, N., and Russell, C. T.: The distribution of reconnection geometry in flux transfer events using energetic ion, plasma and magnetic data, , 89, 3843–3854, https://doi.org/10.1029/JA089iA06p03843, 1984. 124

Daughton, W. and Karimabadi, H.: Kinetic theory of collisionless tearing at the magnetopause, Journal of Geophysical Research (Space Physics), 110, A03217, https://doi.org/10.1029/2004JA010751, 2005. 125

Dimmock, A. P. and Nykyri, K.: The statistical mapping of magnetosheath plasma properties based on THEMIS measurements in the magnetosheath interplanetary medium reference frame, Journal of Geophysical Research (Space Physics), 118, 4963–4976, https://doi.org/10.1002/jgra.50465, 2013. 124

Dimmock, A. P., Nykyri, K., and Pulkkinen, T. I.: A statistical study of magnetic field fluctuations in the dayside magnetosheath and their dependence on upstream solar wind conditions, Journal of Geophysical Research (Space Physics), 119, 6231–6248, https://doi.org/10.1002/2014JA020009, 2014. 124

Dimmock, A. P., Pulkkinen, T. I., Osmane, A., and Nykyri, K.: The dawn-dusk asymmetry of ion density in the dayside magnetosheath and its annual variability measured by THEMIS, Annales Geophysicae, 34, 511–528, https://doi.org/10.5194/angeo-34-511-2016, 2016. 124

Drake, J. F. and Lee, Y. C.: Kinetic theory of tearing instabilities, Physics of Fluids, 20, 1341–1353, https://doi.org/10.1063/1.862017, 1977. 125

Dungey, J. W.: Interplanetary Magnetic Field and the Auroral Zones, , 6, 47–48, https://doi.org/10.1103/PhysRevLett.6.47, 1961. 124

Dunlop, M. W., Zhang, Q. H., Bogdanova, Y. V., Lockwood, M., Pu, Z., Hasegawa, H., Wang, J., Taylor, M. G. G. T., Berchem, J., Lavraud, B., Eastwood, J., Volwerk, M., Shen, C., Shi, J. K., Constantinescu, D., Frey, H., Fazakerley, A. N., Sibeck, D., Escoubet, P., Wild, J. A., and Liu, Z. X.: Extended Magnetic Reconnection across the Dayside Magnetopause, , 107, 025004, https://doi.org/10.1103/PhysRevLett.107.025004, 2011. 124

Eggington, J. W. B., Eastwood, J. P., Mejnertsen, L., Desai, R. T., and Chittenden, J. P.: Dipole Tilt Effect on Magnetopause Reconnection and the Steady-State Magnetosphere-Ionosphere System: Global MHD Simulations, Journal of Geophysical Research (Space Physics), 125, e27510, https://doi.org/10.1029/2019JA027510, 2020. 124, 147

Glocer, A., Dorelli, J., Toth, G., Komar, C. M., and Cassak, P. A.: Separator reconnection at the magnetopause for predominantly northward and southward IMF: Techniques and results, Journal of Geophysical Research (Space Physics), 121, 140–156, https://doi.org/10.1002/2015JA021417, 2016. 124, 138, 150

Gonzalez, W. D. and Mozer, F. S.: A quantitative model for the potential resulting from reconnection with an arbitrary interplanetary magnetic field, , 79, 4186, https://doi.org/10.1029/JA079i028p04186, 1974. 124

Haaland, S., Paschmann, G., Øieroset, M., Phan, T., Hasegawa, H., Fuselier, S. A., Constantinescu, V., Eriksson, S., Trattner, K. J., Fadanelli, S., Tenfjord, P., Lavraud, B., Norgren, C., Eastwood, J. P., Hietala, H., and Burch, J.: Characteristics of the Flank Magnetopause: MMS Results, Journal of Geophysical Research (Space Physics), 125, e27623, https://doi.org/10.1029/2019JA027623, 2020. 127, 128, 138, 150

Hesse, M., Aunai, N., Zenitani, S., Kuznetsova, M., and Birn, J.: Aspects of collisionless magnetic reconnection in asymmetric systems, Physics of Plasmas, 20, 061210, https://doi.org/10.1063/1.4811467, 2013. 124, 125, 147, 151, 152

Hill, T. W.: Magnetic merging in a collisionless plasma, , 80, 4689, https://doi.org/10.1029/JA080i034p04689, 1975. 124

Jelínek, K., Němeček, Z., and Šafránková, J.: A new approach to magnetopause and bow shock modeling based on automated region identification, Journal of Geophysical Research (Space Physics), 117, A05208, https://doi.org/10.1029/2011JA017252, 2012. 126, 129

Kaymaz, Z.: IMP 8 magnetosheath field comparisons with models, Annales Geophysicae, 16, 376–387, https://doi.org/10.1007/s00585-998-0376-3, 1998. 152

King, J. H. and Papitashvili, N. E.: Solar wind spatial scales in and comparisons of hourly Wind and ACE plasma and magnetic field data, Journal of Geophysical Research (Space Physics), 110, A02104, https://doi.org/10.1029/2004JA010649, 2005. 126

Kobel, E. and Fluckiger, E. O.: A model of the steady state magnetic field in the magnetosheath, , 99, 23 617–23 622, https://doi.org/10.1029/94JA01778, 1994. 124, 127, 129, 133, 134, 135, 136

Komar, C. M. and Cassak, P. A.: The local dayside reconnection rate for oblique interplanetary magnetic fields, Journal of Geophysical Research (Space Physics), 121, 5105–5120, https://doi.org/10.1002/2016JA022530, 2016. 152

Komar, C. M., Fermo, R. L., and Cassak, P. A.: Comparative analysis of dayside magnetic reconnection models in global magnetosphere simulations, Journal of Geophysical Research (Space Physics), 120, 276–294, https://doi.org/10.1002/2014JA020587, 2015. 124, 125, 128, 137, 138, 139, 140, 149, 150

Lin, R. L., Zhang, X. X., Liu, S. Q., Wang, Y. L., and Gong, J. C.: A three-dimensional asymmetric magnetopause model, Journal of Geophysical Research (Space Physics), 115, A04207, https://doi.org/10.1029/2009JA014235, 2010. 132

Liu, Y.-H., Hesse, M., and Kuznetsova, M.: Orientation of X lines in asymmetric magnetic reconnection—Mass ratio dependency, Journal of Geophysical Research (Space Physics), 120, 7331–7341, https://doi.org/10.1002/2015JA021324, 2015a. 125, 147, 151

Liu, Y.-H., Hesse, M., Guo, F., Daughton, W., Li, H., Cassak, P. A., and Shay, M. A.: Why does Steady-State Magnetic Reconnection have a Maximum Local Rate of Order 0.1?, , 118, 085101, https://doi.org/10.1103/PhysRevLett.118.085101, 2017. 128

Liu, Y.-H., Hesse, M., Li, T. C., Kuznetsova, M., and Le, A.: Orientation and Stability of Asymmetric Magnetic Reconnection X Line, Journal of Geophysical Research (Space Physics), 123, 4908–4920, https://doi.org/10.1029/2018JA025410, 2018. 125, 147, 151

Liu, Z. Q., Lu, J. Y., Wang, C., Kabin, K., Zhao, J. S., Wang, M., Han, J. P., Wang, J. Y., and Zhao, M. X.: A three-dimensional high Mach number asymmetric magnetopause model from global MHD simulation, Journal of Geophysical Research (Space Physics), 120, 5645–5666, https://doi.org/10.1002/2014JA020961, 2015b. 132

Luhmann, J. G., Walker, R. J., Russell, C. T., Crooker, N. U., Spreiter, J. R., and Stahara, S. S.: Patterns of Potential Magnetic Field Merging Sites on the Dayside Magnetopause, , 89, 1739–1742, https://doi.org/10.1029/JA089iA03p01739, 1984. 124

Lukin, A. S., Panov, E. V., Artemyev, A. V., Petrukovich, A. A., Haaland, S., Nakamura, R., Angelopoulos, V., Runov, A., Yushkov, E. V., Avanov, L. A., Giles, B. L., Russell, C. T., and Strangeway, R. J.: Comparison of the Flank Magnetopause at Near-Earth and Lunar Distances: MMS and ARTEMIS Observations, Journal of Geophysical Research (Space Physics), 125, e28406, https://doi.org/10.1029/2020JA028406, 2020. 138, 150

Moore, T. E., Fok, M. C., and Chandler, M. O.: The dayside reconnection X line, Journal of Geophysical Research (Space Physics), 107, 1332, https://doi.org/10.1029/2002JA009381, 2002. 124, 125, 151

Nguyen, G., Aunai, N., Michotte de Welle, B., Jeandet, A., Lavraud, B., and Fontaine, D.: Massive Multi-Mission Statistical Study and Analytical Modeling of the Earth's Magnetopause: 1. A Gradient Boosting Based Automatic Detection of Near-Earth Regions, Journal of Geophysical Research (Space Physics), 127, e29773, https://doi.org/10.1029/2021JA029773, 2022a. 126

Nguyen, G., Aunai, N., Michotte de Welle, B., Jeandet, A., Lavraud, B., and Fontaine, D.: Massive Multi-Mission Statistical Study and Analytical Modeling of the Earth's Magnetopause: 4. On the Near-Cusp Magnetopause Indentation, Journal of Geophysical Research (Space Physics), 127, e29776, https://doi.org/10.1029/2021JA029776, 2022b. 132

Onsager, T. G., Thomsen, M. F., Elphic, R. C., and Gosling, J. T.: Model of electron and ion distributions in the plasma sheet boundary layer, , 96, 20 999–21 011, https://doi.org/10.1029/91JA01983, 1991. 124

Petrinec, S. M., Burch, J. L., Fuselier, S. A., Trattner, K. J., Giles, B. L., and Strangeway, R. J.: On the Occurrence of Magnetic Reconnection Along the Terrestrial Magnetopause, Using Magnetospheric Multiscale (MMS) Observations in Proximity to the Reconnection Site, Journal of Geophysical Research (Space Physics), 127, e29669, https://doi.org/10.1029/2021JA029669, 2022. 132

Phan, T. D., Paschmann, G., Baumjohann, W., Sckopke, N., and Luehr, H.: The magnetosheath region adjacent to the dayside magnetopause: AMPTE/IRM observations, , 99, 121–142, https://doi.org/10.1029/93JA02444, 1994. 152

Phan, T. D., Kistler, L. M., Klecker, B., Haerendel, G., Paschmann, G., Sonnerup, B. U. Ö., Baumjohann, W., Bavassano-Cattaneo, M. B., Carlson, C. W., DiLellis, A. M., Fornacon, K. H., Frank, L. A., Fujimoto, M., Georgescu, E., Kokubun, S., Moebius, E., Mukai, T., Øieroset, M., Paterson, W. R., and Reme, H.: Extended magnetic reconnection at the Earth's magnetopause from detection of bi-directional jets, , 404, 848–850, https://doi.org/10.1038/35009050, 2000. 124

Phan, T. D., Freeman, M. P., Kistler, L. M., Klecker, B., Haerendel, G., Paschmann, G., Sonnerup, B. U. Ö., Baumjohann, W., Bavassano-Cattaneo, M. B., Carlson, C. W., DiLellis, A. M., Fornacon, K. H., Frank, L. A., Fujimoto, M., Georgescu, E., Kokubun, S., Moebius, E., Mukai, T., Paterson, W. R., and Reme, H.: Evidence for an extended reconnection line at the dayside magnetopause, Earth, Planets and Space, 53, 619–625, https://doi.org/10.1186/BF03353281, 2001. 124

Phan, T. D., Hasegawa, H., Fujimoto, M., Oieroset, M., Mukai, T., Lin, R. P., and Paterson, W.: Simultaneous Geotail and Wind observations of reconnection at the subsolar and tail flank magnetopause, , 33, L09104, https://doi.org/10.1029/2006GL025756, 2006. 124

Phan, T. D., Paschmann, G., Gosling, J. T., Oieroset, M., Fujimoto, M., Drake, J. F., and Angelopoulos, V.: The dependence of magnetic reconnection on plasma β and magnetic shear: Evidence from magnetopause observations, , 40, 11–16, https://doi.org/10.1029/2012GL054528, 2013. 126

Pu, Z. Y., Xiao, C. J., Zhang, X. G., Huang, Z. Y., Fu, S. Y., Liu, Z. X., Dunlop, M. W., Zong, Q. G., Carr, C. M., Réme, H., Dandouras, I., Fazakerley, A., Phan, T., Zhang, T. L., Zhang, H., and Wang, X. G.: Double Star TC-1 observations of component reconnection at the dayside magnetopause: a preliminary study, Annales Geophysicae, 23, 2889–2895, https://doi.org/10.5194/angeo-23-2889-2005, 2005. 124

Schreier, R., Swisdak, M., Drake, J. F., and Cassak, P. A.: Three-dimensional simulations of the orientation and structure of reconnection X-lines, Physics of Plasmas, 17, 110 704–110 704, https://doi.org/10.1063/1.3494218, 2010. 147

Scurry, L., Russell, C. T., and Gosling, J. T.: A statistical study of accelerated flow events at the dayside magnetopause, , 99, 14,815–14,829, https://doi.org/10.1029/94JA00793, 1994. 124

Shue, J. H., Song, P., Russell, C. T., Steinberg, J. T., Chao, J. K., Zastenker, G., Vaisberg, O. L., Kokubun, S., Singer, H. J., Detman, T. R., and Kawano, H.: Magnetopause location under extreme solar wind conditions, JGR, 103, 17 691–17 700, https://doi.org/10.1029/98JA01103, 1998. 126, 127, 132

Sibeck, D. G., Lopez, R. E., and Roelof, E. C.: Solar wind control of the magnetopause shape, location, and motion, , 96, 5489–5495, https://doi.org/10.1029/90JA02464, 1991. 129, 132

Sonnerup, B. U. Ö.: Magnetopause reconnection rate, , 79, 1546–1549, https://doi.org/10.1029/JA079i010p01546, 1974. 124

Souza, V. M., Gonzalez, W. D., Sibeck, D. G., Koga, D., Walsh, B. M., and Mendes, O.: Comparative study of three reconnection X line models at the Earth's dayside magnetopause using in situ observations, Journal of Geophysical Research (Space Physics), 122, 4228–4250, https://doi.org/10.1002/2016JA023790, 2017. 124, 138, 150

Sun, W., Slavin, J. A., Nakamura, R., Heyner, D., Trattner, K. J., Mieth, J. Z. D., Zhao, J., Zong, Q.-G., Aizawa, S., Andre, N., and Saito, Y.: Dayside magnetopause reconnection and flux transfer events under radial interplanetary magnetic field (IMF): BepiColombo Earth-flyby observations, Annales Geophysicae, 40, 217–229, https://doi.org/10.5194/angeo-40-217-2022, 2022. 132

Swisdak, M. and Drake, J. F.: Orientation of the reconnection X-line, , 34, L11106, https://doi.org/10.1029/2007GL029815, 2007. 124, 125

Swisdak, M., Rogers, B. N., Drake, J. F., and Shay, M. A.: Diamagnetic suppression of component magnetic reconnection at the magnetopause, Journal of Geophysical Research (Space Physics), 108, 1218, https://doi.org/10.1029/2002JA009726, 2003. 125, 126

Toledo-Redondo, S., André, M., Aunai, N., Chappell, C. R., Dargent, J., Fuselier, S. A., Glocer, A., Graham, D. B., Haaland, S., Hesse, M., Kistler, L. M., Lavraud, B., Li, W., Moore, T. E., Tenfjord, P., and Vines, S. K.: Impacts of Ionospheric Ions on Magnetic Reconnection and Earth's Magnetosphere Dynamics, Reviews of Geophysics, 59, e00707, https://doi.org/10.1029/2020RG000707, 2021. 126

Trattner, K. J., Mulcock, J. S., Petrinec, S. M., and Fuselier, S. A.: Location of the reconnection line at the magnetopause during southward IMF conditions, , 34, L03108, https://doi.org/10.1029/2006GL028397, 2007. 132, 147, 149, 151

Trattner, K. J., Petrinec, S. M., Fuselier, S. A., Omidi, N., and Sibeck, D. G.: Evidence of multiple reconnection lines at the magnetopause from cusp observations, Journal of Geophysical Research (Space Physics), 117, A01213, https://doi.org/10.1029/2011JA017080, 2012a. 134, 136

Trattner, K. J., Petrinec, S. M., Fuselier, S. A., Omidi, N., and Sibeck, D. G.: Evidence of multiple reconnection lines at the magnetopause from cusp observations, Journal of Geophysical Research (Space Physics), 117, A01213, https://doi.org/10.1029/2011JA017080, 2012b. 124

Trattner, K. J., Burch, J. L., Ergun, R., Fuselier, S. A., Gomez, R. G., Grimes, E. W., Lewis, W. S., Mauk, B., Petrinec, S. M., Pollock, C. J., Phan, T. D., Vines, S. K., Wilder, F. D., and Young, D. T.: The response time of the magnetopause reconnection location to changes in the solar wind: MMS case study, , 43, 4673–4682, https://doi.org/10.1002/2016GL068554, 2016. 124

Trattner, K. J., Burch, J. L., Ergun, R., Eriksson, S., Fuselier, S. A., Giles, B. L., Gomez, R. G., Grimes, E. W., Lewis, W. S., Mauk, B., Petrinec, S. M., Russell, C. T., Strangeway, R. J., Trenchi, L., and Wilder, F. D.: The MMS Dayside Magnetic Reconnection Locations During Phase 1 and Their Relation to the Predictions of the Maximum Magnetic Shear Model, Journal of Geophysical Research (Space Physics), 122, 11,991–12,005, https://doi.org/10.1002/2017JA024488, 2017. 124, 132

Trattner, K. J., Petrinec, S. M., and Fuselier, S. A.: The Location of Magnetic Reconnection at Earth's Magnetopause, , 217, 41, https://doi.org/10.1007/s11214-021-00817-8, 2021. 124, 132, 133, 149, 150

Tsyganenko, N. A. and Stern, D. P.: Modeling the global magnetic field of the large-scale Birkeland current systems, , 101, 27 187–27 198, https://doi.org/10.1029/96JA02735, 1996. 127, 129, 133, 134, 135, 136

van der Walt, S., Schönberger, J. L., Nunez-Iglesias, J., Boulogne, F., Warner, J. D., Yager, N., Gouillart, E., Yu, T., and the scikit-image contributors: scikit-image: image processing in Python, PeerJ, 2, e453, https://doi.org/10.7717/peerj.453, URL https://doi.org/10.7717/peerj.453, 2014. 130

Vasyliunas, V. M.: Theoretical models of magnetic field line merging, 1., Reviews of Geophysics and Space Physics, 13, 303–336, https://doi.org/10.1029/RG013i001p00303, 1975. 124

Šafránková, J., Přech, L., Němeček, Z., and Sauvaud, J. A.: Density profile in the magnetosheath adjacent to the magnetopause, Advances in Space Research, 30, 1693–1703, https://doi.org/10.1016/S0273-1177(02)00438-6, 2002. 126

Walsh, B. M., Komar, C. M., and Pfau-Kempf, Y.: Spacecraft measurements constraining the spatial extent of a magnetopause reconnection X line, , 44, 3038–3046, https://doi.org/10.1002/2017GL073379, 2017. 124

Zhang, H., Fu, S., Pu, Z., Lu, J., Zhong, J., Zhu, C., Wan, W., and Liu, L.: Statistics on the Magnetosheath Properties Related to Magnetopause Magnetic Reconnection, , 880, 122, https://doi.org/10.3847/1538-4357/ab290e, 2019. 124

Zhou, M., Ashour-Abdalla, M., Deng, X., Pang, Y., Fu, H., Walker, R., Lapenta, G., Huang, S., Xu, X., and Tang, R.: Observation of Three-Dimensional Magnetic Reconnection in the Terrestrial Magnetotail, Journal of Geophysical Research (Space Physics), 122, 9513–9520, https://doi.org/10.1002/2017JA024597, 2017. 124

Conclusions and Perspectives

Conclusions

After more than sixty years since the discovery of the magnetic reconnection process and its crucial role in connecting the Earth's magnetosphere to the interplanetary medium, the location of the process on the magnetopause remains a major aspect that is not yet fully understood. Going beyond the disruptive but simple idea proposed by Dungey [1961] where the southward IMF reconnects along the equator and nortwhard IMF does in the lobes, indeed is tremendously difficult, owing to the multiscale character of the problem.

Many models have since then been proposed and mainly fall into two main categories. On the one hand, those following a local approach, focus on determining the orientation of the X-line given only the local conditions, and then may construct a global line from following these local orientations. On the other hand, those following a global approach determine the position of the X-line directly and entirely from the global state of the magnetopause. All these models revolve around the same idea that the X-line either is oriented or located along the direction that makes its growth or its steady state rate the fastest. They differ in the way to account for the specific effect(s) that actually lead to faster rates, such as considering the magnetic energy available for reconnection, or minimizing diamagnetic suppression, maximizing the overall magnetic shear on the magnetopause, etc.

Over the years, these models have been tested through mainly two ways. First, by confronting various X-line predictions to single or several signatures of reconnection obtained from in-situ spacecraft measurements. This methodology encompasses a significant level of uncertainty associated with, first, the high level of fluctuations in the plasma and field measurements, second, the difficulty of determining the causal upstream conditions of the observed events, and finally the very local character of in-situ measurements. As a result, it has remained challenging to draw relevant conclusions regarding the performance of one model versus others in their ability to predict the global location of the X-line.

The second main methodological approach is based on using global simulations of the magnetosphere. In this approach, the location of the X-line can directly be measured. However, the difficulty here stands in knowing to what extent the physical formalism used (often resistive MHD), or the upstream causal IMF/Solar wind conditions, are realistic. IMF and solar wind conditions impacting where reconnection locates constitute a vast parameter space that is today inaccessible to parametric studies using high resolution simulations. None of the models so far perfectly match the measured X-line position for all tested IMF orientations.

In short, above methodological approaches are either too noisy and local, or global but only numerical and with a limited coverage of the causal parameter space. We critically lack a global and consistent perspective of the system from observational means. We now have access to decades of data from multiple missions that have explored the system along various orbital and upstream conditions. This constitutes a unique opportunity to tackle the challenge of reaching this global observational overview. This has been the broad ambition behind this thesis.

The orientation of the IMF is of major importance in structuring the magnetosheath and we have thus given it a central role in this thesis. Just downstream of the bow shock, the IMF drapes around the obstacle in way that strongly depends on its orientation in the solar wind. More specifically, the detailed 3D and global reconstruction of the draping geometry allowed us to distinguish three broad draping regimes on the dayside depending on how radial the IMF is. For intermediate IMF cone angles, our results demonstrate how being frozen in the magnetosheath flow constrains the draping of the magnetic field. In that case, the draping is found to be associated with at large

scale current sheet at mid-depth of the magnetosheath, that, by construction, is not present in the current-free magnetostatic model widely used for modeling magnetopause reconnection. As a result, the observed draping is fundamentally and significantly different from that predicted by the model.

The draping geometry, for a given IMF orientation, will then constrain how the magnetic field amplitude and plasma density distribute throughout the magnetosheath. Along with the magnetic orientation imposed by the draping adjacent to the magnetopause, the magnetic amplitude and plasma density, will be key players in how reconnection evolves at the current layer. Our results indicate how the IMF orientation drives the distribution of the magnetic field amplitude and plasma density. We clearly show the magnetic field piles-up onto the magnetopause for all IMF orientations. The IMF cone angle has the dominant effect on the magnetic pileup, which is found to decrease as the IMF becomes more radial. An effect that is well understood and corroborated with velocity data, given that as the IMF turns more radial, the solar wind more freely flows along field lines and easily circumvent the magnetopause. The pileup dependence on the IMF clock angle is more subtle and our results suggest it is intimately linked to magnetic reconnection at the magnetopause. Indeed, the increase of the amplitude from the bow shock is found strikingly similar throughout most of the magnetosheath thickness and only starts to differ in the last 40% of the layer when the IMF clock angle changes. The amplitude nearby the magnetopause is found to decrease as the IMF turns from northward to southward orientations, as expected from the flux erosion effect attributed to magnetopause reconnection. Interestingly, the flux erosion does not show a linear relation with the IMF clock angle but rather exhibits an abrupt transition as soon as the IMF passes 60°. The spatial structure of the flow in the magnetosheath shows consistent signatures, being slower along the Sun-Earth line for northward IMF orientations, and the same clock angle dependence of the tangential acceleration that may possibly be related to reconnection outflows.

The magnetic pileup in the magnetosheath, and in particular nearby the magnetopause, has been known to squeeze the plasma out of the subsolar region, parallel to the magnetic field, thereby creating a so-called plasma depletion layer. Using our spatial reconstruction procedure, this work reveals the spatial structure of this Plasma Depletion Layer (PDL) along with its dependence on the IMF orientation. More specifically, we found that no PDL exists for radial IMF, as theoretically expected since, again, plasma flows freely out of the subsolar region along field lines. As soon as the IMF becomes more inclined from the Sun-Earth line, a PDL is clearly observed and deepens as the IMF cone angle increases along with the aforementioned increase of the magnetic pileup. Interestingly, this deepening continues up to the point where the density nearby the magnetopause becomes even lower than just downstream of the bow shock, leaving a density maximum at about mid-depth of the magnetosheath. Similarly to the magnetic pileup, the effect of the IMF clock angle is less obvious but seems to become more pronounced within the 10-20°% of the magnetosheath the closest to the magnetopause, where the depletion is seen to be deeper for northward IMF conditions.

These variations of the density and magnetic field, across the depth of the magnetosheath, are not the same in the quasi-parallel and quasi-perpendicular sides of the layer. As expected, we show the quasi-perpendicular side of the magnetosheath to have the largest field amplitudes. This asymmetry increases as the IMF becomes more radial, up to a point, for strictly radial IMF not visible in our dataset, where it is expected to vanish. An important outcome of our study is that this asymmetry decreases as one approaches the magnetopause, meaning that asymmetries expected downstream of the bow shock are not relevant for magnetopause reconnection. The asymmetry in the plasma density is more complex. Just downstream of the bow shock, and as expected from the jump conditions given a specific IMF orientation, the density is seen to be larger on the quasi-perpendicular side of the magnetosheath. Like for the magnetic field amplitude, this asymmetry does not stay constant throughout the magnetosheath. Contrary to the magnetic pileup, however, the density asymmetry even reverses, with higher densities in the quasi-parallel side. This can be understood by the effect of the PDL, induced by the magnetic field pileup nearby

the magnetopause, whose asymmetry favors the quasi-perpendicular side. We have seen no effect of the IMF clock angle in the symmetry density or magnetic amplitude.

Previous results have led us to a fairly consistent and global picture of the dayside magnetosheath, in particular adjacent to the magnetopause. Our next focus has thus been on reconstructing the spatial distribution of key quantities for reconnection on the magnetopause surface itself. Our first result has shown, as expected from previous findings related to the draping geometry, that, for intermediate IMF cone angle orientations, the magnetic shear on the quasi-parallel side of the magnetopause greatly differs from what is widely assumed. The magnetic shear is generally considered as the first parameter driving the location of the X-line on the current layer. However, physically, one can expect constraints to also originate from other quantities, more fundamentally considered, usually, in reconnection theory. We have therefore reconstructed, along with the magnetic shear, global maps of the current density and reconnection rate, on the magnetopause. Although expected to be correlated to one another, the different quantities show distinct distributions on the magnetopause. Our maps show many characteristics and variations depending on the IMF cone angle. One of the most interesting is the observed important decrease of the reconnection rate when the IMF becomes more radial, consistently with the decrease of the magnetic amplitude in the adjacent magnetosheath. In contrast, for the current density, this variation is more complex and its amplitude goes from being dominated by the magnetic shear to being mainly associated with the amplitude jump.

Following the so-called global approach, we have constructed candidate X-lines that maximize the different aforementioned quantities. We find the evolution of these lines on the magnetopause for different IMF clock angles and dipole tilt angles drastically changes when the IMF turns from radial to perpendicular orientations. The IMF cone angle therefore seems an important parameter to consider in order to discriminate between the different predictions, although generally neglected.

X-lines have also been constructed following the local approach and compared to the ones obtained from a global maximization. The main outcome of this comparison is to show the inconsistency between these two approaches. Namely, the global maximization leads to local orientations that by no means align with that resulting from local effects observed in local reconnection models. But above all, the local orientation resulting from a global maximization may lead to arbitrarily small merging components. For instance, in the case of lines maximizing the magnetic shear, we observe an abrupt decrease of the merging components caused by the sharp turn of the X-line as it reaches anti-parallel regions from the dayside, and resulting in a sharp decrease of the local reconnection rate.

What is needed to go forwards?

Towards a new X-line model?

This PhD thesis started in a context where multiple X-lines models had been proposed in the literature but none was convincingly shown to achieve better performances than others, either from a numerical [Komar et al., 2015] or observational standpoint [Qudsi et al., 2023; Souza et al., 2017].

Our work offered to step back from the idea of pursuing yet another way to compare them, but rather offered a new perspective on the problem by bringing observational constrains from the reconstruction of the spatial distributions of key quantities on the magnetopause.

It is clear, from findings of Chapter 5 that global and local approaches to the localization of X-lines are not consistent with each other. The fact that the global approach results in X-lines for which the subsequent local orientation not only does not respect predictions of local physical models, but also can end up with arbitrarily small reconnecting components with respect to the total field, appears as a serious defect.

On the other hand, the orientation of the X-line, constrained by various physical effects in the local approach, necessitate additional arguments to obtain a global scale prediction. These arguments are necessarily grounded in the global properties of the magnetopause. For instance,

Moore et al. [2002] proposed that the X-line would pass through the point(s) on the magnetopause where the reconnecting components would be the largest. This constraint followed the idea that such location would probably be more prone to the development of reconnection. However, in the light of what we showed in Chapter 5, the components of the magnetic field are far from being the sole properties to realistically constrains where reconnection lines could pass.

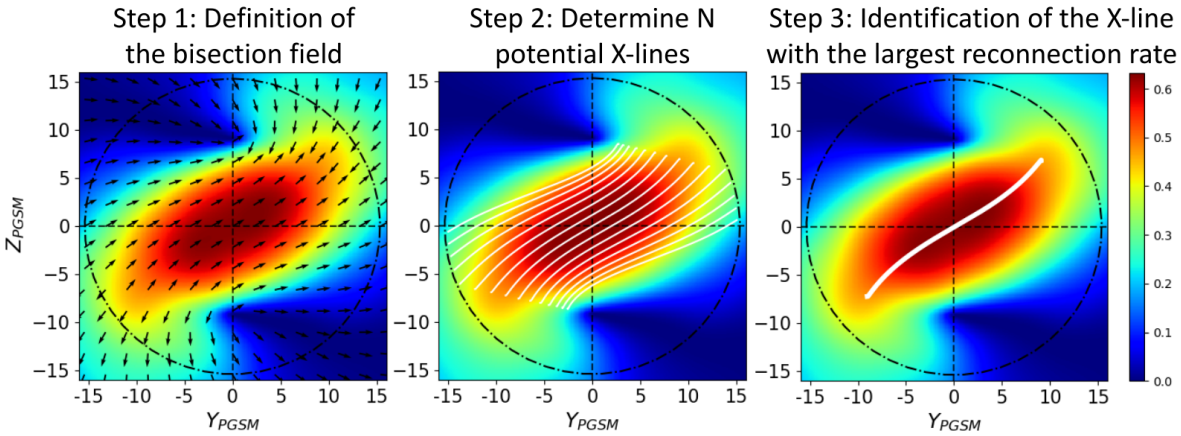

Figure 1: The color maps display the spatial distribution of the MHD scaling law for the local reconnection rate [Cassak and Shay, 2007] derived from in-situ measurements. In the left panel, black vectors bisect the local magnetic fields vectors. In the middle and right panels, the white lines depict potential and dominant X-lines integrated from the bisection field, respectively.

Here we propose not only a way to determine where a single X-line would pass on the magnetopause, but also a mechanism explaining why only one should exist in the first place, in the system. We propose an X-line existing on the magnetopause will locally orient so to maximize the local reconnection rate. Building on the results of local reconnection studies [Aunai et al., 2016; Hesse et al., 2013; Liu et al., 2018], we concretely propose such orientation to be the local bisection of upstream magnetic fields. As an example, the left panel of Figure 1 shows, for an IMF clock angle of 130°, all local orientations an X-line could take depending on where it passes on the magnetopause. Finding a single, global X-line from this so-called bisection field, can be done through a gedankenexperiment consisting in imagining how that X-line can be *physically* favored over all other potential ones. We thus assume that, at a given time, multiple X-lines exist. Whether their multiplicity results from the history of the system in unsteady IMF conditions, or because a global tearing instability grows with an infinite number of X-lines, does not matter. We argue that, if steady state is imposed from now on, one X-line, in particular, we reconnect flux more rapidly than others, owing to the global inhomogeneity of the current sheet. As a result, and as visible on the Figure 2, all other X-lines will embedded in the separatrices of that so-called dominant X-line, and above all in the plasma jets expelled from it. As the others X-lines are all expelled from the system and, in the absence of external forcing, the exhaust emenating from the dominant one enlarges preventing further tearing onset, the dominant X-line soon becomes the sole reconnection line on the magnetopause.

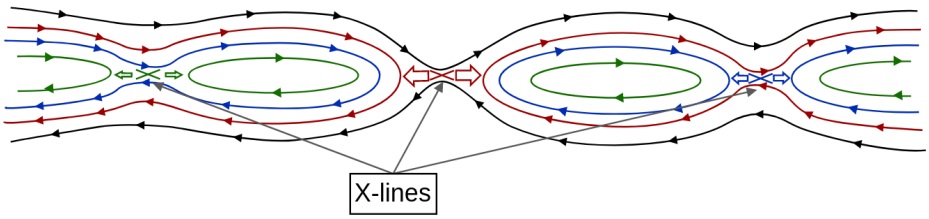

Figure 2: Schematic showing multiple X-lines, with the central one having a higher reconnection rate. This dominance causes expulsion of flanking X-lines, which become embedded within the separatrices and stronger reconnection outflows generated by the dominant X-line.

The procedure to build a dominant X-line, i.e. the one having the largest integrated reconnection rate, is relatively simple once the bisection field and reconnection rate map are known. From an initial X-line guess, associated to a total integrated reconnection rate R_0, one can move by an infinitesimal step into the direction where the next line considered has a larger integrated reconnection rate R_1. Subsequent iterations are performed until converging towards the line presenting the largest integrated reconnection rate with sufficient spatial precision. The result of this procedure is represented on the rightmost panel of Figure 1. A preliminary and encouraging test for our model is proposed in Figure 3. The left panel shows the color coded reconnection rate estimated from the Cassak-Shay scaling law in a global MHD simulation setup for a northward IMF orientation and a dipole tilt angle of 15°. In that case, the X-line obtained following the global maximization of the underlying reconnection rate estimate clearly does not match the measured position of the separator. On the right panel, we show the same reconnection rate estimate this time obtained, as in Chapter 5, from in-situ measurements. Superimposed to the reconnection rate is the local bisection field, and the line towards which our procedure converges. Clearly this line more convincingly matches the separator obtained in the simulation. This promising result calls for further investigations in the forthcoming months.

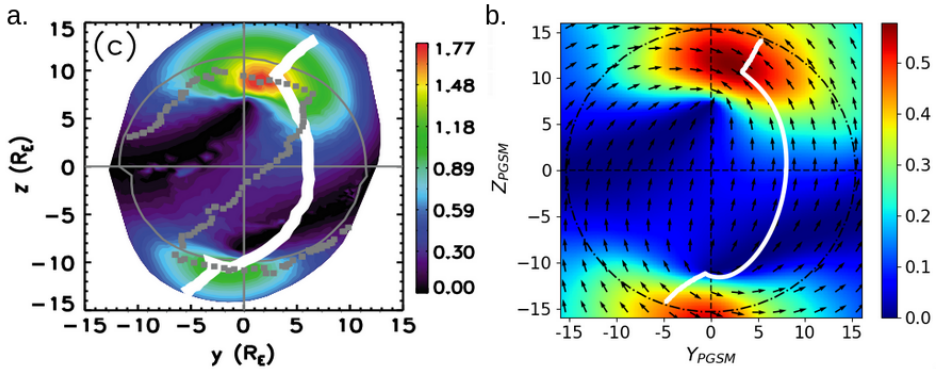

Figure 3: The color maps correspond to the MHD scaling law for the local reconnection rate [Cassak and Shay, 2007] from a simulation [Komar et al., 2015] in panel a and from in-situ data in panel b. In panel a, the gray line represents the line that globally maximizes the reconnection rate, and the white line corresponds to the magnetic separator obtained in the simulation. The white line in panel b corresponds to the X-line predicted by the new X-line model.

Towards better upstream conditions?

Existing studies evaluating X-line models against in-situ magnetopause reconnection observations [Qudsi et al., 2023; Souza et al., 2017], such as reversal jets, have not conclusively identified a dominant model. Inaccuracies in determining upstream IMF and solar wind conditions, critical for establishing magnetic reconnection boundary conditions, likely contribute significantly to the uncertainty in evaluating different X-line models. The inaccurate determination of the causal IMF/solar wind is made even more critical by the limited number of in-situ reconnection signatures usually used in these studies. These signatures are not only challenging to identify but also relatively rare due to infrequent spacecraft encounters with the magnetopause.

There are two ways to reach more conclusive results on the evaluation of X-line models with in-situ observations. The first is to significantly increase the statistics of the in-situ observations, as discussed in the following perspective *Towards discriminating models with massive reconnection signatures?*. The second is to reduce the error in determining the boundary conditions of magnetic reconnection for the considered in-situ observations by more accurately obtaining the upstream conditions.

Studies employing upstream conditions often rely on the OMNI database (e.g. Dimmock and Nykyri [2013]; Zhang et al. [2019]), which correspond to solar wind and IMF data measured at L1

and propagated to the bow shock nose. This entails estimating the bow shock position and applying a propagation model. While OMNI's model incorporates IMF orientation for a more nuanced approach than simple ballistic propagation, the propagation used remains relatively simple. For instance, it excludes solar wind compression and expansion but, instead, allows unphysical "interpenetration" of the solar wind: when a fast solar wind measured at the L1 later than a slow solar wind, is predicted to pass ahead and arrive at the bow shock before the slow solar wind. Additionally, the validity of the OMNI prediction has never been thoroughly evaluated. Other studies (e.g. Trattner et al. [2021]) can directly use the measurements of one of the solar monitors at L1 and propagate them to the magnetopause. The propagation can be adjusted by correlating the measurements in the magnetosheath to the IMF variations by visual inspection. However, this method is not appropriate for statistical studies and hinders reproducibility.

To obtain accurate upstream conditions, it is necessary to consider several parameters, such as solar wind velocity and IMF orientation. It is also important to use the appropriate solar wind monitor. This last aspect is often neglected in the different propagation methods. For instance, let us consider the case of January 7, 2016, when an EDR was observed near the subsolar magnetopause at 09:36:10 UT by the MMS-3 spacecraft [Trattner et al., 2021]. This case is of particular interest because there are four solar wind monitors (WIND, DSCOVR, ACE, and THB) in an interesting configuration to study the propagation of the solar wind, as shown in Figure 4. The WIND and DSCOVR (resp. ACE and THB) spacecraft are aligned at $Y_{GSM} \sim 40$ Re (resp. $Y_{GSM} \sim -30$ Re) while having different radial separations. Additionally, the DSCOVR and ACE spacecraft have almost the X_{GSM} position.

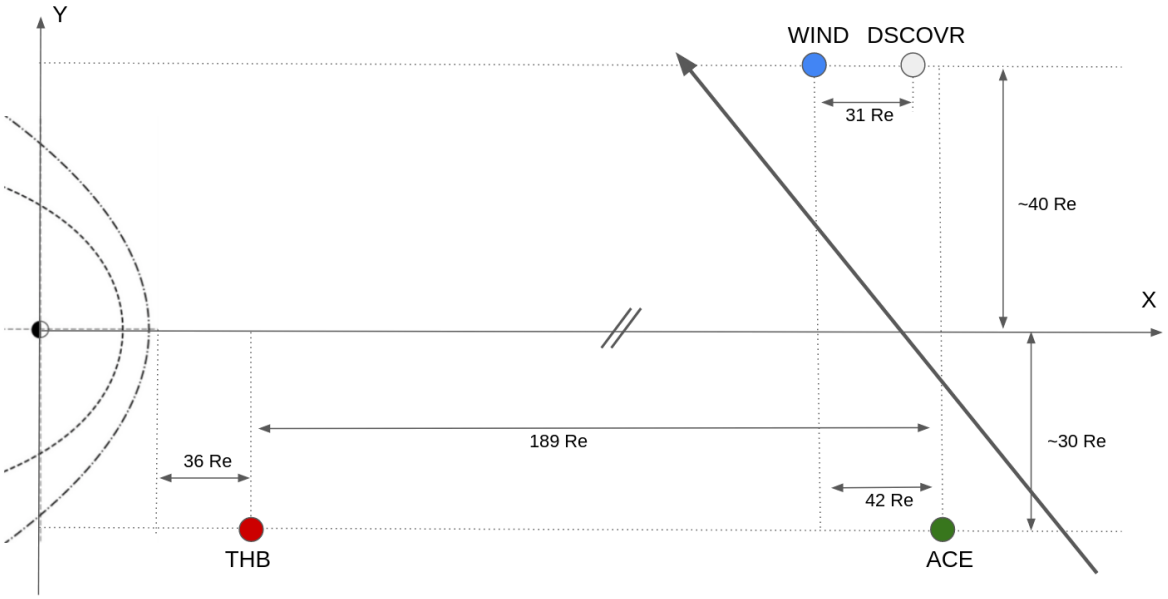

Figure 4: Configuration of the THEMIS-B, ACE, Wind, and DSCOVR spacecraft within the interplanetary medium on January 7, 2016, at approximately 09:30 UT. The gray arrow represents the IMF in the ecliptic plane.

Figure 5 shows the B_y component of the IMF measured by the different solar wind monitors. These measurements are propagated to the magnetopause and compared with the in-situ observations of the MMS-3 probe within the magnetosheath. Near the EDR event, ACE (panel b) provides the best estimate of the upstream conditions. An offset of the three peaks between 07:45 UT and 08:45 UT is noticeable, possibly due to an expansion of the solar wind. Interestingly, even though the spacecraft is much closer to Earth and is aligned with ACE, the data from the THB spacecraft (panel a) seems to have slightly less agreement with the magnetosheath measurements near the magnetopause while having a better agreement before 07:30 UT. Although the ACE and DSCOVR spacecraft are nearly equidistant from Earth, their measurements are relatively different (panels b and c). Panel c and d demonstrate a strong agreement between DSCOVR and WIND

data, indicating that radial propagation is adequate for short distances, but not consistent with the MMS-3's measurements. This example shows that the choice of the solar wind monitor is critical in determining the upstream conditions. Although comparing available solar monitors data to magnetosheath measurements near in-situ reconnection observations is feasible for individual cases, this approach becomes impractical for large-scale statistical studies.

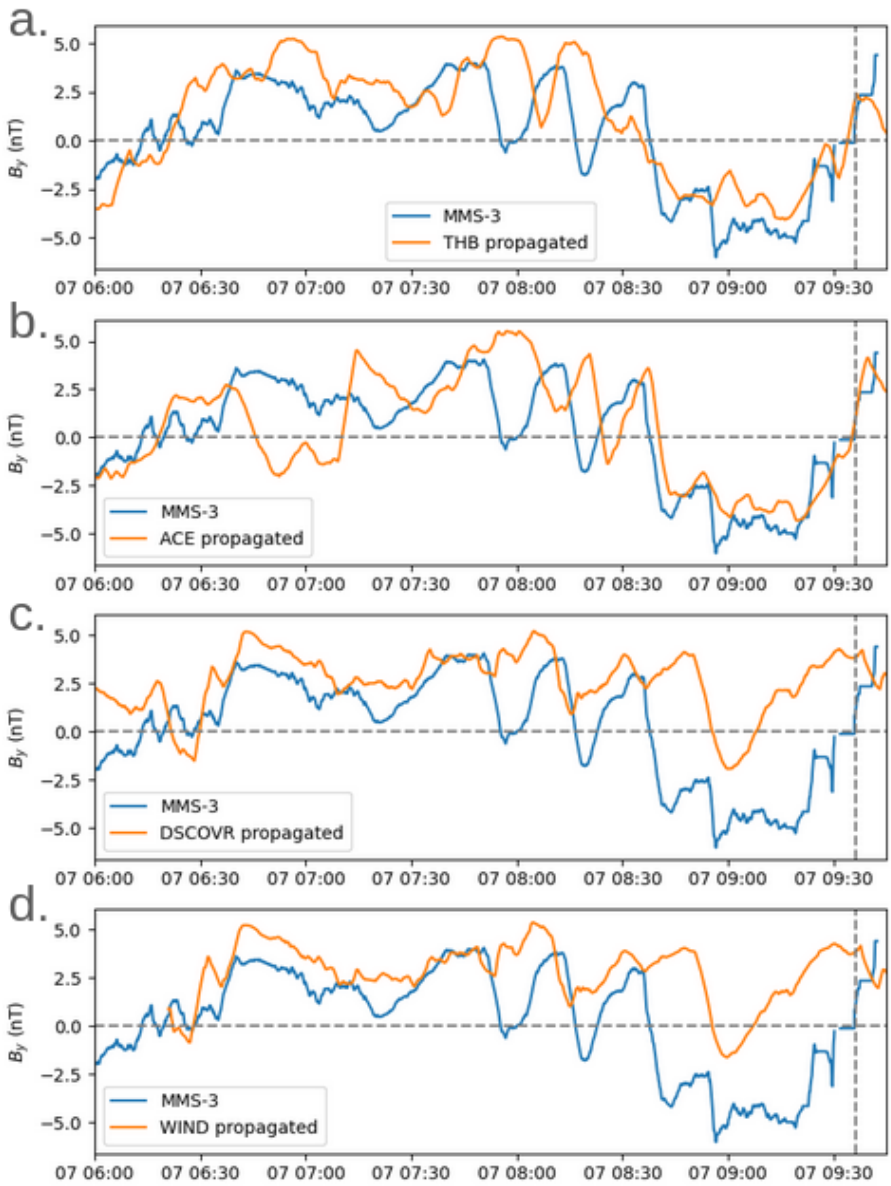

Figure 5: In all the panels is represented the B_y component of the magnetic field in the magnetosheath measured by the MMS-3 spacecraft on January 7, 2016 between 06:00 UT and 09:45 UT. The vertical dashed line correspond to the time of an EDR observation at the magnetopause at 09:36:10 UT. Panels a, b, c, and d show the B_y component of the IMF measured by the THEMIS-B, ACE, DSCOVR, and WIND spacecraft, respectively. The measurements have been propagated to the magnetopause, taking into account the solar wind velocity (550 km.s^{-1}), spacecraft distances to the bow shock, and a propagation time of approximately 9 minutes in the magnetosheath.

While the propagation of the IMF in the interplanetary medium may seem relatively simple, since it is mostly radial, in reality many parameters must be taken into account for accurate predictions. These include IMF orientation, solar wind speed and direction, solar wind monitor position, and, crucially, incorporating data from multiple monitors. While classical propagation methods struggle with such intricate dependencies, machine learning approaches appear well-suited to tackle this inherently complex task. Specifically, employing neural networks offers a data-driven

methodology that could learn to predict not only the orientation of the IMF near the bow shock but also its alterations, such as compression and expansion, during its propagation from L1 to the vicinity of Earth. The proposed neural network could be trained and evaluated using the 17 million solar wind measurements identified in Chapter 2 near the bow shock and data from multiple solar wind monitors. I supervised two interns who investigated the feasibility of this neural network approach. Although their investigation was really preliminary, the initial results suggest promising potential for this method.

Towards magnetopause maps with unsteady upstream conditions?

All the maps and studies we have done in this thesis implicitly assume the IMF orientation is steady. This means the time at which the IMF orientation is picked up in OMNI data is the same no matter where located on the magnetopause. In reality, conditions at the magnetopause should result from multiple IMF orientations, as IMF rotations often occur over time scales smaller than typical propagation times from the bow shock to the magnetopause terminator [Walsh et al., 2018]. It therefore seems important to be able to map the conditions at the magnetopause by considering a different IMF depending on where located on the boundary.

In Chapter 3, we have used a spatial reconstruction of the plasma flow in the magnetosheath. Using this flow, we have been able to compute the transport time in the magnetosheath from the bow shock to any point on the dayside magnetopause. This transport time is then used to pick the IMF orientation in OMNI.

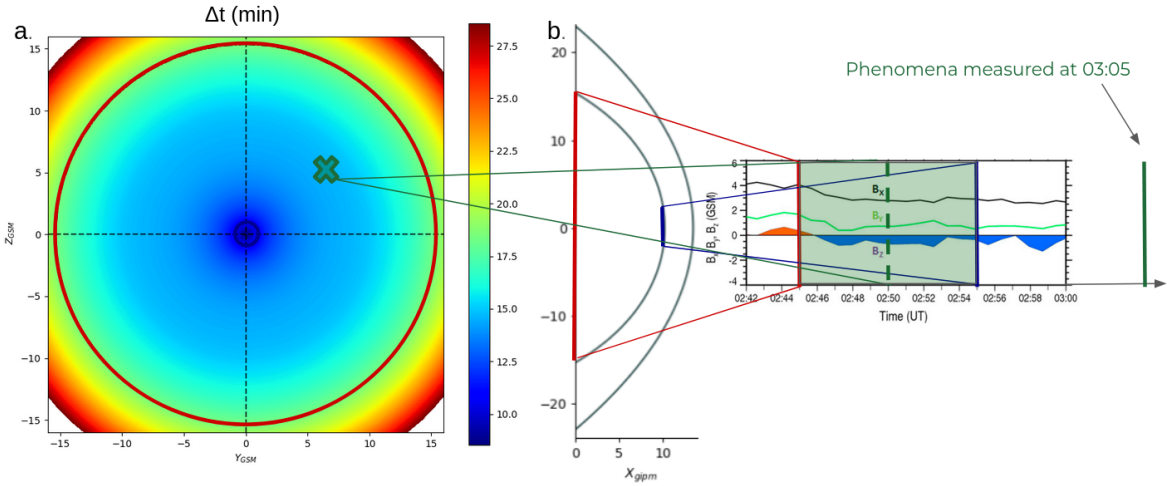

Figure 6: Panel a corresponds to the time it takes for the IMF to propagate from the bow shock to the magnetopause in minutes, determined by integrating the in-situ velocity measurements. The red and blue circles indicate the terminator and the vicinity to the subsolar point of the magnetopause, respectively. The green cross represents the location of a considered event at the magnetopause. Panel b shows a schematic illustrating the attribution of different IMF orientations to the various positions of the magnetopause surface for the event measured at 03:05 UT (green vertical line). The IMF orientation measured at the blue and red vertical lines are attributed to subsolar region and the terminator of the magnetopause, respectively. The green dashed vertical line corresponds to the IMF condition for the considered event. The green area represents all of the IMF orientation found on the dayside magnetopause surface.

Figure 6 represents the idea behind this computation. Panel a shows the magnetopause from the Sun vantage point and represents the color coded transport time from a point on the magnetopause to the bow shock. We see that it takes approximately 8 minutes for the plasma to reach the magnetopause on the subsolar region, and up to about 20 minutes for the terminator regions. This time delay long enough to alter maps since substantial IMF rotation often occur within 10 minutes, in which case the terminator region will "see" and IMF different from the subsolar region, leading to a "distorted" map compared to one assuming steady state. Panel b shows a time series of the magnetic field components from OMNI corresponding to all IMF orientations that

contribute to the state of the magnetopause at a given time.

Figure 7 illustrates how a magnetopause map can change upon the time reversal of the B_z component. This can be seen as the intersection of the paraboloid magnetopause surface with an incoming tangential and planar current layer where B_z reverses. Further work is needed in that direction to identify to what extent this non steadiness actually is crucial or not to explain specific events.

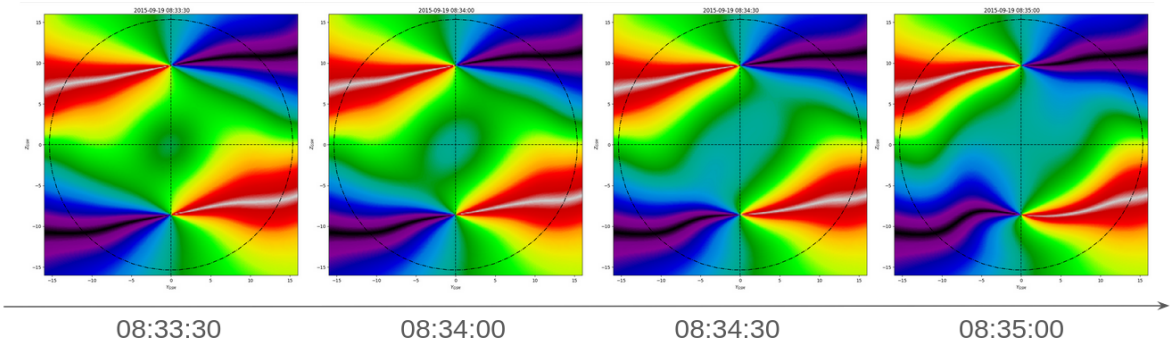

Figure 7: Global distributions of the magnetic shear angle across the Earth's dayside magnetopause on September 19, 2005, between 08:33:30 UT and 08:35:00 UT. These maps are determined using a magnetic draping formed by multiple IMF orientations produced during the rotation of the IMF from a southward to a northward orientation.

Towards discriminating models with massive reconnection signatures?

This thesis has been dedicated to characterize and understand the constraints that could act on magnetic reconnection on the magnetopause on a global scale. We have proposed different X-line candidates, and even a preliminary X-line model in these perspectives section. No matter how promising these results may be, they represent at best half the way towards answering the question of the location of reconnection at the magnetopause. The other half, which is not the easiest part of the way, now consists in correlating these constraints with actual reconnection signatures, and identify which seems to better correspond to where reconnection actually occur. Collecting reconnection signatures is, however, more easily said than done. Since the MMS era, we have now candidate crossings of electron diffusion regions [Lenouvel et al., 2021], the closest one can get from an actual X-line. However, we, as a community, have less than a hundred of those, among which many are strongly subject to the observer's own empirical decisions (Nais Fargette private communication). Moreover, considering only EDRs for specific IMF orientations reduces the statistics even more, so that relevant conclusions cannot be drawn. Hoshi et al. [2018] and Trenchi et al. [2008] using THEMIS and Double Star data, respectively, reported several hundred reconnection jets on the magnetopause surface, for different coarse sectors of IMF orientations. The pattern visible from the jet orientation (and on Figure 8) clearly indicate the underlying existence of an X-line from which accelerated plasma emanate. However, the low statistics again leave a substantial amount of noise, and it is impossible to disentangle the proper role of the IMF clock and cone angles, and dipole tilt angles. Furthermore, depending on an ad hoc definition of "what a jet is" may bias the representation of what actually is the reconnection flow on the magnetopause for a given IMF orientation. Further work, undertaken at LPP, now consists in extracting from multiple missions, all crossings of the magnetopause boundary layer, to later reconstruct the "true" state of plasma flows therein, infer whether it may emanate from an X-line and correlate it with maps developed in this thesis.

Towards a parametric global MHD study?

Finally, the maps we can produce from observations, even with some non-stationnarity will always be limited to large scale overviews, missing all dynamical aspects ongoing at the magnetopause.

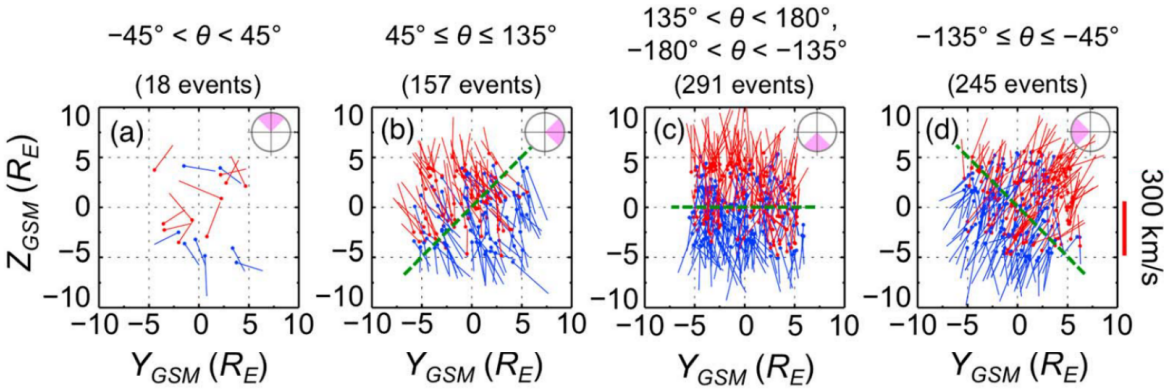

Figure 8: Spatial distribution of dayside reconnection jets within the GSM (YZ) plane under various IMF conditions: northward (a), westward (b), southward (c), and eastward (d). Blue and red bars represent southward and northward jets, respectively, with their length indicating their relative velocity to the magnetosheath. The green line correspond to the orientation bisecting the IMF clock angle and passing by the subsolar point of the magnetopause. Figure adapted from Hoshi et al. [2018].

What happens to an X-line as the IMF rotate either slowly or rapidly? Does the location of an X-line only depend on upstream conditions or does it also depend on the specificities of the magnetopause history? Does an X-line have the same orientation if looked at different scales, or is an X-line roughly oriented along a certain direction locally if looked "from far enough" actually really tortuous if looked closer and in greater details? What is are the roles of ion and electron kinetic effects in locating reconnection on the magnetopause? To address these many questions and all others I didn't write, observations must be complemented by numerical modeling. In the forthcoming two years, I will work as a postdoctoral researcher at Goddard Space Flight Center and try to answer some of these questions using global MHD models.

Bibliography

Aunai, N., Hesse, M., Lavraud, B., Dargent, J., and Smets, R.: Orientation of the X-line in asymmetric magnetic reconnection, Journal of Plasma Physics, 82, 535820401, https://doi.org/10.1017/S0022377816000647, 2016. 162

Cassak, P. A. and Shay, M. A.: Scaling of asymmetric magnetic reconnection: General theory and collisional simulations, Physics of Plasmas, 14, 102114, https://doi.org/10.1063/1.2795630, 2007. 162, 163

Dimmock, A. P. and Nykyri, K.: The statistical mapping of magnetosheath plasma properties based on THEMIS measurements in the magnetosheath interplanetary medium reference frame, Journal of Geophysical Research (Space Physics), 118, 4963–4976, https://doi.org/10.1002/jgra.50465, 2013. 163

Dungey, J. W.: Interplanetary Magnetic Field and the Auroral Zones, , 6, 47–48, https://doi.org/10.1103/PhysRevLett.6.47, 1961. 159

Hesse, M., Aunai, N., Zenitani, S., Kuznetsova, M., and Birn, J.: Aspects of collisionless magnetic reconnection in asymmetric systems, Physics of Plasmas, 20, 061210, https://doi.org/10.1063/1.4811467, 2013. 162

Hoshi, Y., Hasegawa, H., Kitamura, N., Saito, Y., and Angelopoulos, V.: Seasonal and Solar Wind Control of the Reconnection Line Location on the Earth's Dayside Magnetopause, Journal of Geophysical Research (Space Physics), 123, 7498–7512, https://doi.org/10.1029/2018JA025305, 2018. 167, 168

Komar, C. M., Fermo, R. L., and Cassak, P. A.: Comparative analysis of dayside magnetic reconnection models in global magnetosphere simulations, Journal of Geophysical Research (Space Physics), 120, 276–294, https://doi.org/10.1002/2014JA020587, 2015. 161, 163

Lenouvel, Q., Génot, V., Garnier, P., Toledo-Redondo, S., Lavraud, B., Aunai, N., Nguyen, G., Gershman, D. J., Ergun, R. E., Lindqvist, P. A., Giles, B., and Burch, J. L.: Identification of Electron Diffusion Regions with a Machine Learning Approach on MMS Data at the Earth's Magnetopause, Earth and Space Science, 8, e01530, https://doi.org/10.1029/2020EA001530, 2021. 167

Liu, Y.-H., Hesse, M., Li, T. C., Kuznetsova, M., and Le, A.: Orientation and Stability of Asymmetric Magnetic Reconnection X Line, Journal of Geophysical Research (Space Physics), 123, 4908–4920, https://doi.org/10.1029/2018JA025410, 2018. 162

Moore, T. E., Fok, M. C., and Chandler, M. O.: The dayside reconnection X line, Journal of Geophysical Research (Space Physics), 107, 1332, https://doi.org/10.1029/2002JA009381, 2002. 162

Qudsi, R. A., Walsh, B. M., Broll, J., Atz, E., and Haaland, S.: Statistical Comparison of Various Dayside Magnetopause Reconnection X-Line Prediction Models, Journal of Geophysical Research (Space Physics), 128, e2023JA031644, https://doi.org/10.1029/2023JA031644, 2023. 161, 163

Souza, V. M., Gonzalez, W. D., Sibeck, D. G., Koga, D., Walsh, B. M., and Mendes, O.: Comparative study of three reconnection X line models at the Earth's dayside magnetopause using in situ observations, Journal of Geophysical Research (Space Physics), 122, 4228–4250, https://doi.org/10.1002/2016JA023790, 2017. 161, 163

Trattner, K. J., Fuselier, S. A., Petrinec, S. M., Burch, J. L., Ergun, R., and Grimes, E. W.: Long and Active Magnetopause Reconnection X Lines During Changing IMF Conditions, Journal of Geophysical Research (Space Physics), 126, e28926, https://doi.org/10.1029/2020JA028926, 2021. 164

Trenchi, L., Marcucci, M. F., Pallocchia, G., Consolini, G., Bavassano Cattaneo, M. B., di Lellis, A. M., RèMe, H., Kistler, L., Carr, C. M., and Cao, J. B.: Occurrence of reconnection jets at the dayside magnetopause: Double Star observations, Journal of Geophysical Research (Space Physics), 113, A07S10, https://doi.org/10.1029/2007JA012774, 2008. 167

Walsh, B. M., Welling, D. T., Zou, Y., and Nishimura, Y.: A Maximum Spreading Speed for Magnetopause Reconnection, , 45, 5268–5273, https://doi.org/10.1029/2018GL078230, 2018. 166

Zhang, H., Fu, S., Pu, Z., Lu, J., Zhong, J., Zhu, C., Wan, W., and Liu, L.: Statistics on the Magnetosheath Properties Related to Magnetopause Magnetic Reconnection, , 880, 122, https://doi.org/10.3847/1538-4357/ab290e, 2019. 163

Appendix A

Estimation of the magnetic field divergence

The estimation of the divergence of the magnetic field allows to assess the validity of the reconstruction of the magnetic field with in-situ measurements. The divergence is computed with the magnetic field normalized by amplitude of the IMF, and the distances are normalized by 1 Re. The normalization by 1 Re seems a reasonable choice because the reconstructed features at smaller scales are difficult to interpret physically due to the increasing importance of noise relative to true spatial variations. Since a perfectly null magnetic field divergence is not realistically achievable with our ergodic approach, we can estimate that, given the normalization, values significantly less than 1 would validate our reconstruction method. To assess the validity of the divergence computation, we calculated the divergence of the curl of the magnetic field ($\nabla.(\nabla \times \mathbf{B}/\mathrm{B}_{imf})$) and obtained values of about 10^{-15} , which supports the conclusion that the divergence is well-computed.

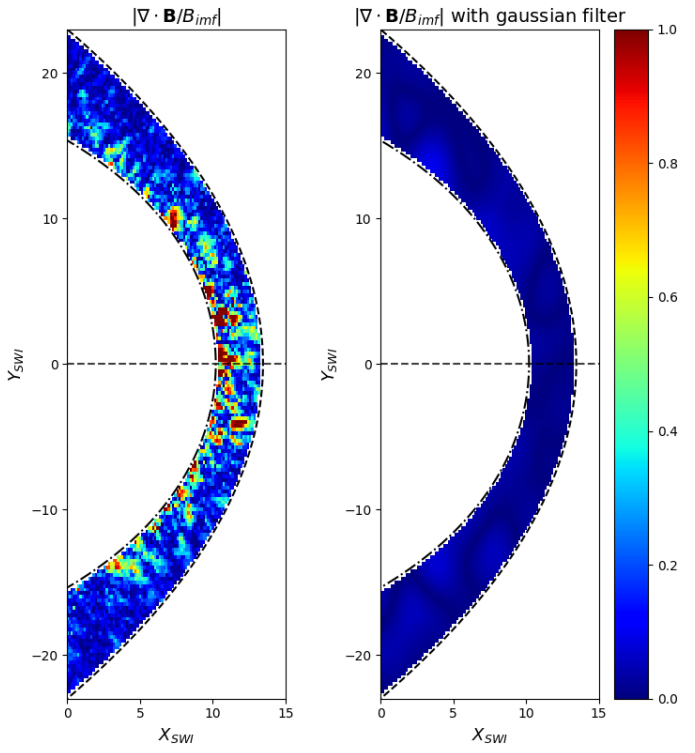

Figure 1: Absolute value of the magnetic field divergence in the equatorial plane and the same quantity after applying a Gaussian filter (σ = 1 Re) in the left and right panels, respectively. The divergence is computed with the magnetic field normalized by amplitude of the IMF, and the distances are normalized by 1 Re. The dashed and dotted-dashed lines represent the bow shock and magnetopause, respectively.

The left panel of Figure 1 shows the absolute value of the magnetic field divergence ($|\nabla.\mathbf{B}/\mathrm{B}_{imf}|$) in the equatorial plane considering data with IMF cone angles greater than or equal to 75° ($|\theta_{co}| \geq 75°$). Throughout most of the dayside magnetosheath, the magnetic field divergence remains lower than 0.2, but localized regions exhibit values exceeding 0.5 or even 1. Applying a 3D Gaussian filter with a standard deviation of about 1 Re significantly reduces the magnitude of divergence values as shown in the right panel of Figure 1. This smoothing suppresses the small-scale noise that contributes to produce high positive and negative values of the divergence in the unfiltered map.

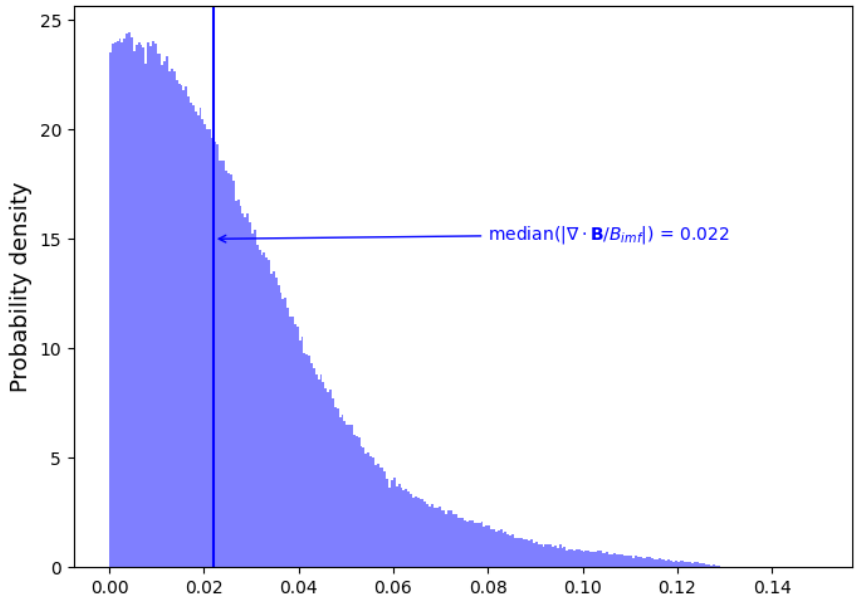

Figure 2: Density probability of the absolute value of the magnetic field divergence after applying a Gaussian filter (σ = 1 Re) in the 3D volume of the dayside magnetosheath. The vertical blue line corresponds to the median value of the magnetic field divergence.

Figure 2 show the distribution of the values of the smoothed magnetic field divergence (Figure 1, right panel) in the total 3D volume of the dayside magnetosheath. All values are significantly lower than 1, with a median of 0.022, which a posteriori validates our reconstruction method.

Appendix B

The magnetostatic model of Kobel and Fluckiger 1994

Due to its relative simplicity, the Kobel and Fluckiger [1994] model is a widely used (e.g. Longmore et al. [2006], Turc et al. [2014], Vandas et al. [2020]) magnetostatic model that assumes a magnetic field in vacuum. This model is also used to predict the magnetic field only at the magnetopause, rather than in the global magnetosheath, in what is often referred to as the Cooling et al. [2001] model. This restricted version of the Kobel and Fluckiger [1994] model has been used in several studies of the magnetic reconnection process (e.g. Fuselier et al. [2019, 2021]; Qudsi et al. [2023]; Trattner et al. [2007, 2012a,b, 2016, 2017, 2021]).

The Kobel and Fluckiger [1994] model uses a magnetic scalar potential Ψ (Equation B.1) defined between parabolic and confocal approximations of the magnetopause and bow shock surfaces to compute the magnetosheath magnetic with a gradient in parabolic coordinates.

$$\Psi = B_{0x} C \left(\frac{\sigma^2 - \tau^2}{2} - \sigma_0^2 \ln \frac{\sigma}{\sigma_0} \right) + \left(B_{0y} \cos\varphi + B_{0z} \sin\varphi \right) C\tau \left(\sigma + \frac{\sigma_0^2}{\sigma} \right) \tag{B.1}$$

In Equation B.1, B_{0x}, B_{0y}, and B_{0z} represent the components of the IMF, σ_0 and C are constants that can be computed with Equation B.4, and σ, τ, and φ correspond to the parabolic coordinates. Equations B.2 detail the relation between the cartesian (x, y, and z) and parabolic coordinates. In the Equations B.2, B.3 and B.4, x_0 and x_1 correspond to the standoff distances, y_0 and y_1 to the terminator ($x = 0$) distances, x_c and x_s to the focal points of the magnetopause and bow shock, respectively.

$$\begin{cases} x &= x_c + \frac{\sigma^2 - \tau^2}{2} \\ y &= \sigma\tau\cos\varphi \\ z &= \sigma\tau\sin\varphi \end{cases} \tag{B.2}$$

$$\begin{cases} x_c &= x_0 - \frac{y_0^2}{4x_0} \\ x_s &= x_1 - \frac{y_1^2}{4x_1} \end{cases} \tag{B.3}$$

$$\begin{cases} C &= \frac{\sigma_1^2}{\sigma_1^2 - \sigma_0^2} \\ \sigma_0 &= \sqrt{2(x_0 - x_c)} \\ \sigma_1 &= \sqrt{2(x_1 - x_s)} \end{cases} \tag{B.4}$$

The boundaries' parabolic surfaces in the Kobel and Fluckiger [1994] model must be confocal, meaning that $x_s = x_c$. Additionally, this focal point must be set such as $x_c = x_0/2$.

Equation B.5 detail the calculation of the magnetic field with the gradient in parabolic coordinates with h_σ, h_τ and h_φ corresponding to the Lamé coefficients defined in Equation B.6. Equation B.7 describes the transformation for converting the magnetic field from parabolic to cartesian coordinates.

$$\begin{cases} B_\sigma &= \frac{1}{h_\sigma}\left(B_{0x}C\left(\sigma-\frac{\sigma_0^2}{\sigma}\right)+\left(B_{0y}\cos\varphi+B_{0z}\sin\varphi\right)C\tau\left(1-\frac{\sigma_0^2}{\sigma^2}\right)\right) \\ B_\tau &= \frac{1}{h_\tau}\left(-B_{0x}C\tau+\left(B_{0y}\cos\varphi+B_{0z}\sin\varphi\right)C\left(\sigma+\frac{\sigma_0^2}{\sigma}\right)\right) \\ B_\varphi &= \frac{1}{h_\varphi}\left(\left(-B_{0y}\sin\varphi+B_{0z}\cos\varphi\right)C\tau\left(\sigma+\frac{\sigma_0^2}{\sigma}\right)\right) \end{cases} \tag{B.5}$$

$$\begin{cases} h_\sigma &= \sqrt{\sigma^2+\tau^2} \\ h_\tau &= h_\sigma \\ h_\varphi &= \sigma\tau \end{cases} \tag{B.6}$$

$$\begin{cases} B_x &= B_\sigma\frac{\sigma}{h_\sigma}-B_\tau\frac{\tau}{h_\tau} \\ B_y &= B_\sigma\frac{\tau}{h_\sigma}\cos\varphi+B_\tau\frac{\sigma}{h_\tau}\cos\varphi-B_\varphi\sin\varphi \\ B_z &= B_\sigma\frac{\tau}{h_\sigma}\sin\varphi+B_\tau\frac{\sigma}{h_\tau}\sin\varphi+B_\varphi\cos\varphi \end{cases} \tag{B.7}$$

Since the magnetic scalar potential Ψ is exclusively valid between confocal and parabolic magnetopause and bow shock, the last step is to determine these boundaries with the equation system B.8 [Romashets and Vandas, 2019], which can be rewritten as Equation B.9. θ, R_{mp} and R_{bs} correspond to the azimuth angle (see 2.7.5), positional radius of the magnetopause, and bow shock, respectively.

$$\begin{cases} 4(x-x_0)(x_0-x_c)+y^2+z^2=0 \\ 4(x-x_1)(x_1-x_s)+y^2+z^2=0 \\ x_c=x_s=\frac{x_0}{2} \end{cases} \tag{B.8}$$

$$\sin^2(\theta)R_{mp,bs}^2+4(x_{0,1}-x_0/2)\cos(\theta)R_{mp,bs}-4(x_{0,1}-x_0/2)x_{0,1}=0 \tag{B.9}$$

Bibliography

Cooling, B. M. A., Owen, C. J., and Schwartz, S. J.: Role of the magnetosheath flow in determining the motion of open flux tubes, , 106, 18 763–18 776, https://doi.org/10.1029/2000JA000455, 2001. 173

Fuselier, S. A., Trattner, K. J., Petrinec, S. M., Pritchard, K. R., Burch, J. L., Cassak, P. A., Giles, B. L., Lavraud, B., and Strangeway, R. J.: Stationarity of the Reconnection X-Line at Earth's Magnetopause for Southward IMF, Journal of Geophysical Research (Space Physics), 124, 8524–8534, https://doi.org/10.1029/2019JA027143, 2019. 173

Fuselier, S. A., Webster, J. M., Trattner, K. J., Petrinec, S. M., Genestreti, K. J., Pritchard, K. R., LLera, K., Broll, J. M., Burch, J. L., and Strangeway, R. J.: Reconnection X-Line Orientations at the Earth's Magnetopause, Journal of Geophysical Research (Space Physics), 126, e29789, https://doi.org/10.1029/2021JA029789, 2021. 173

Kobel, E. and Fluckiger, E. O.: A model of the steady state magnetic field in the magnetosheath, , 99, 23 617–23 622, https://doi.org/10.1029/94JA01778, 1994. 173

Longmore, M., Schwartz, S. J., and Lucek, E. A.: Rotation of the magnetic field in Earth's magnetosheath by bulk magnetosheath plasma flow, Annales Geophysicae, 24, 339–354, https://doi.org/10.5194/angeo-24-339-2006, 2006. 173

Qudsi, R. A., Walsh, B. M., Broll, J., Atz, E., and Haaland, S.: Statistical Comparison of Various Dayside Magnetopause Reconnection X-Line Prediction Models, Journal of Geophysical Research (Space Physics), 128, e2023JA031644, https://doi.org/10.1029/2023JA031644, 2023. 173

Romashets, E. P. and Vandas, M.: Analytic Modeling of Magnetic Field in the Magnetosheath and Outer Magnetosphere, Journal of Geophysical Research (Space Physics), 124, 2697–2710, https://doi.org/10.1029/2018JA026006, 2019. 174

Trattner, K. J., Mulcock, J. S., Petrinec, S. M., and Fuselier, S. A.: Location of the reconnection line at the magnetopause during southward IMF conditions, , 34, L03108, https://doi.org/10.1029/2006GL028397, 2007. 173

Trattner, K. J., Petrinec, S. M., Fuselier, S. A., Omidi, N., and Sibeck, D. G.: Evidence of multiple reconnection lines at the magnetopause from cusp observations, Journal of Geophysical Research (Space Physics), 117, A01213, https://doi.org/10.1029/2011JA017080, 2012a. 173

Trattner, K. J., Petrinec, S. M., Fuselier, S. A., and Phan, T. D.: The location of reconnection at the magnetopause: Testing the maximum magnetic shear model with THEMIS observations, Journal of Geophysical Research (Space Physics), 117, A01201, https://doi.org/10.1029/2011JA016959, 2012b. 173

Trattner, K. J., Burch, J. L., Ergun, R., Fuselier, S. A., Gomez, R. G., Grimes, E. W., Lewis, W. S., Mauk, B., Petrinec, S. M., Pollock, C. J., Phan, T. D., Vines, S. K., Wilder, F. D., and Young, D. T.: The response time of the magnetopause reconnection location to changes in the solar wind: MMS case study, , 43, 4673–4682, https://doi.org/10.1002/2016GL068554, 2016. 173

Trattner, K. J., Burch, J. L., Ergun, R., Eriksson, S., Fuselier, S. A., Giles, B. L., Gomez, R. G., Grimes, E. W., Lewis, W. S., Mauk, B., Petrinec, S. M., Russell, C. T., Strangeway, R. J., Trenchi, L., and Wilder, F. D.: The MMS Dayside Magnetic Reconnection Locations During Phase 1 and Their Relation to the Predictions of the Maximum Magnetic Shear Model, Journal of Geophysical Research (Space Physics), 122, 11,991–12,005, https://doi.org/10.1002/2017JA024488, 2017. 173

Trattner, K. J., Petrinec, S. M., and Fuselier, S. A.: The Location of Magnetic Reconnection at Earth's Magnetopause, , 217, 41, https://doi.org/10.1007/s11214-021-00817-8, 2021. 173

Turc, L., Fontaine, D., Savoini, P., and Kilpua, E. K. J.: A model of the magnetosheath magnetic field during magnetic clouds, Annales Geophysicae, 32, 157–173, https://doi.org/10.5194/angeo-32-157-2014, 2014. 173

Vandas, M., Nemecek, Z., Safrankova, J., Romashets, E. P., and Hajoš, M.: Comparison of Observed and Modeled Magnetic Fields in the Earth's Magnetosheath, Journal of Geophysical Research (Space Physics), 125, e27 705, https://doi.org/10.1029/2019ja027705, 2020. 173

Appendix C

List of Acronyms

AU Astronomical Unit. 7

AUC Area Under Curve. 54, 55

BDF Backward Differentiation Formula. 85

EDR Electron Diffusion Region. 13, 15, 16, 47, 164, 165

FN False Negative. 54

FP False Positive. 54

FPR False Positive Rate. 54, 55

FTE Flux Transfer Event. 17

GBC Gradient Boosting classifier. 49–52, 55, 61–64, 77

GBR Gradient Boosting Regressor. 64, 65, 74, 77, 104

GSE Geocentric Solar Ecliptic. 68

GSM Geocentric Solar Magnetospheric. 42, 44, 45, 47, 68, 69, 72, 73, 85, 86, 103, 127

HCS Heliospheric Current Sheet. 7

IDR Ion Diffusion Region. 13

IGRF International Geomagnetic Reference Field. 129

IMF Interplanetary Magnetic Field. 1, 7–9, 14–16, 19, 21, 22, 24–29, 40, 41, 48–50, 56, 58, 60–62, 64, 66–73, 77, 84–96, 102–118, 124–127, 129–152, 159–168, 171, 173

ISEE International Sun-Earth Explorer. 15

KF94 **?**. 127, 129, 132–136, 140, 141, 150

KNN K-Nearest Neighbors. 74, 76, 77, 85, 86, 88, 127, 128

MCL Maximum Current Density Line. 131, 138, 140, 142–147

MHD Magnetohydrodynamics. 13, 14, 18, 20–22, 26, 27, 84, 90, 96, 127, 162, 168

MLT Magnetic Local Time. 128

MMS Magnetospheric Multiscale. 15, 16, 28, 47, 48, 54, 85, 103, 126, 164, 165, 167

MRL Maximum Reconnection Rate Line. 131, 139, 140, 142–147

MSL Maximum Magnetic Shear Line. 130–132, 134, 136, 137, 140, 142, 144–149, 151

MVA Minimum Variance Analysis. 20

PDL Plasma Depletion Layer. 2, 102, 108, 111, 114, 116, 117, 160

PGSM Pseudo-Geocentric Solar Magnetospheric. 69, 70, 77, 127, 130, 131

PIC Particle-in-cell. 21–23

RMSE Root Mean Square Error. 60, 64–67

ROC Receiving Operator Curve. 54

S91 **?**. 129, 132

SM Solar-Magnetic. 70

SWI Solar Wind Interplanetary magnetic field. 68–72, 77, 85, 86, 88, 103, 105

T96 **?**. 127, 129, 132–135, 141

THEMIS Time History of Events and Macroscale Interactions during Substorms. 27, 45, 46, 49–52, 54, 55, 63, 77, 85, 103, 126, 164, 165, 167

TN True Negative. 54

TP True Positive. 54

TPR True Positive Rate. 54, 55

université PARIS-SACLAY

ÉCOLE DOCTORALE
Astronomie
et Astrophysique
d'Île-de-France (AAIF)

Titre: Étude statistique des contraintes globales gouvernant la reconnexion magnétique à la magnétopause terrestre

Mots clés: Reconnexion Magnétique, Magnetopause, Magnétogaine, Magnetosphere

Résumé: La reconnexion magnétique est le mécanisme principal à l'œuvre dans le couplage entre la magnétosphère terrestre et le vent solaire magnétisé. L'efficacité du processus dépend grandement d'où il se déroule sur la magnétopause. La localisation de la ligne X en fonction des propriétés du milieu interplanétaire reste, à ce jour, l'une des questions clés de la physique magnétosphérique en raison de son caractère multi-échelles. L'une des principale difficulté tient dans notre quasi complète méconnaissance de l'environnement plasma et magnétique à grande échelle sur la magnétopause, et comment celles-ci évoluent avec les conditions interplanétaires. Ces propriétés sont aujourd'hui accessibles uniquement au travers de modèles, analytiques ou numériques. Cette thèse apporte de nouvelles contraintes observationnelle au problème de la localisation de la reconnexion en proposant la reconstruction et l'analyse des variations spatiales et grande échelle des variations spatiales du plasma et champ magnétique dans la magnétogaine et sur la magnétopause Un nouvelle méthode est développée afin de collecter et traiter deux décennies de données in-situ des missions Cluster, Double Star, THEMIS et MMS. Nous proposons en premier lieu de reconstruire la structure globale et 3D du champ magnétique drapé dans la magnétogaine, démontrant que l'hypothèse d'un drapé magnétostatique sans courant ne correspond pas aux observations pour environ 30% des orientations du champ interplanétaire. Nous examinons ensuite la variation, dans la magnétogaine, de l'amplitude du champ magnétique et de la densité du plasma, ainsi que leur dépendance en l'orientation du champ interplanétaire, en soulignant leur couplage non linéaire avec la reconnexion à la magnétopause. Enfin, la reconstruction des variations spatiales, sur la magnétopause, du cisaillement magnétique, de la densité de courant et du taux de reconnexion, en fonction de l'orientation du champ interplanétaire et du dipôle terrestre, nous a permis de mieux comprendre les rôles respectifs des contraintes globales et locales dans la localisation possible de la X-line.

Title: Statistical Study of the Global Constraints Governing Magnetic Reconnection at the Earth's Magnetopause.

Keywords: Magnetic reconnection, Magnetopause, Magnetosheath, Magnetosphere

Abstract: Magnetic reconnection is the primary mechanism through which the Earth's magnetosphere couples to the surrounding magnetized solar wind. The efficiency of this coupling largely depends on where the reconnection occurs on the magnetopause. Determining the location of so-called reconnection X-lines, as a function of the upstream interplanetary conditions, remains a long-standing challenge in magnetospheric physics due to its multiscale character. Progress is hampered by the fact that the plasma and field properties that constrain where reconnection can develop on the magnetopause are themselves poorly understood, and so far only accessed through global magnetohydrodynamics simulations. This thesis brings new observational constraints to this problem through the reconstruction of 3D global spatial variations of the plasma and magnetic field on the dayside magnetosheath and magnetopause. A new methodology was developed to collect and process two decades of in-situ measurements from the Cluster, Double Star, THEMIS, and MMS missions. We first reconstructed the global 3D magnetic draping of the interplanetary magnetic field (IMF) in the magnetosheath, whose structure is demonstrated to be controlled by the plasma flow in this region in a way that invalidates widely used vacuum magnetostatic draping assumptions in about 30% of the IMF orientations. We then examine the variation of magnetic field amplitude and plasma density in the magnetosheath and their dependence on the IMF orientation, and highlight their nonlinear coupling with magnetopause reconnection. Finally reconstructions of the spatial distributions magnetic shear, current density and reconnection rate on the dayside magnetopause,for different dipole tilts and IMF orientations, allowed us to better understand the interplay between local and global constraints on the location of reconnection X-lines.

Université Paris-Saclay
Espace Technologique / Immeuble Discovery
Route de l'Orme aux Merisiers RD 128 / 91190 Saint-Aubin, France